UNICAMP

UNIVERSIDADE ESTADUAL DE CAMPINAS
Faculdade de Engenharia Mecânica

SAON CRISPIM VIEIRA

Horizontal Two-Phase Slug Flow Travelling Wave

Escoamento Bifásico Horizontal no Padrão Pistonado Modelado como *Travelling Wave*

Campinas

2022

SAON CRISPIM VIEIRA

Horizontal Two-Phase Slug Flow Travelling Wave

Escoamento Bifásico Horizontal no Padrão Pistonado Modelado como *Travelling Wave*

Tese de Doutorado apresentada à Faculdade de Engenharia Mecânica da Universidade Estadual de Campinas como parte dos requisitos exigidos para a obtenção do título de Doutor em Engenharia Mecânica, na Área de Térmica e Fluidos

Thesis presented to the School of Mechanical Engineering of the University of Campinas in partial fulfillment of the requirements for the degree of Doctor in Mechanical Engineering with emphasis in Thermal and Fluids.

Supervisor/Orientador: Prof. Dr. Marcelo Souza de Castro

Co-supervisor/Coorientador: Prof. Dr. Adriano Todorovic Fabro

ESTE TRABALHO CORRESPONDE À VERSÃO FINAL DA TESE DE DOUTORADO DEFENDIDA PELO ALUNO SAON CRISPIM VIEIRA, E ORIENTADA PELO PROF. DR. MARCELO SOUZA DE CASTRO.

Campinas

2022

Ficha catalográfica
Universidade Estadual de Campinas
Biblioteca da Área de Engenharia e Arquitetura
Rose Meire da Silva - CRB 8/5974

V673h

Vieira, Saon Crispim, 1985-
Horizontal two-phase slug flow travelling wave / Saon Crispim Vieira. – Campinas, SP : [s.n.], 2022.

Orientador: Marcelo Souza de Castro.
Coorientador: Adriano Todorovic Fabro.
Tese (doutorado) – Universidade Estadual de Campinas, Faculdade de Engenharia Mecânica.

1. Escoamento bifásico. 2. Cadeias de Markov. 3. Ondas viajantes. 4. Sistemas dinâmicos. I. Castro, Marcelo Souza de, 1986-. II. Fabro, Adriano Todorovic. III. Universidade Estadual de Campinas. Faculdade de Engenharia Mecânica. IV. Título.

Informações para Biblioteca Digital

Título em outro idioma: Escoamento bifásico horizontal no padrão pistonado modelado como travelling wave
Palavras-chave em inglês:
Two-Phase Flow
Markov chains
Travelling waves
Dynamical systems
Área de concentração: Térmica e Fluídos
Titulação: Doutor em Engenharia Mecânica
Banca examinadora:
Marcelo Souza de Castro [Orientador]
Oscar Maurício Hernandez Rodriguez
Jorge Luiz Balino
Angela Ourivio Nieckele
Marcelo Amorim Savi
Data de defesa: 15-08-2022
Programa de Pós-Graduação: Engenharia Mecânica

Identificação e informações acadêmicas do(a) aluno(a)
- ORCID do autor: https://orcid.org/0000-0001-8785-9237
- Currículo Lattes do autor: http://lattes.cnpq.br/1026695160236823

UNIVERSIDADE ESTADUAL DE CAMPINAS
FACULDADE DE ENGENHARIA MECÂNICA

TESE DE DOUTORADO

Horizontal Two-Phase Slug Flow Travelling Wave

Escoamento Bifásico Horizontal no Padrão Pistonado Modelado como *Travelling Wave*

Author/Autor: Saon Crispim Vieira

Supervisor/Orientador: Prof. Dr. Marcelo Souza de Castro
Co-supervisor/Coorientador: Prof. Dr. Adriano Todorovic Fabro

A Banca Examinadora composta pelos membros abaixo aprovou esta Tese de Doutorado:

Prof. Dr. Marcelo Souza de Castro
DE/FEM/UNICAMP

Prof. Dr. Oscar Mauricio Hernandez Rodriguez
EESC/USP

Prof. Dr. Jorge Luis Baliño
Poli/USP

Profa. Dra. Angela Ourivio Nieckele
PUC-Rio

Prof. Dr. Marcelo Amorim Savi
COPPE/UFRJ

A Ata de Defesa com as respectivas assinaturas dos membros encontra-se no SIGA/Sistema de Fluxo de Dissertação/Tese e na Secretaria do Programa da Unidade.

Campinas, 15 de Agosto de 2022

DEDICATÓRIA

Dedico este trabalho aos meus pais Eva e Manoel, à minha irmã Sávila e ao meu amor Nathalia Luiza Andreazza.

AGRADECIMENTOS

À minha família, embora distante, sempre em meus pensamentos, devo a eles tudo o que sou. Obrigado a meus pais Eva e Manoel e à minha irmã Sávila pelo suporte incondicional durante toda a minha vida.

A Nathalia Luiza Andreazza pelo amor, carinho, incentivo e compreensão. Sem você nada seria possível.

Aos meus amigos humanoides e peludos que tanto contribuíram nesta jornada, pela amizade, paciência, bons momentos e todo o ócio que me moldaram em quem sou.

Ao Prof. Dr. Marcelo Souza de Castro e ao Prof. Dr. Adriano Todorovic Fabro pela orientação, confiança, paciência, amizade, apoio e disposição incondicionais que contribuíram tanto para minha formação.

A banca examinadora, pela disponibilidade e indispensáveis contribuições para este trabalho.

A todos os professores e funcionários da Faculdade de Engenharia Mecânica – UNICAMP pelos ensinamentos e apoio que contribuíram tanto para meu desenvolvimento acadêmico e profissional.

À PETROBRAS pelo incentivo e apoio financeiro ao projeto de pesquisa que estimulou a realização deste trabalho.

Ao Programa de Pós-Graduação em Engenharia Mecânica pela oportunidade de formação e aperfeiçoamento profissional.

A todos colegas e amigos do CEPETRO e ALFA Research Group por todo o apoio, ajuda, amizade e ótimo ambiente de convívio que tornaram os dias de trabalho mais agradáveis.

RESUMO

Escoamentos bifásicos gás-líquido intermitentes são padrões comuns em geometrias horizontais e atraem atenção e grande esforço de pesquisa devido à sua importância para aplicações industriais e de engenharia. Um dos padrões de fluxo gás-líquido mais comuns e ao mesmo tempo complexos é o fluxo em golfadas, que é tipicamente modelado com base em uma célula unitária variando de uma bolha de gás alongada com um filme de líquido em padrão de fluxo segregado e uma golfada de líquido aerada. Ambos os padrões compõem uma estrutura repetitiva com notáveis características estocásticas de suas regiões alternadas. Nesta tese, uma abordagem de modelagem é proposta para o escoamento em golfadas em tubulações horizontais com o objetivo geral de investigar a dinâmica do perfil de ondas de fração de vazio, de um ponto de vista determinístico, e suas propriedades estatísticas, a partir de um modelo estocástico. Um modelo de dois fluidos determinístico rigoroso e parcimonioso para os padrões estratificado e disperso é proposto, além de um modelo estocástico simples, mas fisicamente inspirado, para o escoamento intermitente em tubulações horizontais considerando a transição entre os padrões segregado e disperso. Apesar das hipóteses fundamentalmente diferentes, mostra-se que uma conexão pode ser proposta entre os tempos de transição aleatórios e o comportamento caótico do modelo determinístico. A descrição da transição entre os dois padrões de fluxo na célula unitária é abordada, tal que um modelo de transição é proposto, fundamentado no conceito de *bublance* e os processos de conversão de energia correspondentes na região do comprimento de mistura após o salto hidráulico.

Para a abordagem determinística, um modelo para prever o escoamento horizontal bifásico gás-líquido *slug* como uma onda viajante é apresentado incluindo os efeitos de viscosidade e tensão superficial para toda a célula unitária nas regiões dispersas e estratificadas. O modelo de dois fluidos é desenvolvido para os padrões estratificado e disperso, incluindo todos os mecanismos físicos relevantes identificados para a formação, crescimento e propagação da célula unitária, levando a um modelo bem colocado e delimitado. Uma abordagem *bottom-up* é proposta, baseada nas ordens de grandeza de cada termo do modelo. Em seguida, são desenvolvidos sequencialmente os modelos que descrevem o fluxo dinâmico do sistema no espaço de fase para ambos os padrões em uma e duas dimensões.

Para o modelo estocástico, um modelo de cadeia de Markov de dois estados é proposto para representar a dinâmica estocástica do escoamento em golfadas desenvolvido em tubos horizontais. Cada estado representa as regiões do pistão de líquido ou da bolha alongada e as probabilidades

de transição ditam se um dado estado tende a manter-se ou mudar-se. Também, a ordem da cadeia de Markov é investigada. Estações de medição com dois sensores resistivos de fio duplo são usadas para obter a série temporal da fração de vazios e uma representação de dois estados correspondente. Mostra-se que o modelo de cadeia de Markov pode representar com sucesso as estatísticas de segunda ordem dos dados, como a autocorrelação e a densidade espectral de potência, dada uma escolha apropriada da ordem da cadeia. Subsequentemente, as estatísticas de algumas características de golfadas são estimadas usando a abordagem proposta e sua interpretação como variáveis aleatórias derivadas do processo estocástico de fração de vazios é discutida.

Uma análise do padrão de golfadas como um sistema dinâmico no espaço de fases é posteriormente realizada e comparada com os mesmos dados experimentais utilizados para a identificação do modelo estocástico proposto. A estimação da dimensão adequada do sistema não linear é apresentada e discutida. A dimensão do sistema e o caos são quantificados e a reconstrução do espaço de fase é discutida. Mostra-se que a variabilidade nos tempos de transição entre o centro de duas órbitas na dinâmica caótica tridimensional do espaço de fase reconstruído está diretamente relacionada aos tempos de transição estocásticos descritos pelo modelo de cadeia de Markov de dois estados proposto. Por fim, os resultados numéricos dos modelos analíticos uni e bidimensionais no espaço de fases são apresentados e os resultados são interpretados em termos das séries temporais experimentais. As séries temporais de alguns parâmetros de fluxo relevantes são obtidas baseadas em modelos e então usadas para discutir a física relevante para os padrões de escoamento segregado e disperso, além dos fenômenos de transição. Mostra-se que o limiar de transição proposto depende da direção da transição entre os padrões, indicando assim o fenômeno da histerese. Para o modelo unidimensional, a solução do perfil de onda da fração de vazio da célula unitária obtida representa um avanço em relação ao modelo atualmente disponível. No entanto, a oscilação da fração de vazio não é possível devido à topologia do sistema dinâmico unidmensional. Para o modelo bidimensional, obtém-se uma solução periódica e destaca-se a importância da viscosidade turbulenta para a estabilização do sistema. Um diagrama de bifurcação do modelo estratificado bidimensional também é investigado. Tal diagrama é construído com os pontos fixos e suas estabilidades correspondentes, onde destacam-se as principais características do sistema dinâmico e as condições necessárias para o perfil de onda oscilatório da fração de vazio. Posteriormente, o modelo bidimensional é integrado utilizando os critérios de transição propostos. Os resultados obtidos remontam uma

célula unitária típica e mostraram que esta estratégia é muito promissora para outros esquemas numéricos. Este trabalho abre caminho para mais interpretações físicas e *insights* sobre a dinâmica complexa do escoamento em golfadas.

Palavras–chave: Escoamento bifásico, Cadeias de Markov, Ondas viajantes, Sistemas dinâmicos.

ABSTRACT

Intermittent flows are common patterns in horizontal geometries and attract attention and great research effort due to its importance for industrial and engineering applications. One of the most common and at same time complex gas-liquid flow pattern is the slug flow, which is typically modelled based on a unit cell varying from an elongated gas bubble with a liquid film in segregated flow pattern and an aerated liquid slug. Both patterns compose a whole repeating structure with remarkable stochastic characteristics of its alternating regions. In this thesis, a two-fold modelling approach is proposed for the slug flow in horizontal pipes with the overall aim of investigating the void fraction wave profile dynamics, from a deterministic point of view, and its statistical properties, from a stochastic model. A rigorous and parsimonious deterministic two-fluid model for the stratified and dispersed patterns is proposed in addition to a simple but physically insightful stochastic model for slug flow in horizontal pipes transition times between the segregated and dispersed flow patterns. Despite of fundamentally different assumptions, it is shown a connection between the random transition times and the chaotic behaviour of the deterministic model. The description of the transition between the two flow patterns in the slug is addressed, where a physically and data-driven based transition model is proposed, based on the concept of bublance and the corresponding energy conversion processes in the region of the mixing length after the hydraulic jump.

For the deterministic approach, a model for predicting the horizontal two-phase gas-liquid slug flow as a travelling wave is presented including the viscosity and surface tension effects for the entire unity cell on the dispersed and stratified regions. The two-fluid model is developed for the stratified and dispersed patterns, including all the identified relevant physical mechanisms for the unit cell formation, growth and propagation, leading to a well-posed and bounded model. A bottom-up approach is proposed, based on the orders of magnitude of each model term. Then, the models are sequentially developed to describe the dynamical system flow in phase space for both patterns in one and two dimensions.

For the stochastic model, a two-state Markov chain model is proposed to represent the stochastic dynamics of the developed slug flow in horizontal pipes as a simple but insightful description of the phenomenon. Each state represents either the liquid slug or the elongated bubble regions and the transition probabilities dictate a given discrete time measurement to stay at a given state or change. Also, the order of the Markov chain is investigated. Measurement stations with two double wire resistive sensors are used to obtain the void fraction time series and a corresponding two-state representation. It is shown that the Markov chain model can successfully represent second-order statistics of the measurement, such as the autocorrelation and power spectral density, given an appropriate choice of the chain order. Subsequently, statistics of some slug flow features are estimated using the proposed approach and their interpretation as random variables derived from the void fraction stochastic process is discussed.

An analysis of the slug flow pattern as a dynamical system on the phase space is subsequently performed and compared to the same experimental data used to the identification of the proposed stochastic model. The estimation of the suitable dimension of the non-linear system is presented and discussed. The system dimension and chaos is quantified and the reconstruction of the phase space is discussed. It is shown that the variability in the transition times between the center of two orbits in the three-dimensional chaotic dynamics of the reconstructed phase space is directly related to the stochastic transition times described by the proposed two-state Markov chain model. Finally, the numerical results from the one and two-dimensional phase-space analytical models are presented and the results are interpreted in terms of the experimental time series. Model-based time series of some relevant flow parameters are obtained and then used to discuss the relevant physics for segregated and dispersed flow patterns and transition phenomena. It is shown that the proposed transition threshold depends on the direction of the transition between the patterns, thus indicating the phenomenon of hysteresis. For the one-dimensional model, the obtained slug unit void fraction wave profile solution represents an advance when compared to the currently available model. However, the oscillation of the void fraction is not possible due to the topology of the dynamical system. For the two-dimensional model, a periodic solution is obtained and the importance of the turbulent viscosity for the stabilization of the system is highlighted. A bifurcation diagram of the two-dimensional stratified model is also investigated. It is constructed with the fixed points and their corresponding stability and it highlights the main features of the dynamical system and the necessary conditions for the void fraction profile and oscillation. Subsequently, the two-dimensional model is integrated using the proposed transition criteria. The obtained results follows very closely a typical unit cell and and it shown that this strategy is very promising for further numerical schemes. The proposed investigation paves the way for further physical interpretation and insights on the complex dynamics of the slug flow.

Keywords: Two-phase flow, Markov Chain, Travelling Wave, Dynamical System.

LIST OF FIGURES

LIST OF TABLES

LIST OF ABBREVIATIONS AND ACRONYMS

PDE	Partial Differential Equation
ODE	Ordinary Differential Equation
SNR	Signal-to-noise ratio
PSD	Power spectral density
CPSD	Cross-power spectral density
BCC	Basic cross-correlation
GCC	Generalised cross-correlation methods
SCOT	Smoothed coherence transform
KDE	Kernel density estimator
PDF	Probability density function
SS	Stratified separated flow pattern
DB	Dispersed bubbles flow pattern
MC	Markov chain
CFD	Computational Fluid Dynamics
Petrobras	Petróleo Brasileiro S.A
Unicamp	Universidade Estadual de Campinas

LIST OF SYMBOLS

g	Gravitational acceleration
D	Pipe internal diameter
A	Pipe internal cross sectional area
S	Pipe internal perimeter
θ	Pipe inclination from the horizontal
$\mathbb{E}$	Probability expectancy
Var	Variance
Cov	Covariance
$\mathscr{F}$	Fourier transform
j	Imaginary unit
$*$	Convolution operator
$\langle\rangle_k$	Area average operator for phase k
$\frac{\mathrm{D}}{\mathrm{D}t}$	Total derivative operator
$\langle\rangle^i$	Composite space-time average operator
∇_s	Surface divergent operator
t	Time
τ	Time lag or delay
ω	Circular frequency
z	Length along pipe axis
κ	Wavenumber
η	Length along pipe axis in a travelling wave reference frame

ξ	Dimensionless travelling wave space coordinate
k	Phase subscript: 1 - liquid; 2 - gas
α_k	Volume fraction of phase k
α	Gas volume fraction or the void fraction
w	First order derivative of the void fraction on the dimensionless travelling wave space coordinate
u	Second order derivative of the void fraction on the dimensionless travelling wave space coordinate
h	Liquid height
$\tilde{h}$	Dimensionless liquid height
$\hat{\gamma}^i$	Average interface curvature
$\hat{\gamma}$	Dimensionless average interface curvature
ρ_k	Specific mass of phase k
$\Delta\rho$	Difference of specific masses
v_k	In situ velocity of phase k
v_s	Slip velocity
v_k^i	In situ interface velocity of phase k
j_k	Superficial velocity of phase k
Γ_k	Mass source rate per volume of phase k
p_k	Pressure of phase k
p	Reference pressure
p_k^i	Interface pressure of phase k
τ_{zz}^k	Viscous stress tensors zz component of phase k

T_{zz}^{k}	Turbulent Reynolds tensors zz components of phase k
$\hat{M}_k$	Averaged specifc momentum transfer rate through the interface of phase k
σ_{21}	Fluids interfacial tension
μ_k	Dynamic viscosity of phase k
ν_k^T	Turbulent kinematic viscosity of phase k
C_{ν}^{eq}	Total equivalent kinematic viscosity velocity profile covariance shape factors of phase k
ν_k^{eq}	Total equivalent kinematic viscosity of phase k
$\vec{Q}$	Vectors of conserved variables
$\vec{F}$	Vectors of fluxes
$\vec{S_S}$	Vectors of sources
τ_k^i	Interface shear stress of phase k
τ_k^w	Wall shear stress of phase k
ν_k	Kinematic viscosity of phase k
A_k	Pipe cross sectional area occupied by phase k
S_K	Pipe internal wetted perimeter of phase k
S_i	Interface perimeter
f_k^w	Wall fanning friction factor of phase k
f_i	Interface fanning friction factor
r_b	Bubble average radius
d_b	Bubble average diameter
C_p	Pressure difference coefficient at the gas-liquid interface for bubbly flows
C_D	Bubble drag coefficient

C_V	Bubble added mass coefficient
C_C	Bubble collision coefficient
ϵ	Dissipated turbulent specific energy rate
$v'^{\bar{2}}_{\kappa}$	Mean squared turbulent velocity fluctuation on wavenumber κ
v^*	Turbulent friction velocity
τ^t_κ	Turbulent stress on wavenumber κ
τ^s_κ	Surface tension stress on wavenumber κ
d_{max}	Maximum stable bubble diameter
d_s	Maximum non-deformable spherical bubbles diameter or Broadkey diameter
d_{ce}	Limiting segregation bubble diameter
d_{ct}	Critical segregation bubble diameter
d_{cts}	Critical segregation bubble swarm diameter
F_B	Bubble buoyancy force
F_D	Bubble drag force
F_T	Bubble turbulent force
e_k	Averaged total specific energy of phase k
$\vec{v}_k$	Mean velocity vector of phase k
$\vec{v}_i$	Interface velocity
h_k	Averaged specific enthalpy of phase k
τ_k	Deviatoric viscous stress tensor of phase k
T_k	Turbulent stress tensor of phase k
$\vec{q}_k$	Averaged total specific energy vector diffusion flux of phase k

E_k^i	Averaged total specific energy flux through the interface of phase k
Q_k^w	Averaged total specific energy flux through the pipe inner wall of phase k
$S_k^{\Delta\nu}$	Net specific power source of phase k
u_k	Averaged specific internal energy of phase k
e_k^{Re}	Averaged Turbulent fluctuations specific kinetic energy of phase k
q_k^T	Averaged axial energy flux thermal component of phase k
q_k^{Re}	Averaged axial energy flux turbulent kinetic energy component of phase k
e_k^i	Averaged specific energy fluxes through the interface carried by the mass flux of phase k
q_k^i	Averaged heat flux through the interface of phase k
E_s	The net interface specific power exchange
$S^{\Delta\nu}$	Total mixture net specific power source
E_t	Mixture turbulent specific energy
E_s	Surface specific energy
S_{mf}	Net energy source dissipated at the mean flow
η_{eff}^i	Energy transfer efficiency of process i
H_i	Surface potential energy
h_i	Specific surface potential energy
A_i	Interfacial area
a_i	Density of interfacial area,
s_i	Source of interfacial area density
$\bar{e}_k^{Re}$	Stationary homogeneous component of the specific turbulent kinetic energy
${e'}_k^{Re}$	Non-stationary and non homogeneous undefined component of the specific turbulent kinetic energy

ϵ	The averaged turbulence kinetic energy dissipation rate
J	Mixture superficial velocity
V_{TB}	Taylor bubble velocity
β	Intermittency factor
f_U	Unit cell frequency
L_i	Length of structure i: U - Unit cell; F - Taylor bubble; S - Liquid piston; M - Mixture zone at the liquid piston;
u_k	Relative velocity of phase k in relation to V_{TB}
M_k	Relative volumetric flux of phase k in relation to V_{TB}
Re	Reynolds dimensionless number
Fr	Froude dimensionless number
We	Weber dimensionless number
E_o	Eötvös dimensionless number
ρ	Ratio of specific masses
ν	Ratio of kinematic viscosities
m_k	Relative flux Froude dimensionless number
I_d	Dynamically evaluated classification function that indicates the flow pattern transition
$F_{CA}\left(\alpha\right)$	Convective acceleration function term of the travelling wave model
$F_{FB}\left(\alpha\right)$	Force balance function term of the travelling wave model
$F_{\Delta P}\left(\alpha\right)$	Pressure difference between phases function term of the travelling wave model
$F_{Vi}\left(\alpha\right)$	ith viscosity dissipation function term of the travelling wave model
$F_{SFi}\left(\alpha, w\right)$	ith surface force term of the travelling wave model

$R_{1,2}(\tau)$	Cross-correlation
$S_{1,2}(\omega)$	Cross-power spectral density (CPSD)
$\Psi_g(\omega)$	Frequency weighing function
$\gamma_{1,2}(\omega)$	Ordinary coherence function
$\delta(\tau)$	Dirac delta function
$h_S(\tau)$	Impulse response function
x_n	System state: liquid slug ($x_n = 0$), Taylor bubble ($x_n = 1$)
X_n	System state random variable
$P\left(X_n = x_n \mid X_{n-1} = x_{n-1}\right)$	Transition conditional probability
t_{lg}	State transition probability from liquid slug to Taylor bubble
t_{gl}	State transition probability from Taylor bubble to liquid slug

CONTENTS

1 INTRODUCTION

Multiphase flows are of common occurrence in numerous natural and industrial processes. One of the most common is the gas-liquid flow, where the phases are distributed in different geometric arrangements, which are called flow patterns. These patterns depend on fluids properties (density, viscosity, surface tension) and flow conditions (flow rates, pipe diameter and slope, etc) (Shoham, 2006; Ishii; Hibiki, 2011). In gas-liquid horizontal flows the stratified, annular, bubbles and intermittent flows are the most common patterns, each one with its own characteristics. The correct definition of the flow pattern and its characteristics is of ultmost importance for industrial purposes, as the presence of an specific pattern may lead to severe problems. In the case of the oil industry, flow assurance problems are related to the occurrence of an specific flow pattern (Shippen; Bailey, 2012). Efforts have been made during the last decades to propose models for the transition between such flow patterns (Taitel; Dukler, 1976; Barnea, 1987), as well as modelling the flow pattern itself leading to pressure drop and void fraction calculation, for example (Shoham, 2006).

One of the most common and at same time complex gas-liquid flow pattern is the slug flow, as depicted in the Fig. 1.1. The slug flow is typically modelled based on a unit cell varying from an elongated air bubble with a liquid film in segregated flow pattern (considered stratified flow) of length L_F, to a liquid slug with/without dispersed gas bubble swarm that detach from the bigger elongated air bubble due to the turbulent recirculation zone forming the aerated liquid piston, of length L_S. Both patterns compose a whole almost periodic structure with length L_U called a unit cell (Taitel; Barnea, 1990; Fabre; Liné, 1992; Fagundes Netto *et al.*, 1999). These structures are connected by a turbulent recirculating zone with length L_M where the flow pattern transition occurs (Wallis, 1969; Shoham, 2006). One remarkable interesting aspect of the slug flow is its stochastic characteristic of alternating regions (Sarica *et al.*, 2011; Soedarmo *et al.*, 2019).

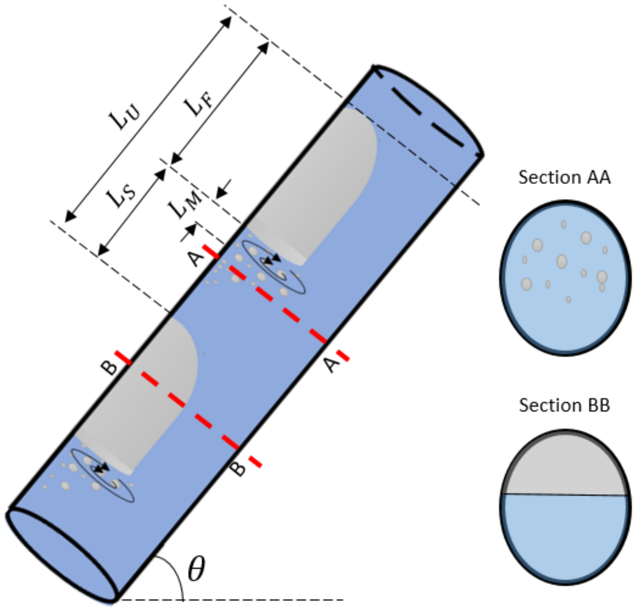

Figure 1.1 – Slug flow pattern unit cell with the separated, dispersed and recirculating zones.

The void fractions are represented by α_S, α_F and α_U for the liquid slug, Taylor bubble or film and unit cell regions, respectively. The liquid and gas average velocities at the liquid slug region are v_L and v_B, respectively. At the elongated bubble region, the average velocities of the liquid and gas are v_F and v_G, respectively. Finally, the elongated bubble translational velocity is denoted by V_{TB}. It is commonly assumed that at the elongated bubble, the liquid and gas velocities vary with the film thickness variation. This is not the case at the slug region, where it is assumed that the flow can be considered homogeneous, making v_L and v_B approximately equal (Taitel; Barnea, 1990; Shoham, 2006).

The elongated gas bubble with a liquid film in segregated flow pattern is called Taylor bubble, being the bigger propagating bullet shape gas pocket, whose shape is due to the geometric profile of the liquid height waveform. It can be divided in the nose, body, hydraulic jump and tail regions as illustrated in Figure 1.2 (Taitel; Barnea, 1990; Fagundes Netto *et al.*, 1999):

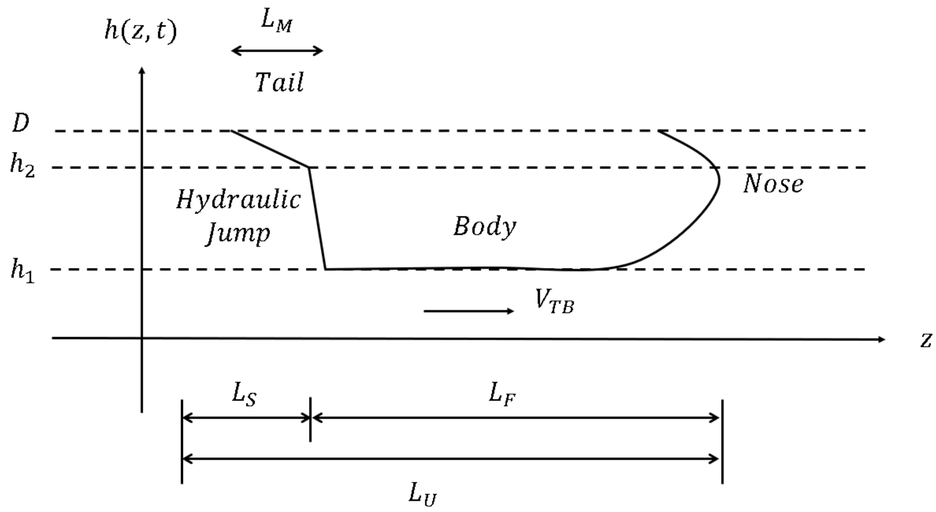

Figure 1.2 – Taylor bubble regions.

where, in Fig 1.2, D is the pipe diameter, h_1 is the liquid film height and h_2 is the liquid height where the bubble tail starts, after the hydraulic jump.

1.1 Literature Review

The study of the horizontal slug flow pattern formation mechanisms has historically been carried out with the investigation of the point at which the stratified flow pattern becomes unstable using a linear stability model framework, leading to Kelvin Helmholtz instability theory. It is adopted in flow pattern maps to delineate the boundary between the stratified and slug flow patterns. The transition occurs as the gas accelerates over the wave crest, where the pressure in the gas phase decreases due to the Bernoulli effect. If this effect is greater than gravity force then the wave tends to grow, otherwise it will decay. In order to the flow in the slug pattern to form, it is necessary that the interfacial waves around the stratified flow pattern equilibrium solution, i.e., at the elongated gas bubble, grow until they touch the upper dorsal line of the pipe, at which point there is a transition to the dispersed pattern forming the liquid piston (Taitel; Dukler, 1976; Barnea, 1987; Shoham, 2006).

1.1.1 Non-Linear Waves

The classical linear Kelvin Helmholtz instability theory neglects viscosity and surface tension effects, considering only small amplitudes disturbances around the stratified equilibrium state. Therefore, despite being able to assess whether such disturbances will grow or not, it cannot be used to evaluate higher amplitudes non-linear waves like the slug flow or roll waves. It theses cases, such effects cannot be neglected as the waves grow having bigger amplitudes with discontinuities and shock formation.

Non-linear roll waves were historically studied applying the traveling wave coordinate transformation in the shallow water system of PDE's for rectangular channels. Thus, the obtained non-linear system of ODE's fixed points, stability, system response and phase space portrait were evaluated. It has been shown that including only the parietal stresses and without considering the effective turbulent viscosity in the model, the system does not have a continuous periodic solution, although it is possible to construct a periodic discontinuous solution by joining the found non-periodic continuous solutions by parts. However, with the inclusion of the effective turbulent viscosity effects, there are continuous periodic solutions around Hopf and homoclinic bifurcations as stable limit cycles. It should be noted that no interfacial tension effects were considered in these studies (Dressler, 1949; Needham; Merkin, 1984; Needham *et al.*, 2008).

Giddings (2017) and Giddings e Billingham (2019) adopted a similar framework for studying the slug flow in rectangular channels neglecting the interfacial tension effects. In their work, the waves crest do not touch the upper dorsal line of the channel, hence, the transition to the dispersed pattern at the liquid piston is neglected. They reported the existence of periodic solutions around Hopf and homoclinic bifurcations as stable limit cycles, however the parameter search space was arbitrary. They solved the same model as a boundary valued problem and the full field shallow water equations were discretized by a finite difference scheme, obtaining similar results.

Vaidheeswaran *et al.* (2016) studied non-linear waves in the horizontal stratified flow pattern at a rectangular channels. They solved numerically, by a finite difference scheme, the fixed flux approximation of the two fluid model. The effects of the pressure difference between the phases due to gravity where considered as well as the interfacial tension effects by the long wave approximation and the effective turbulent viscosity. It was observed limit cycles solutions as periodic stable waves due to viscous dissipation at wave fronts and a chaotic response with the growth of the channel inclination, where the chaos was quantified by the largest Lyapunov exponent. Bertodano *et al.* (2016) extended these studies to a circular pipe geometry under similar premises obtaining similar qualitative results. It should be noted that these studies pointed out the physical mechanism that should be considered in the model, in order to have a well-posed and bounded model that describes the material/mass wave growth beyond the Kelvin–Helmholtz instability limit.

Robinson *et al.* (2008) studied non-linear material waves in the vertical dispersed bubbles flow pattern, commonly observed in a glass of Guinness draught beer and other applications. They solved numerically, by a finite difference scheme, the fixed flux approximation of the two fluid model. The effects of the interfacial pressure difference between the phases where included along with the effective turbulent viscosity, drag, added mass and collision forces. It should be noted that these studies pointed out the physical mechanism that should be considered in the model, in order to have a well-posed and bounded model that describes the correct mass/material wave speed (Park *et al.*, 1999; Robinson *et al.*, 2008; Bertodano *et al.*, 2013; Bertodano *et al.*, 2016).

1.1.2 Slug Capturing

The segregated and dispersed flow patterns alternating structures observed in the slug flow pattern can be fully modeled from the fundamental principles of mass and linear momentum conservation laws through the application of averaging operators, leading to the one dimensional Two-Fluid model (Bergles *et al.*, 1981; Ishii; Hibiki, 2011; Morel, 2015). The resulting equations can be fully solved in different ways leading to two approaches: slug tracking and slug capturing.

In the slug tracking model, the unit cell waveform and its statistics are imposed as boundary conditions, such information is propagated in a nonlinear waveguide modeled by the two-fluid model in a Lagrangian approach, where the Taylor bubble nose and tail are tracked as they propagate. Despite modeling the unit cells propagation, this model does not explain the physical mechanisms involved in the unit cells formation as they are imposed at the boundary. Thus, the accuracy of the results is affected and limited by the model used to generate those boundary conditions (Barnea; Taitel, 1993; Rosa *et al.*, 2015).

The slug capturing model was proposed in order to address the aforementioned issues by modelling the physical mechanisms that lead to the unit cell slug formation. However, this model requires finer meshes and high order numerical schemes with shock capture capabilities, which makes it computationally intensive. Issa e Kempf (2003) modelled the stratified flow pattern at a circular pipeline, solving the full two-fluid model numerically using a first-order fully implicit scheme in time, and a first-order finite volume upwind scheme in space, where it was included the effects of the pressure difference between the phases due to the gravity, one of the conditions necessary to have a well-posed model that develops the Kelvin-Helmholtz instability, as stated in the non-linear wave section 1.1.1. Bonizzi (2003), Bonizzi e Issa (2003) and Bonizzi *et al.* (2009) extended the model including the gas entrainment into the liquid slug body. Although satisfactory results were obtained, the results are affected by the closure relationships employed and several were tested. Carneiro (2006) included the interfacial tension effects by the long wave approximation adopting the same numerical scheme but neglecting the gas entrainment into the liquid slug body, obtaining satisfactory results.

1.1.3 Unit Cell Mechanistic Model

In order to obtain a model with reasonable accuracy and minimum complexity, that is, a parsimonious model for practical applications, the slug flow pattern is classically addressed using the unit cell model. It states a void fraction periodic travelling wave that is equivalent to a square-pulse train between the equilibrium void fraction solutions α_S and α_F for the alternating dispersed bubbles and segregated flow patterns, respectively, as illustrated in Figure 1.3. The intermittency factor β is the pulse train duty cycle (time fraction in which it is in an active high state or the stratified flow pattern), the unit cell length L_U is the inverse of the fundamental wavenumber κ, the Taylor bubble velocity V_{TB} is the void fraction non-dispersive wave phase velocity, which is equivalent to the kinematic wave velocity detailed in the Annex A, while the frequency of passage of the unit cell f_U is the inverse of the void fraction wave transit time period (Wallis, 1969; Shoham, 2006; Vieira *et al.*, 2021).

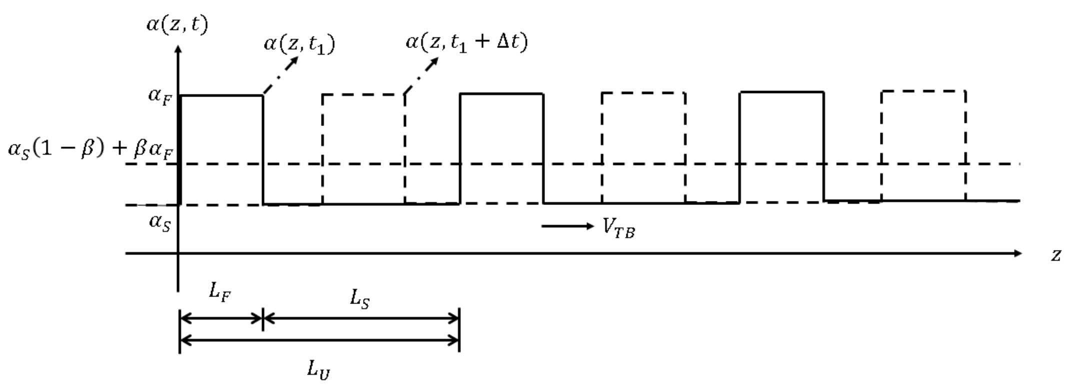

Figure 1.3 – Unit cell square pulse train model.

The flow pattern manifests itself as a void fraction waveform whose properties can be decomposed into an average term $\bar{\alpha}$ associated with oscillations around the average $\alpha'(z,t)$, that is

$$\alpha\left(z,t\right)=\bar{\alpha}+\alpha'\left(z,t\right). \tag{1.1}$$

The average void fraction is given by

$$\bar{\alpha}=\alpha_U=\frac{1}{L_u}\int_0^{L_u}\alpha\left(z,t\right)dz=\frac{1}{L_u}\left(\alpha_F L_F+\alpha_S L_S\right)=\alpha_F\beta+\alpha_S\left(1-\beta\right), \tag{1.2}$$

where α_F and α_S are the equilibrium void fraction solutions in the Taylor bubble and slug body regions, respectively, as shown in Figure 1.3. Assuming a wave mode expansion, such wave can be represented by the following ansatz (Vieira *et al.*, 2021)

$$\alpha'\left(z,t\right)=\sum_{n=1}^{\infty}A_n e^{j\left(\kappa_n z-\omega_n t\right)}, \tag{1.3}$$

$$\alpha'\left(z,t\right)=\sum_{n=1}^{\infty}A_n e^{j\kappa_n\left(z-c_p t\right)}, \tag{1.4}$$

where A_n is the complex Fourier Series coefficient, κ_n is the wavenumber, j is the imaginary unit and c_p is the wave phase velocity given by

$$c_p=\frac{\omega_n}{\kappa_n}=V_{TB}, \tag{1.5}$$

$$A_n=\left(\alpha_F-\alpha_S\right)\beta\mathrm{sinc}\left(n\pi\beta\right)e^{-jn\pi\beta}. \tag{1.6}$$

Therefore, the void fraction wave in the unit cell model approach is given by

$$\alpha\left(z,t\right)=\alpha_U+\sum_{n=1}^{\infty}A_n e^{j\kappa_n\left(z-V_{TB}t\right)}. \tag{1.7}$$

The unit cell variables for the Taylor bubble and slug body parts can be calculated using the classical models from the literature considering a constant stratified liquid film thickness at the Taylor bubble part, allowing that the same procedure can be repeated for all fields considered periodic, in this case, the velocities v_k for each phase (Taitel; Dukler, 1976; Gomez *et al.*, 2000; Shoham, 2006).

The unit cell mechanistic model can be extended by including the variable liquid film height profile at the Taylor bubble region. The traveling wave transformation is then applied in the higher order terms of the mass and momentum conservation equations for the stratified flow pattern only, neglecting the interfacial tension and effective turbulent viscosity effects, leading to a first order ODE. Similarly to the stated in the non-linear roll waves Section 1.1.1, non-linear dynamic systems with one-dimensional flows cannot have periodic solutions (Strogatz; Dichter, 2016). However, one can build a periodic discontinuous solution by joining the higher order found non-periodic continuous solutions by parts with closure experimental relations for the aerated liquid piston (Dukler; Hubbard, 1975; Taitel; Barnea, 1990).

1.1.4 Taylor Bubble Velocity Estimator

The Taylor bubble velocity can be estimated based on the time delay Δt_{TB} from measurements at two sensors at some known distance d as

$$V_{TB} = \frac{d}{\Delta t_{TB}}. \tag{1.8}$$

Several techniques have been developed during the last decades to estimate Δt_{TB} based on the cross-correlation of the measured signals, defined as $R_{1,2}(\tau)$

$$R_{1,2}(\tau) = \mathbb{E}\left[\alpha(z_1, t)\alpha(z_1 + d, t + \tau)\right], \tag{1.9}$$

where τ is the time lag, z_1 the first measurement station position and $\alpha(z_1, t)$ and $\alpha(z_1+d, t+\tau)$ are the void fractions measured at each measurement position, considering the second measured station sample is a space-time delayed version of the propagating field measured at the first station. The most trivial case is known as the basic cross-correlation (BCC) and it can be estimated from the inverse Fourier transform approach as

$$R_{1,2}(\tau) = \mathscr{F}^{-1}\left\{S_{1,2}(\omega)\right\}, \tag{1.10}$$

where $\mathscr{F}^{-1}$ stands for the inverse Fourier transform and $S_{1,2}(\omega)$ is the cross-power spectral density (CPSD). The CPSD is estimated from finite length measurements using the segment averaging method, also known as the Welch's method (Shin; Hammond, 2008). It consists in segmenting the full measurement in N_b separate time blocks, or segments, of same length T_b and then calculating the CPSD for the ith segment. For each segment, a Hanning window is used to reduce the effects of leakage and thus improving the resolution of closely spaced frequency components. Typically, an overlapping from 25% to 50% between subsequent segments is also applied, so that the information lost due to the shape of the windowing function can be recovered for the estimation. In this work, $1/3$ of overlap is used.

This basic estimator can be greatly enhanced by generalised cross-correlation methods (GCC) (Hassab; Boucher, 1979). In this approach, a frequency domain pre-filtering is applied on the CPSD prior to the inverse Fourier transform aiming at enhancing the signals with better signal-to-noise ratio (SNR) and to pre-whitening the signals are such that the peak of the cross-correlation is sharpened (Gao *et al.*, 2006). The generalised cross-correlation $R^g_{1,2}(\tau)$ in this case is given as

$$R^g_{1,2}(\tau) = \mathscr{F}^{-1}\left\{\Psi_g \omega S_{1,2}(\omega)\right\}, \tag{1.11}$$

where $\Psi_g(\omega)$ if the frequency weighing function.

Amongst the GCC methods, the smoothed coherence transform (SCOT) is very appealing for estimating the velocity of the Taylor bubble because it combines a pre-withening, which removes the dispersive effects of travelling waves, with a weighting by the coherence function, which decreases the influence of frequency bands with low SNR. For the case of travelling bubbles, or mass waves, the wave dispersion is mostly due to changes on the format of the bubble along the pipe. The SCOT weighing is given by:

$$\Psi_g(\omega) = \frac{\gamma_{1,2}(\omega)}{|S_{1,2}(\omega)|}, \tag{1.12}$$

where $\gamma_{1,2}(\omega)$ is the ordinary coherence function from the estimation of the CPSD (Shin; Hammond, 2008). The latter gives a frequency dependent measure of the linear relation between both sensors. It can be shown that $\gamma_{1,2}(\omega) = 1$ for linearly related noise free signals and $\gamma_{1,2}(\omega) = 0$ for uncorrelated signals. Values in between indicate that the signals are only partially linearly related. Typically, this is due to noise contamination, the presence of extra sources affecting one of the sensors and/or non-linearities. It can be shown that (Gao *et al.*, 2006)

$$R^g_{1,2}(\tau) = \mathscr{F}^{-1}\left\{\Psi_g(\omega) S_{1,2}(\omega)\right\} = h_S(\tau) * \delta(\tau + \Delta t_{TB}), \tag{1.13}$$

where $*$ stands for the convolution operator, $\delta(\tau + \Delta t_{TB})$ is the Dirac delta function and $h_S(\tau)$ is an impulse response function which depends on the noise content of the CPSD estimation. For $\gamma_{1,2}(\omega) = 1$, i.e., a perfect linear relation between the two sensors, it can be shown that $R^g_{1,2}(\tau) = \delta(\tau + \Delta t_{TB})$, i.e., the cross-correlation function is sharpened to a single peak at Δt_{TB}, which significantly highlights the delay estimate.

Both BCC and SCOT GCC estimators have analytical expressions available for the variance of the time delay estimate $\hat{\tau}_{peak}$ (Gao *et al.*, 2006)

$$\sigma_{\hat{\tau}_{peak}}^{BCC} = \left(\frac{\pi}{T} \frac{1-\gamma^2}{\gamma^2} \frac{\int_{\omega_0}^{\omega_1} \omega^2 \left| S_{1,2}(\omega) \right|^2 d\omega}{\int_{\omega_0}^{\omega_1} \omega^2 \left| S_{1,2}(\omega) \right| d\omega} \right)^{1/2}, \tag{1.14}$$

$$\sigma_{\hat{\tau}_{peak}}^{SCOT} = \left(\frac{3\pi}{T} \frac{1-\gamma^2}{\gamma^2} \frac{1}{(\omega_0 + \Delta\omega)^3 - \omega_0^3} \right)^{1/2}, \tag{1.15}$$

where T is the observation time on the CPSD estimate and γ is a constant value assuming the CPSD coherence function $\gamma_{1,2}(\omega) = \gamma$ in the frequency band $\omega_0 \leq \omega < \omega_1$ and zero elsewhere and $\Delta\omega = \omega_1 - \omega_0$.

Finally, it is important to highlight that the random error $\sigma_{\hat{\tau}_{peak}}^{BCC}$ or $\sigma_{\hat{\tau}_{peak}}^{SCOT}$ is insignificant compared to error due to the time resolution, the latter being only a function of the measurement bandwidth. In practice, given the measurement sampling frequency, it means that time resolution Δt has to be much shorter than the time for the Taylor travels from one sensor to the next, i.e., the time delay Δt_{TB}.

1.1.5 Markov Chain

Models for gas-liquid flows depend on several experimental data and closure laws. It is not different for the slug flow in which the unit cell lengths, translational velocities, slug frequencies and other parameters are experimentally adjusted. The measurement of such characteristics is performed by several means. As described by Soto-Cortes *et al.* (2021), there are visual (High-speed cameras and Doppler Velocimetry) and non-visual techniques such as electric (capacitive and resistance) probes and gamma-ray induction. In the most common field operations, visual access to the flow is not possible, thus, non-visual techniques are used to measure a time-series of determined quantity and then post-processing techniques are applied.

In the case of time-traced measurements of void fraction, common for slug flows, it is necessary to select a correct threshold to separate the elongated bubble and dispersed slug regions. In most cases, this is based on a subjective selection. To avoid such subjectivity Soto-Cortes *et al.* (2021) and Soedarmo *et al.* (2019) proposed objective methodologies based on statistical analysis to select the threshold for slug and pseudo-slug flows, respectively. However, the proposed approach does not investigate the multi-modality on the histogram around the regions of Taylor bubble, as recently observed by Rodrigues *et al.* (2020), for instance.

Several authors use a Markov chain theory to characterise the dynamic behaviour of different multiphase flow patterns, defined in terms of the transition probability distribution. Zhong-Ke *et al.* (2013) used the network generation based on Markov transition probability to build complex weighted directed networks. The results indicated that the constructed network can inherit the main characteristics of the time series. Moreover, the weighted clustering coefficient proved to be an important threshold to characterise the dynamic behaviour in transitions among different flow patterns. Mahvash e Ross (2008) proposed a continuous hidden Markov Chain-based pattern identification approach in two-phase flow. Measurements were based on a optical fiber probe to obtain a time series of whose amplitude is related to the instantaneous void fraction. The proposed approach has a good potential in identifying two-phase flow patterns. Recently, Ali *et al.* (2020) developed a data-driven methodology for classifying the dynamics and construction of the cluster-based model through the Markov Chain theory based on X-ray computed tomography of multiphase flows.

Despite its applications on several aspects of multiphase flows, the Markov chain approach has been used under the framework of complex time series analysis. Although such approaches give important contribution to the understanding of multiphase flows, a simpler but insightful stochastic model can lead to significant and fundamental insights on the complex physics of two-phase flow.

1.2 Objectives

The overall objective of this thesis is to investigate the void fraction wave profile in the horizontal slug flow pattern and its statistical properties, using a parsimonious model that captures the essential physical mechanisms that explain the unit cell formation, its evolution dynamics and the intermittent state transitioning between segregated and dispersed flow patterns, compared to available experimental data. Specifically, this thesis aims at:

- proposing a simple and physically insightful stochastic model for slug flow in horizontal pipes transition between the dispersed and segregated patterns;
- proposing a rigorous and parsimonious deterministic two-fluid model for the stratified and dispersed flow patterns;
- proposing a transition criterion between the segregate and dispersed bubble patterns in the slug flow;
- exploring the physical connections between the two models with seemingly unrelated assumptions.

1.3 Contributions

The results presented in this thesis add the following contributions:

- The two-fluid model is developed for the stratified and dispersed patterns, including all the identified relevant physical mechanisms for the unit cell formation, growth and propagation, leading to a well-posed and bounded model, as its building blocks for the stratified and dispersed bubbles flow patterns are well-posed and bounded according to the literature. No work reviewed considered all the mechanisms adopted for the flow patterns of interest all together for circular cross section pipelines with such rigour. In order to obtain a parsimonious model, reasonable assumptions were adopted for the slug flow pattern that allowed a great model simplification through the constant flow solution and the travelling wave transformation, without compromising generality. The assumptions are: incompressibility due to low phases velocities when compared to sound velocities, i.e., low Mach numbers and an approximately constant Taylor bubble propagation velocity, hypothesis that are supported by a vast literature and experimental observations. This allows converting a non-linear system of PDE's into ODE's by condensing the analysis of the system dynamics in a phase space for the void fraction series, a simpler model, where one is able to investigate the system dynamics in order to understand the slug flow pattern influencing parameters and the transitions between the separate and dispersed alternating flow patterns.

- In a bottom-up approach, based on the orders of magnitude of each model term, models are sequentially developed that describe the dynamical system flow in the phase space for both patterns in one, two and three dimensions.

- A physically based transition model is proposed, based on energy conversion processes in the region of the mixing length after the hydraulic jump.

- The available raw experimental data are analyzed and compared with the model, where all relevant parameters of the unit cell are identified, converting it to the traveling wave coordinate system, through a correlation-based estimation approach of the Taylor bubble velocity from two double wire measurement station, directly applied to the data with no need of pre-processing and analytical expressions are available for the error estimate.

- The system chaos was quantified and the phase space was reconstructed from the experimental data where the minimum number of dimensions for the deterministic dynamics of the slug flow was estimated as three, which has a physical interpretation, that the variability of the unit cell parameters derive from a three-dimensional chaotic dynamics and that such dimensionality is only achieved with the inclusion of the terms of the interfacial tensions.

- The system states where estimated by a simple data-driven non-parametric automatic approach and a two-state Markov chain model was proposed to represent the stochastic process model dynamics of developed slug flow in horizontal pipes aiming at a simple but intuitive description of the phenomenon, successfully modeling the statistical behavior of unit cell parameters. The Markov chain was related to the reconstructed phase space as a model for the transition probabilities between the equilibrium void fractions solutions at the center of the orbits separated by the transition surfaces.

1.4 Thesis Outline

This thesis is organised as follows:

- In Chapter 2, the slug flow hydraulic model is developed and presented for the stratified and dispersed flow patterns.

- In Chapter 3, a physically based transition model is proposed, based on energy conversion processes in the region of the mixing length after the hydraulic jump and the slug flow transitions are modelled as a two-state Markov chain. Some relevant statistical moments of the model are analytically derived.

- In Chapter 4, the results are presented and discussed. The available experimental data is analyzed and compared with the proposed analytical model, where all relevant parameters of the unit cell are identified, converting it to the traveling wave coordinate system. The proposed stochastic model based on the two-state Markov chain model is identified. The numerical results from the theoretical model are presented. A bottom up approach is proposed by increasing the system dimension in the phase space from its first order approximation.

- Finally, Chapter 5 gives some concluding remarks and suggestions for further work.

2 HYDRAULIC MODEL

In this chapter, the hydraulic model is presented. First, the two-fluid model for the stratified and dispersed flow patterns are developed and possible closure relationships are listed, being presented as PDE's systems in the conservative form. Subsequently, some simplifying assumptions are adopted in order to make the slug flow pattern analysis more tractable, ending on the constant flux solution. Then the equations are written in the traveling wave coordinate system. Finally, the obtained non-linear autonomous dynamical systems that represent the slug flow pattern is derived.

2.1 Two-fluid Model

In this section, the Two-fluid Model is reviewed and presented along with the suitable closure models. At the end, the resulting systems of PDE's is then presented in the conservative form.

As a result of the cross sectional area and time averaged mass and linear momentum conservation laws for the phase k at a pipeline, one has the one-dimensional Two-fluid Model (Bergles *et al.*, 1981; Ishii; Hibiki, 2011; Morel, 2015)

$$\frac{\partial}{\partial t}\left(\alpha_k \rho_k\right) + \frac{\partial}{\partial z}\left(\alpha_k \rho_k v_k\right) = \Gamma_k, \tag{2.1}$$

and

$$\frac{\partial}{\partial t}\left(\alpha_k \rho_k v_k\right) + \frac{\partial}{\partial z}\left(\alpha_k \rho_k v_k^2 + \alpha_k p_k\right) = \frac{\partial}{\partial z}\left[\alpha_k\left(\tau_{zz}^k + T_{zz}^k\right)\right] + \alpha_k \rho_k g_z + p_k \frac{\partial \alpha_k}{\partial z} + \hat{M}_k, \tag{2.2}$$

where α_k, ρ_k, v_k and p_k are respectively the volume fraction, specific mass, in-situ velocity and pressure, Γ_k is the mass source rate per unit volume, τ_{zz}^k and T_{zz}^k are the viscous and turbulent Reynolds stress tensors zz components and $\hat{M}_k$ is the averaged momentum transfer through the interface and the wetted pipe wall. The subscript k indicates the heavier and lighter phases, 1 and 2, respectively for the liquid and gas. The volume fractions are related as

$$\alpha_1 + \alpha_2 = 1. \tag{2.3}$$

In the following sections, the required closure models will be detailed for each flow pattern. Nonetheless, there are few closure model for the zz component of the cross sectional area averaged turbulent stress tensors for the two-phase flow case. To do so, the single phase flow inspired approach is adopted for each phase. It uses the Boussinesq hypothesis and yields an equivalent effective viscosity concept ν_k^{eq} of the phase k that encompasses the effects of the velocity profile covariance shape factors C_ν^{eq} and eddy turbulent viscosities ν_k^T (Fullmer *et al.*, 2011; Drew; Passman, 2014; Bertodano *et al.*, 2016), i.e.,

$$\alpha_k \left(\tau_{zz}^k + T_{zz}^k\right) = \rho_k \alpha_k \nu_k^{eq} \frac{\partial v_k}{\partial z}, \tag{2.4}$$

$$\nu_k^{eq} = C_\nu^{eq} \left(\nu_k + \nu_k^T\right). \tag{2.5}$$

It should be noted that the viscous and turbulent stresses transversal components are analytically eliminated by the averaging process, therefore, not adopting them is not a simplification.

2.1.1 Separated Phases Flow

In the separated phases flow case, as the interface is well defined, the total averaged momentum source $\hat{M}_k$ is given by the stresses and momentum flux through the interface and wall boundaries (Bergles *et al.*, 1981; Ishii; Hibiki, 2011)

$$\hat{M}_k = v_k^i \Gamma_k + \left(p_k^i - p_k\right) \frac{\partial \alpha_k}{\partial z} + \tau_k^i \frac{S_i}{A} + \tau_k^w \frac{S_k}{A}, \tag{2.6}$$

where, regarding the phase k, p_k^i and v_k^i are, respectively, the interface pressure and velocity, τ_k^i and τ_k^w are the shear stresses at the interface and wall, S_i and S_k are the interface and wetted wall perimeters, respectively. Considering a flat gas-liquid interface, the pipe cross section geometry is illustrated in Figure 2.1, where the flow geometric parameters are (Shoham, 2006)

$$\tilde{h} = 2\left(\frac{h}{D}\right) - 1, \tag{2.7}$$

$$S_i = D\sqrt{1 - \tilde{h}^2}, \tag{2.8}$$

$$S_2 = D \arccos\left(\tilde{h}\right), \tag{2.9}$$

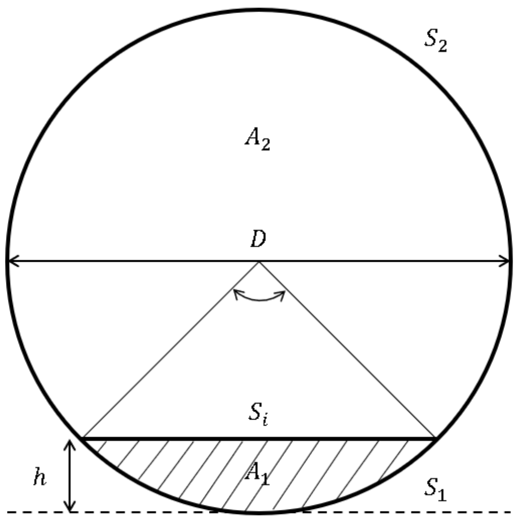

Figure 2.1 – Pipe cross section

$$S_1 = S - S_2, \tag{2.10}$$

and $\tilde{h}$, S_i, S_k and S are the dimensionless liquid height, interface, phase k and inner pipe wetted perimeters, respectively. The void fraction α is given by

$$\alpha = \left(\frac{S_2 - \tilde{h}S_i}{S}\right) = \frac{1}{\pi}\left[\arccos\left(\tilde{h}\right) - \tilde{h}\sqrt{1-\tilde{h}^2}\right]. \tag{2.11}$$

Despite the void fraction α and liquid height h having a two-way relationship, the function above does not have an explicit inverse, making it difficult to change variables

$$\frac{\partial \alpha}{\partial h} = -\frac{S_i}{A} = -\frac{4}{\pi D}\sqrt{1-\tilde{h}^2}. \tag{2.12}$$

The cross sectional area averaged pressure p_k of each phase k can be written with respect to a reference pressure added to a deviation due to the average hydrostatic gradient and the surface tension jump from the interface to the geometric center of area. The reference pressure is arbitrary, but it is convenient to choose the pressure of the gas phase at the interface p_2^i, considering that the cross section hydrostatic variation in the gas phase is much smaller and usually neglected. However, this choice leads to the fact that the pressure variation in the liquid phase is not only due to the hydrostatics, but also to the pressure jump at the interface caused by surface tension. Using the area average operator $\langle\rangle_k$ definition (Bergles *et al.*, 1981; Ishii; Hibiki, 2011)

$$\langle\rangle_k = \frac{1}{A_k}\int_{A_k} dA_k = \frac{1}{\alpha_k A}\int_{A_k} dA_k, \tag{2.13}$$

where A_k is the cross sectional area occupied by the phase k. Therefore, the averaged pressure fields in the domain occupied by each phase k are given by (Bonizzi, 2003)

$$p_k = \langle p\rangle_k = \left\langle p_k^i + \rho_k g_y\,(h-y)\right\rangle_k = \left\langle p_k^i\right\rangle_k + \left\langle \rho_k g_y\,(h-y)\right\rangle_k . \tag{2.14}$$

Hence

$$p_1 = p_1^i + \frac{1}{\alpha_1 A}\int_0^{h(z)} \rho_1 g_y\,(h-y)\,b\,(y)\,dy, \tag{2.15}$$

and

$$p_2 = p_2^i + \frac{1}{\alpha_2 A}\int_{h(z)}^{D} \rho_2 g_y\,(h-y)\,b\,(y)\,dy, \tag{2.16}$$

where the interface pressures p_k^i and specific masses ρ_k are constants with respect to the vertical direction y, only varying in the axial z direction, and $b\,(y)$ is the cross sectional chord length. Both sides of the equations are rearranged and derived with respect to the axial z direction using the Leibniz rule

$$A\frac{\partial}{\partial z}\left(\alpha_1 p_1\right) = A\frac{\partial}{\partial z}\left(\alpha_1 p_1^i\right) + \frac{\partial}{\partial z}\left[\int_0^{h(z)} \rho_1 g_y\,(h-y)\,b\,(y)\,dy\right], \tag{2.17}$$

$$\frac{\partial}{\partial z}\left(\alpha_1 p_1\right) = \frac{\partial}{\partial z}\left(\alpha_1 p_1^i\right) + \alpha_1\rho_1 g_y\frac{\partial h}{\partial z}, \tag{2.18}$$

$$A\frac{\partial}{\partial z}\left(\alpha_2 p_2\right) = A\frac{\partial}{\partial z}\left(\alpha_2 p_2^i\right) + \frac{\partial}{\partial z}\left[\int_{h(z)}^{D} \rho_2 g_y\,(h-y)\,b\,(y)\,dy\right], \tag{2.19}$$

$$\frac{\partial}{\partial z}\left(\alpha_2 p_2\right) = \frac{\partial}{\partial z}\left(\alpha_2 p_2^i\right) + \alpha_2\rho_2 g_y\frac{\partial h}{\partial z}. \tag{2.20}$$

The difference between the pressure fields of each phase k at the interface can be modeled using the concept of interfacial tension through the Young-Laplace Equation (Bergles *et al.*, 1981; Ishii; Hibiki, 2011; Panton, 2013), i.e.,

$$p_1^i - p_2^i = -\sigma_{21}\hat{\gamma}^i, \tag{2.21}$$

$$\hat{\gamma}^i(z) = \frac{\frac{\partial^2 h}{\partial z^2}}{\left[1 + \left(\frac{\partial h}{\partial z}\right)^2\right]^{\frac{3}{2}}}, \tag{2.22}$$

where σ_{21} is the fluids interfacial tension and $\hat{\gamma}^i$ is the average interface curvature field that can be calculated from the non-linear relationship between the liquid height field h and the void fraction field α, Equation 2.11. The average curvature $\hat{\gamma}^i$ can be approximated using the long wave theory approximation, where for high wavelengths and small deviations from the equilibrium liquid height h the average curvature can be approximated by (Barnea; Taitel, 1994):

$$\hat{\gamma}^i(z) \approx \frac{\partial^2 h}{\partial z^2}. \tag{2.23}$$

However, the suitability of this approximation other than for stability analysis for small deviations from equilibrium positions is questionable. In the case of the slug flow pattern for example, where there are mass shocks and discontinuities in the void fraction fields, this assumption is no longer valid. However, even complete, the flat gas-liquid interface model has limitations, especially in the Taylor bubble nose region, where the curvature along the cross section is clearly also present, nevertheless, in this case, this is outside the scope of this work.

The phase k wall and interface shear stresses τ_k^w and τ_i are given (Wallis, 1969; Shoham, 2006)

$$\tau_k^w = -\frac{1}{2} f_k^w \rho_k v_k |v_k|, \tag{2.24}$$

$$\tau_i = \tau_2^i = -\tau_1^i = -\frac{1}{2} f_i \rho_2 (v_2 - v_1) |(v_2 - v_1)|, \tag{2.25}$$

where f_k^w and f_i are the phase k wall and interface Fanning friction factors, respectively. They are calculated using classical models from literature through the hydraulic diameter concept and the Colebrook–White equation, where the smooth interface friction factor is approximated by the gas phase friction factor using the slip velocity based Reynolds number (Taitel; Dukler, 1976; Shoham, 2006). For stratified flows with high void fractions, the liquid film friction is strongly affected by the gas-liquid interface friction, hence the classical model based on the

Colebrook–White equation is not suitable (Shoham, 2006). Therefore, the liquid film friction model should include the void fraction or the gas-liquid interface friction in its formulation, as it was done in the following examples:

- Ouyang e Aziz (1996) model:

$$f_1 = \frac{1.6291}{Re_{SL}^{0.5161}} \left[\frac{\alpha v_2}{(1-\alpha)\, v_1} \right]^{0.0926}, \tag{2.26}$$

$$Re_{SL} = \frac{\rho_1 (1-\alpha)\, v_1 D}{\mu_1}, \tag{2.27}$$

- Spedding e Hand (1997) model:

$$f_1 = \frac{24}{Re_{SL}}, \quad \text{if} \quad Re_L \leqslant 2100, \tag{2.28}$$

$$f_1 = 0.0262 \left[(1-\alpha)\, Re_{SL} \right]^{-0.139}, \quad \text{if} \quad Re_L > 2100, \tag{2.29}$$

$$Re_L = \frac{\rho_1 v_1 D_1}{\mu_1}, \tag{2.30}$$

- Nossen *et al.* (2000) model:

$$\frac{1}{\sqrt{f_1}} = \frac{1}{\sqrt{f_1^{Haaland}}} + \left(\frac{1}{\sqrt{f_1^{Hand}}} - \frac{1}{\sqrt{f_1^{Haaland}}} \right) \tanh\left(2000 Fr\right) \frac{S_i}{S_1}, \tag{2.31}$$

$$\frac{1}{\sqrt{f_1^{Haaland}}} = 2 \left\{ -1.8 \log \left[\frac{6.9}{Re} + \left(\frac{\epsilon}{3.7} \right)^{1.11} \right] \right\}, \tag{2.32}$$

$$Re = \frac{\rho_1 v_1 D}{\mu_1}, \tag{2.33}$$

$$Fr = \frac{\tau_i}{(\rho_1 - \rho_2)\, g D \cos\theta}. \tag{2.34}$$

Modeling the interfacial friction factor is more challenging, due to the fact that the gas-liquid interface is deformable with the eventual presence of waves that can amplify the averaged momentum transfer rate through the interface when compared to the smooth interface. Consequently, the wavy interface friction factor must take this effect into account because the slug flow interface is not smooth. It can be modelled by (Andritsos; Hanratty, 1987; Shoham, 2006; Bonizzi *et al.*, 2009)

$$f_i = f_2, \quad \text{if} \quad \alpha v_2 \leqslant j_{2t}, \tag{2.35}$$

$$f_i = f_2 \left\{ 1 + 15\sqrt{\frac{h}{D}} \left[\frac{\alpha v_2}{j_{2t}} - 1 \right] \right\}, \quad \text{if} \quad \alpha v_2 > j_{2t}, \tag{2.36}$$

$$j_{2t} = 5\sqrt{\frac{\rho_{20}}{\rho_2}}, \tag{2.37}$$

where j_{2t} is the critical gas superficial velocity that indicates the inception of wave growth, ρ_{20} and ρ_2 the gas density at a reference atmospheric pressure and operational conditions, respectively. Another possible closure relation is given by (Andreussi; Persen, 1987; Bonizzi *et al.*, 2009)

$$f_i = f_2, \quad \text{if} \quad F \leqslant 0.36, \tag{2.38}$$

$$f_i = f_2 \left\{ 1 + 29.7 \left(F - 0.36 \right)^{0.67} \left(\frac{h}{D} \right)^{0.2} \right\}, \quad \text{if} \quad F > 0.36, \tag{2.39}$$

$$F = \sqrt{\frac{\rho_2}{(\rho_1 - \rho_2)}} \frac{(v_2 - v_1)}{\sqrt{\alpha g \cos\theta \frac{A}{S_i}}}, \tag{2.40}$$

where F is the dimensionless Froude number. This model seems more appropriated as it is based on the inviscid Kelvin-Helmholtz instability and the slip velocity.

Considering the aforementioned assumptions for closure models, i.e., that there is no mass transfer between the phases $\Gamma_k = 0$ and the gas phase pressure at the interface p_2^i as the reference pressure p, then the averaged mass and linear momentum conservation laws for each phase are rewritten as

$$\frac{\partial}{\partial t} \left(\alpha_1 \rho_1 \right) + \frac{\partial}{\partial z} \left(\alpha_1 \rho_1 v_1 \right) = 0, \tag{2.41}$$

$$\frac{\partial}{\partial t}(\alpha_2\rho_2) + \frac{\partial}{\partial z}(\alpha_2\rho_2 v_2) = 0, \tag{2.42}$$

$$\begin{aligned}\frac{\partial}{\partial t}(\alpha_1\rho_1 v_1) + \frac{\partial}{\partial z}\left(\alpha_1\rho_1 v_1^2 + \alpha_1 p\right) =& -\alpha_1\rho_1 g\sin\theta - \alpha_1\rho_1 g\cos\theta\frac{\partial h}{\partial z} \\ &+ p\frac{\partial \alpha_1}{\partial z} + \frac{\partial}{\partial z}\left(\rho_1\alpha_1\nu_1^{eq}\frac{\partial v_1}{\partial z}\right) + \alpha_1\frac{\partial}{\partial z}\left(\sigma_{21}\hat{\gamma}^i\right) \\ &+ \frac{1}{2}\frac{S_i}{A}f_i\rho_2\left(v_2 - v_1\right)|(v_2 - v_1)| - \frac{1}{2}\frac{S_1}{A}f_1^w\rho_1 v_1|v_1|,\end{aligned} \tag{2.43}$$

$$\begin{aligned}\frac{\partial}{\partial t}(\alpha_2\rho_2 v_2) + \frac{\partial}{\partial z}\left(\alpha_2\rho_2 v_2^2 + \alpha_2 p\right) =& -\alpha_2\rho_2 g\sin\theta - \alpha_2\rho_2 g\cos\theta\frac{\partial h}{\partial z} \\ &+ p\frac{\partial \alpha_2}{\partial z} + \frac{\partial}{\partial z}\left(\rho_2\alpha_2\nu_2^{eq}\frac{\partial v_2}{\partial z}\right) \\ &- \frac{1}{2}\frac{S_i}{A}f_i\rho_2\left(v_2 - v_1\right)|(v_2 - v_1)| - \frac{1}{2}\frac{S_2}{A}f_2^w\rho_2 v_2|v_2|.\end{aligned} \tag{2.44}$$

Note that the two fluid model equations above form a system of PDE's in the conservative form with a source term

$$\frac{\partial \vec{Q}}{\partial t} + \frac{\partial \vec{F}}{\partial z} = \vec{S_S}, \tag{2.45}$$

where the $\vec{Q}$, $\vec{F}$ and $\vec{S_S}$ are the vectors of conserved variables, its fluxes and sources. They are given by

$$\vec{Q} = \begin{bmatrix} q_1 \\ q_2 \\ q_3 \\ q_4 \end{bmatrix} = \begin{bmatrix} \alpha_1\rho_1 \\ \alpha_2\rho_2 \\ \alpha_1\rho_1 v_1 \\ \alpha_2\rho_2 v_2 \end{bmatrix}, \tag{2.46}$$

$$\vec{F} = \begin{bmatrix} f_1 \\ f_2 \\ f_3 \\ f_4 \end{bmatrix} = \begin{bmatrix} \alpha_1\rho_1 v_1 \\ \alpha_2\rho_2 v_2 \\ \alpha_1\rho_1 v_1^2 + \alpha_1 p \\ \alpha_2\rho_2 v_2^2 + \alpha_2 p \end{bmatrix}, \tag{2.47}$$

$$\vec{S_S} = \begin{bmatrix} s_1 \\ s_2 \\ s_3 \\ s_4 \end{bmatrix} = \begin{bmatrix} 0 \\ 0 \\ s_3 \\ s_4 \end{bmatrix}, \tag{2.48}$$

where

$$s_3 = -\alpha_1\rho_1 g \sin\theta - \alpha_1\rho_1 g \cos\theta \frac{\partial h}{\partial \alpha_1}\frac{\partial \alpha_1}{\partial z} + p\frac{\partial \alpha_1}{\partial z} + \frac{\partial}{\partial z}\left(\rho_1\alpha_1\nu_1^{eq}\frac{\partial v_1}{\partial z}\right) + \alpha_1\frac{\partial}{\partial z}\left(\sigma_{21}\hat{\gamma}^i\right) + \frac{1}{2}\frac{S_i}{A}f_i\rho_2\left(v_2 - v_1\right)\left|\left(v_2 - v_1\right)\right| - \frac{1}{2}\frac{S_1}{A}f_1^w\rho_1 v_1|v_1|, \tag{2.49}$$

$$s_4 = -\alpha_2\rho_2 g \sin\theta - \alpha_2\rho_2 g \cos\theta \frac{\partial h}{\partial \alpha_2}\frac{\partial \alpha_2}{\partial z} + p\frac{\partial \alpha_2}{\partial z} + \frac{\partial}{\partial z}\left(\rho_2\alpha_2\nu_2^{eq}\frac{\partial v_2}{\partial z}\right) - \frac{1}{2}\frac{S_i}{A}f_i\rho_2\left(v_2 - v_1\right)\left|\left(v_2 - v_1\right)\right| - \frac{1}{2}\frac{S_2}{A}f_2^w\rho_2 v_2|v_2|. \tag{2.50}$$

2.1.2 Dispersed Phases Flow

In the dispersed phases flow case, the total averaged momentum source $\hat{M}_k$ combines the momentum flux through the interface and the flux induced by wall boundaries parietal stresses (Ishii; Hibiki, 2011; Morel, 2015), i.e.,

$$\hat{M}_k = v_k^i\Gamma_k + \left(p_k^i - p_k\right)\frac{\partial \alpha_k}{\partial z} + \hat{M}_k^i + \tau_k^w\frac{S_k}{A}. \tag{2.51}$$

The phases parietal stresses τ_k^w act mainly in the liquid phase wetting the duct inner wall perimeter S. However, it is affected by the whole mixture properties. Therefore

$$\tau_1^w = \bar{\tau_w}, \tag{2.52}$$

$$\tau_2^w = 0. \tag{2.53}$$

The average parietal mixture shear stress $\bar{\tau_w}$ can be modelled by the two-phase multiplier ϕ_d^2, or the homogeneous model (Wallis, 1969; Shoham, 2006), as

$$\frac{\bar{\tau_w} S}{A} = -\phi_d^2 \frac{2}{D} \frac{f_1}{\rho_1} \rho_m v_m |\rho_m v_m| = -\phi_d^2 \frac{2}{D} \frac{f_1}{\rho_1} (\rho_1 \alpha_1 v_1 + \rho_2 \alpha_2 v_2) |(\rho_1 \alpha_1 v_1 + \rho_2 \alpha_2 v_2)|, \quad (2.54)$$

$$\frac{\bar{\tau_w} S}{A} = -\frac{2}{D} \rho_m f_m J|J| = -\frac{2}{D} \rho_m f_m (\alpha_1 v_1 + \alpha_2 v_2) |(\alpha_1 v_1 + \alpha_2 v_2)|, \quad (2.55)$$

where f_1 and f_m are the Fanning friction factors for the liquid phase and the mixture, respectively, $\rho_m v_m$ is the total mass flow, J is the mixture velocity and D is the pipe internal diameter. Another possible model using the two-phase multiplier concept is given by (Malnes, 1982; Bonizzi; Issa, 2003; Bendlksen *et al.*, 1991)

$$\frac{\bar{\tau_w} S}{A} = -\frac{2}{D} \rho_1 f_d v_m |v_m|, \quad (2.56)$$

$$f_d = \phi_d f_1^{Hand}, \quad (2.57)$$

$$\phi_d = \frac{1}{1-\alpha} \left[1 + 15.3 \frac{\alpha}{\sqrt{1-\alpha}} \frac{v_\infty}{v_m} \right], \quad (2.58)$$

$$v_\infty = 1.18 \left[\frac{g\sigma (\rho_1 - \rho_2)}{\rho_1^2} \right]^{0.25}, \quad (2.59)$$

where v_∞ is the bubble rise velocity in an infinite medium and f_1^{Hand} is the liquid phase Fanning friction factor given by Equation 2.29.

From the linear momentum jump condition at the gas-liquid interface, the interfacial momentum fluxes between phases are equal in magnitude but in opposite directions (Ishii; Hibiki, 2011), thus

$$\hat{M}_1^i + \hat{M}_2^i = 0. \quad (2.60)$$

Therefore, considering the aforementioned definition, that there is no mass transfer between the phases $\Gamma_k = 0$ and $p_2 \approx p_2^i$, as the bubbles are small and the gas density is much smaller than liquid density, it yields for both phases

$$\hat{M}_1 = (p_1^i - p_1) \frac{\partial \alpha_1}{\partial z} - \hat{M}_2 + \bar{\tau_w} \frac{S}{A}, \quad (2.61)$$

$$\hat{M}_2 = \hat{M}_2^i. \tag{2.62}$$

As it was done previously, the gas phase pressure at the interface p_2^i is considered as the reference pressure p. Therefore, the pressure fields will be written from the reference pressure added the hydrostatic deviations and interface jumps. Considering the bubbles as spheres spaced in a regular lattice under potential flow, yields (Stuhmiller, 1977; Bertodano *et al.*, 2016)

$$p_1^i - p_1 = -C_p \rho_1 \left(v_2 - v_1\right)^2, \tag{2.63}$$

where p_1, p_1^i and C_p are the averaged liquid pressure, the liquid pressure at the gas-liquid interface and the pressure difference coefficient, respectively, and $C_p = 1/4$ for dilute spheres in potential flow. It should be noted that in case of distorted bubbles regime, the pressure difference coefficient should be estimated from experimental data, with reported values of $C_p = 1$ as reasonable in some applications (Bertodano *et al.*, 2016). Therefore, the averaged momentum transfer for the liquid phase $\hat{M}_1$ is given by

$$\hat{M}_1 = -C_p \rho_1 \left(v_2 - v_1\right)^2 \frac{\partial \alpha_1}{\partial z} - \hat{M}_2 + \bar{\tau_w} \frac{S}{A}. \tag{2.64}$$

Again, the difference between the pressure fields of each phase k at the interface can be modeled using the concept of interfacial tension through the Young-Laplace Equation (Bergles *et al.*, 1981; Ishii; Hibiki, 2011; Panton, 2013)

$$p_1^i - p_2^i = -\sigma_{21} \hat{\gamma}^i, \tag{2.65}$$

$$\hat{\gamma}^i \left(z\right) = \frac{2}{r_b}, \tag{2.66}$$

where σ_{21} is the fluids interfacial tension, $\hat{\gamma}^i$ the average interface curvature field and r_b the bubble's average radius. Hence, the pressure fields for both phases are related as

$$p_1 = p_2 - \sigma_{21} \frac{2}{r_b} + C_p \rho_1 \left(v_2 - v_1\right)^2. \tag{2.67}$$

As the interfaces are not unique and distributed over the dispersed phase, the overall averaged gas-liquid interfacial shear stresses τ_k^i manifest through the drag $\hat{M}_k^D$, added mass $\hat{M}_k^V$ and collision $\hat{M}_k^C$ forces over the dispersed bubbles leading to an averaged interfacial momentum transfer for the gas phase $\hat{M}_2$ (Ishii; Hibiki, 2011; Morel, 2015; Bertodano *et al.*, 2016)

$$\hat{M}_2 = \hat{M}_2^i = \hat{M}_2^D + \hat{M}_2^V + \hat{M}_2^C, \tag{2.68}$$

$$\hat{M}_2^D = -\alpha_2 \rho_1 \left(\frac{3C_D}{8r_b} \right) (v_2 - v_1) \left| (v_2 - v_1) \right|, \tag{2.69}$$

$$\hat{M}_2^V = -\alpha_2 \rho_1 C_V \left(\frac{\partial v_2}{\partial t} + v_2 \frac{\partial v_2}{\partial z} - \frac{\partial v_1}{\partial t} - v_1 \frac{\partial v_1}{\partial z} \right), \tag{2.70}$$

$$\hat{M}_2^C = -\frac{\partial}{\partial z} \left[C_C \frac{(1+\alpha_1)(1-\alpha_1)^3}{2\alpha_1^3} C_V (\rho_2 + C_V \rho_1)(v_2 - v_1)^2 \right], \tag{2.71}$$

where r_b, C_D, C_V, C_C are the bubble's average radius, drag, added mass and collision coefficients, respectively.

The bubble's average radius will be given by the Kolmogorov-Hinze theory (Kolmogorov, 1949; Hinze, 1955). As they occur in the wake of the Taylor bubble, after the hydraulic jump under strong turbulence and recirculation, it is reasonable to consider the pattern as finely dispersed under conditions near to the transition boundary, which is visible in the alternate succession of liquid slugs and Taylor bubbles in the slug flow pattern (Barnea; Brauner, 1985).

The drag coefficient for the bubble swarm on the spherical or distorted turbulent regime can be modelled by (Tomiyama *et al.*, 1998)

$$C_D = \frac{C_{DT}}{\sqrt{1-\alpha}}, \tag{2.72}$$

$$C_{DT} = \max\{ \frac{24}{Re_b} \left(1 + 0.15 Re_b^{0.687} \right), \frac{8}{3} \frac{E_o}{E_o + 4} \}, \tag{2.73}$$

$$Re_b = \frac{\rho_1 v_s d_b}{\mu_1}, \tag{2.74}$$

$$E_o = \frac{g (\rho_1 - \rho_2) d_b^2}{\sigma_{21}}, \tag{2.75}$$

where Re_b and E_o are the bubbles Reynolds and Eötvös numbers. The added mass coefficient is $C_V = 1/2$ in the limit for an isolated sphere, being modified in order to consider the bubble swarm effects as (Ishii; Hibiki, 2011)

$$C_V = \frac{1}{2}\frac{(1-2\alpha)}{(1-\alpha)}. \tag{2.76}$$

The spherical bubbles collision coefficient is given by (Bertodano *et al.*, 2016)

$$C_C = \frac{1.8}{1+\left(\frac{\tau_e}{\tau_b}\right)}, \tag{2.77}$$

where τ_e and τ_b are the bubble's time constants of the bubble-induced eddies and inertia, respectively. It should be noted that in case of large distorted bubbles regime, the added mass coefficient C_V and the bubbles collision coefficient C_C should be estimated from experimental data, with reported values of $C_V = 2$ and $C_C = 0.18$ as reasonable in some applications (Bertodano *et al.*, 2016).

Considering the aforementioned definitions and closure models, that there is no mass transfer between the phases $\Gamma_k = 0$ and the gas phase pressure at the interface p_2^i as the reference pressure p, the averaged mass and linear momentum conservation laws for each phase are rewritten as

$$\frac{\partial}{\partial t}(\alpha_1\rho_1) + \frac{\partial}{\partial z}(\alpha_1\rho_1 v_1) = 0, \tag{2.78}$$

$$\frac{\partial}{\partial t}(\alpha_2\rho_2) + \frac{\partial}{\partial z}(\alpha_2\rho_2 v_2) = 0, \tag{2.79}$$

$$\begin{aligned}\frac{\partial}{\partial t}(\alpha_1\rho_1 v_1) + \frac{\partial}{\partial z}\left(\alpha_1\rho_1 v_1^2 + \alpha_1 p\right) = & -\alpha_1\rho_1 g\sin\theta + \frac{\partial}{\partial z}\left(\rho_1\alpha_1\nu_1^{eq}\frac{\partial v_1}{\partial z}\right) + p\frac{\partial \alpha_1}{\partial z} - \hat{M}_2 \\ & + \bar{\tau_w}\frac{S}{A} - \alpha_1\frac{\partial}{\partial z}\left[C_p\rho_1 (v_2 - v_1)^2 - \sigma_{21}\frac{2}{r_b}\right] \\ & - C_p\rho_1 (v_2 - v_1)^2\frac{\partial \alpha_1}{\partial z},\end{aligned} \tag{2.80}$$

$$\frac{\partial}{\partial t}(\alpha_2\rho_2 v_2) + \frac{\partial}{\partial z}\left(\alpha_2\rho_2 v_2^2 + \alpha_2 p\right) = -\alpha_2\rho_2 g\sin\theta + \frac{\partial}{\partial z}\left(\rho_2\alpha_2\nu_2^{eq}\frac{\partial v_2}{\partial z}\right) + p\frac{\partial \alpha_2}{\partial z} + \hat{M}_2. \tag{2.81}$$

The two fluid model equations above form a system of PDE's in the conservative form with a source term as

$$\frac{\partial \vec{Q}}{\partial t} + \frac{\partial \vec{F}}{\partial z} = \vec{S_D}, \tag{2.82}$$

where the $\vec{Q}$, $\vec{F}$ and $\vec{S_D}$ are the vectors of conserved variables, it's fluxes and sources and are given by

$$\vec{Q} = \begin{bmatrix} q_1 \\ q_2 \\ q_3 \\ q_4 \end{bmatrix} = \begin{bmatrix} \rho_1\alpha_1 \\ \rho_2\alpha_2 \\ \alpha_1\rho_1 v_1 \\ \alpha_2\rho_2 v_2 \end{bmatrix}, \tag{2.83}$$

$$\vec{F} = \begin{bmatrix} f_1 \\ f_2 \\ f_3 \\ f_4 \end{bmatrix} = \begin{bmatrix} \alpha_1\rho_1 v_1 \\ \alpha_2\rho_2 v_2 \\ \alpha_1\rho_1 v_1^2 + \alpha_1 p \\ \alpha_2\rho_2 v_2^2 + \alpha_2 p \end{bmatrix}, \tag{2.84}$$

$$\vec{S_D} = \begin{bmatrix} s_1 \\ s_2 \\ s_3 \\ s_4 \end{bmatrix} = \begin{bmatrix} 0 \\ 0 \\ s_3 \\ s_4 \end{bmatrix}, \tag{2.85}$$

where

$$\begin{aligned} s_3 = &- \alpha_1\rho_1 g \sin\theta + \frac{\partial}{\partial z}\left(\rho_1\alpha_1\nu_1^{eq}\frac{\partial v_1}{\partial z}\right) + p\frac{\partial \alpha_1}{\partial z} - \hat{M}_2 + \bar{\tau}_w\frac{S}{A} \\ &- \alpha_1\frac{\partial}{\partial z}\left[C_p\rho_1\left(v_2 - v_1\right)^2 - \sigma_{21}\frac{2}{r_b}\right] - C_p\rho_1\left(v_2 - v_1\right)^2\frac{\partial \alpha_1}{\partial z}, \end{aligned} \tag{2.86}$$

$$s_4 = -\alpha_2\rho_2 g \sin\theta + \frac{\partial}{\partial z}\left(\rho_2\alpha_2\nu_2^{eq}\frac{\partial v_2}{\partial z}\right) + p\frac{\partial \alpha_2}{\partial z} + \hat{M}_2. \tag{2.87}$$

2.1.3 Composite Two Fluid Flow Model

Equations 2.45 and 2.82 form a composite system of PDE's for the separate and dispersed phases flow that can be combined in one model

$$\frac{\partial \vec{Q}}{\partial t} + \frac{\partial \vec{F}}{\partial z} = I_d\vec{S_S} + \left(1 - I_d\right)\vec{S_D}, \tag{2.88}$$

where the source term oscillates between $\vec{S_S}$ and $\vec{S_D}$ depending on the dynamically evaluated flow pattern represented by the sigmoid function I_d over a classification boundary that will be defined in the Chapter 3, alternating from one flow pattern to another, as the unit cell model suggests.

2.2 Simplified Model

In this section, the simplified model is presented. Some simplifying assumptions are adopted in order to make the slug flow pattern analysis more tractable, ending on the constant flux solution.

The slug flow pattern is characterized by slow kinematic mass waves given by *quasi*-periodic oscillations of the void fraction and the phases velocities between the stratified and dispersed bubble flow patterns. The flow can be modeled as incompressible given its low Mach number. Under these premises, the incompressible averaged mass and momentum conservation laws equations for each phase are written in its non conservative form as

$$\frac{\partial \alpha_k}{\partial t} + \frac{\partial}{\partial z}\left(\alpha_k v_k\right) = 0, \tag{2.89}$$

$$\rho_k \frac{\partial v_k}{\partial t} + \rho_k v_k \frac{\partial v_k}{\partial z} = -\frac{\partial p}{\partial z} - \rho_k g \sin\theta + \frac{\rho_k \nu_k^{eq}}{\alpha_k} \frac{\partial}{\partial z}\left(\alpha_k \frac{\partial v_k}{\partial z}\right) + \frac{\hat{M}_k}{\alpha_k}, \tag{2.90}$$

where it was considered a constant equivalent kinematic viscosity, a hypothesis that proved to be wrong, being discussed in the following chapters.

However, the pressure does not oscillate in this *quasi*-periodic aspect, slowly decreasing as the flow loses its energy. So, the modeling should eliminate the pressure variable in order to tackle this *quasi*-periodic oscillations. This can be done by subtracting the incompressible averaged momentum conservation law equations for each phase, which yields (Bertodano *et al.*, 2016)

$$\begin{aligned}\rho_1 \frac{\partial v_1}{\partial t} + \rho_1 v_1 \frac{\partial v_1}{\partial z} - \rho_2 \frac{\partial v_2}{\partial t} - \rho_2 v_2 \frac{\partial v_2}{\partial z} = &- \left(\rho_1 - \rho_2\right) g \sin\theta \\ &+ \frac{\rho_1 \nu_1^{eq}}{\alpha_1} \frac{\partial}{\partial z}\left(\alpha_1 \frac{\partial v_1}{\partial z}\right) - \frac{\rho_2 \nu_2^{eq}}{\alpha_2} \frac{\partial}{\partial z}\left(\alpha_2 \frac{\partial v_2}{\partial z}\right) \\ &+ \frac{\hat{M}_1}{\alpha_1} - \frac{\hat{M}_2}{\alpha_2}.\end{aligned} \tag{2.91}$$

2.2.1 Separated Phases Model

In the separated phases case, considering the aforementioned definitions and closure models discussed in Section 2.1.1, the subtracted momentum equation is given by

$$\begin{aligned} \rho_1 \frac{\partial v_1}{\partial t} + \rho_1 v_1 \frac{\partial v_1}{\partial z} - \rho_2 \frac{\partial v_2}{\partial t} - \rho_2 v_2 \frac{\partial v_2}{\partial z} = &- (\rho_1 - \rho_2)\, g \sin\theta - (\rho_1 - \rho_2)\, g \cos\theta \frac{\partial h}{\partial \alpha_2} \frac{\partial \alpha_2}{\partial z} \\ &+ \sigma_{21} \frac{\partial \hat{\gamma}^i}{\partial z} \\ &+ \frac{\rho_1 \nu_1^{eq}}{\alpha_1} \frac{\partial}{\partial z} \left(\alpha_1 \frac{\partial v_1}{\partial z} \right) - \frac{\rho_2 \nu_2^{eq}}{\alpha_2} \frac{\partial}{\partial z} \left(\alpha_2 \frac{\partial v_2}{\partial z} \right) \\ &+ \frac{1}{\alpha_1 \alpha_2} \frac{1}{2} \frac{S_i}{A} f_i \rho_2 (v_2 - v_1) \left| (v_2 - v_1) \right| \\ &- \frac{1}{2} \frac{S_1}{A} f_1^w \frac{\rho_1}{\alpha_1} v_1 |v_1| + \frac{1}{2} \frac{S_2}{A} f_2^w \frac{\rho_2}{\alpha_2} v_2 |v_2|. \end{aligned} \tag{2.92}$$

The equation can be rewritten

$$\begin{aligned} \rho_1 \frac{\mathrm{D} v_1}{\mathrm{D} t} - \rho_2 \frac{\mathrm{D} v_2}{\mathrm{D} t} = &- (\rho_1 - \rho_2)\, g \sin\theta - (\rho_1 - \rho_2)\, g \cos\theta \frac{\partial h}{\partial \alpha_2} \frac{\partial \alpha_2}{\partial z} + \sigma_{21} \frac{\partial \hat{\gamma}^i}{\partial z} \\ &+ \frac{\rho_1 \nu_1^{eq}}{\alpha_1} \frac{\partial}{\partial z} \left(\alpha_1 \frac{\partial v_1}{\partial z} \right) - \frac{\rho_2 \nu_2^{eq}}{\alpha_2} \frac{\partial}{\partial z} \left(\alpha_2 \frac{\partial v_2}{\partial z} \right) \\ &+ \frac{1}{\alpha_1 \alpha_2} \frac{1}{2} \frac{S_i}{A} f_i \rho_2 (v_2 - v_1) \left| (v_2 - v_1) \right| \\ &- \frac{1}{2} \frac{S_1}{A} f_1^w \frac{\rho_1}{\alpha_1} v_1 |v_1| + \frac{1}{2} \frac{S_2}{A} f_2^w \frac{\rho_2}{\alpha_2} v_2 |v_2|. \end{aligned} \tag{2.93}$$

where the total derivative operator is defined as

$$\frac{\mathrm{D} v_k}{\mathrm{D} t} = \frac{\partial v_k}{\partial t} + v_k \frac{\partial v_k}{\partial z}. \tag{2.94}$$

2.2.2 Dispersed Phase Model

Similarly, in the dispersed phases case, the subtracted momentum equation is given by

$$\begin{aligned}\rho_1\frac{\partial v_1}{\partial t}+\rho_1 v_1\frac{\partial v_1}{\partial z}-\rho_2\frac{\partial v_2}{\partial t}-\rho_2 v_2\frac{\partial v_2}{\partial z}=&-\left(\rho_1-\rho_2\right)g\sin\theta+\frac{1}{\alpha_1}\bar{\tau_w}\frac{S}{A}\\&+\frac{\rho_1\nu_1^{eq}}{\alpha_1}\frac{\partial}{\partial z}\left(\alpha_1\frac{\partial v_1}{\partial z}\right)-\frac{\rho_2\nu_2^{eq}}{\alpha_2}\frac{\partial}{\partial z}\left(\alpha_2\frac{\partial v_2}{\partial z}\right)\\&-\frac{\partial}{\partial z}\left[C_p\rho_1\left(v_2-v_1\right)^2-\sigma_{21}\frac{2}{r_b}\right]\\&-\frac{C_p\rho_1}{\alpha_1}\left(v_2-v_1\right)^2\frac{\partial\alpha_1}{\partial z}-\frac{1}{\alpha_1\alpha_2}\hat{M}_2,\end{aligned}\tag{2.95}$$

Assuming a constant bubble radius and using the total derivative operator defined in Equation 2.94, the equation can be rewritten as

$$\begin{aligned}\rho_1\frac{\mathrm{D}v_1}{\mathrm{D}t}-\rho_2\frac{\mathrm{D}v_2}{\mathrm{D}t}=&-\left(\rho_1-\rho_2\right)g\sin\theta-\frac{C_p\rho_1}{\alpha_1}\left(v_2-v_1\right)^2\frac{\partial\alpha_1}{\partial z}\\&-2C_p\rho_1\left(v_2-v_1\right)\left(\frac{\partial v_2}{\partial z}-\frac{\partial v_1}{\partial z}\right)\\&+\frac{\rho_1\nu_1^{eq}}{\alpha_1}\frac{\partial}{\partial z}\left(\alpha_1\frac{\partial v_1}{\partial z}\right)-\frac{\rho_2\nu_2^{eq}}{\alpha_2}\frac{\partial}{\partial z}\left(\alpha_2\frac{\partial v_2}{\partial z}\right)+\frac{1}{\alpha_1}\bar{\tau_w}\frac{S}{A}-\frac{1}{\alpha_1\alpha_2}\hat{M}_2.\end{aligned}\tag{2.96}$$

The averaged interfacial momentum transfer for the gas phase $\hat{M}_2$ manifest through the drag $\hat{M}_2^D$, added mass $\hat{M}_2^V$ and collision $\hat{M}_2^C$ forces described in Equations 2.69 to 2.71, that are rewritten as

$$\hat{M}_2^V=-\alpha_2\rho_1 C_V\left(\frac{\mathrm{D}v_2}{\mathrm{D}t}-\frac{\mathrm{D}v_1}{\mathrm{D}t}\right),\tag{2.97}$$

$$\begin{aligned}\hat{M}_2^C=&C_C C_V\left(\rho_2+C_V\rho_1\right)\left(v_2-v_1\right)^2\left[\frac{\alpha_2^2\left(\alpha_1^2+2\alpha_1+3\right)}{2\alpha_1^4}\right]\frac{\partial\alpha_1}{\partial z}\\&-C_C C_V\left(\rho_2+C_V\rho_1\right)\frac{\left(1+\alpha_1\right)\alpha_2^3}{\alpha_1^3}\left(v_2-v_1\right)\left(\frac{\partial v_2}{\partial z}-\frac{\partial v_1}{\partial z}\right),\end{aligned}\tag{2.98}$$

Consequently,

$$
\begin{aligned}
\left(1+\frac{C_V}{\alpha_1}\right)\rho_1\frac{\mathrm{D}v_1}{\mathrm{D}t}-\left(1+\frac{C_V}{\rho\alpha_1}\right)\rho_2\frac{\mathrm{D}v_2}{\mathrm{D}t}&=-\left(\rho_1-\rho_2\right)g\sin\theta\\
&-\left\{\frac{C_p\rho_1}{\alpha_1}+C_CC_V\left(\rho_2+C_V\rho_1\right)\left[\frac{\alpha_2\left(\alpha_1^2+2\alpha_1+3\right)}{2\alpha_1^5}\right]\right\}\left(v_2-v_1\right)^2\frac{\partial\alpha_1}{\partial z}\\
&+\left[C_CC_V\left(\rho_2+C_V\rho_1\right)\frac{\left(1+\alpha_1\right)\alpha_2^2}{\alpha_1^4}-2C_p\rho_1\right]\left(v_2-v_1\right)\left(\frac{\partial v_2}{\partial z}-\frac{\partial v_1}{\partial z}\right)\\
&+\frac{\rho_1\nu_1^{eq}}{\alpha_1}\frac{\partial}{\partial z}\left(\alpha_1\frac{\partial v_1}{\partial z}\right)-\frac{\rho_2\nu_2^{eq}}{\alpha_2}\frac{\partial}{\partial z}\left(\alpha_2\frac{\partial v_2}{\partial z}\right)\\
&+\frac{1}{\alpha_1}\frac{\bar{\tau_w}S}{A}+\frac{\rho_1}{\alpha_1}\left(\frac{3C_D}{8r_b}\right)\left(v_2-v_1\right)|\left(v_2-v_1\right)|,
\end{aligned}
\tag{2.99}
$$

where the densities ratio is defined by

$$
\rho=\frac{\rho_2}{\rho_1}. \tag{2.100}
$$

2.2.3 Constant Flux Solution

The two incompressible averaged mass conservation law equations for both phases are added in order to obtain a constant mixture volumetric flux solution (Bertodano *et al.*, 2016):

$$
\frac{\partial}{\partial t}(\overbrace{\alpha_1+\alpha_2}^{=1})+\frac{\partial}{\partial z}\left(\alpha_1v_1+\alpha_2v_2\right)=\frac{\partial J}{\partial z}=0, \tag{2.101}
$$

where the average mixture volumetric flux $J\left(t\right)$ is a constant in space for any incompressible flow. This result is important because it allows the reduction of one degree of freedom since the phases velocities v_k are interrelated by the mixture volumetric flux J:

$$
v_2=\frac{J-\alpha_1v_1}{\alpha_2}. \tag{2.102}
$$

Therefore, it is only necessary to solve one averaged mass conservation law equation and the subtracted momentum equation can be described by one phase velocity becoming a modified two-phase shallow water equation on circular pipes.

2.3 Travelling Wave

In this section, the travelling wave solution for the slug flow is addressed. It is such that the two-phase flow variables fields described over the (z,t) plane are stationary in time, if described in the transformed coordinate system over the (η, t') plane (Dukler; Hubbard, 1975; Taitel; Barnea, 1990; Fagundes Netto *et al.*, 1999; Needham; Merkin, 1984; Needham *et al.*, 2008; Giddings, 2017; Giddings; Billingham, 2019). Therefore, the following Galilean transformation change of coordinates is used, in order to create a Lagrangian frame of reference (Panton, 2013),

$$\eta = z - V_{TB} t, \tag{2.103}$$

$$t' = t. \tag{2.104}$$

In the matrix form, it yields

$$\begin{bmatrix} \eta \\ t' \end{bmatrix} = \begin{bmatrix} 1 & -V_{TB} \\ 0 & 1 \end{bmatrix} \begin{bmatrix} z \\ t \end{bmatrix}. \tag{2.105}$$

The differential operators can be rewritten using the chain rule

$$\frac{\partial}{\partial t} = \frac{\partial t'}{\partial t}\frac{\partial}{\partial t'} + \frac{\partial \eta}{\partial t}\frac{\partial}{\partial \eta} = \frac{\partial}{\partial t'} - V_{TB}\frac{\partial}{\partial \eta}, \tag{2.106}$$

$$\frac{\partial}{\partial z} = \frac{\partial t'}{\partial z}\frac{\partial}{\partial t'} + \frac{\partial \eta}{\partial z}\frac{\partial}{\partial \eta} = \frac{\partial}{\partial \eta}, \tag{2.107}$$

In this new coordinate frame (η, t'), the flow variables are going to be constant in time varying only in the transformed space η. Therefore

$$\frac{\partial}{\partial t} = -V_{TB}\frac{\partial}{\partial \eta}, \tag{2.108}$$

$$\frac{\partial^n}{\partial x^n} = \frac{\partial^n}{\partial \eta^n}, \tag{2.109}$$

where n is the derivative operator order.

2.3.1 Mass Conservation Equations

Applying the travelling wave transformation to the incompressible averaged mass conservation equations yields

$$-V_{TB}\frac{\partial \alpha_k}{\partial \eta} + \frac{\partial}{\partial \eta}\left(\alpha_k v_k\right) = \frac{\partial}{\partial \eta}\left[\alpha_k\left(v_k - V_{TB}\right)\right] = 0, \tag{2.110}$$

$$\frac{\partial M_k}{\partial \eta} = 0, \tag{2.111}$$

where the relative velocity u_k and relative volumetric flux M_k are defined as

$$u_k = v_k - V_{TB}, \tag{2.112}$$

$$M_k = \alpha_k u_k. \tag{2.113}$$

Therefore, the solution of the mass conservation equations are analytical, configuring an initial value problem where constant relative volumetric fluxes M_k are the solutions. This result is important, since the velocity fields v_k are defined by the void fraction field, closing the problem kinematics

$$v_k = V_{TB} + \frac{M_k}{\alpha_k}. \tag{2.114}$$

The constant mixture volumetric flux solution, discussed in Section 2.2.3, can be rewritten as

$$\alpha_1 \left(v_1 - V_{TB}\right) + \alpha_2 \left(v_2 - V_{TB}\right) = J - V_{TB}, \tag{2.115}$$

$$M_1 + M_2 = J - V_{TB}, \tag{2.116}$$

which means that the velocity fields are a function of the void fraction α and are completely defined by the following constants: mixture volumetric flux J, Taylor bubble velocity V_{TB} and the relative volumetric flux of the gas phase M_2. It should be noted that, although estimated by closure models, the constant relative volumetric flux of the gas phase M_2 is an input parameter that can be identified from experimental data.

2.3.1.1 Bubble Entrainment

The constant relative volumetric fluxes M_k of the phase k, obtained through the constant mixture volumetric flux solution, take an additional and important meaning at the slug mixing region on the Taylor bubble tail after the hydraulic jump, which is where the gas relative volumetric flux M_2 can be related to the shedding or pickup rate. Assuming that in order to have a stable unit cell, the bubbles that detach from the Taylor bubble tail are assimilated by the next Taylor bubble represents a dynamic equilibrium where $M_2 \leqslant 0$ represents the bubble entrainment at the liquid slug (Dukler; Hubbard, 1975; Shoham, 2006).

Furthermore, the gas relative volumetric flux M_2 and the Taylor bubble velocity V_{TB} are the remaining input parametric quantities to fully define the dynamical system alongside the already known PVT and transport properties and the closure models. These quantities can be estimated from correlations and classical models from the literature at any point of the unit cell, as they are constants. It follows at the aerated liquid piston that

$$M_2 = \alpha_S \left(v_B - V_{TB}\right). \tag{2.117}$$

The Taylor Bubble velocity V_{TB} is given by (Bendiksen, 1984; Shoham, 2006)

$$V_{TB} = \left(1.05 + 0.15\sin^2\theta\right) J + \left(0.54\cos\theta + 0.35\sin\theta\right)\sqrt{gD}, \quad \text{if} \quad Fr < 3.5, \tag{2.118}$$

$$V_{TB} = 1.2J + 0.35\sin\theta\sqrt{gD}, \quad \text{if} \quad Fr \geqslant 3.5, \tag{2.119}$$

The gas in-situ velocity v_B at the aerated liquid slug is estimated by the Drift Flux model (Wallis, 1969; Shoham, 2006)

$$v_B = 1.2J + 1.53\left[\frac{g\sigma_{21}\left(\rho_1 - \rho_2\right)}{\rho_1^2}\right]^{0.25}\left(1 - \alpha_S\right)^{0.5}\sin\theta, \tag{2.120}$$

The void fraction α_S at the aerated liquid slug can be modelled by the following closure relationships:

- Gomez *et al.* (2000) model:

$$\alpha_S = 1 - e^{-\left(7.85\times10^{-3}\theta + 2.48\times10^{-6}Re_{LS}\right)} \tag{2.121}$$

$$Re_{LS} = \frac{\rho_1 J D}{\mu_1} \tag{2.122}$$

- Barnea e Brauner (1985) model:

$$\alpha_S = 0.058\left[2\sqrt{\frac{0.4\sigma_{21}}{\left(\rho_1 - \rho_2\right)g}}\left(\frac{\rho_1}{\sigma}\right)^{0.6}\left(\frac{2}{D}f_m J^3\right)^{0.4} - 0.725\right]^2 \tag{2.123}$$

- Zhang *et al.* (2003) model:

$$\alpha_S = 1 - \left[1 + \frac{T_{sm}}{3.16\sqrt{(\rho_1 - \rho_2)\, g\sigma_{21}}} \right]^{-1} \tag{2.124}$$

$$T_{sm} = \frac{1}{C_e} \left[\frac{1}{2}\rho_m f_m J^2 + \frac{D}{4} \frac{\rho_1 (1-\alpha_F)(V_{TB} - v_F)(J - v_F)}{L_S} \right] \tag{2.125}$$

$$C_e = \frac{2.5 - |\sin\theta|}{2} \tag{2.126}$$

Despite having experimental data support, the model by Gomez *et al.* (2000) presents a regression that does not depend on critical parameters for the description of the bubble formation mechanism, such as surface tension, for example. The model by Barnea e Brauner (1985) is grounded on physical processes but assumes as a hypothesis spherical bubbles over the transition boundary with critical diameter, assumptions that are questionable regarding model generalization. The mechanistic model by Zhang *et al.* (2003) is based on energy transfer mechanisms converting turbulent kinetic energy T_{sm} to bubble surface energy. However, it neglects the coalescence mechanisms and the efficiency in the energy conversion process, aspects dealt by the fit of the experimental data.

Another approach is to deal with the gas relative volumetric flux M_2 as a whole using the bubble entrainment models available in the literature instead of treat each variable:

- Nydal e Andreussi (1991) model:

$$M_2 = 0.076\frac{S_i}{D}(V_{TB} - v_F) - 0.15, \tag{2.127}$$

- Chanson (1996) model:

$$M_2 = (1-\alpha_F)(V_{TB} - v_F)\,\zeta\,(Fr - 1)^{\varepsilon}, \tag{2.128}$$

$$Fr = \frac{(V_{TB} - v_F)}{\sqrt{g(1-\alpha_F)\frac{A}{S_i}}}, \tag{2.129}$$

$$\zeta = 0.018, \quad \varepsilon = 1.245, \quad \text{if} \quad 2.5 < Fr < 7, \tag{2.130}$$

$$\zeta = 0.014, \quad \varepsilon = 1.4, \quad \text{if} \quad 7 \leqslant Fr < 30. \tag{2.131}$$

The model by Nydal e Andreussi (1991) presents a correlation having experimental data support on aerated slugs in a near horizontal pipe running on tap water and air. The model by Chanson (1996) correlates the energy dissipation on a hydraulic jump with the entrainment rate. Interestingly, both models have an entrainment onset depending on the relative velocity on the Taylor bubble velocity.

2.3.1.2 Periodic Solution

The mass balance of the phase k can be done differently for the periodic solution only, by integrating the mass flow rates at a fixed cross section over the slug unit transit time (Taitel; Barnea, 1990; Shoham, 2006). Therefore,

$$j_k = \frac{1}{t_u}\int_0^{t_u} \alpha_k v_k \mathrm{d}t = \frac{1}{t_u}\left(\int_0^{t_s} \alpha_k v_k \mathrm{d}t + \int_{t_s}^{t_s+t_f} \alpha_k v_k \mathrm{d}t\right), \tag{2.132}$$

where t_u, t_f and t_s are the slug unit, Taylor bubble and liquid slug transit times, respectively. Using the travelling wave transformation, it yields

$$j_k = \frac{1}{L_U}\int_0^{L_S} \alpha_k v_k \mathrm{d}\eta + \frac{1}{L_U}\int_{L_S}^{L_S+L_F} \alpha_k v_k \mathrm{d}\eta, \tag{2.133}$$

where L_U, L_F and L_S are the slug unit, Taylor bubble and liquid slug lengths, respectively. From the constant mixture volumetric flux solution, it is rewritten as

$$\alpha_k v_k = M_k + \alpha_k V_{TB}. \tag{2.134}$$

Substituting, it leads to

$$j_k = M_k + \frac{V_{TB}}{L_U}\left(\int_0^{L_S} \alpha_k \mathrm{d}\eta + \int_{L_S}^{L_S+L_F} \alpha_k \mathrm{d}\eta\right). \tag{2.135}$$

The equation can then be rewritten as

$$\frac{j_k - M_k}{V_{TB}} = \bar{\alpha_k} = \frac{1}{L_S + L_F}\left(\int_0^{L_S} \alpha_k \mathrm{d}\eta + \int_{L_S}^{L_S+L_F} \alpha_k \mathrm{d}\eta\right), \tag{2.136}$$

where $\bar{\alpha_k}$ is the slug unit average phase k volumetric fraction that is completely defined by the parametric inputs. Considering that the slug length L_S can be estimated through a closure relationship, the mass balance given above can be used to calculate the length of the Taylor bubble region L_F from the integration of the void fraction wave solution profile for the dispersed and segregated patterns separately. One can simplify the mass balance for two particular cases involving the constant equilibrium solutions (Taitel; Barnea, 1990; Shoham, 2006):

- Constant liquid slug and Taylor bubble void fractions giving the pulse train solution:

$$\frac{j_k - M_k}{V_{TB}} = \alpha_k^S \frac{L_S}{L_U} + \alpha_k^F \frac{L_F}{L_U} = \alpha_k^S (1-\beta) + \alpha_k^F \beta, \tag{2.137}$$

- Constant liquid slug void fraction:

$$\frac{j_k - M_k}{V_{TB}} = \alpha_k^S \frac{L_S}{L_U} + \frac{1}{L_U} \int_{L_S}^{L_S+L_F} \alpha_k \mathrm{d}\eta. \tag{2.138}$$

2.3.2 Momentum Conservation Equations

The appearance of the relative velocity in the mass equation solution suggests a change of variables in the problem. To do so, first, the differential operators for the new variables must be rewritten considering the travelling wave reference frame, a constant Taylor bubble velocity V_{TB} and the mass equation solution as

$$\frac{\partial^n v_k}{\partial \eta^n} = \frac{\partial^n u_k}{\partial \eta^n}, \tag{2.139}$$

$$\frac{\mathrm{D} v_k}{\mathrm{D} t} = \frac{\partial v_k}{\partial t} + v_k \frac{\partial v_k}{\partial z} = -V_{TB} \frac{\partial v_k}{\partial \eta} + v_k \frac{\partial v_k}{\partial \eta} = (v_k - V_{TB}) \frac{\partial v_k}{\partial \eta} = u_k \frac{\partial u_k}{\partial \eta} = \frac{\partial}{\partial \eta}\left(\frac{u_k^2}{2}\right), \tag{2.140}$$

$$v_s = v_2 - v_1 = u_2 - u_1 = u_s, \tag{2.141}$$

$$\frac{\partial u_k}{\partial \eta} = \frac{\partial}{\partial \eta}\left(\frac{M_k}{\alpha_k}\right) = -\frac{M_k}{\alpha_k^2}\frac{\partial \alpha_k}{\partial \eta}, \tag{2.142}$$

$$\frac{\partial}{\partial \eta}\left(\frac{u_k^2}{2}\right) = -\frac{M_k^2}{\alpha_k^3}\frac{\partial \alpha_k}{\partial \eta}, \tag{2.143}$$

$$\frac{\partial}{\partial \eta}\left(\alpha_k \frac{\partial u_k}{\partial \eta}\right) = -\frac{\partial}{\partial \eta}\left(\frac{M_k}{\alpha_k}\frac{\partial \alpha_k}{\partial \eta}\right) = \frac{M_k}{\alpha_k^2}\left(\frac{\partial \alpha_k}{\partial \eta}\right)^2 - \frac{M_k}{\alpha_k}\frac{\partial^2 \alpha_k}{\partial \eta^2}. \tag{2.144}$$

In the separated phases flow case as discussed in Section 2.2.1, the subtracted momentum equation 2.93 is rewritten considering the aforementioned change of variables

$$\begin{aligned}\rho_1 \frac{\partial}{\partial \eta}\left(\frac{u_1^2}{2}\right) - \rho_2 \frac{\partial}{\partial \eta}\left(\frac{u_2^2}{2}\right) =& - \Delta\rho g \sin\theta - \Delta\rho g \cos\theta \frac{\partial h}{\partial \alpha_2}\frac{\partial \alpha_2}{\partial \eta} + \sigma_{21}\frac{\partial \hat{\gamma}^i}{\partial \eta} \\ &+ \frac{\rho_1 \nu_1^{eq}}{\alpha_1}\frac{\partial}{\partial \eta}\left(\alpha_1 \frac{\partial u_1}{\partial \eta}\right) - \frac{\rho_2 \nu_2^{eq}}{\alpha_2}\frac{\partial}{\partial \eta}\left(\alpha_2 \frac{\partial u_2}{\partial \eta}\right) \\ &- \frac{1}{\alpha_1\alpha_2}\frac{\tau_i S_i}{A} + \frac{1}{\alpha_1}\frac{\tau_1^w S_1}{A} - \frac{1}{\alpha_2}\frac{\tau_2^w S_2}{A},\end{aligned} \tag{2.145}$$

$$\begin{aligned}\left(\frac{M_1^2}{\alpha_1^3} + \rho\frac{M_2^2}{\alpha_2^3}\right)\frac{\partial \alpha_2}{\partial \eta} =& - (1-\rho)\, g \sin\theta - \frac{1}{\rho_1\alpha_1\alpha_2}\frac{\tau_i S_i}{A} + \frac{1}{\rho_1\alpha_1}\frac{\tau_1^w S_1}{A} - \frac{1}{\rho_1\alpha_2}\frac{\tau_2^w S_2}{A} \\ &+ (1-\rho)\, g\cos\theta\left(\frac{A}{S_i}\right)\frac{\partial \alpha_2}{\partial \eta} + \frac{\sigma_{21}}{\rho_1}\frac{\partial \hat{\gamma}^i}{\partial \eta} \\ &+ \nu_1^{eq}\left[\frac{M_1}{\alpha_1^3} - \rho\nu\frac{M_2}{\alpha_2^3}\right]\left(\frac{\partial \alpha_2}{\partial \eta}\right)^2 + \nu_1^{eq}\left[\frac{M_1}{\alpha_1^2} + \rho\nu\frac{M_2}{\alpha_2^2}\right]\frac{\partial^2 \alpha_2}{\partial \eta^2}.\end{aligned} \tag{2.146}$$

In the dispersed phases flow case as discussed in Section 2.2.2, the subtracted momentum equation 2.99 is also rewritten considering the aforementioned change of variables

$$\begin{aligned}\left(1 + \frac{C_V}{\alpha_1}\right)\rho_1\frac{\partial}{\partial \eta}\left(\frac{u_1^2}{2}\right) - \left(1 + \frac{C_V}{\rho\alpha_1}\right)\rho_2\frac{\partial}{\partial \eta}\left(\frac{u_2^2}{2}\right) =& -\Delta\rho g\sin\theta \\ &+ \left\{\frac{C_p\rho_1}{\alpha_1} + C_C C_V\left(\rho_2 + C_V\rho_1\right)\left[\frac{\alpha_2\left(\alpha_1^2 + 2\alpha_1 + 3\right)}{2\alpha_1^5}\right]\right\}\left(u_2 - u_1\right)^2\frac{\partial \alpha_2}{\partial z} \\ &+ \left[C_C C_V\left(\rho_2 + C_V\rho_1\right)\frac{\left(1+\alpha_1\right)\alpha_2^2}{\alpha_1^4} - 2C_p\rho_1\right]\left(u_2 - u_1\right)\left(\frac{\partial u_2}{\partial z} - \frac{\partial u_1}{\partial z}\right) \\ &+ \frac{\rho_1\nu_1^{eq}}{\alpha_1}\frac{\partial}{\partial \eta}\left(\alpha_1\frac{\partial u_1}{\partial \eta}\right) - \frac{\rho_2\nu_2^{eq}}{\alpha_2}\frac{\partial}{\partial \eta}\left(\alpha_2\frac{\partial u_2}{\partial \eta}\right) \\ &+ \frac{1}{\alpha_1}\frac{\bar{\tau_w} S}{A} - \frac{1}{\alpha_1\alpha_2}\hat{M}_2^D,\end{aligned} \tag{2.147}$$

$$\begin{aligned}&\left[\left(1 + \frac{C_V}{\alpha_1}\right)\frac{M_1^2}{\alpha_1^3} + \left(1 + \frac{C_V}{\rho\alpha_1}\right)\rho\frac{M_2^2}{\alpha_2^3}\right]\frac{\partial \alpha_2}{\partial \eta} = - (1-\rho)\, g\sin\theta + \frac{1}{\rho_1\alpha_1}\frac{\bar{\tau_w} S}{A} - \frac{1}{\rho_1\alpha_1\alpha_2}\hat{M}_2^D \\ &+ \left\{\frac{C_p}{\alpha_1} + C_C C_V\left(\rho + C_V\right)\left[\frac{\alpha_2\left(\alpha_1^2 + 2\alpha_1 + 3\right)}{2\alpha_1^5}\right]\right\}\left(\frac{M_2}{\alpha_2} - \frac{M_1}{\alpha_1}\right)^2\frac{\partial \alpha_2}{\partial \eta} \\ &- \left[C_C C_V\left(\rho + C_V\right)\frac{\left(1+\alpha_1\right)\alpha_2^2}{\alpha_1^4} - 2C_p\right]\left(\frac{M_2}{\alpha_2} - \frac{M_1}{\alpha_1}\right)\left(\frac{M_2}{\alpha_2^2} + \frac{M_1}{\alpha_1^2}\right)\frac{\partial \alpha_2}{\partial \eta} \\ &+ \nu_1^{eq}\left[\frac{M_1}{\alpha_1^3} - \rho\nu\frac{M_2}{\alpha_2^3}\right]\left(\frac{\partial \alpha_2}{\partial \eta}\right)^2 + \nu_1^{eq}\left[\frac{M_1}{\alpha_1^2} + \rho\nu\frac{M_2}{\alpha_2^2}\right]\frac{\partial^2 \alpha_2}{\partial \eta^2},\end{aligned} \tag{2.148}$$

where

$$\Delta\rho = \rho_1 - \rho_2, \tag{2.149}$$

and

$$\nu = \frac{\nu_2^{eq}}{\nu_1^{eq}}. \tag{2.150}$$

In addition to the ratios of specific masses ρ and relative kinematic viscosities ν, the following dimensionless numbers are defined

$$\xi = \frac{\eta}{D}, \tag{2.151}$$

$$\hat{\gamma} = D\hat{\gamma}^i, \tag{2.152}$$

$$m_k = \frac{M_k}{\sqrt{gD}}, \tag{2.153}$$

$$Re = \frac{\sqrt{gD}D}{\nu_1^{eq}}, \tag{2.154}$$

$$We = \frac{\rho_1 g D^2}{\sigma_{21}}, \tag{2.155}$$

where, considering a characteristic velocity $\sqrt{gD}$, the variables ξ, $\hat{\gamma}$, m_k, Re and We are the dimensionless travelling wave space, averaged interface curvature, relative flux Froude, Reynolds and Weber numbers, respectively. The differential operators for the new dimensionless travelling wave space variable must be rewritten

$$\frac{\partial^n}{\partial \eta^n} = \frac{1}{D^n}\frac{\partial^n}{\partial \xi^n}. \tag{2.156}$$

For the separate phases flow case, the subtracted momentum equation 2.146 is rewritten as

$$\left(\frac{m_1^2}{\alpha_1^3}+\rho\frac{m_2^2}{\alpha_2^3}\right)\frac{\partial\alpha_2}{\partial\xi}=-\left(1-\rho\right)\sin\theta-\frac{1}{\rho_1 g\alpha_1\alpha_2}\frac{\tau_i S_i}{A}+\frac{1}{\rho_1 g\alpha_1}\frac{\tau_1^w S_1}{A}-\frac{1}{\rho_1 g\alpha_2}\frac{\tau_2^w S_2}{A}$$
$$+\left(1-\rho\right)\cos\theta\left(\frac{A}{S_i D}\right)\frac{\partial\alpha_2}{\partial\xi}+\frac{1}{We}\frac{\partial\hat{\gamma}}{\partial\xi}$$
$$+\frac{1}{Re}\left[\frac{m_1}{\alpha_1^3}-\rho\nu\frac{m_2}{\alpha_2^3}\right]\left(\frac{\partial\alpha_2}{\partial\xi}\right)^2+\frac{1}{Re}\left[\frac{m_1}{\alpha_1^2}+\rho\nu\frac{m_2}{\alpha_2^2}\right]\frac{\partial^2\alpha_2}{\partial\xi^2}. \tag{2.157}$$

Moreover, for the dispersed phase flow case, the subtracted momentum equation 2.148 is also given as

$$\left[\left(1+\frac{C_V}{\alpha_1}\right)\frac{m_1^2}{\alpha_1^3}+\left(1+\frac{C_V}{\rho\alpha_1}\right)\rho\frac{m_2^2}{\alpha_2^3}\right]\frac{\partial\alpha_2}{\partial\xi}=-\left(1-\rho\right)\sin\theta+\frac{1}{\rho_1 g\alpha_1}\frac{\bar{\tau_w}S}{A}-\frac{1}{\rho_1 g\alpha_1\alpha_2}\hat{M}_2^D$$
$$+\left\{\frac{C_p}{\alpha_1}+C_C C_V\left(\rho+C_V\right)\left[\frac{\alpha_2\left(\alpha_1^2+2\alpha_1+3\right)}{2\alpha_1^5}\right]\right\}\left(\frac{m_2}{\alpha_2}-\frac{m_1}{\alpha_1}\right)^2\frac{\partial\alpha_2}{\partial\xi}$$
$$-\left[C_C C_V\left(\rho+C_V\right)\frac{\left(1+\alpha_1\right)\alpha_2^2}{\alpha_1^4}-2C_p\right]\left(\frac{m_2}{\alpha_2}-\frac{m_1}{\alpha_1}\right)\left(\frac{m_2}{\alpha_2^2}+\frac{m_1}{\alpha_1^2}\right)\frac{\partial\alpha_2}{\partial\xi}$$
$$+\frac{1}{Re}\left[\frac{m_1}{\alpha_1^3}-\rho\nu\frac{m_2}{\alpha_2^3}\right]\left(\frac{\partial\alpha_2}{\partial\xi}\right)^2+\frac{1}{Re}\left[\frac{m_1}{\alpha_1^2}+\rho\nu\frac{m_2}{\alpha_2^2}\right]\frac{\partial^2\alpha_2}{\partial\xi^2}. \tag{2.158}$$

The previous equations for the separated and dispersed phases flow can be united in one model depending on the dynamically evaluated flow pattern represented by the sigmoid function I_d over a classification boundary, alternating from one flow pattern to another, as the unit cell model suggests (Section 2.1.3), which leads to

$$F_{CA}\left(\alpha\right)\frac{\partial\alpha}{\partial\xi}=F_{FB}\left(\alpha\right)+F_{\Delta P}\left(\alpha\right)\frac{\partial\alpha}{\partial\xi}+F_{V1}\left(\alpha\right)\left(\frac{\partial\alpha}{\partial\xi}\right)^2+F_{V2}\left(\alpha\right)\frac{\partial^2\alpha}{\partial\xi^2}+\frac{\left(1-I_d\right)}{We}\frac{\partial\hat{\gamma}}{\partial\xi}, \tag{2.159}$$

where F_{CA}, F_{FB}, $F_{\Delta P}$, F_{V1} and F_{V2} are the convective acceleration, force balance, pressure difference between phases and viscosity dissipation terms, respectively

$$F_{CA}\left(\alpha\right)=\left[\left(1+I_d\frac{C_V}{\alpha_1}\right)\frac{m_1^2}{\alpha_1^3}+\left(1+I_d\frac{C_V}{\rho\alpha_1}\right)\rho\frac{m_2^2}{\alpha_2^3}\right], \tag{2.160}$$

$$\begin{aligned}F_{FB}\left(\alpha\right)=&-\left(1-\rho\right)\sin\theta-\frac{1}{\rho_1 g\alpha_1\alpha_2}\left[\left(1-I_d\right)\frac{\tau_i S_i}{A}+I_d\hat{M}_2^D\right]\\&+\frac{1}{\rho_1 g\alpha_1}\left[\left(1-I_d\right)\frac{\tau_1^w S_1}{A}+I_d\frac{\bar{\tau_w}S}{A}\right]-\frac{\left(1-I_d\right)}{\rho_1 g\alpha_2}\frac{\tau_2^w S_2}{A},\end{aligned} \tag{2.161}$$

$$F_{\Delta P}\left(\alpha\right)=\left(1-I_d\right)\left(1-\rho\right)\cos\theta\left(\frac{A}{S_iD}\right)$$
$$+I_d\left\{\frac{C_p}{\alpha_1}+C_CC_V\left(\rho+C_V\right)\left[\frac{\alpha_2\left(\alpha_1^2+2\alpha_1+3\right)}{2\alpha_1^5}\right]\right\}\left(\frac{m_2}{\alpha_2}-\frac{m_1}{\alpha_1}\right)^2 \tag{2.162}$$
$$+I_d\left[C_CC_V\left(\rho+C_V\right)\frac{\left(1+\alpha_1\right)\alpha_2^2}{\alpha_1^4}-2C_p\right]\left(\frac{m_1}{\alpha_1}-\frac{m_2}{\alpha_2}\right)\left(\frac{m_2}{\alpha_2^2}+\frac{m_1}{\alpha_1^2}\right),$$

$$F_{V1}\left(\alpha\right)=\frac{1}{Re}\left(\frac{m_1}{\alpha_1^3}-\rho\nu\frac{m_2}{\alpha_2^3}\right), \tag{2.163}$$

$$F_{V2}\left(\alpha\right)=\frac{1}{Re}\left(\frac{m_1}{\alpha_1^2}+\rho\nu\frac{m_2}{\alpha_2^2}\right). \tag{2.164}$$

As the void fraction wave has shocks with jumps in the slug flow pattern, it is not possible to use the long wave approximation to model the interfacial tension effects (Barnea; Taitel, 1994). Therefore, the mean curvature gradient is calculated using the chain rule

$$\frac{\partial\hat{\gamma}^i}{\partial z}=\frac{\partial}{\partial z}\left\{\frac{\frac{\partial^2h}{\partial z^2}}{\left[1+\left(\frac{\partial h}{\partial z}\right)^2\right]^{\frac{3}{2}}}\right\}=\frac{\frac{\partial^3h}{\partial z^3}}{\left[1+\left(\frac{\partial h}{\partial z}\right)^2\right]^{\frac{3}{2}}}-3\frac{\partial h}{\partial z}\frac{\left(\frac{\partial^2h}{\partial z^2}\right)^2}{\left[1+\left(\frac{\partial h}{\partial z}\right)^2\right]^{\frac{5}{2}}}. \tag{2.165}$$

The combined averaged momentum equation can be written either as a function of the void fraction α or the liquid height h which can be seen as a non-linear coordinate change, especially in the case of dispersed phases flow but with direct physical sense for segregated patterns only, being equivalent flow problem formulations. It is preferable to write the problem as a function of the void fraction α as it is a more general quantity, which allows directly dealing with the problem in the dispersed bubble pattern in the aerated piston section, for example. However, it is necessary a change in the variables through the generalised high-order chain rule through the Faà di Bruno's formulas

$$\frac{\partial^3h}{\partial z^3}=\frac{\partial^3h}{\partial\alpha^3}\left(\frac{\partial\alpha}{\partial z}\right)^3+3\frac{\partial^2h}{\partial\alpha^2}\frac{\partial\alpha}{\partial z}\frac{\partial^2\alpha}{\partial z^2}+\frac{\partial h}{\partial\alpha}\frac{\partial^3\alpha}{\partial z^3}, \tag{2.166}$$

$$\frac{\partial^2h}{\partial z^2}=\frac{\partial^2h}{\partial\alpha^2}\left(\frac{\partial\alpha}{\partial z}\right)^2+\frac{\partial h}{\partial\alpha}\frac{\partial^2\alpha}{\partial z^2}. \tag{2.167}$$

Therefore

$$\frac{\partial\hat{\gamma}^i}{\partial z} = \frac{1}{\left[1+\left(\frac{\partial h}{\partial\alpha}\frac{\partial\alpha}{\partial z}\right)^2\right]^{\frac{3}{2}}}\left[\frac{\partial^3 h}{\partial\alpha^3}\left(\frac{\partial\alpha}{\partial z}\right)^3 + 3\frac{\partial^2 h}{\partial\alpha^2}\frac{\partial\alpha}{\partial z}\frac{\partial^2\alpha}{\partial z^2} + \frac{\partial h}{\partial\alpha}\frac{\partial^3\alpha}{\partial z^3}\right]$$
$$- \frac{3\frac{\partial h}{\partial\alpha}\frac{\partial\alpha}{\partial z}}{\left[1+\left(\frac{\partial h}{\partial\alpha}\frac{\partial\alpha}{\partial z}\right)^2\right]^{\frac{5}{2}}}\left[\left(\frac{\partial^2 h}{\partial\alpha^2}\right)^2\left(\frac{\partial\alpha}{\partial z}\right)^4 + 2\frac{\partial h}{\partial\alpha}\frac{\partial^2 h}{\partial\alpha^2}\left(\frac{\partial\alpha}{\partial z}\right)^2\frac{\partial^2\alpha}{\partial z^2} + \left(\frac{\partial h}{\partial\alpha}\right)^2\left(\frac{\partial^2\alpha}{\partial z^2}\right)^2\right]. \tag{2.168}$$

The high-order derivatives of the implicitly defined inverse function $h(\alpha)$ are calculated from the stratified flow pattern geometric relations discussed in Section 2.1.1 through the Faà di Bruno's formulas again as

$$\frac{\partial h}{\partial\alpha} = -\frac{A}{S_i}, \tag{2.169}$$

$$\frac{\partial^2 h}{\partial\alpha^2} = \frac{2DA^2\tilde{h}}{S_i^4}, \tag{2.170}$$

$$\frac{\partial^3 h}{\partial\alpha^3} = -\frac{16A^4}{\pi S_i^7}\left(1+3\tilde{h}^2\right). \tag{2.171}$$

Substituting

$$\frac{\partial\hat{\gamma}^i}{\partial z} = \frac{1}{\left[1+\left(\frac{A}{S_i}\frac{\partial\alpha}{\partial z}\right)^2\right]^{\frac{3}{2}}}\left[-\frac{16A^4\left(1+3\tilde{h}^2\right)}{\pi S_i^7}\left(\frac{\partial\alpha}{\partial z}\right)^3 + \frac{6DA^2\tilde{h}}{S_i^4}\frac{\partial\alpha}{\partial z}\frac{\partial^2\alpha}{\partial z^2} - \frac{A}{S_i}\frac{\partial^3\alpha}{\partial z^3}\right]$$
$$+ \frac{\frac{3A}{S_i}\frac{\partial\alpha}{\partial z}}{\left[1+\left(\frac{A}{S_i}\frac{\partial\alpha}{\partial z}\right)^2\right]^{\frac{5}{2}}}\left[\frac{4D^2A^4\tilde{h}^2}{S_i^8}\left(\frac{\partial\alpha}{\partial z}\right)^4 - \frac{4DA^3\tilde{h}}{S_i^5}\left(\frac{\partial\alpha}{\partial z}\right)^2\frac{\partial^2\alpha}{\partial z^2} + \frac{A^2}{S_i^2}\left(\frac{\partial^2\alpha}{\partial z^2}\right)^2\right]. \tag{2.172}$$

Using the dimensionless numbers and differential operators as defined above, one has the dimensionless mean curvature gradient

$$\frac{1}{We}\frac{\partial\hat{\gamma}}{\partial\xi} = \frac{\frac{1}{We}}{\left[1+\left(\frac{A}{S_iD}\frac{\partial\alpha}{\partial\xi}\right)^2\right]^{\frac{3}{2}}}\left[-\frac{16A^4\left(1+3\tilde{h}^2\right)}{SS_i^7}\left(\frac{\partial\alpha}{\partial\xi}\right)^3+\frac{6A^2\tilde{h}}{S_i^4}\frac{\partial\alpha}{\partial\xi}\frac{\partial^2\alpha}{\partial\xi^2}-\frac{A}{S_iD}\frac{\partial^3\alpha}{\partial\xi^3}\right]$$
$$+\frac{3\frac{1}{We}\frac{A}{S_iD}\frac{\partial\alpha}{\partial\xi}}{\left[1+\left(\frac{A}{S_iD}\frac{\partial\alpha}{\partial\xi}\right)^2\right]^{\frac{5}{2}}}\left[\frac{4A^4\tilde{h}^2}{S_i^8}\left(\frac{\partial\alpha}{\partial\xi}\right)^4-\frac{4A^3\tilde{h}}{S_i^5D}\left(\frac{\partial\alpha}{\partial\xi}\right)^2\frac{\partial^2\alpha}{\partial\xi^2}+\left(\frac{A}{S_iD}\right)^2\left(\frac{\partial^2\alpha}{\partial\xi^2}\right)^2\right]. \tag{2.173}$$

The dimensionless mean curvature gradient can be rewritten:

$$\frac{(1-I_d)}{We}\frac{\partial\hat{\gamma}}{\partial\xi} = F_{SF1}(\alpha,w)\left(\frac{\partial\alpha}{\partial\xi}\right)^3+F_{SF2}(\alpha,w)\frac{\partial\alpha}{\partial\xi}\frac{\partial^2\alpha}{\partial\xi^2}+F_{SF3}(\alpha,w)\frac{\partial^3\alpha}{\partial\xi^3}$$
$$F_{SF4}(\alpha,w)\left(\frac{\partial\alpha}{\partial\xi}\right)^5+F_{SF5}(\alpha,w)\left(\frac{\partial\alpha}{\partial\xi}\right)^3\frac{\partial^2\alpha}{\partial\xi^2}+F_{SF6}(\alpha,w)\frac{\partial\alpha}{\partial\xi}\left(\frac{\partial^2\alpha}{\partial\xi^2}\right)^2, \tag{2.174}$$

where the surface force terms F_{SFi} are defined

$$F_{SF1}(\alpha,w) = -\frac{1}{We}\frac{(1-I_d)}{\left[1+\left(\frac{A}{S_iD}\frac{\partial\alpha}{\partial\xi}\right)^2\right]^{\frac{3}{2}}}\frac{16A^4\left(1+3\tilde{h}^2\right)}{SS_i^7} \tag{2.175}$$

$$F_{SF2}(\alpha,w) = \frac{1}{We}\frac{(1-I_d)}{\left[1+\left(\frac{A}{S_iD}\frac{\partial\alpha}{\partial\xi}\right)^2\right]^{\frac{3}{2}}}\frac{6A^2\tilde{h}}{S_i^4} \tag{2.176}$$

$$F_{SF3}(\alpha,w) = -\frac{1}{We}\frac{(1-I_d)}{\left[1+\left(\frac{A}{S_iD}\frac{\partial\alpha}{\partial\xi}\right)^2\right]^{\frac{3}{2}}}\frac{A}{S_iD} \tag{2.177}$$

$$F_{SF4}(\alpha,w) = \frac{1}{We}\frac{(1-I_d)}{\left[1+\left(\frac{A}{S_iD}\frac{\partial\alpha}{\partial\xi}\right)^2\right]^{\frac{5}{2}}}\frac{12A^5\tilde{h}^2}{S_i^9D} \tag{2.178}$$

$$F_{SF5}(\alpha,w) = -\frac{1}{We}\frac{(1-I_d)}{\left[1+\left(\frac{A}{S_iD}\frac{\partial\alpha}{\partial\xi}\right)^2\right]^{\frac{5}{2}}}\frac{12A^4\tilde{h}}{S_i^6D^2} \tag{2.179}$$

$$F_{SF6}(\alpha,w) = \frac{1}{We}\frac{(1-I_d)}{\left[1+\left(\frac{A}{S_iD}\frac{\partial\alpha}{\partial\xi}\right)^2\right]^{\frac{5}{2}}}3\left(\frac{A}{S_iD}\right)^3 \tag{2.180}$$

Therefore

$$
\begin{aligned}
F_{CA}\left(\alpha\right)\frac{\partial\alpha}{\partial\xi} = {} & F_{FB}\left(\alpha\right) + F_{\Delta P}\left(\alpha\right)\frac{\partial\alpha}{\partial\xi} + F_{V1}\left(\alpha\right)\left(\frac{\partial\alpha}{\partial\xi}\right)^2 + F_{V2}\left(\alpha\right)\frac{\partial^2\alpha}{\partial\xi^2} \\
& + F_{SF1}\left(\alpha, w\right)\left(\frac{\partial\alpha}{\partial\xi}\right)^3 + F_{SF2}\left(\alpha, w\right)\frac{\partial\alpha}{\partial\xi}\frac{\partial^2\alpha}{\partial\xi^2} + F_{SF3}\left(\alpha, w\right)\frac{\partial^3\alpha}{\partial\xi^3} \\
& + F_{SF4}\left(\alpha, w\right)\left(\frac{\partial\alpha}{\partial\xi}\right)^5 + F_{SF5}\left(\alpha, w\right)\left(\frac{\partial\alpha}{\partial\xi}\right)^3\frac{\partial^2\alpha}{\partial\xi^2} + F_{SF6}\left(\alpha, w\right)\frac{\partial\alpha}{\partial\xi}\left(\frac{\partial^2\alpha}{\partial\xi^2}\right)^2 .
\end{aligned}
\tag{2.181}
$$

This model is the most complete within the scope of this work and will be analysed and solved in the next sections.

2.3.3 Pressure Coupling

It is desirable to know the coupling between the void fraction and pressure waves. In engineering applications, it is much simpler to measure pressures by non-intrusive methods than the void fraction itself. The solution obtained so far gives an estimate of the void fraction waves, which can be used to obtain the correspoding pressure waves. This is given the fact that the constant flux solution completely defines the velocities from the void fraction and, therefore, everything else as the parietal shear stresses, etc. The simplest way to do so is from the averaged linear momentum mixture model. It is obtained when the averaged linear momentum equations for both phases of the complete composite two fluid flow model are added (Ishii; Hibiki, 2011), i.e.,

$$
\begin{aligned}
\frac{\partial}{\partial t}\left(\rho_1\alpha_1 v_1 + \rho_2\alpha_2 v_2\right) + \frac{\partial}{\partial x}\left(\rho_1\alpha_1 v_1^2 + \rho_2\alpha_2 v_2^2 + p\right) = {} & \rho_m g_z + \tau_w\frac{S}{A} - \left(1 - I_d\right)\rho_m g\cos\theta\frac{\partial h}{\partial z} \\
& + \left(1 - I_d\right)\alpha_1\sigma_{21}\frac{\partial\hat{\gamma}^i}{\partial z} \\
& - I_d\frac{\partial}{\partial z}\left[\alpha_1 C_p\rho_1\left(v_2 - v_1\right)^2\right] \\
& + \frac{\partial}{\partial z}\left(\rho_1\alpha_1\nu_1^{eq}\frac{\partial v_1}{\partial z}\right) \\
& + \frac{\partial}{\partial z}\left(\rho_2\alpha_2\nu_2^{eq}\frac{\partial v_2}{\partial z}\right) .
\end{aligned}
\tag{2.182}
$$

Applying the travelling wave transformation, yields

$$
\begin{aligned}
-V_{TB}\frac{\partial}{\partial\eta}\left(\rho_1\alpha_1 v_1+\rho_2\alpha_2 v_2\right)+\frac{\partial}{\partial\eta}\left(\rho_1\alpha_1 v_1^2+\rho_2\alpha_2 v_2^2+p\right) = {} & \rho_m g_z+\tau_w\frac{S}{A} \\
& -\left(1-I_d\right)\rho_m g\cos\theta\frac{\partial h}{\partial\eta} \\
& +\left(1-I_d\right)\alpha_1\sigma_{21}\frac{\partial\hat{\gamma}^i}{\partial\eta} \\
& -I_d\frac{\partial}{\partial\eta}\left[\alpha_1 C_p\rho_1\left(v_2-v_1\right)^2\right] \\
& +\frac{\partial}{\partial\eta}\left(\rho_1\alpha_1\nu_1^{eq}\frac{\partial v_1}{\partial\eta}\right) \\
& +\frac{\partial}{\partial\eta}\left(\rho_2\alpha_2\nu_2^{eq}\frac{\partial v_2}{\partial\eta}\right),
\end{aligned} \tag{2.183}
$$

and

$$
\begin{aligned}
\frac{\partial}{\partial\eta}\left[-V_{TB}\left(\rho_1\alpha_1 v_1+\rho_2\alpha_2 v_2\right)+\left(\rho_1\alpha_1 v_1^2+\rho_2\alpha_2 v_2^2\right)+p\right] = {} & \rho_m g_z+\tau_w\frac{S}{A} \\
& -\left(1-I_d\right)\rho_m g\cos\theta\frac{\partial h}{\partial\eta} \\
& +\left(1-I_d\right)\alpha_1\sigma_{21}\frac{\partial\hat{\gamma}^i}{\partial\eta} \\
& -I_d\frac{\partial}{\partial\eta}\left[\alpha_1 C_p\rho_1\left(v_2-v_1\right)^2\right] \\
& +\frac{\partial}{\partial\eta}\left(\rho_1\alpha_1\nu_1^{eq}\frac{\partial v_1}{\partial\eta}+\rho_2\alpha_2\nu_2^{eq}\frac{\partial v_2}{\partial\eta}\right).
\end{aligned} \tag{2.184}
$$

The equation is integrated in order to obtain the pressure field

$$
p=p_0+p_{ca}+p_\nu+p_\Delta+p_f, \tag{2.185}
$$

where p_0 is a integration constant that reflects the average pressure around which the pressure dynamically oscillates, τ_w the average parietal shear stress, I_d the dynamically evaluated classification function that indicates the flow pattern transition, p_{ca}, p_ν, p_Δ, p_f are the pressure oscillation components induced by the convective acceleration, viscous dissipation, pressures differences between phases and the body forces and shear stresses contributions, respectively. They are given by

$$
p_{ca}=\rho_1\alpha_1\left(V_{TB}-v_1\right)v_1+\rho_2\alpha_2\left(V_{TB}-v_2\right)v_2, \tag{2.186}
$$

$$p_{\nu}=\rho_1\alpha_1\nu_1^{eq}\frac{\partial v_1}{\partial\eta}+\rho_2\alpha_2\nu_2^{eq}\frac{\partial v_2}{\partial\eta}, \tag{2.187}$$

$$p_{\Delta}=-\int_{t_0}^{t}\left\{I_d\frac{\partial}{\partial\eta}\left[\alpha_1 C_p\rho_1\left(v_2-v_1\right)^2\right]+\left(1-I_d\right)\left(\rho_m g\cos\theta\frac{\partial h}{\partial\eta}-\alpha_1\sigma_{21}\frac{\partial\hat{\gamma}^i}{\partial\eta}\right)\right\}\partial\eta, \tag{2.188}$$

$$p_f=\int_{t_0}^{t}\left(\rho_m g_z+\tau_w\frac{S}{A}\right)\partial\eta, \tag{2.189}$$

The combined parietal shear stresses are given by

$$\tau_w\frac{S}{A}=\left(1-I_d\right)\tau_1^w\frac{S_1}{A}+\left(1-I_d\right)\tau_2^w\frac{S_2}{A}+I_d\bar{\tau_w}\frac{S}{A}. \tag{2.190}$$

2.4 Phase Space

In this section, the equations for the slug flow void fraction model are cast in terms of a phase space. Considering the complete model with the viscous and interfacial terms, it yields

$$\begin{aligned}F_{SF3}\left(\alpha,w\right)\frac{\partial^3\alpha}{\partial\xi^3}&=-F_{FB}\left(\alpha\right)+\left[F_{CA}\left(\alpha\right)-F_{\Delta P}\left(\alpha\right)\right]\frac{\partial\alpha}{\partial\xi}-F_{V1}\left(\alpha\right)\left(\frac{\partial\alpha}{\partial\xi}\right)^2-F_{V2}\left(\alpha\right)\frac{\partial^2\alpha}{\partial\xi^2}\\&-F_{SF1}\left(\alpha,w\right)\left(\frac{\partial\alpha}{\partial\xi}\right)^3-F_{SF2}\left(\alpha,w\right)\frac{\partial\alpha}{\partial\xi}\frac{\partial^2\alpha}{\partial\xi^2}-F_{SF4}\left(\alpha,w\right)\left(\frac{\partial\alpha}{\partial\xi}\right)^5\\&-F_{SF5}\left(\alpha,w\right)\left(\frac{\partial\alpha}{\partial\xi}\right)^3\frac{\partial^2\alpha}{\partial\xi^2}-F_{SF6}\left(\alpha,w\right)\frac{\partial\alpha}{\partial\xi}\left(\frac{\partial^2\alpha}{\partial\xi^2}\right)^2\end{aligned} \tag{2.191}$$

It can be written as an autonomous three-dimensional non-linear dynamical system by the defining the following three states

$$\frac{\partial\alpha}{\partial\xi}=w, \tag{2.192}$$

$$\frac{\partial^2\alpha}{\partial\xi^2}=\frac{\partial w}{\partial\xi}=u, \tag{2.193}$$

$$\frac{\partial^3\alpha}{\partial\xi^3}=\frac{\partial}{\partial\xi}\frac{\partial^2\alpha}{\partial\xi^2}=\frac{\partial u}{\partial\xi}, \tag{2.194}$$

$$\frac{\partial u}{\partial \xi} = f_3(\alpha, w, u) = -\frac{F_{FB}(\alpha)}{F_{SF3}(\alpha, w)} + \frac{[F_{CA}(\alpha) - F_{\Delta P}(\alpha)]}{F_{SF3}(\alpha, w)} w - \frac{F_{V1}(\alpha)}{F_{SF3}(\alpha, w)} w^2 - \frac{F_{V2}(\alpha)}{F_{SF3}(\alpha, w)} u - \frac{F_{SF1}(\alpha, w)}{F_{SF3}(\alpha, w)} w^3 - \frac{F_{SF2}(\alpha, w)}{F_{SF3}(\alpha, w)} wu - \frac{F_{SF4}(\alpha, w)}{F_{SF3}(\alpha, w)} w^5 - \frac{F_{SF5}(\alpha, w)}{F_{SF3}(\alpha, w)} w^3 u - \frac{F_{SF6}(\alpha, w)}{F_{SF3}(\alpha, w)} wu^2, \tag{2.195}$$

Consequently, the equation can be written in a compact form as a three dimensional model on the phase space

$$\frac{\partial \vec{H}_3}{\partial \xi} = \vec{F}_3\left(\vec{H}_3\right), \tag{2.196}$$

$$\vec{H}_3 = \begin{bmatrix} \alpha \\ w \\ u \end{bmatrix}, \tag{2.197}$$

$$\vec{F}_3\left(\vec{H}_3\right) = \begin{bmatrix} w \\ u \\ f_3\left(\vec{H}_3\right) \end{bmatrix}. \tag{2.198}$$

Although more complete, this model only applies to the stratified flow pattern, since the leading order term only exists when $I_D = 0$.

2.4.1 Steady State Solution

The steady state solutions, or the fixed points, are given by the equilibrium force balance

$$F_{FB}(\alpha) = 0. \tag{2.199}$$

If $I_d = 0$, it gives the classical equilibrium solutions for the stratified flow pattern (Taitel; Dukler, 1976; Shoham, 2006)

$$F_{FB}(\alpha) = -(1-\rho)\sin\theta - \frac{1}{\rho_1 g \alpha_1 \alpha_2}\frac{\tau_i S_i}{A} + \frac{1}{\rho_1 g \alpha_1}\frac{\tau_1^w S_1}{A} - \frac{1}{\rho_1 g \alpha_2}\frac{\tau_2^w S_2}{A} = 0. \tag{2.200}$$

Subsequently, simplifying assumption are made such that one and two dimensional systems are proposed.

2.4.2 One Dimensional Model

The one-dimensional model is cast by neglecting the surface tension and viscous terms, which yields

$$\frac{\partial\alpha}{\partial\xi} = \frac{F_{FB}(\alpha)}{F_{CA}(\alpha) - F_{\Delta P}(\alpha)}. \tag{2.201}$$

Note that it is a first-order system, thus it does not have oscillatory solutions for topological reasons (Strogatz; Dichter, 2016). If only the stratified flow pattern is considered, making $I_d = 0$, then this model yields the the Taylor bubble profile with variable film height (Taitel; Barnea, 1990), given by

$$\frac{\partial\alpha}{\partial\xi} = \frac{-(1-\rho)\sin\theta - \frac{1}{\rho_1 g\alpha_1\alpha_2}\frac{\tau_i S_i}{A} + \frac{1}{\rho_1 g\alpha_1}\frac{\tau_1^w S_1}{A} - \frac{1}{\rho_1 g\alpha_2}\frac{\tau_2^w S_2}{A}}{\frac{m_1^2}{\alpha_1^3} + \rho\frac{m_2^2}{\alpha_2^3} - (1-\rho)\cos\theta\left(\frac{A}{S_i D}\right)}. \tag{2.202}$$

This equation has a singularity, which will cause jumps in the calculated void fraction field in its vicinity. These jumps correspond to the Taylor bubble nose and the hydraulic jump near the tail (Taitel; Barnea, 1990)

$$\frac{m_1^2}{\alpha_1^3} + \rho\frac{m_2^2}{\alpha_2^3} - (1-\rho)\cos\theta\left(\frac{A}{S_i D}\right) = 0. \tag{2.203}$$

This singularity can be approximated considering that $\rho \ll 1$

$$Fr = -\frac{(v_1 - V_{TB})}{\sqrt{\alpha_1 g\cos\theta\left(\frac{A}{S_i}\right)}} = 1, \tag{2.204}$$

where Fr is the stratified flow pattern Froude number (Bonizzi, 2003). Therefore, the jumps occur when there is a transition between subcritical to supercritical flow. Bearing in mind that patterns transitions occur close to these jumps, then the transition boundary is near to the void fraction values that characterizes lead to this singularity.

2.4.3 Two Dimensional Model

The two dimensional model is obtained by neglecting the surface tension term, which yields

$$F_{V2}(\alpha)\frac{\partial^2\alpha}{\partial\xi^2} + F_{V1}(\alpha)\left(\frac{\partial\alpha}{\partial\xi}\right)^2 + \left[F_{\Delta P}(\alpha) - F_{CA}(\alpha)\right]\frac{\partial\alpha}{\partial\xi} + F_{FB}(\alpha) = 0 \tag{2.205}$$

It can be written as a autonomous two dimensional non-linear dynamical system as

$$\frac{\partial \alpha}{\partial \xi} = w, \tag{2.206}$$

$$\frac{\partial w}{\partial \xi} = -\frac{F_{V1}(\alpha)}{F_{V2}(\alpha)}w^2 - \frac{F_{\Delta P}(\alpha) - F_{CA}(\alpha)}{F_{V2}(\alpha)}w - \frac{F_{FB}(\alpha)}{F_{V2}(\alpha)}. \tag{2.207}$$

The equation can be cast in a more compact form as

$$\frac{\partial \vec{H}_2}{\partial \xi} = \vec{F}_2\left(\vec{H}_2\right), \tag{2.208}$$

where

$$\vec{H}_2 = \begin{bmatrix} \alpha \\ w \end{bmatrix}, \tag{2.209}$$

and

$$\vec{F}_2\left(\vec{H}_2\right), = \begin{bmatrix} w \\ -\frac{F_{V1}(\alpha)}{F_{V2}(\alpha)}w^2 - \frac{F_{\Delta P}(\alpha) - F_{CA}(\alpha)}{F_{V2}(\alpha)}w - \frac{F_{FB}(\alpha)}{F_{V2}(\alpha)} \end{bmatrix}. \tag{2.210}$$

The slug flow pattern manifests itself as a high amplitude quasi periodic oscillation of the void fraction and other related variables. In the context of a two dimensional autonomous dynamic system, this behaviour can be understood as a limit cycle (Strogatz; Dichter, 2016; Giddings, 2017), as it is a isolated periodic trajectory on a two-dimensional non-linear dynamic system.

Given the oscillatory behavior of the slug flow pattern, which alternates between the dispersed bubble and stratified flow patterns as the unit cell model suggests, then two fixed points at least are expected, one in each flow pattern. Moreover, these fixed points must be unstable, otherwise the system would be drawn to the equilibrium solutions and stop oscillating, added to the fact that the slug initiation mechanism from the stratified solution is a Kelvin Helmholtz instability, indicating an unstable fixed point at the segregated flow pattern (Barnea, 1987; Barnea; Taitel, 1994; Shoham, 2006).

2.5 Concluding Remarks

The two-fluid model was developed for the stratified and dispersed flow patterns, including all the identified relevant physical mechanisms for the unit cell formation, growth and propagation, leading to a well-posed and bounded model, as its building blocks for the stratified and dispersed bubbles flow patterns are well-posed and bounded according to the literature, when all aforementioned mechanisms are taken into account. No work reviewed considered all the mechanisms adopted for the flow patterns of interest all together for circular cross section pipelines with such rigour. However, in order to obtain a parsimonious model, reasonable assumptions were adopted for the slug flow pattern that allowed a great model simplification through the constant flux solution and the travelling wave transformation, without compromising generality.

The assumptions are: (i) incompressibility due to low phases velocities when compared to sound velocities, i.e., low Mach numbers; and (ii) an approximately constant Taylor bubble propagation velocity, hypotheses that are supported by a vast literature and experimental observations. These allowed converting a non-linear system of PDE's into ODE's that will be used subsequently, in chapter 4 to condensate the analysis of the system dynamics in a phase space for the void fraction series. From this simpler model, it is possible to investigate the system dynamics in order to understand the slug flow pattern influencing parameters and the transitions between the separate and dispersed alternating flow patterns. Also, in chapter 4 a bottom-up approach is proposed, based on the orders of magnitude of each model term. The models were sequentially developed describing the dynamical system flow in phase space for both patterns in one, two and three dimensions.

3 TRANSITION MODEL

The composite two fluid flow model combines the source terms for the separated and dispersed phases flow through the dynamically evaluated flow pattern represented by the sigmoid function I_d over a classification boundary. It alternates from one flow pattern to another, as the unit cell model suggests for the slug flow. The adequate description of this transition is fundamental for the slug flow model.

In this chapter, the description of the function I_d is addressed. A physically and data-driven based transition model is presented, based on energy conversion processes in the region of the mixing length after the hydraulic jump. First, the transition domain bounds are discussed, allowing to have an estimate of the region where the transition occurs and its parameters. Subsequently, the existence and stability of the dispersed bubble flow pattern is evaluated, giving the first proposed transition criterion based on the bublance concept (Mazzitelli; Lohse, 2009; Lance; Bataille, 1991), a dimensionless number defined such as for values lower than unity, the flow is dominated by turbulence (dispersed) and if greater than unity, the flow is dominated by buoyancy (segregated), representing the interaction between bubbles and turbulent phenomena. Afterwards, the energy conversion mechanisms is mapped and discussed, giving the second proposed transition criterion based on the maximum dissipated mean flow energy. The proposed transition criteria is discussed together with a data-driven identified one in order to craft a two-state Markov Chain model, describing the stochastic nature of the uni cell. Finally, an estimate of the turbulent equivalent kinematic viscosity is discussed.

3.1 Transition Bounds

In this section, the void fraction transition bounds are addressed and discussed. In an overview, one can already set void fraction transition limits α_T where the dispersed pattern is not possible, starting with the theoretical sphere packing limit in a unit volume, therefore, the dispersed phase flow pattern is only possible when $\alpha_T < 0.52$ (Barnea, 1987; Shoham, 2006).

Through the available experimental observations, it is also reasonable to establish that the transition to the dispersed flow pattern occurs after the hydraulic jump, as suggested by the unit cell model represented in Figures 1.1 and 1.2 (Taitel; Barnea, 1990; Fagundes Netto *et al.*, 1999; Shoham, 2006). Therefore $\alpha_T < \alpha_{HJ}$, where α_{HJ} is calculated by the critical stratified Froude number as

$$Fr\left(\alpha_{HJ}\right) = -\frac{\left(v_1 - V_{TB}\right)}{\sqrt{\left(1-\alpha_{HJ}\right) g \cos\theta \left(\frac{A}{S_i}\right)}} = 1. \tag{3.1}$$

Additionaly, it is also reasonable to state that the transition has already occurred in the vicinity of lower root for the dispersed pattern α_D. It implies that $\alpha_T > \alpha_D$, where

$$F_{FB}\left(\alpha_D\right) = -\left(1-\rho\right)\sin\theta - \frac{1}{\rho_1 g\left(1-\alpha_D\right)\alpha_D}\hat{M}_2^D - \frac{1}{\rho_1 g\left(1-\alpha_D\right)}\frac{\bar{\tau_w}S}{A} = 0. \tag{3.2}$$

These relations give the flow pattern transition function I_d its domain bounds, being summarised as

$$\alpha_D < \alpha_T < \min\left(\alpha_{HJ}, 0.52\right). \tag{3.3}$$

3.2 Dispersed Flow Pattern Transition Mechanisms

The existence or not of the dispersed pattern must be debated, which generally translates into the dynamic balance between the processes of coalescence or breakup of the dispersed bubbles. The coalescence processes are usually described through a force balance in the transverse direction regarding the main flow, where there is coalescence if the resulting force leads to bubble accumulation along the pipe dorsal line (Taitel; Dukler, 1976; Barnea; Brauner, 1985; Barnea, 1987; Shoham, 2006). The breakup processes are due to turbulence, being described through mechanisms of mechanical energy transfer from the mean flow to the fields fluctuations given by turbulent kinetic energy and to the dispersed bubbles, assuming that a fraction of the dissipated total energy is converted into surface potential energy in the bubbles (Zhang *et al.*, 2003; Brown; Dellar, 2007).

3.2.1 Bubble Breakup

Bubble deformation and breakup processes are due to the net energy transfer over the gas-liquid interface, taking into account the kinetic energy of the mean and turbulent flow, the bubble's surface potential energy and the work of interfacial tension forces over the interface (Vela-Martín; Avila, 2021). A bubble submerged in a two-phase turbulent flow is subjected to turbulent stresses that deform it, depending on the strain level, the surface potential energy can reach the activation threshold, when its breakage finally occurs. Bubble breakage occurs when the forces induced by turbulent fluctuations, that act to break the bubble, overcome the surface tension forces, that act to hold the bubble together or restore its initial underformed geometry (Andersson; Andersson, 2006).

Therefore, a criterion for bubble breakage can be produced by comparing the forces induced by turbulence and the surface tension using dimensional analysis. However, the bubble does not interact with all turbulent structures, if the eddies are larger than the bubble, a translation movement will be produced instead of deformation, which will only occur from the interaction with turbulent structures of equal or smaller sizes than the bubble. The turbulent stress τ_κ^t induced by the dynamic pressure fluctuation due to the mean squared turbulent velocity fluctuation $\bar{v'^2_\kappa}$ on the wavenumber κ is estimated by (Kolmogorov, 1949; Hinze, 1955)

$$\tau_\kappa^t \propto \frac{1}{2}\rho_1 \bar{v'^2_\kappa}. \tag{3.4}$$

The surface tension stress τ_κ^s on the wavenumber κ is estimated by

$$\tau_\kappa^s \propto 4\frac{\sigma_{21}}{d_{max}}. \tag{3.5}$$

The ratio of both forces is proportional to the critical Weber number We_c, i.e.,

$$\frac{\tau_\kappa^t}{\tau_\kappa^s} \propto \frac{\rho_1 \bar{v'^2_\kappa} d_{max}}{\sigma_{21}} = We_c. \tag{3.6}$$

The mean squared turbulent velocity fluctuation $\bar{v'^2_\kappa}$ on the wavenumber κ in the inertial sub-range of the turbulent energy cascade is given by (Pope *et al.*, 2000)

$$\bar{v'^2_\kappa} = 2\left(\frac{\epsilon}{\kappa}\right)^{\frac{2}{3}}, \tag{3.7}$$

where ϵ is the dissipated turbulent specific energy rate, assuming the incompressible single-phase turbulent model is representative for the turbulent structures until the limit of bubble formation. Therefore, considering the bubble wavenumber $\kappa = 1/d_{max}$ and substituting, the maximum stable diameter is what balances both stresses and can be summarized as (Kolmogorov, 1949; Hinze, 1955)

$$d_{max} = We_c^{\frac{3}{5}}\left(\frac{\sigma_{21}}{\rho_1}\right)^{\frac{3}{5}} \epsilon^{-\frac{2}{5}}, \tag{3.8}$$

where the maximum stable diameter d_{max} is assumed to be the representative bubble diameter d_b from now on.

The total dissipated turbulent specific energy rate ϵ for the steady state two-phase dispersed flow pattern in pipes is given by (Barnea *et al.*, 1982; Shoham, 2006)

$$\epsilon = \frac{\partial p}{\partial z}\frac{J}{\rho_m} = -\tau_w \frac{S}{A}\frac{J}{\rho_m} = \frac{2}{D} f_m J^3. \tag{3.9}$$

The major limitation in adopting this approach for the liquid piston modelling at the slug flow pattern is that the dissipated turbulent kinetic energy in the liquid piston is under-estimated by neglecting the net specific power change at the hydraulic jump, especially in the mixing length region L_m, as the flow is not steady neither developed.

The experimentally characterized critical Weber number We_c for the steady state two-phase dispersed bubbles flow pattern in pipes can be modelled by:

- Calderbank (1958) model:

$$We_c = \left(0.725 + 4.15\sqrt{\alpha}\right)^{\frac{5}{3}}, \tag{3.10}$$

- Andreussi *et al.* (1999) model:

$$We_c = 1.05\left(1 + 51.7\alpha^{1.5}\right). \tag{3.11}$$

The maximum bubble diameter d_s where the bubbles are spherical, non-deformable and behave like solid spheres with low rates of collision and coalescence is given by (Barnea *et al.*, 1982; Clift *et al.*, 2005; Shoham, 2006)

$$d_s = \sqrt{\frac{0.4\sigma_{21}}{(\rho_1 - \rho_2)g}}. \tag{3.12}$$

If the maximum stable diameter d_{max} is smaller than the maximum non-deformable spherical bubble diameter threshold, called Broadkey diameter d_s, the coalescence phenomenon is not possible, as it occurs when the bubble lose their spherical shape being distorted, ascending in a oscillating trajectory and dragging the neighboring bubbles into its wake (Barnea *et al.*, 1982; Barnea, 1987; Clift *et al.*, 2005; Shoham, 2006).

3.2.2 Bubble Coalescence

The main forces acting at the bubble in the transverse direction regarding the main flow are the buoyancy, drag and turbulent forces F_B, F_D and F_T respectively, given by (Taitel; Dukler, 1976; Barnea, 1987; Brennen, 2005; Shoham, 2006)

$$F_B = g\cos\theta\left(\rho_1 - \rho_2\right)\left(\frac{\pi d_b^3}{6}\right), \tag{3.13}$$

$$F_D = -\frac{1}{2}C_D\rho_1\left(v_{2t} - v_{1t}\right)\left|\left(v_{2t} - v_{1t}\right)\right|\left(\frac{\pi d_b^2}{4}\right), \tag{3.14}$$

$$F_T = \frac{1}{2}\rho_1 v'^2\left(\frac{\pi d_b^2}{4}\right), \tag{3.15}$$

where v' is the averaged radial velocity fluctuations that can be estimated by the turbulent friction velocity. Considering a steady state developed flow, its root mean square value is estimated by (Pope *et al.*, 2000; Shoham, 2006)

$$v' \approx \bar{v'^2}^{0.5} = v^* = \left(\frac{\tau_1^w}{\rho_1}\right)^{\frac{1}{2}} = v_1\left(\frac{f_1}{2}\right)^{\frac{1}{2}}. \tag{3.16}$$

Only the liquid phase was considered because it is the one that contributes the most, since it has the largest share of the turbulent kinetic energy. The coalescence process will occur if the resulting force leads to bubble migration and accumulation at the pipe top dorsal line, what can be represented by a conservative limiting force equilibrium, where the net force is zero, hence there is no bubble movement or drag force neither (Barnea, 1987; Shoham, 2006)

$$F_B = F_T. \tag{3.17}$$

The force equilibrium can be written in terms of the limiting segregation bubble diameter d_{ce}

$$d_{ce} = \frac{3}{8}\frac{\rho_1}{\left(\rho_1 - \rho_2\right)}\frac{f_1 v_1^2}{g\cos\theta}. \tag{3.18}$$

Therefore, if the estimated bubble diameter is bigger than the calculated threshold, i.e, $d_b > d_{ce}$, the dispersed flow pattern should transition to the separated one due to bubble coalescence. This criterion is already included in the Barnea (1987) model, however, it is used together with the spherical and non-deformable Broadkey bubble diameter d_s, which does not apply in the case of the slug flow. So, the interest lies in the case when distorted bubbles coalesce due to the resulting force. At first glance, the problem with this model is that it is too conservative, as the forces balance assumes zero net forces without movement, which is not observed in practice. Alternatively, one can estimate the segregation gas velocity v_{sb} in a transversely stagnant liquid as one has only axial movement due to the mean flow (Brennen, 2005)

$$F_B = F_D, \tag{3.19}$$

$$v_{sb} = \left[\frac{4}{3}\frac{g\cos\theta\,(\rho_1 - \rho_2)}{\rho_1 C_D} d_b\right]^{\frac{1}{2}}. \tag{3.20}$$

Then, the coalescence process will take place if the averaged radial turbulent velocity fluctuations is less than the segregation gas velocity v_{sb} by a $\mathcal{O}(0)$ factor K (Brennen, 2005)

$$\left(\frac{v_{sb}}{v'}\right)^2 = K^2 = \frac{8}{3}\frac{g\cos\theta\,(\rho_1 - \rho_2)}{\rho_1 f_1 v_1^2 C_D} d_{ct} = \frac{1}{C_D}\frac{d_{ct}}{d_{ce}}, \tag{3.21}$$

$$d_{ct} = K^2 C_D d_{ce}. \tag{3.22}$$

Therefore, if the estimated bubble diameter is bigger than the calculated threshold, i.e, $d_b > d_{ct}$, the dispersed flow pattern should transition to the separated one due to bubble coalescence. The $\mathcal{O}(0)$ factor K can be estimated experimentally, meaning how bigger the turbulent diffusive process needs to be in order to overcome the phase segregation process.

3.2.3 Proposed Bubble Transition Criterion

The same process can be described for the bubbles swarm as opposed to an individual bubble. This is done by using the averaged specific momentum transfer rate that must be in equilibrium, obtained from the subtracted momentum equation for the dispersed phases case in the pipe cross section direction, perpendicular to the pipe axis mean flow direction, similarly to what was done in the section 2.2.2, Equation 2.95 (Ishii; Hibiki, 2011), i.e.,

$$\hat{M}_2 = -\alpha\,(1-\alpha)\,(\rho_1 - \rho_2)\,g\cos\theta. \tag{3.23}$$

The averaged specific momentum transfer rate in a transversely stagnant liquid with only transverse axial movement due to the mean flow is given by

$$\hat{M}_2 = \hat{M}_2^D = -\alpha\rho_1 \left(\frac{3C_D}{4d_b}\right) v_{sw}^2, \tag{3.24}$$

where $\hat{M}_2^D$ is the drag averaged specific momentum transfer rate, given by (Ishii; Hibiki, 2011; Morel, 2015). The bubble swarm ascending velocity v_{sw} in a stagnant medium is calculated and expressed in function of v_{sb} from Equation 3.20, yielding

$$\rho_1 \left(\frac{3C_D}{4d_b}\right) v_{sw}^2 = (1-\alpha)(\rho_1 - \rho_2)\, g\cos\theta, \tag{3.25}$$

$$v_{sw}^2 = (1-\alpha)\,\frac{4}{3}\frac{g\cos\theta\,(\rho_1-\rho_2)}{\rho_1 C_D} d_b = (1-\alpha)\, v_{sb}^2. \tag{3.26}$$

Then, the coalescence process will take place if the averaged turbulent kinetic energy due to the turbulent velocity fluctuations is less than the kinetic energy due to the segregation bubble swarm velocity v_{sw} by a $\mathcal{O}(0)$ factor B. The parameter B is the bublance (Mazzitelli; Lohse, 2009; Lance; Bataille, 1991), it is defined such as for values lower than unity, the flow is dominated by turbulence (dispersed) and if greater than unity, the flow is dominated by buoyancy (segregated). This criterion was developed and adopted because it is more universal, as it is based on the swarm rather than an individual bubble and is physically linked to the buoyancy and turbulence competing mechanisms. This criterion is physically translated into the bubble swarm buoyancy ascension process, that will only be interrupted if superimposed by the Brownian motion induced by the turbulence that tends to diffuse the bubble swarm. This overlap can be seen energetically by comparing the kinetic energies of the described antagonistic movements, or statistically, since the kinetic energy of the fluctuations is equivalent to the covariance of the velocity fluctuations. Therefore, the bublance B is defined as (Mazzitelli; Lohse, 2009; Lance; Bataille, 1991)

$$B = \frac{1}{2}\alpha\frac{v_{sw}^2}{v'^2}. \tag{3.27}$$

The averaged specific turbulent kinetic energy e_k^{Re} is estimated from the trace of the Reynolds stress tensor that relates with the averaged turbulent velocity fluctuations v' (Pope *et al.*, 2000; Zhang *et al.*, 2003; Shoham, 2006), hence the Bublance B is redefined as

$$v'^2 \approx \frac{2}{3} e_k^{Re}, \tag{3.28}$$

$$B = \frac{3}{4} \alpha \frac{v_{sw}^2}{e_k^{Re}}. \tag{3.29}$$

From the bubble swarm ascending velocity v_{sw} defined in Equation 3.26, the Bublance B is redifined

$$B = \frac{\alpha(1-\alpha)}{C_D} \frac{g \cos\theta (\rho_1 - \rho_2)}{\rho_1 e_k^{Re}} d_b. \tag{3.30}$$

The limiting segregation bubble diameter d_{ce} defined in the Equation 3.18 at Section 3.2.2 is rewritten in terms of the averaged specific turbulent kinetic energy

$$d_{ce} = \frac{1}{2} \frac{\rho_1}{(\rho_1 - \rho_2)} \frac{e_k^{Re}}{g \cos\theta}. \tag{3.31}$$

Substituting, it is obtained a definition that resembles the Barnea e Brauner (1985) bubble diameter comparison criterion

$$B = \frac{1}{2} \alpha \frac{(1-\alpha)}{C_D} \frac{d_b}{d_{ce}}. \tag{3.32}$$

From the maximum stable diameter defined in the Equation 3.8 at Section 3.2.1, the Bublance can be rewritten

$$B = \alpha(1-\alpha) \frac{(\rho_1 - \rho_2)}{\rho_1} \frac{1}{C_D} We_c^{\frac{3}{5}} \left[g \cos\theta \left(\frac{\sigma_{21}}{\rho_1} \right)^{\frac{3}{5}} \frac{\epsilon^{-\frac{2}{5}}}{e_k^{Re}} \right]. \tag{3.33}$$

what indicates that the Bublance is directly connected with the average turbulent kinetic energy.

3.3 Mechanical Energy Transfer Mechanisms

Attention should be paid to the mean flow total dissipated energy rate discussed in Section 3.2.1 used in the estimation of bubble diameters expressed by Equation 3.9. They are based on relations for developed steady-state flow, a subject that will be addressed in the next sections, as the slug flow is not steady neither developed.

3.3.1 Averaged Energy Equation

The three-dimensional averaged total specific energy conservation equation for each phase k is given by (Ishii; Hibiki, 2011; Morel, 2015; Drew; Passman, 2014)

$$\frac{\partial}{\partial t}\left(\alpha_k \rho_k e_k\right)+\nabla\cdot\left(\alpha_k \rho_k \vec{v}_k h_k\right) = \nabla\cdot\left[\alpha_k\left(\tau_k + T_k\right)\vec{v}_k\right]+\alpha_k\rho_k\vec{g}\cdot\vec{v}_k-\nabla\cdot\left(\alpha_k\vec{q}_k\right)-E_k^i-Q_k^w, \quad (3.34)$$

where e_k, $\vec{v}_k$, h_k, τ_k, T_k, $\vec{q}_k$, E_k^i and Q_k^w are the averaged total specific energy, mean velocity vector, specific enthalpy, deviatoric viscous and turbulent stress tensors, specific energy vector diffusion fluxes and energy fluxes through the interface and pipe inner wall, respectively. The pipe mean flow occurs in the pipe axis direction z. Hence, the mean velocity vector $\vec{v}_k$ has zero mean velocities components at the pipe cross section perpendicular to the pipe axis, thus

$$\vec{v}_k \approx 0\vec{i} + 0\vec{j} + v_k\vec{k}. \quad (3.35)$$

However, zero average velocities do not imply that fluctuations will be neglected, since such fluctuations are considered in the two-phase Reynolds turbulent stress tensor definition from the spatiotemporal averaging operator, where the two-phase Reynolds turbulent stress tensor is the velocity field spatiotemporal covariance (Ishii; Hibiki, 2011; Morel, 2015; Drew; Passman, 2014). Therefore, the assumption presented at Equation 3.35 implies that the velocities fluctuations components around the mean are taken in to account by the turbulent stress tensor and kinetic energy diffusion flux. Subsequently, the convective operator can be rewritten

$$\frac{\partial}{\partial t}\left(\alpha_k \rho_k e_k\right) + \nabla\cdot\left(\alpha_k \rho_k \vec{v}_k h_k\right) = \frac{\partial}{\partial t}\left(\alpha_k \rho_k e_k\right) + \frac{\partial}{\partial z}\left(\alpha_k \rho_k v_k h_k\right). \quad (3.36)$$

The net power source term $S_k^{\Delta\nu}$ that encompasses the energy diffusion and dissipation along the pipe cross section perpendicular to the pipe axis is defined as

$$S_k^{\Delta\nu} = \nabla\cdot\left[\alpha_k\left(\tau_k + T_k\right)\vec{v}_k\right] - \frac{\partial}{\partial z}\left[\alpha_k\left(\tau_{zz}^k + T_{zz}^k\right)v_k\right] - \nabla\cdot\left(\alpha_k\vec{q}_k\right) + \frac{\partial}{\partial z}\left(\alpha_k q_k\right), \quad (3.37)$$

where, this term takes into account the power flow due to the work of shear stresses and moment diffusion from the longitudinal direction transferred to the transverse direction of the flow. As the average velocities field in the flow transverse directions are null, all the power flow represented by $S_k^{\Delta\nu}$ is integrally transferred to the velocity fluctuations. Without this change in variables, the energy equation would not have a dissipative term.

From this definition, the averaged total specific energy conservation equation is rewritten for the one-dimensional problem

$$\begin{aligned}\frac{\partial}{\partial t}\left(\alpha_k\rho_k e_k\right)+\frac{\partial}{\partial z}\left(\alpha_k\rho_k v_k h_k\right)=\frac{\partial}{\partial z}\left[\alpha_k\left(\tau_{zz}^k+T_{zz}^k\right)v_k\right]\\+\alpha_k\rho_k g_z v_k-\frac{\partial}{\partial z}\left(\alpha_k q_k\right)-E_k^i-Q_k^w+S_k^{\Delta\nu}.\end{aligned}\tag{3.38}$$

The averaged total specific energy e_k has its mean flow kinetic, internal and turbulent fluctuations kinetic energy components, u_k and e_k^{Re}, respectively. The averaged axial energy flux q_k has its thermal and turbulent kinetic energy components, q_k^T and q_k^{Re}, respectively. The averaged energy fluxes through the interface E_k^i is composed by the total energy e_k^i carried by the mass flux between the phases Γ_k, the work of the interface stresses $v_k^i M_k^i$ and the heat flux q_k^i through the interface (Ishii; Hibiki, 2011; Morel, 2015; Drew; Passman, 2014)

$$e_k=u_k+\frac{v_k^2}{2}+e_k^{Re},\tag{3.39}$$

$$h_k=e_k+\frac{p}{\rho_k},\tag{3.40}$$

$$q_k=q_k^T+q_k^{Re},\tag{3.41}$$

$$E_k^i=\Gamma_k e_k^i-M_k^i v_k^i+q_k^i.\tag{3.42}$$

As the scope of this work is a incompressible isothermal adiabatic flow, the averaged total energy conservation equation for each phase k is due exclusively to it's mechanical components, hence, the averaged internal energy u_k is a constant whose derivative is zero and the thermal heat fluxes q_k^T and Q_k^w are zero and going to be neglected. Therefore, the equation is rewritten from the updated definitions as

$$\begin{aligned}\frac{\partial}{\partial t}\left(\alpha_k\rho_k\frac{v_k^2}{2}+\alpha_k\rho_k e_k^{Re}\right)+\frac{\partial}{\partial z}\left(\alpha_k\rho_k v_k\frac{v_k^2}{2}+\alpha_k\rho_k v_k e_k^{Re}+\alpha_k v_k p\right)=\frac{\partial}{\partial z}\left[\alpha_k\left(\tau_{zz}^k+T_{zz}^k\right)v_k\right]\\+\alpha_k\rho_k g_z v_k\\-\frac{\partial}{\partial z}\left(\alpha_k q_k^{Re}\right)\\-E_k^i+S_k^{\Delta\nu},\end{aligned}\tag{3.43}$$

$$E_k^i = -M_k^i v_k^i. \tag{3.44}$$

The averaged mechanical energy equation is obtained by multiplying the averaged linear momentum equation by the phase velocity v_k. After some algebraic manipulations it yields (Ishii; Hibiki, 2011; Morel, 2015; Drew; Passman, 2014)

$$\begin{aligned}\frac{\partial}{\partial t}\left(\alpha_k \rho_k \frac{v_k^2}{2}\right) + \frac{\partial}{\partial z}\left(\alpha_k \rho_k v_k \frac{v_k^2}{2}\right) + v_k \frac{\partial}{\partial z}\left(\alpha_k p_k\right) =& \frac{\partial}{\partial z}\left[\alpha_k \left(\tau_{zz}^k + T_{zz}^k\right)\right] v_k + \alpha_k \rho_k g_z v_k \\ &+ M_k^i v_k + \tau_k^w \frac{S_k}{A} v_k,\end{aligned} \tag{3.45}$$

where it was considered that both phases are at the same pressure p. Subtracting the averaged mechanical energy equation from the total energy equation, one has the averaged turbulent fluctuations kinetic energy equation (Ishii; Hibiki, 2011; Morel, 2015; Drew; Passman, 2014)

$$\begin{aligned}\frac{\partial}{\partial t}\left(\alpha_k \rho_k e_k^{Re}\right) + \frac{\partial}{\partial z}\left(\alpha_k \rho_k v_k e_k^{Re} + \alpha_k q_k^{Re}\right) = \left[\alpha_k \left(\tau_{zz}^k + T_{zz}^k - p\right)\right] \frac{\partial v_k}{\partial z} - \tau_k^w \frac{S_k}{A} v_k \\ - E_k^i - M_k^i v_k + S_k^{\Delta\nu}.\end{aligned} \tag{3.46}$$

The averaged turbulent fluctuations kinetic energy equation has the convective and diffusive transport terms with a net energy source due to the stresses and viscous dissipation. Applying the travelling wave transformation, it yields

$$\frac{\partial}{\partial \eta}\left[\rho_k M_k e_k^{Re} + \alpha_k q_k^{Re}\right] = \left[\alpha_k \left(\tau_{zz}^k + T_{zz}^k - p\right)\right] \frac{\partial v_k}{\partial \eta} - \tau_k^w \frac{S_k}{A} v_k - E_k^i - M_k^i v_k + S_k^{\Delta\nu}. \tag{3.47}$$

3.3.2 Averaged Mixture Energy Equation and Interface Net Power Exchange

The averaged turbulent fluctuations kinetic energy equation for each phase k are added in order to achieve the total mixture turbulent energy equation as

$$\begin{aligned}\frac{\partial}{\partial \eta}\left[\rho_1 M_1 e_1^{Re} + \rho_2 M_2 e_2^{Re} + \alpha_1 q_1^{Re} + \alpha_2 q_2^{Re}\right] =& \left[\alpha_1 \left(\tau_{zz}^1 + T_{zz}^1 - p\right)\right] \frac{\partial v_1}{\partial \eta} \\ &+ \left[\alpha_2 \left(\tau_{zz}^2 + T_{zz}^2 - p\right)\right] \frac{\partial v_2}{\partial \eta} \\ &- \left(\tau_1^w \frac{S_1}{A} v_1 + \tau_2^w \frac{S_2}{A} v_2\right) - \left(E_1^i + E_2^i\right) \\ &- M_2^i \left(v_2 - v_1\right) + \left(S_1^{\Delta\nu} + S_2^{\Delta\nu}\right).\end{aligned} \tag{3.48}$$

From the energy jump condition, the net energy flux at interface is due to the work done by the surface tension that is going to change the surface potential energy and be dissipated, eventually. Therefore, one defines the net interface power exchange E_s as (Ishii; Hibiki, 2011; Morel, 2015; Drew; Passman, 2014)

$$E_s = E_1^i + E_2^i = \sigma \left\langle \nabla_s \left(\vec{v_i} \right) \right\rangle^i , \tag{3.49}$$

where $\langle\rangle^i$, ∇_s and $\vec{v_i}$ are the composite space-time average operator, the surface divergent and the interface velocity, respectively. The total mixture net power source term $S^{\Delta\nu}$ that encompasses the energy diffusion and dissipation along the pipe cross section perpendicular to the pipe axis is defined as

$$S^{\Delta\nu} = S_1^{\Delta\nu} + S_2^{\Delta\nu}. \tag{3.50}$$

Therefore, the averaged total mixture turbulent energy equation is rewritten as:

$$E_t + E_s = S_{mf} + S^{\Delta\nu}, \tag{3.51}$$

$$E_t = \frac{\partial}{\partial \eta} \left[\rho_1 M_1 e_1^{Re} + \rho_2 M_2 e_2^{Re} + \alpha_1 q_1^{Re} + \alpha_2 q_2^{Re} \right] , \tag{3.52}$$

$$\begin{aligned} S_{mf} = \left[\alpha_1 \left(\tau_{zz}^1 + T_{zz}^1 - p \right) \right] \frac{\partial v_1}{\partial \eta} + \left[\alpha_2 \left(\tau_{zz}^2 + T_{zz}^2 - p \right) \right] \frac{\partial v_2}{\partial \eta} \\ - \left(\tau_1^w \frac{S_1}{A} v_1 + \tau_2^w \frac{S_2}{A} v_2 \right) - M_2^i \left(v_2 - v_1 \right) , \end{aligned} \tag{3.53}$$

where E_t and S_{mf} are the mixture turbulent energy and the net energy source dissipated at the mean flow and injected as turbulent and surface energy E_s, respectively. The result expressed in Equation 3.53, reveals the energy sources that will be converted into turbulent and surface specific energy. However, in addition to the expected work of viscous and turbulent tensors and the parietal forces, there is a term $M_2^i \left(v_2 - v_1 \right)$ related to the work of interfacial forces. Therefore, it is expected that there is a component of turbulent specific energy specifically linked to the work of interfacial forces.

The net energy source has a viscous, parietal stress and slip components. Hence, one can define

$$E_t = \eta_{eff}^t S_{mf}, \tag{3.54}$$

$$E_s = \eta^s_{eff} S_{mf}, \tag{3.55}$$

$$S^{\Delta\nu} = \eta^{\Delta\nu}_{eff} S_{mf}, \tag{3.56}$$

$$\eta^t_{eff} + \eta^s_{eff} + \eta^{\Delta\nu}_{eff} = 1, \tag{3.57}$$

where η^t_{eff}, η^s_{eff} and $\eta^{\Delta\nu}_{eff}$ are the fraction of the mean flow dissipated energy transferred as turbulent kinetic energy, surface work used in bubble creation and dissipated, respectively.

Similar results are obtained from the averaged total specific energy equations, instead of the averaged turbulent fluctuations kinetic energy equations, as previously presented:

$$\frac{\partial}{\partial \eta}\left(\rho_k M_k \frac{v_k^2}{2} + \rho_k M_k e_k^{Re} + \alpha_k q_k^{Re} + \alpha_k v_k p\right) = \frac{\partial}{\partial \eta}\left[\alpha_k \left(\tau^k_{zz} + T^k_{zz}\right) v_k\right] + \alpha_k \rho_k g_z v_k - E^i_k + S^{\Delta\nu}_k. \tag{3.58}$$

Adding the averaged total specific energy equations yields

$$\begin{aligned}\frac{\partial}{\partial \eta}\left(\rho_1 M_1 \frac{v_1^2}{2} + \rho_2 M_2 \frac{v_2^2}{2}\right) + E_t + J\frac{\partial p}{\partial \eta} =& \frac{\partial}{\partial \eta}\left[\alpha_1 \left(\tau^1_{zz} + T^1_{zz}\right) v_1\right] + \frac{\partial}{\partial \eta}\left[\alpha_2 \left(\tau^2_{zz} + T^2_{zz}\right) v_2\right] \\ &+ \rho_m v_m g_z - E_s + S^{\Delta\nu}.\end{aligned} \tag{3.59}$$

From the definitions stated at Equations 3.49, 3.50 and 3.52, one has

$$\begin{aligned}E_t + E_s = S_{mf} + S^{\Delta\nu} = &- \frac{\partial}{\partial \eta}\left(\rho_1 M_1 \frac{v_1^2}{2} + \rho_2 M_2 \frac{v_2^2}{2}\right) - J\frac{\partial p}{\partial \eta} + \rho_m v_m g_z \\ &+ \frac{\partial}{\partial \eta}\left[\alpha_1 \left(\tau^1_{zz} + T^1_{zz}\right) v_1\right] + \frac{\partial}{\partial \eta}\left[\alpha_2 \left(\tau^2_{zz} + T^2_{zz}\right) v_2\right] + S^{\Delta\nu},\end{aligned} \tag{3.60}$$

where the source term is written differently from that of Equation 3.53, but it can be shown that they are equivalent, leading to

$$\begin{aligned}S_{mf} = &- \frac{\partial}{\partial \eta}\left(\rho_1 M_1 \frac{v_1^2}{2} + \rho_2 M_2 \frac{v_2^2}{2}\right) - J\frac{\partial p}{\partial \eta} + \rho_m v_m g_z \\ &+ \frac{\partial}{\partial \eta}\left[\alpha_1 \left(\tau^1_{zz} + T^1_{zz}\right) v_1\right] + \frac{\partial}{\partial \eta}\left[\alpha_2 \left(\tau^2_{zz} + T^2_{zz}\right) v_2\right].\end{aligned} \tag{3.61}$$

3.3.3 Mean Flow Specific Power source

Using the Boussinesq hypothesis that leads to an equivalent effective viscosity concept, the net specific energy rate source dissipated at the mean flow and injected as turbulent and surface energy defined in the Equation 3.61 is given by

$$\begin{aligned} S_{mf} = & -\frac{\partial}{\partial \eta}\left(\rho_1 M_1 \frac{v_1^2}{2} + \rho_2 M_2 \frac{v_2^2}{2}\right) - J\frac{\partial p}{\partial \eta} + \rho_m v_m g_z \\ & + \frac{\partial}{\partial \eta}\left[\rho_1 \alpha_1 \nu_1^{eq} \frac{\partial}{\partial \eta}\left(\frac{v_1^2}{2}\right)\right] + \frac{\partial}{\partial \eta}\left[\rho_2 \alpha_2 \nu_2^{eq} \frac{\partial}{\partial \eta}\left(\frac{v_2^2}{2}\right)\right]. \end{aligned} \tag{3.62}$$

As the mixture model is adopted, both phases are considered at the same pressure. Thus, the pressure differences between phases will be neglected. It follows from Section 2.3.3 that:

$$p = p_0 + p_{ca} + p_\nu + p_f, \tag{3.63}$$

$$p_{ca} = -\rho_1 M_1 v_1 - \rho_2 M_2 v_2, \tag{3.64}$$

$$p_\nu = \rho_1 \alpha_1 \nu_1^{eq} \frac{\partial v_1}{\partial \eta} + \rho_2 \alpha_2 \nu_2^{eq} \frac{\partial v_2}{\partial \eta}, \tag{3.65}$$

$$p_f = \int_{t_0}^{t} \left(\rho_m g_z + \tau_w \frac{S}{A}\right) \partial \eta. \tag{3.66}$$

Therefore

$$\begin{aligned} S_{mf} = & \rho_m g_z \left(v_m - J\right) - \tau_w \frac{S}{A} J \\ & - \rho_1 M_1 \frac{\partial}{\partial \eta}\left[\frac{\left(v_1 - J\right)^2}{2}\right] - \rho_2 M_2 \frac{\partial}{\partial \eta}\left[\frac{\left(v_2 - J\right)^2}{2}\right] \\ & + \frac{\partial}{\partial \eta}\left\{\rho_1 \alpha_1 \nu_1^{eq} \frac{\partial}{\partial \eta}\left[\frac{\left(v_1 - J\right)^2}{2}\right]\right\} + \frac{\partial}{\partial \eta}\left\{\rho_2 \alpha_2 \nu_2^{eq} \frac{\partial}{\partial \eta}\left[\frac{\left(v_2 - J\right)^2}{2}\right]\right\}. \end{aligned} \tag{3.67}$$

The major limitation of the dissipated specific energy rate models presented in Section 3.2.1 when adopted for the slug flow pattern is that the dissipated turbulent kinetic specific energy rate in the liquid piston is underestimated by neglecting the net specific power injection at the hydraulic jump, especially in the mixing length region L_m. The presented formulation is for a developed steady state flow, where the net power source is given by simplifying Equation 3.67 to

$$S_{mf} = \rho_m g_z \left(v_m - J\right) - \tau_w \frac{S}{A} J \approx -\tau_w \frac{S}{A} J. \tag{3.68}$$

3.3.4 Surface Energy

The total and specific surface potential energies are given by (Zhang *et al.*, 2003; Andersson; Andersson, 2006; Brown; Dellar, 2007; Vela-Martín; Avila, 2021)

$$H_i = \sigma_{21} A_i, \tag{3.69}$$

$$h_i = \sigma_{21} \frac{A_i}{V} = \sigma_{21} a_i, \tag{3.70}$$

where H_i, h_i, A_i, V and a_i are the total and specific surface potential energies, interfacial area, element unit volume and density of interfacial area, respectively. The interfacial area a_i is a transported quantity (Ishii; Hibiki, 2011; Morel, 2015)

$$\frac{\partial a_i}{\partial t} + \frac{\partial}{\partial z}\left(v_i a_i\right) = s_i, \tag{3.71}$$

where v_i and s_i are the interface velocity and source of interfacial area density, respectively. The total surface specific potential energy h_i is a quantity transported alongside the interface. Hence, multiplying the interfacial area transport equation by a constant surface tension σ_{21} and assuming that the interface velocity can be approximated by the gas phase velocity

$$\frac{\partial h_i}{\partial t} + \frac{\partial}{\partial z}\left(v_2 h_i\right) = E_s. \tag{3.72}$$

Applying the travelling wave transformation yields

$$\frac{\partial}{\partial \eta}\left[\left(v_2 - V_{TB}\right) h_i\right] = \frac{\partial}{\partial \eta}\left[\frac{M_2}{\alpha} h_i\right] = E_s. \tag{3.73}$$

The total surface specific energy h_i is calculated combining the dispersed (DB) and separated (SS) flow patterns (Zhang *et al.*, 2003; Andersson; Andersson, 2006; Brown; Dellar, 2007)

$$h_i^{DB} = \sigma \frac{6\alpha}{d_b}, \tag{3.74}$$

$$h_i^{SS} = \sigma \frac{S_i}{A}. \tag{3.75}$$

Therefore

$$h_i = I_d h_i^{DB} + (1 - I_d)\, h_i^{SS} = I_d \sigma \frac{6\alpha}{d_b} + (1 - I_d)\, \sigma \frac{S_i}{A}. \tag{3.76}$$

Substituting in Equation 3.73 yields

$$\frac{\partial}{\partial \eta} \left\{ \frac{\sigma M_2}{\alpha} \left[I_d \frac{6\alpha}{d_b} + (1 - I_d) \frac{S_i}{A} \right] \right\} = E_s = \eta_{eff}^s S_{mf}. \tag{3.77}$$

Hoque e Aoki (2005) studied the energy dissipation due to bubble entrainment reporting that around $\eta_{eff}^s \approx 25\%$ of the hydraulic jump total energy loss is dissipated as surface work. However, it is reported that only $\eta_{eff}^s \approx 1 - 2\%$ in the plunging jet case. Both interpretations are reasonable as a mechanism for bubble entrainment for the slug flow (Hoque; Aoki, 2005; Brown; Dellar, 2007).

The aforementioned energy balances are global, since after the application of the averaging operators, all spatial information in the pipe section was lost. However, bubbles interact energetically with flow structures with similar or shorter wavelengths, so that a large fraction of the dissipated energy is not available for bubble formation. Therefore, only a fraction of the turbulent part of the flow kinetic energy is available for bubble creation, depending on the wavelengths match between the structures (Zhang *et al.*, 2003; Andersson; Andersson, 2006; Brown; Dellar, 2007; Vela-Martín; Avila, 2021).

3.3.5 Turbulent Kinetic Energy

The averaged axial turbulent kinetic energy flux q_k^{Re} is a diffusion process that can be modelled by

$$q_k^{Re} = -\zeta_k \frac{\partial e_k^{Re}}{\partial z} = -\zeta_k \frac{\partial e_k^{Re}}{\partial \eta}. \tag{3.78}$$

where ζ_k is a unknown diffusivity to be identified or later defined. Due to the difference between the specific masses, the turbulent kinetic energy of the gas phase is much lower than that of the liquid phase, hence, it will be neglected ($\rho_2 e_2^{Re} \ll \rho_1 e_1^{Re}$). Therefore, the averaged turbulent mixture kinetic specific energy Equations 3.52 and 3.54 is rewritten as

$$\frac{\partial e_1^{Re}}{\partial \eta} - \frac{\rho_1 M_1}{\alpha_1 \zeta_1} e_1^{Re} = -\frac{\eta_{eff}^t}{\alpha_1 \zeta_1} \int S_{mf} \partial \eta \tag{3.79}$$

which is a first order differential equation. It is known that at the hydraulic jump the source term is impulsive, giving a sudden energy injection in the system, and the model response represents a turbulence decay during a turbulent recirculating zone with mixing length L_M, as illustrated in Figure 1.1, that can be estimated from available closure models and compared to the impulsive response of a first order differential equation as (Dukler; Hubbard, 1975).

$$\frac{\rho_1 M_1}{\alpha_1 \zeta_1} \approx \frac{1}{L_m} \tag{3.80}$$

$$L_m = 0.3 \frac{(v_F - J)^2}{2 g_z} \tag{3.81}$$

where v_F is the liquid film velocity right before the hydraulic jump.

3.3.6 Transition Criterion

Considering the aforementioned dynamics and energy transmission mechanisms, the transition from the stratified to the dispersed pattern will occur close to the point at the unit cell where the mean flow power injection is maximum, as a fraction of the total injected energy its going to be converted in surface work producing bubbles. The opposite transition can be associated with the minimal mean flow power injection resulting in bubble coalescence. Additionally, the final criterion should be confined at the domain bounds as stated in the Section 3.1 and it is combined with the a $\mathcal{O}(0)$ critical bubblance threshold B_c by comparing the estimated bubble diameter d_b with the critical diameter d_{ce}, as stated in the Section 3.2.3. Therefore, the proposed transition criterion is given by

$$\alpha_D < \alpha_T < \min\left(\alpha_{HJ}, 0.52\right), \tag{3.82}$$

$$B_c = \frac{1}{2} \alpha \frac{(1-\alpha)}{C_D} \frac{d_b}{d_{ce}} \tag{3.83}$$

$$\frac{\partial S_{mf}}{\partial \eta} = 0. \tag{3.84}$$

Due to the difference between the specific masses, the gas phase contribution is much lower than that of the liquid phase, so it can be neglected ($\rho_2 \ll \rho_1$). In order to estimate only the power injection, the viscosity effects will also be neglected, as it dissipates energy. Therefore, from the Equation 3.67 for the horizontal case

$$S_{mf} \approx f_1^w \rho_1 \frac{v_1^2}{2}\frac{S_1}{A} J - \rho_1 M_1 v_1 \frac{\partial v_1}{\partial \eta} + J \rho_1 M_1 \frac{\partial v_1}{\partial \eta}. \tag{3.85}$$

The mean flow specific power injection derivative is rewritten in terms of the relative velocity defined in Equation 2.112 at Section 2.3.1 as

$$\begin{aligned}\frac{\partial S_{mf}}{\partial \eta} \approx & \frac{\rho_1 J}{2A} S_1 v_1^2 \frac{\partial f_1^w}{\partial \alpha}\frac{\partial \alpha}{\partial \eta} + \frac{\rho_1 J}{2A} f_1^w v_1^2 \frac{\partial S_1}{\partial \alpha}\frac{\partial \alpha}{\partial \eta} + \frac{\rho_1 J}{A} V_{TB} f_1^w S_1 \frac{\partial u_1}{\partial \eta} + \frac{\rho_1 J}{A} f_1^w S_1 \frac{\partial}{\partial \eta}\left(\frac{u_1^2}{2}\right) \\ & + \rho_1 M_1 \left(J - V_{TB}\right) \frac{\partial^2 u_1}{\partial \eta^2} - \rho_1 M_1 \frac{\partial^2}{\partial \eta^2}\left(\frac{u_1^2}{2}\right).\end{aligned} \tag{3.86}$$

It follows the relative velocities derivatives definitions in addition to the ones defined in Section 2.3.2

$$\frac{\partial^2 u_1}{\partial \eta^2} = -\frac{M_1}{\alpha_1^2}\frac{\partial^2 \alpha_1}{\partial \eta^2} + 2\frac{M_1}{\alpha_1^3}\left(\frac{\partial \alpha_1}{\partial \eta}\right)^2 = \frac{M_1}{\alpha_1^2}\frac{\partial^2 \alpha}{\partial \eta^2} + 2\frac{M_1}{\alpha_1^3}\left(\frac{\partial \alpha}{\partial \eta}\right)^2, \tag{3.87}$$

$$\frac{\partial^2}{\partial \eta^2}\left(\frac{u_1^2}{2}\right) = -\frac{M_1^2}{\alpha_1^3}\frac{\partial^2 \alpha_1}{\partial \eta^2} + 3\frac{M_1^2}{\alpha_1^4}\left(\frac{\partial \alpha_1}{\partial \eta}\right)^2 = \frac{M_1^2}{\alpha_1^3}\frac{\partial^2 \alpha}{\partial \eta^2} + 3\frac{M_1^2}{\alpha_1^4}\left(\frac{\partial \alpha}{\partial \eta}\right)^2. \tag{3.88}$$

The liquid wet perimeter derivatives are calculated from the geometric definitions at Section 2.1.1 given by:

$$\frac{\partial S_1}{\partial \tilde{h}} = \frac{D}{\sqrt{1-\tilde{h}^2}} = \frac{D^2}{S_i}, \tag{3.89}$$

and

$$\frac{\partial S_1}{\partial \alpha} = \frac{\partial S_1}{\partial \tilde{h}}\frac{\partial \tilde{h}}{\partial h}\frac{\partial h}{\partial \alpha} = -\frac{2DA}{S_i^2}. \tag{3.90}$$

Substituting, it yields

$$\begin{aligned}\frac{\partial S_{mf}}{\partial \eta} \approx & \frac{\rho_1 J}{2A} S_1 v_1^2 \frac{\partial f_1^w}{\partial \alpha}\frac{\partial \alpha}{\partial \eta} - \frac{\rho_1 J}{2A} f_1^w v_1^2 \frac{2DA}{S_i^2}\frac{\partial \alpha}{\partial \eta} + \frac{\rho_1 J}{A} V_{TB} f_1^w S_1 \frac{M_1}{\alpha_1^2}\frac{\partial \alpha}{\partial \eta} + \frac{\rho_1 J}{A} f_1^w S_1 \frac{M_1^2}{\alpha_1^3}\frac{\partial \alpha}{\partial \eta} \\ & + \rho_1 M_1 \left(J - V_{TB}\right)\left[\frac{M_1}{\alpha_1^2}\frac{\partial^2 \alpha}{\partial \eta^2} + 2\frac{M_1}{\alpha_1^3}\left(\frac{\partial \alpha}{\partial \eta}\right)^2\right] - \rho_1 M_1 \left[\frac{M_1^2}{\alpha_1^3}\frac{\partial^2 \alpha}{\partial \eta^2} + 3\frac{M_1^2}{\alpha_1^4}\left(\frac{\partial \alpha}{\partial \eta}\right)^2\right].\end{aligned} \tag{3.91}$$

Finally, considering the dimensionless traveling wave coordinate expressed in Equation 2.151 in Section 2.3.2, then

$$\begin{aligned}\frac{\partial S_{mf}}{\partial \eta} \approx \; & \frac{\rho_1 J}{2A} S_1 v_1^2 \frac{\partial f_1^w}{\partial \alpha} \frac{1}{D} \frac{\partial \alpha}{\partial \xi} - \frac{\rho_1 J}{2A} f_1^w v_1^2 \frac{2DA}{S_i^2} \frac{1}{D} \frac{\partial \alpha}{\partial \xi} \\ & + \frac{\rho_1 J}{A} V_{TB} f_1^w S_1 \frac{M_1}{\alpha_1^2} \frac{1}{D} \frac{\partial \alpha}{\partial \xi} + \frac{\rho_1 J}{A} f_1^w S_1 \frac{M_1^2}{\alpha_1^3} \frac{1}{D} \frac{\partial \alpha}{\partial \xi} \\ & + \rho_1 M_1 \left(J - V_{TB}\right) \left[\frac{M_1}{\alpha_1^2} \frac{1}{D^2} \frac{\partial^2 \alpha}{\partial \xi^2} + 2 \frac{M_1}{\alpha_1^3} \left(\frac{1}{D} \frac{\partial \alpha}{\partial \xi} \right)^2 \right] \\ & - \rho_1 M_1 \left[\frac{M_1^2}{\alpha_1^3} \frac{1}{D^2} \frac{\partial^2 \alpha}{\partial \xi^2} + 3 \frac{M_1^2}{\alpha_1^4} \left(\frac{1}{D} \frac{\partial \alpha}{\partial \xi} \right)^2 \right].\end{aligned} \tag{3.92}$$

The roots of this function form a surface in three-dimensional phase space that configures the transitional boundary between the stratified and dispersed flow patterns

$$\begin{aligned}\frac{\partial S_{mf}}{\partial \eta} \approx \; & \frac{\rho_1 M_1^2}{D^2} \left[2 \left(J - V_{TB}\right) \frac{1}{\alpha_1^3} - 3 M_1 \frac{1}{\alpha_1^4} \right] w^2 \\ & + \rho_1 J \left(\frac{1}{2AD} S_1 v_1^2 \frac{\partial f_1^w}{\partial \alpha} - \frac{f_1^w v_1^2}{S_i^2} + \frac{V_{TB} M_1}{AD} \frac{f_1^w S_1}{\alpha_1^2} + \frac{M_1^2}{AD} \frac{f_1^w S_1}{\alpha_1^3} \right) w \\ & + \frac{\rho_1 M_1^2}{D^2} \left[\left(J - V_{TB}\right) \frac{1}{\alpha_1^2} - M_1 \frac{1}{\alpha_1^3} \right] u \\ & = 0.\end{aligned} \tag{3.93}$$

3.4 Two-state Markov Chain Model

As discussed in previous sections, the slug flow is typically modelled as a unit cell varying from a Taylor bubble region in the segregated flow pattern and a liquid slug region in the dispersed bubble flow pattern. In this section, we propose that the complex dynamics of such alternating structures can be approximated by a stochastic process.

Assuming the void fraction measurements are made at a constant sampling rate Δ and the regularly sampled void fraction, i.e. $\alpha_n = \alpha(t = n\Delta)$, a very simple model for this process can be cast in the form of a two-state Markov chain (Norris, 1997; Soize, 2017), which follows closely the representation given by Fabre *et al.* (1989) for the time evolution of the flow structure. Each state represents either the Taylor bubble or the liquid slug, then the Markov chain (MC) is characterised by the probabilities of the sequence maintain or changing its state at the n-th sample given the previous samples, i.e. $P\left(X_n = x_n \mid X_{n-1} = x_{n-1}\right)$ for a first order

Markov chain, where $x_n = 1$ for the Taylor bubble and $x_n = 0$ for the liquid slug. This model is schematically represented in Figure 3.1.

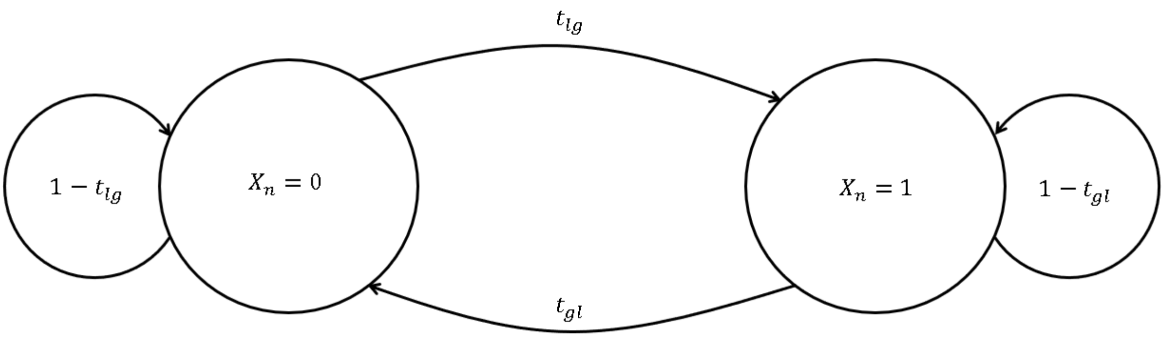

Figure 3.1 – Two-state Markov chain model diagram for liquid slug ($X_n = 0$) and Taylor bubble ($X_n = 1$). State transition probability from liquid slug to Taylor bubble t_{lg} and from Taylor bubble to liquid slug t_{gl}.

3.4.1 State Classification

The void fraction time series classification in a discrete sequence of two states is a separate problem and several approaches to solve it can be adopted, being a classic classification problem, where one can adopt tools for tabular data disregarding sequential properties or specific tools for time series data (Géron, 2017).

As suggested by the unit cell model depicted in the Figure 1.3, it is expected that the void fraction time series data are naturally separated into two groups, one with higher void fractions and another with the lower ones, separated according to a given threshold. Therefore, intuitively, it is not necessary to consider the sequential aspect of the data, which allows us to pose the problem as an unsupervised clustering problem for a one-dimensional tabular data, where the raw measured void fraction α_n is the only available data feature.

The more straightforward approach is to use the K-means algorithm, as it separates the samples in groups of equal variance (Géron, 2017). However, one can adopt the even simpler Otsu method, largely used in image processing, as it is equivalent to the K-means algorithm for one-dimensional problems (Otsu, 1979; Liu; Yu, 2009). The main advantage of this method is that it allows classifying the void fraction time series in a simple, unsupervised and non-parametric way, automatically estimating the aforementioned threshold directly from data, without any other input or intervention. One could use more advanced techniques for time series, considering the sequential aspects of the data or even with a greater number of classes, separating, for example, the Taylor bubble nose and tail regions. However, this is outside the scope of this work.

The classification threshold identified from the data should be closely related to the transition criteria developed in the Sections 3.2.3 and 3.3.6, therefore one should compare them by discussing how physically representative they are.

3.4.2 State Transition Conditional Probabilities

The state transition conditional probability from liquid slug to Taylor bubble is defined as t_{lg}

$$t_{lg} = P\left(X_n = 1 | X_{n-1} = 0\right), \tag{3.94}$$

while the state transition conditional probability from Taylor bubble to liquid slug is defined as t_{gl}

$$t_{gl} = P\left(X_n = 0 | X_{n-1} = 1\right), \tag{3.95}$$

where $0 \leq t_{lg,gl} \leq 1$.

The discrete probability density function at the n-th sample $\boldsymbol{\pi}^n$ can be given from the marginal probabilities for each state, given as:

$$\begin{aligned} P\left(X_n = 0\right) = {} & P\left(X_n = 0 \mid X_{n-1} = 0\right) P\left(X_{n-1} = 0\right) \\ & + P\left(X_n = 0 \mid X_{n-1} = 1\right) P\left(X_{n-1} = 1\right), \end{aligned} \tag{3.96}$$

$$\begin{aligned} P\left(X_n = 1\right) = {} & P\left(X_n = 1 \mid X_{n-1} = 0\right) P\left(X_{n-1} = 0\right) \\ & + P\left(X_n = 1 \mid X_{n-1} = 1\right) P\left(X_{n-1} = 1\right), \end{aligned} \tag{3.97}$$

Rearranging in matrix form, yields:

$$\boldsymbol{\pi}^n = \boldsymbol{\pi}^{n-1}\mathbf{P}, \tag{3.98}$$

where the joint discrete probabilities state transition matrix is given in terms of the conditional state transition probabilities as

$$\mathbf{P} = \begin{bmatrix} P\left(X_n = 0 \mid X_{n-1} = 0\right) & P\left(X_n = 1 \mid X_{n-1} = 0\right) \\ P\left(X_n = 0 \mid X_{n-1} = 1\right) & P\left(X_n = 1 \mid X_{n-1} = 1\right) \end{bmatrix} = \begin{bmatrix} 1 - t_\alpha & t_\alpha \\ t_\beta & 1 - t_\beta \end{bmatrix}. \tag{3.99}$$

The chain is stationary when $\boldsymbol{\pi}^n = \boldsymbol{\pi}^{n-1}$ which yields an eigenproblem $\boldsymbol{\pi}^n = \boldsymbol{\pi}^n \mathbf{P}$ with eigenvalue $\lambda_1 = 1$ and corresponding eigenvector $\boldsymbol{\phi}_1$:

$$\boldsymbol{\phi}_1 = \begin{bmatrix} \frac{t_{gl}}{t_{lg}+t_{gl}} \\ \frac{t_{lg}}{t_{lg}+t_{gl}} \end{bmatrix}. \tag{3.100}$$

Consequently, its steady-state distribution is:

$$\boldsymbol{\pi} = \begin{bmatrix} \pi_0 \\ \pi_1 \end{bmatrix} = \boldsymbol{\phi}_1 = \begin{bmatrix} \frac{t_{gl}}{t_{lg}+t_{gl}} \\ \frac{t_{lg}}{t_{lg}+t_{gl}} \end{bmatrix}. \tag{3.101}$$

By increasing the MC model order, the state of m previous samples other than the immediately previous one are also taken into account at the state transition conditional probabilities of the sequence, i.e., $P\left(X_n = x_n \mid X_{n-1} = x_{n-1}, X_{n-1} = x_{n-2}, \ldots X_{n-m} = x_{n-m}\right)$ (Katz, 1981). This introduces a finite memory to the chain related to its order, hence, instead of a transition matrix, now one has a transition tensor of order m. Although it can, in principle, improve the Markov Chain model, it also significantly increases the number of parameters for estimation, with the increasing number of possible transition probabilities. It might require significantly longer measurements times which limits its practical uses and imposes a parsimonious approach for the order selection of the model. Ideally, a first order model should succeed in adequately representing a certain phenomenon even with longer time dependency (Rafteryt, 1985).

3.4.3 Statistical Moments of the First Order MC Model

Some relevant statistical moments can be analytically derived for the proposed steady-state two-state first order MC model. The mean value of the series is given by:

$$\mathbb{E}\left(X_n\right) = \sum_{n=0}^{1} x_n \pi_n = \frac{t_{lg}}{t_{lg} + t_{gl}}, \tag{3.102}$$

where $\mathbb{E}(\cdot)$ stands for the mathematical expectation. Note that this statistical moment is identical to the intermittency factor, i.e., β:

$$\mathbb{E}\left(X_n\right) = \beta, \tag{3.103}$$

The variance $Var\left(X_n\right)$ is given by:

$$\mathrm{Var}\left(X_n\right) = \mathbb{E}\left(X_n^2\right) - \mathbb{E}\left(X_n\right)^2 = \sum_{n=0}^{1} x_n^2 \pi_n - \sum_{n=0}^{1} (x_n \pi_n)^2 = \frac{t_{lg} t_{gl}}{(t_{lg} + t_{gl})^2}. \tag{3.104}$$

The autocovariance is defined as:

$$\mathrm{Cov}\left(X_n, X_{n+\tau}\right) = \mathbb{E}\left\{\left[X_n - \mathbb{E}\left(X_n\right)\right]\left[X_{n+\tau} - \mathbb{E}\left(X_{n+\tau}\right)\right]\right\}, \tag{3.105}$$

which yields

$$\mathrm{Cov}\left(X_n, X_{n+\tau}\right) = \mathbb{E}\left(X_n X_{n+\tau}\right) - \mathbb{E}\left(X_n\right)^2 = \mathbb{E}\left(X_n X_{n+\tau}\right) - \left(\frac{t_{lg}}{t_{lg} + t_{gl}}\right)^2. \tag{3.106}$$

The term $\mathbb{E}\left(X_n X_{n+\tau}\right)$ is the autocorrelation and can be evaluated as

$$\mathbb{E}\left(X_n X_{n+\tau}\right) = \sum_{n=0}^{1} x_n x_{n+\tau} P\left(X_{n+\tau} = x_{n+\tau} \cap X_n = x_n\right), \tag{3.107}$$

from which

$$P\left(X_{n+\tau} = x_{n+\tau} \cap X_n = x_n\right) = P\left(X_{n+\tau} = x_{n+\tau} \mid X_n = x_n\right) P\left(X_n = x_n\right), \tag{3.108}$$

Bearing in mind that the only non-null terms of the sum are given when $X_n = 1$, thus

$$\mathbb{E}\left(X_n X_{n+\tau}\right) = P\left(X_n = 1 \mid X_{n+\tau} = 1\right) P\left(X_n = 1\right) \tag{3.109}$$

Recalling that $P\left(X_n = 1\right) = \mathbb{E}\left(X_n\right)$, then recursively from the chain using Eq. 3.98, term $P\left(X_n = 1 \mid X_{n+\tau} = 1\right) = \mathbf{P}_{2,2}^{\tau}$, which is second row and second column term of the matrix $\mathbf{P}^{\tau}$. Finally, it yields:

$$\mathrm{Cov}\left(X_n, X_{n+\tau}\right) = \mathrm{ab}^{|\tau|}, \tag{3.110}$$

where $\mathrm{a} = t_{lg} t_{gl} \left(t_{lg} + t_{gl}\right)^{-2}$ and $\mathrm{b} = \left(1 - t_{lg} - t_{gl}\right)$, and normalised by the variance gives $\mathrm{Cov}\left(X_n, X_{n+\tau}\right) / \mathrm{Var}\left(X_n\right) = \mathrm{b}^{|\tau|}$.

Moreover, the power spectral density (PSD) can be obtained from the Fourier transform of Eq. 3.110 as

$$F(\omega) = \frac{1}{2\pi} \sum_{\tau=-\infty}^{+\infty} \mathrm{a}\mathrm{b}^{|\tau|} e^{-j\omega\Delta\tau} = \frac{\mathrm{a}}{2\pi} \sum_{\tau=-\infty}^{+\infty} \mathrm{b}^{|\tau|} e^{-j\omega\Delta\tau} = \frac{\mathrm{a}}{2\pi} \left[1 + 2 \sum_{\tau=1}^{+\infty} \mathrm{b}^{\tau} \cos(\omega\Delta\tau) \right]. \tag{3.111}$$

By definition, $|\mathrm{b}| < 1$ thus the infinite series converges to

$$F(\omega) = \frac{\mathrm{a}}{2\pi} \left[\frac{1 - \mathrm{b}^2}{1 - 2\mathrm{b}\cos(\Delta\omega) + \mathrm{b}^2} \right] = \frac{\mathrm{a}}{2\pi} \left[\frac{1 - \mathrm{b}^2}{1 + \mathrm{b}^2 - 2\mathrm{b}\cos(2\pi\omega/\omega_s)} \right]. \tag{3.112}$$

Note that this is a periodic function in $-\omega_s/2 < \omega < \omega_s/2$, where $\Delta\omega = 2\pi\omega/\omega_s$, ω_s is the sampling frequency in rad/s. This periodicity is expected due to the discrete nature of the MC sequence. Finding the similar analytical expressions of the proposed higher order two-state Markov Chain is beyond the scope of this work.

3.5 Turbulent Viscosity

The cross sectional area averaged turbulent stress tensors for the two-phase flow case is usually neglected in some applications, especially in one dimensional models. But, this generates the need to include artificial dissipation in the numerical methods to allow the solution with shocks and discontinuities (Munkejord, 2006; Nguyen, 2016), like the ones observed in the slug flow pattern. Therefore, although there is no obvious closure model, this term must remain in the model for further adjustments posing a system identification problem, where it should be noted that due to the flow pattern transition, it is probable that a set of parameters has to be estimated for each flow pattern.

The incompressible space-time averaged two-phase turbulent Reynolds stress tensor is defined from the autocovariance of the velocity field $\vec{v}_k$ whose trace is the averaged turbulent specific kinetic energy e_k^{Re} and is rewritten using the Boussinesq hypothesis as (Ishii; Hibiki, 2011; Drew; Passman, 2014; Morel, 2015)

$$T^1 = \rho_1 \nu_1^T \left(\nabla \vec{v}_1 + \nabla \vec{v}_1^T \right), \tag{3.113}$$

where the gas phase was neglected due to its lower specific mass that leads to a low contribution to the averaged turbulent kinetic energy.

Information about the three-dimensional fields were lost when applying the averaging operators in the pipeline cross-sectional area, like the velocity profile. As turbulence is an intrinsically three-dimensional phenomenon (Pope *et al.*, 2000), it cannot be directly modeled by a one dimensional approach. Consequently, the equivalent dissipation phenomenon applied to the context of one-dimensional flow is adopted (Bertodano *et al.*, 2016). As this application uses the one-dimensional two-fluid model, the spatio-temporal averaging operator is applied along the pipe cross-section. Hence, such an average operator should be applied to the equivalent turbulent viscosity also (Ishii; Hibiki, 2011).

As the velocity profile information was lost after the averaging, it is not possible to adopt the classical zero equation model using the Prandtl mixture length approach in order to model the effective turbulent viscosity with a simple algebraic equation (Pope *et al.*, 2000).

According to the two time constant $k-\epsilon$ model for two-phase flows (Launder; Spalding, 1973; Kataoka; Serizawa, 1989; Bertodano *et al.*, 1994; Bertodano *et al.*, 1994; Bertodano *et al.*, 2016), the averaged effective kinematic viscosity ν_k^T is broken down into components related to shear induced turbulence due to the wall shear stress ν_k^{TW}, shear induced turbulence due to interface shear stress ν_k^{TI} and bubble-induced turbulence ν_k^{TB}, which despite being called this way, is also induced by shear due to the bubbles vortex shedding caused by the relative velocity between the phases (Sato; Sekoguchi, 1975; Zhang *et al.*, 2006), i.e.

$$\nu_k^T = \nu_k^{TW} + \nu_k^{TI} + \nu_k^{TB}. \tag{3.114}$$

The shear induced turbulence due to the wall shear stress ν_k^{TW} component is given by the standard $k-\epsilon$ model (Launder; Spalding, 1973) as

$$\nu_k^{TW} = C_\mu \frac{e_1^{Re^2}}{\epsilon}, \tag{3.115}$$

and

$$C_\mu = 0.09, \tag{3.116}$$

where ϵ is the averaged turbulence kinetic energy dissipation rate. The bubble induced turbulence component ν_k^{TB} is given by (Sato; Sekoguchi, 1975)

$$\nu_k^{TB} = C_{\mu b} \alpha \frac{d_b}{2} \left| v_2 - v_1 \right|, \tag{3.117}$$

and:

$$C_{\mu b} = 1.2. \tag{3.118}$$

There is no general closure model for the shear induced turbulence at the interface caused by the slip velocity and waves. Then, the turbulent mixing layer model, that is the most analogous classical analytical problem, will be taken as a basis for estimating the effective viscosity (Fullmer *et al.*, 2011; Bertodano *et al.*, 2016). The turbulent viscosity of the self-similar mixing layer is analytically given by (Pope *et al.*, 2000)

$$\nu_k^{TI} = 0.39^2 S\delta \left|v_2 - v_1\right|, \tag{3.119}$$

where S is the spreading rate and δ is the mixing layer thickness. Fullmer *et al.* (2011) estimated the aforementioned coefficients through CFD in order to reproduce the simulated energy dissipation for the Kelvin-Helmholtz waves in an one-dimensional model, in comparison with experimental data from a squared and circular channels closed in both ends with water and kerosene or gasoline in a stratified flow pattern without mean flow, giving the following results for the shear induced turbulence due to interface shear stress ν_k^{TI} component (Fullmer *et al.*, 2011; Bertodano *et al.*, 2016)

$$\nu_k^{TI} = C_{\mu i} \left|v_2 - v_1\right|, \tag{3.120}$$

and

$$C_{\mu i} = 0.0015D. \tag{3.121}$$

Therefore, the effective averaged kinematic turbulent viscosity for the slug flow can be summarized as

$$\nu_k^{T} = C_\mu \frac{e_1^{Re\,2}}{\epsilon} + I_d C_{\mu b} \alpha \frac{d_b}{2} \left|v_2 - v_1\right| + \left(1 - I_d\right) C_{\mu i} \left|v_2 - v_1\right|. \tag{3.122}$$

In addition, as the averaged mean flow power injection and the averaged turbulent kinetic energy e_1^{Re} estimation were dealt in the previous sections with closure pending, so an one equation model approach with a closure relation for the dissipated energy seems to be the best option (Morel, 2015; Bertodano *et al.*, 2016). Therefore, disregarding any spacial shape factor arising from the spatio-temporal averaging operator, the averaged energy dissipation rate is estimated by (Pope *et al.*, 2000)

$$\epsilon = \frac{e_k^{Re\,\frac{3}{2}}}{l_m}, \tag{3.123}$$

where l_m is a typical mixing length scale for pipe flow, given as a function of the liquid hydraulic diameter D_H (Schlichting; Gersten, 1979; Salvo, 2014)

$$l_m = 0.07D_H. \tag{3.124}$$

Therefore, Equation 3.122 is rewritten as

$$\nu_k^T = C_\mu l_m \sqrt{e_k^{Re}} + I_d C_{\mu b} \alpha \frac{d_b}{2} \left| v_2 - v_1 \right| + \left(1 - I_d\right) C_{\mu i} \left| v_2 - v_1 \right|. \tag{3.125}$$

For the estimation of the averaged turbulent effective kinematic viscosity, it is necessary to define the averaged turbulent kinetic energy. This definition will be presented in the next section.

3.5.1 One-dimensional One Equation Model

Turbulence is a complex phenomenon, where even for steady state single-phase flows, there are open issues to be researched currently (Pope *et al.*, 2000). In the case of two-phase flows, the interactions between the phases at the interfaces that can take a great diversity of spatio-temporal topologies make the problem even more complex (Ishii; Hibiki, 2011; Morel, 2015). There are few and restricted closure relationships to model the two-phase turbulent phenomena, where it is common to use the available models for single-phase flows adapted and adjusted experimentally, especially for the dispersed flow patterns where the abstraction of the homogeneous model is consistent (Shoham, 2006).

The slug flow is even more challenging. That is because, in addition to be a two-phase flow, it combines the dispersed and segregated patterns in an alternating and transient sense. Hence, the Reynolds stress tensor is presumably not stationary, homogeneous nor isotropic. In this context, in the absence of better closure models and experimental confirmation suited for the one dimensional pipe flow applications, it is proposed based on the fundamental principles and the information available at the literature that the specific turbulent kinetic energy can be estimated combining a stationary homogeneous component $\bar{e}_k^{Re}$ with a non-stationary and non homogeneous undefined component ${e'}_k^{Re}$

$$e_k^{Re} = \bar{e}_k^{Re} + {e'}_k^{Re}. \tag{3.126}$$

The stationary homogeneous component of the specific turbulent kinetic energy is estimated from the trace of a isotropic Reynolds stress tensor (Pope *et al.*, 2000; Zhang *et al.*, 2003; Shoham, 2006)

$$e_k^{Re} \approx \frac{3}{2}\bar{v'}_k^2, \tag{3.127}$$

where v'_k is the averaged radial velocity fluctuations that can be estimated by the turbulent friction velocity. Its root mean square value is given by

$$v'_k \approx \bar{v'}_k^{2\,0.5} = v_k^* = \left(\frac{\tau_k^w}{\rho_k}\right)^{\frac{1}{2}} = v_k \left(\frac{f_k}{2}\right)^{\frac{1}{2}}. \tag{3.128}$$

Therefore

$$e_k^{Re} \approx \frac{3}{2}\frac{\tau_k^w}{\rho_k} = \frac{3}{4} f_k v_k^2. \tag{3.129}$$

The stationary homogeneous component of the averaged turbulent kinetic energy e_k^{Re} defined in the Equation 3.129 could be used for estimating the averaged effective kinematic viscosity ν_k^T defined in the Equation 3.125. However, such estimate would be undersized at the liquid piston region given the sudden mean flow dissipated energy injection at hydraulic jump, as discussed in Section 3.3.5.

In order to consider the non-stationary and non-homogeneous component of the averaged turbulent kinetic energy, the averaged total specific energy balance performed in Section 3.3 will be adapted and rewritten. Recall, that it is the one-dimensional approach inspired by the classical three-dimensional equation model, following its footsteps and premises.

Due to the difference between the specific masses ($\rho_2 \ll \rho_1$), the mean flow power injection and turbulent kinetic energy of the gas phase is much lower than that of the liquid phase, thus, it will be neglected . Subsequently, the averaged turbulent mixture kinetic specific energy Equations 3.51, 3.52, 3.77 and 3.67 are rewritten as

$$\begin{aligned}
\frac{\partial}{\partial \eta}\left[\rho_1 M_1 e_1^{Re} + \alpha_1 q_1^{Re}\right] = &- \frac{\partial}{\partial \eta}\left\{\frac{\sigma M_2}{\alpha}\left[I_d \frac{6\alpha}{d_b} + (1 - I_d)\frac{S_i}{A}\right]\right\} \\
&- \rho_1 M_1 \frac{\partial}{\partial \eta}\left[\frac{(v_1 - J)^2}{2}\right] + \frac{\partial}{\partial \eta}\left\{\rho_1 \alpha_1 \nu_1^T \frac{\partial}{\partial \eta}\left[\frac{(v_1 - J)^2}{2}\right]\right\} \\
&- \tau_w \frac{S}{A} J + S^{\Delta\nu}
\end{aligned} \tag{3.130}$$

The averaged axial turbulent kinetic energy flux q_k^{Re} is a diffusion process that can be modelled by

$$q_1^{Re} = -\rho_1 \nu_1^T \frac{\partial e_1^{Re}}{\partial z} = -\rho_1 \nu_1^T \frac{\partial e_1^{Re}}{\partial \eta} \tag{3.131}$$

where the diffusivity is the averaged turbulent effective kinematic viscosity (Launder; Spalding, 1973; Kataoka; Serizawa, 1989; Bertodano *et al.*, 2016). Substituting, it yields

$$\begin{aligned} M_1 \frac{\partial e_1^{Re}}{\partial \eta} - \frac{\partial}{\partial \eta}\left(\alpha_1 \nu_1^T \frac{\partial e_1^{Re}}{\partial \eta}\right) = &- \frac{\partial}{\partial \eta}\left\{\frac{\sigma M_2}{\rho_1 \alpha}\left[I_d \frac{6\alpha}{d_b} + (1 - I_d)\frac{S_i}{A}\right]\right\} \\ &- M_1 \frac{\partial}{\partial \eta}\left[\frac{(v_1 - J)^2}{2}\right] + \frac{\partial}{\partial \eta}\left\{\alpha_1 \nu_1^T \frac{\partial}{\partial \eta}\left[\frac{(v_1 - J)^2}{2}\right]\right\} \\ &- \frac{\tau_w}{\rho_1}\frac{S}{A} J + \frac{S^{\Delta\nu}}{\rho_1} \end{aligned} \tag{3.132}$$

The total mixture net power source term $S^{\Delta\nu}$ that encompasses the energy diffusion and dissipation along the pipe cross section perpendicular to the pipe axis, defined in Equation 3.50, can be approximated as (Pope *et al.*, 2000; Morel, 2015)

$$-\frac{S^{\Delta\nu}}{\rho_1} = \epsilon = \frac{e_k^{Re\,\frac{3}{2}}}{l_m}, \tag{3.133}$$

using the averaged turbulence kinetic energy dissipation rate ϵ and the one equation model hypothesis. Consequently, it yields

$$\begin{aligned} M_1 \frac{\partial e_1^{Re}}{\partial \eta} - \frac{\partial}{\partial \eta}\left(\alpha_1 \nu_1^T \frac{\partial e_1^{Re}}{\partial \eta}\right) = &- \frac{\partial}{\partial \eta}\left\{\frac{\sigma M_2}{\rho_1 \alpha}\left[I_d \frac{6\alpha}{d_b} + (1 - I_d)\frac{S_i}{A}\right]\right\} \\ &- M_1 \frac{\partial}{\partial \eta}\left[\frac{(v_1 - J)^2}{2}\right] + \frac{\partial}{\partial \eta}\left\{\alpha_1 \nu_1^T \frac{\partial}{\partial \eta}\left[\frac{(v_1 - J)^2}{2}\right]\right\} \\ &- \frac{\tau_w}{\rho_1}\frac{S}{A} J - \frac{e_k^{Re\,\frac{3}{2}}}{l_m}. \end{aligned} \tag{3.134}$$

This equation is very similar to the classical three-dimensional one equation model that has been adapted to the one-dimensional case in the travelling wave reference frame. This equation can then be integrated to obtain the evolution of the averaged turbulent kinetic energy.

3.6 Concluding Remarks

The description of the dynamically evaluated flow pattern represented by the sigmoid function I_d over a classification boundary is addressed where a physically and data-driven based transition model for the flow pattern classification boundary is presented, based on energy conversion processes in the region of the mixing length after the hydraulic jump.

The transition domain bounds were discussed, allowing to have an estimate of the region where the transition occurs and its parameters. Subsequently, the existence and stability of the dispersed bubble flow pattern were evaluated, giving the first proposed transition criterion based on the bublance concept. Afterwards, the energy conversion mechanisms were mapped and discussed, giving the second proposed transition criterion based on the maximum dissipated mean flow energy. The proposed transition criteria are discussed together with a data-driven identified one in order to craft a two-state Markov Chain model in order to model the stochastic nature of the unit cell. Finally, a discussion on the estimation of the turbulent equivalent kinematic viscosity was presented.

4 RESULTS AND DISCUSSION

In this chapter, the model analysis results are presented. First, the experimental data, obtained from the literature, are briefly presented and then the main features of the unit cell model are identified, i.e., the void fraction at the liquid slug α_S, the void fraction at the elongated bubble α_F, the intermittent factor β, the passing frequency of the unit cell f_U and the Taylor bubble velocity V_{TB}.

The proposed stochastic model based on the two-state Markov chain model is identified. The Otsu's method (Otsu, 1979) is used for selecting both states from the time series. A first order Markov chain model is firstly investigated as a candidate model. But it fails in capturing the longer than the unit cell terms of the stochastic process. Then, a higher-order Markov chain model is estimated and, following the principle of parsimonious and physically interpretable model selection, a criteria for determining the order of the chain is proposed. Then, the unit cell parameters are estimated as random variables.

Subsequently, the experimental data is investigated from a non-linear dynamic system point of view. The void fraction time series is converted to the traveling wave reference frame and the phase space reconstruction is discussed in terms of the Taylor bubble and slug body regions, as determined by the Otsu's method. From this interpretation, the two-state Markov chain stochastic process model, can additionally be interpreted as modelling the transition probabilities between the equilibrium void fractions solutions at the center of the orbits. Thus, the apparent randomness from the stochastic model is an indication of a chaotic behavior.

Finally, the last section presents the numerical results from the theoretical model. A bottom up approach is proposed by increasing the dimension of the system from its first order approximation up to the order identified from the experimental data.

4.1 Experimental Data

The experimental data used came from the work of Rodrigues *et al.* (2020). The data acquisition campaign was performed at the Multiphase Flow Research Center of the Federal University of Technology of Paraná (Brazil) and it is described in detail by Rodrigues *et al.* (2020). The experimental apparatus consists of three pipelines: single-phase water, air and a two-phase one. A mixer is used in the entry region of the two-phase pipeline to ensure that slug formation occurs downstream. The two-phase flow pipeline is a 37.9 m (1469 D) long with 25.8 mm i.d. (D), and it is instrumented with five measurement stations, each one composed of two double wire resistive sensors allowing the Taylor bubble velocity V_{TB} measurement and pressure sensors (Dos Santos *et al.*, 2019). The measured pressure time series have a lower sampling frequency suited only for update the PVT properties, estimate the averaged pressure gradient and calculate superficial velocities. However, the void fraction time series have a 800 Hz sampling rate which is used throughout this work. The exact position of each station along the test section is presented in Fig. 4.1, relating to the pipe internal diameter. Each resistive sensor output is proportional to the instantaneous liquid height, so related to void fraction α.

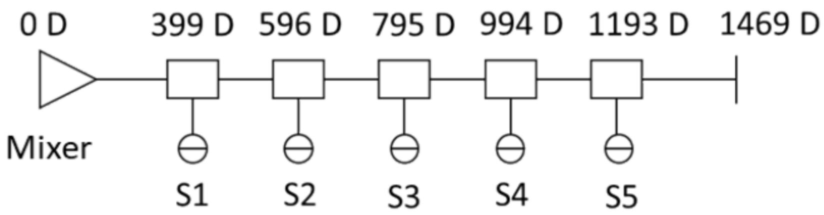

Figure 4.1 – Resistive and pressure sensors locations along the two phase-flow line (Rodrigues *et al.*, 2020).

The experimental results presented here were obtained by using the measurements made in the third station (S3), which is located 795 diameters downstream the mixing zone, which was arbitrarily chosen as a representative measurement of the flow in the pipe. The test matrix consists of eleven experimental conditions, as summarised in Table 4.1.

Table 4.1 – Experimental points: Liquid j_1 and gas j_2 superficial velocities, mixture velocity J, non-slip void fraction λ, average void fraction α_U and pressure gradient dP/dL.

#	$j_1[m/s]$	$j_2[m/s]$	$J[m/s]$	$\lambda[-]$	$\alpha_u[-]$	$\mathrm{d}P/\mathrm{d}L[Pa/m]$
1	0.70	0.31	1.01	0.30	0.18	358.94
2	0.50	0.52	1.02	0.51	0.32	255.01
3	0.30	0.71	1.01	0.70	0.43	145.74
4	1.00	0.54	1.54	0.35	0.22	749.65
5	0.50	1.04	1.54	0.67	0.46	375.78
6	1.50	0.56	2.06	0.27	0.17	1436.21
7	0.75	0.79	1.54	0.51	0.34	573.04
8	1.00	1.09	2.09	0.52	0.35	987.37
9	1.30	0.77	2.07	0.37	0.24	1271.67
10	0.70	1.39	2.09	0.66	0.46	689.75
11	0.50	1.57	2.07	0.76	0.52	472.08

All tests were performed on the slug flow pattern, as predicted by the flow pattern map shown in Figure 4.2. Compressed air and tap water whose properties are summarised in

Table 4.2 were the working fluids. Figure 4.3 presents the measured void fraction waves at the test matrix center, i.e., the experimental point #7.

Table 4.2 – PVT properties.

$\rho_1[kg/m^3]$	955.5
$\rho_2[kg/m^3]$	1.28
$\mu_1[Pas]$	0.963×10^{-3}
$\mu_2[Pas]$	4.5×10^{-5}
$\sigma_{21}[N/m]$	77×10^{-3}

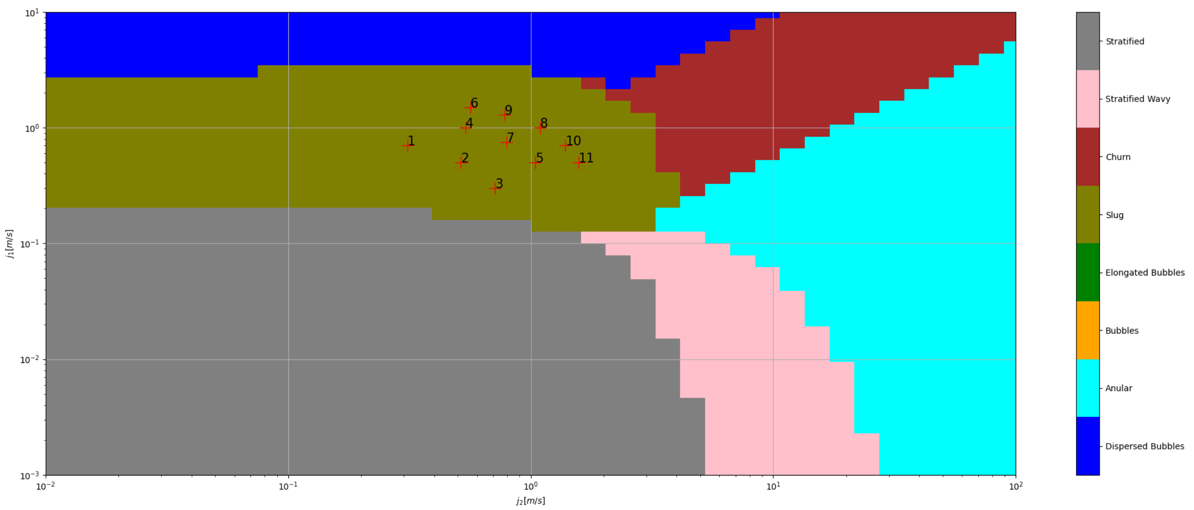

Figure 4.2 – Flow pattern map by (Barnea, 1987) and the experimental points described in Table 4.1 as red crosses.

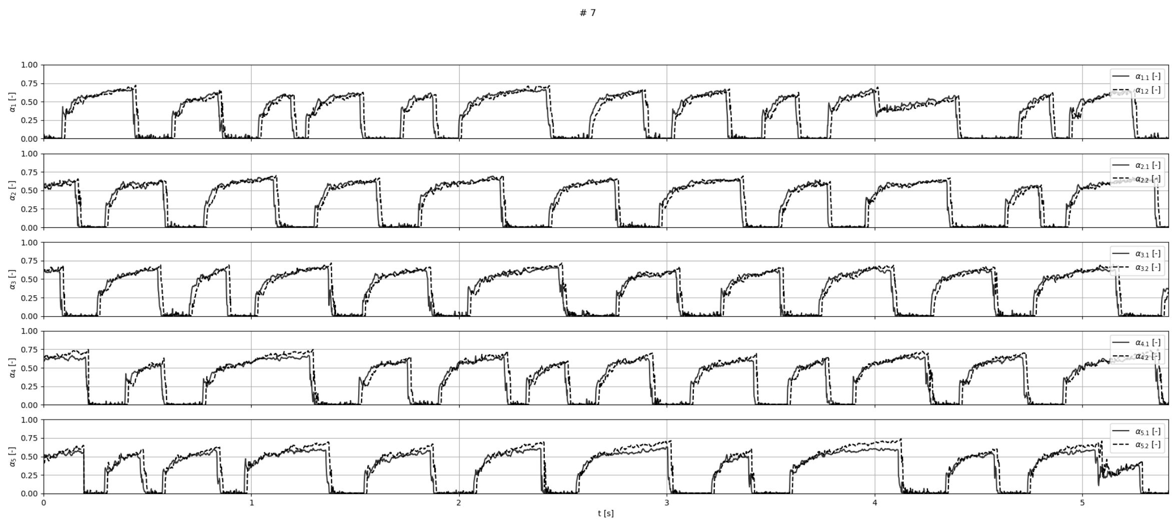

Figure 4.3 – Void fraction waves at the test matrix center - experimental point #7

All post-processing performed on the Rodrigues *et al.* (2020) raw data are shown in the following sections, being the object on the scope of this work.

4.1.1 Unit Cell Characterization

The void fraction time series was processed estimating its probability density functions through kernel methods, where the modes were interpreted as the equilibrium void fractions solutions in the Taylor bubble and slug body regions α_F and α_S respectively. Additionally, the Otsu's method (Otsu, 1979) was used to automatically estimate a threshold that separate the modes of the probability density functions in two groups, in order to build a binary classifier where the void fraction time series where divided into Taylor bubble and slug body classes, leading to a two state square-pulse train as shown in Figure 1.3. Then, this new time series can be interpreted as a two state Markov chain process whose transition matrix and properties were estimated. At last, the void fraction wave phase velocity V_{TB} was estimated through a correlation in the frequency domain giving good results in comparison to the literature. However, due to the stochastic nature of the phenomena, its estimate has inherent biases and uncertainties that should be taken into account.

4.1.1.1 Estimation of Taylor bubble velocity

Figure 4.4 shows a typical result from BCC and GCC with SCOT approaches (see section 1.1.4) applied to a pair of resistive sensors. Note that the SCOT estimator yields a distinct peak at the time delay, as expected from Eq. 1.13. Also, the maximum values of the correlation are slightly off-set from each other. The difference is about twice the time resolution Δt.

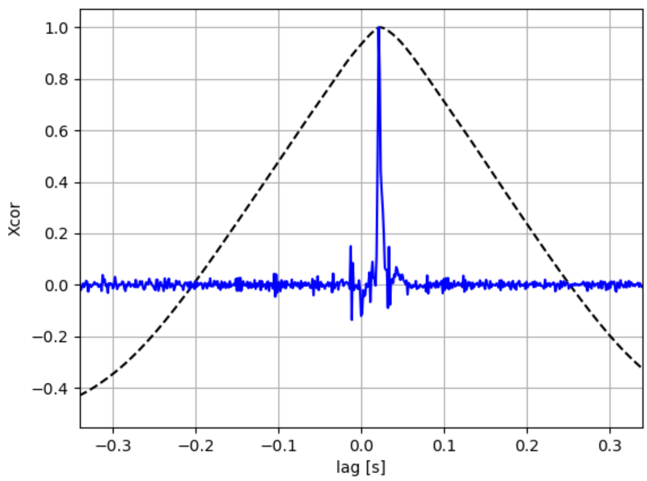

Figure 4.4 – Basic (black dashed line) and generalised (blue full line) cross-correlation with SCOT approaches for a typical experimental point.

Figure 4.5 shows the elongated gas bubble velocity at all of the measurement stations obtained with BCC and SCOT and the corresponding error bars for $\pm 3\sigma_{\hat{\tau}_{peak}}$. Results are compared to the correlation proposed by Bendiksen (1984) and the suggested correction proposed by Rodrigues *et al.* (2020). CPSD are estimated using Hann windowing and 33% overlap.

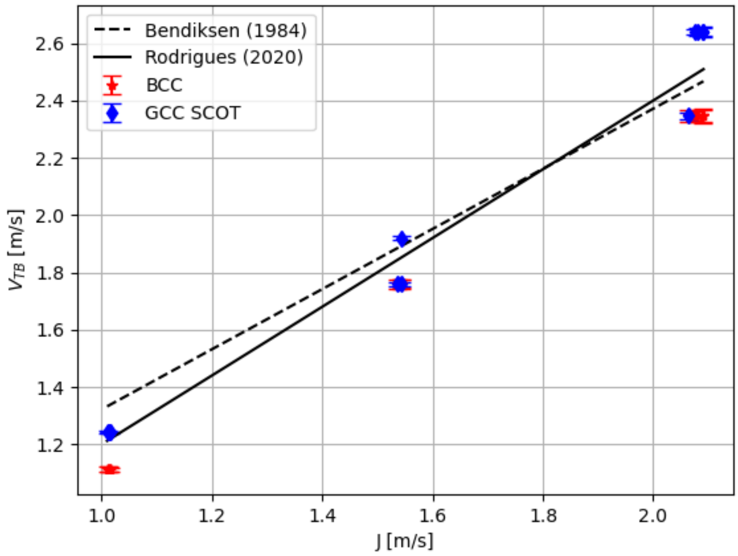

(a) CPSD with 5 segments.

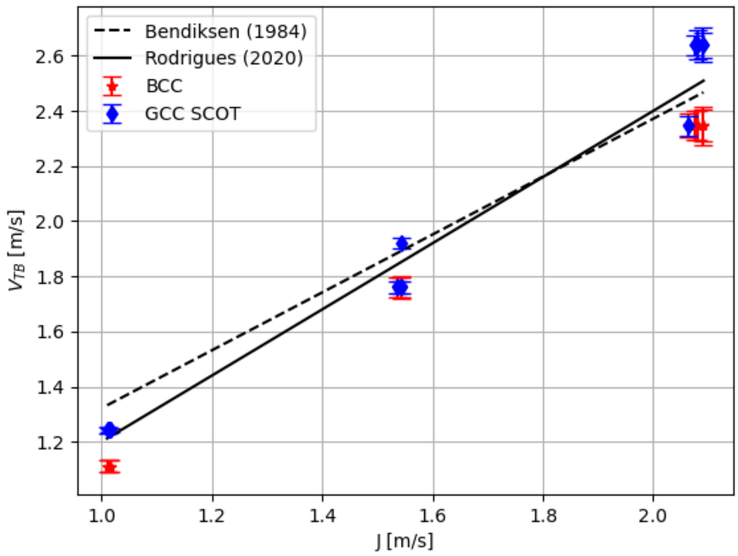

(b) CPSD with 20 segments.

Figure 4.5 – Gas bubble velocity obtained with BCC (red) and GCC (blue) with $\pm 3\sigma_{\hat{\tau}_{peak}}$, Bendiksen (1984) (gray) and Rodrigues *et al.* (2020) (dashed black).

A large difference is observed within the predicted and estimated Taylor bubble velocities, Figure 4.5. It is reasonable to observe such variability since the unit lengths are not always the same, as the bubble velocity depends on several flow parameters and its hydrodynamics, as already observed by several authors (Bendiksen, 1984). However, literature models correctly predict an average value for such velocity. Another point is that literature models for predicting pressure drop and void fraction, e.g., depend on the correct prediction of the elongated bubble velocity (Sarica *et al.*, 2011). Amongst the GCC methods, the smoothed coherence transform (SCOT) was chosen for estimating the gas bubble velocity because it combines a pre-withening, which removes the dispersive effects of travelling waves, with a weighting by the coherence function, which decreases the influence of frequency bands with low SNR (Gao *et al.*, 2006). The estimator features are consistent with the unit cell model since the wave dispersion is mostly due to changes on the format of the bubble along the pipe, for the travelling waves case as Taylor bubbles. However, in the case of developed slug flow with a stable unit cell, it is experimentally observed a low variability in the Taylor bubble velocity. Thus, it configures a simple delay problem and thus with a linear phase and corresponding linear wave dispersion curve (Wallis, 1969; Shoham, 2006).

It should be noted that as such correlation-based methods rely on the average CPSD, thus, the number of segments can affect the estimation because it is an averaging process. The estimated velocity is an average quantity over the time series and it will be more dominated by the frequency bands of greater energy and high coherence. Thus, in this context, the velocity of the most energetic structures will dominate on the results. In the unit cell approach, these regions are directly associated with the jumps and shocks at the nose and tail of the Taylor bubble, as it can be seen in Figure 4.29 and further discussed in Section 4.3.

4.1.1.2 Identification of the liquid slugs and Taylor bubbles

For the identification of the void fraction at the liquid slug α_S and the void fraction at the elongated bubble α_F, it is important to establish a threshold for classifying a sample of the measured time series as either belonging to the elongated bubble or to the liquid slug. Typically, this threshold is dependent on the experimental point thus a completely data-driven approach is proposed.

Figure 4.6 shows some statistical features of all experimental points from the test matrix (Rodrigues *et al.*, 2020). The normalised histogram of the time series gives a measure of the distribution of the void fraction values. A kernel density estimator (KDE) is used to estimate a continuous function for the PDF using a Gaussian kernel, which reveals some interesting features of the distribution for each experimental point. It can be clearly noticed that two regions of lower and higher void fraction are present, as expected, representing the liquid slug and the elongated gas bubble, respectively. For all of the experimental points, the KDE estimator revealed more than one local maximum, thus a multi modal distribution. This feature affects the mean and median values. It can be seen that they are not consistent predictors of a threshold to properly classify each step of the time series as either liquid slug or elongated gas bubble.

The Otsu's approach (Otsu, 1979) is used to find the best threshold for every experimental point. It is a non-parametric and unsupervised method of automatic threshold selection. It is typically used in computer vision and image processing but it can be directly applied to unsupervised decision problems in pattern recognition. It is based on finding the optimal threshold that minimises the intra-class variance between two classes and can be straightforwardly extended to multiple thresholds for several patterns. Given that any point of the time series is classified as either belonging to a liquid slug or to an elongated bubble, the average intermittent factor β can be directly calculated from the transition times in the time series.

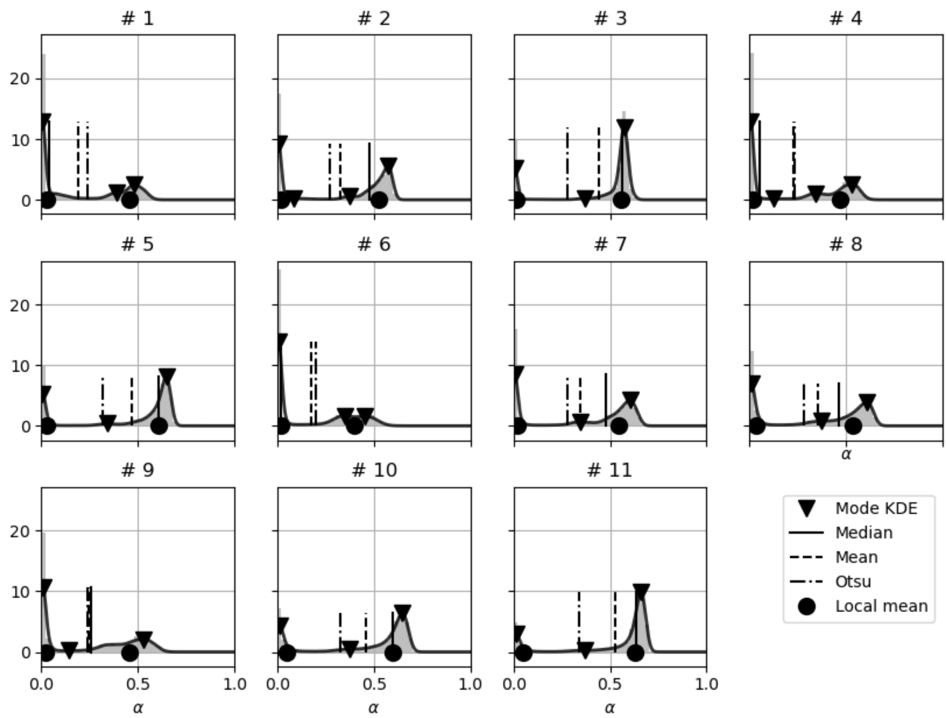

Figure 4.6 – Statistical features of the void fraction time series for all experimental points at a single measurement station. The histogram (grey bars), the KDE (full line), the modes (lower triangle), the median value (full vertical line), the mean value (dashed vertical line), the Otsu threshold (dash-dotted vertical line) and local mean (full circle).

Finally, in the unit cell approach framework, the obtained results that completely characterise the needed parameters in order to reconstruct the unit cell pulse train, i.e., the void fraction at the liquid slug α_S, the void fraction at the elongated bubble α_F, the intermittent factor β, the passing frequency of the unit cell f_U and the Taylor bubble velocity V_{TB}, are summarized in Table 4.3. The f_U is given by the frequency at which the maximum amplitude of the Power Spectral Density (PSD) of the time series occurs. This estimation is not straightforward and will be discussed in details in the next section.

Table 4.3 – Experimental results

Experimental points	$\alpha_S[-]$	$\alpha_F[-]$	$\beta[-]$	$f_u[Hz]$	$V_{TB}[m/s]$
1	0.021	0.448	0.384	1.40	1.11
2	0.043	0.593	0.751	1.10	2.35
3	0.047	0.624	0.824	0.58	2.35
4	0.013	0.521	0.609	3.20	1.11
5	0.009	0.552	0.785	0.96	1.11
6	0.009	0.461	0.471	4.80	1.76
7	0.024	0.600	0.761	1.85	1.76
8	0.010	0.390	0.412	2.00	2.35
9	0.017	0.539	0.623	3.80	1.76
10	0.03	0.531	0.631	1.47	2.35
11	0.017	0.454	0.507	0.62	2.35

4.2 Two-state Markov chain model

In this section, the proposed two-state Markov chain model is investigated. First, the definition of each state from the time series is proposed, then the first order statistics of the estimated Markov chain model is discussed. Finally, the need of the higher order model is physically discussed and addressed.

4.2.1 State classification from the time series

For estimation of the two-state Markov chain model, the obtained threshold from the Otsu's method, as shown in Figure 4.6 is directly applied in the time series, following the two-state model presented in Figure 3.1. Consequently, any measurement higher then the Otsu's threshold is classified as state 1, liquid piston, otherwise it is a state 0, gas bubble. The upper plot of Figure 4.7 shows a typical example of a resulting time series formed from this classification approach, in which each state is then represented by the corresponding values of α_S and α_F, Table 4.3, thus it can be directly compared to the measurement. Clearly, the original measure time series oscillates around the average value of the state, but the transitions are well represented. Notice that, the use of more states may lead to a better description of the slug flow regions representing other regions of the unit cell, such as the turbulent recirculating zone and the elongated bubble nose. For instance, it could potentially improve the description of the slug flow dynamics by a stochastic process. However, it has the drawback of increasing the Markov chain complexity.

4.2.2 Statistics of the first order Markov chain model

In this section, the estimation of the first order Markov chain model and some statistical moments for each experimental point are investigated. The time series of each experimental point is used to estimate the state transition matrix, Eq. 3.99. A Maximum Likelihood Estimator (MLE) is used (Billingsley, 1961; Teodorescu, 2009). Figure 4.7 shows a typical void fraction measurement, experimental point #1, and the two-state time series generated by the Otsu's threshold. Notice that for lower void fraction values, at the liquid slugs, there is very non-uniform region, with rapidly decreasing α values. This is due to the complexity of the liquid slugs at the slug flow. The figure also shows a sample of the two-state Markov chain model synthetically generated from the identified model, i.e., a sample of the stochastic process. Note that it maintains a time structure similar to that of the Otsu's classification on experimental time series but, from a visual inspection, it does not seem similar to the experimental data. Similarly, the periodic model is also not representative of the experimental time series. The differences and similarities are further investigated in terms of some statistical moments of interest.

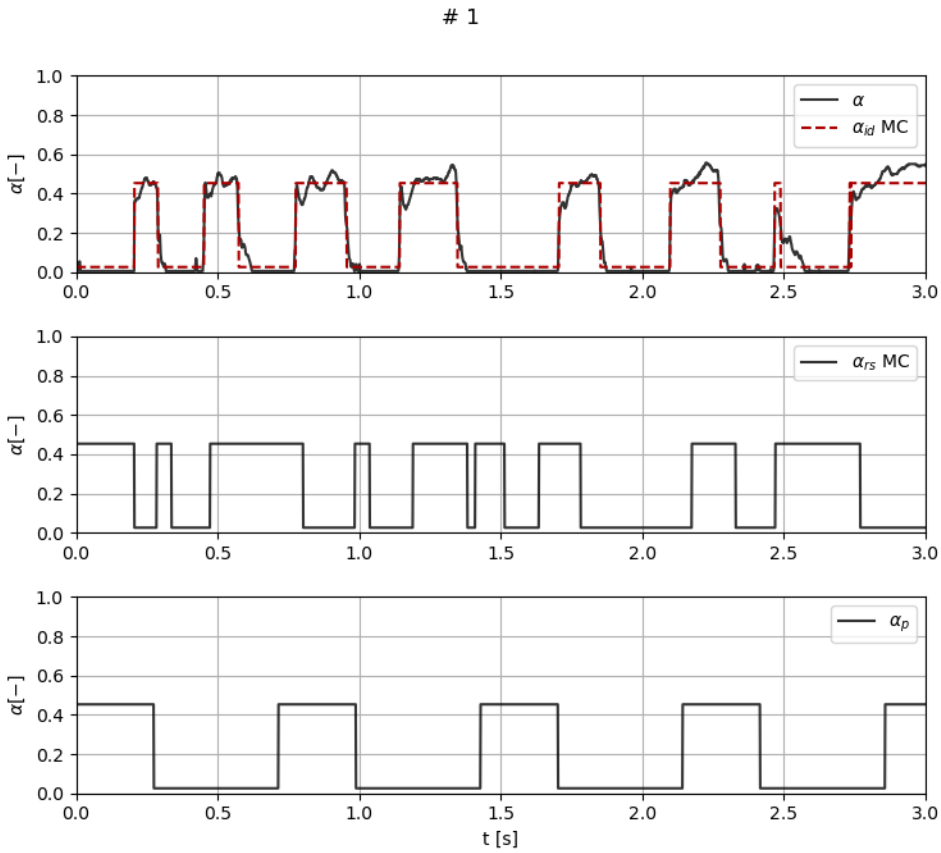

Figure 4.7 – Top curve shows a typical void fraction experimental measurement (black full line) and time series from Otsu threshold (red dashed line) identified. Centre figure shows a random sample time series synthetically generated from the identified Markov chain model. Bottom figure shows a periodic time series with the identified unit cell parameters.

Figure 4.8 shows the autocorrelation estimated for all the experimental points using the original measurement, Otsu's threshold, a sample realisation of the first order Markov chain, the analytical first order MC model, Eq. 3.110, and the periodic model. It can be seen that the autocovariance from the Otsu's threshold presents a very good agreement with the original measurements, which indicates that very little information is lost by the thresholding in a second-order sense. It indicates that the proposed approach captures the second-order statistical features of the original time series. The Markov chain model presents a good agreement only for a short lag, i.e., only short term variations of the time series are well represented by this model. The oscillations on the autocorrelation for higher lags matches those of the periodic model, which indicate the level of periodicity on the signals. Note that for every experimental point, different levels of oscillations are present. In contrast, the Markov chain analytical model does not present these oscillations, i.e., it does not capture periodic fluctuations of longer periods. This effect is emphasised on the analysis of the PSD. However, before that, some aspects of the PSD estimation are highlighted.

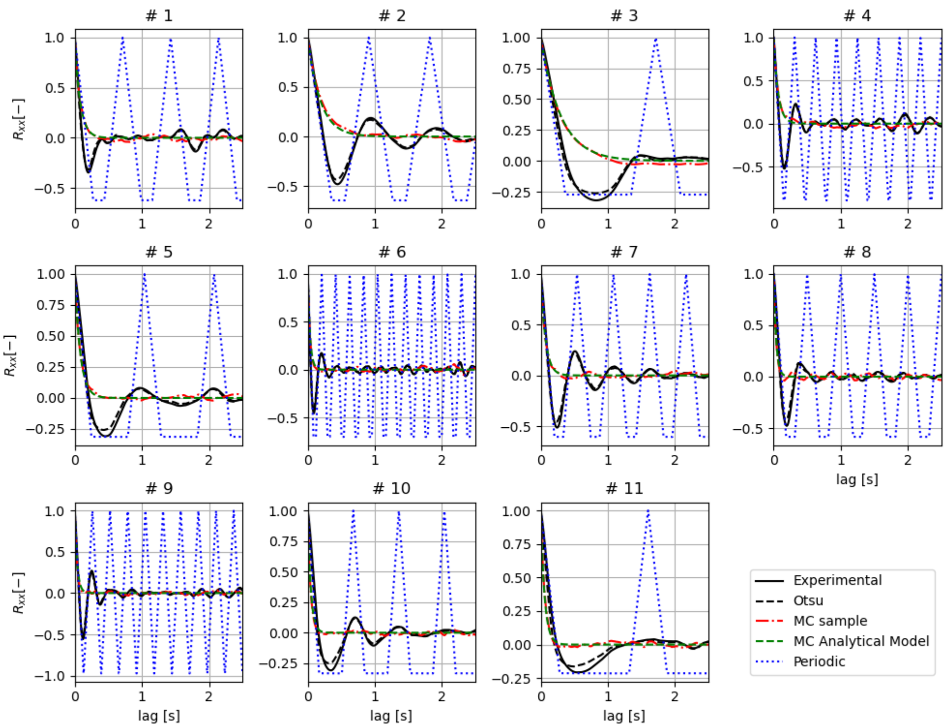

Figure 4.8 – Normalised autocorrelation from each original measurement point (black full line), time series from Otsu threshold (black dashed line), a MC sample (red dash-dotted line), the MC analytical model (green dashed line) and the periodic model (blue dotted line).

Figure 4.9 presents the PSD of a typical measurement point, estimated by using a Welch's segment and average approach (Shin; Hammond, 2008) for different number of blocks N_b. It can be seen that increasing N_b on the Welch segment and average approach has the effect of smoothing the PSD amplitude, as expected. This is shown for $N_b = 5$, $N_b = 10$, $N_b = 15$ and $N_b = 20$. The latter is chosen as a limit case so that a number of slugs can travel along the bench and thus be captured by the measurement. The estimate is based on the Bendiksen (1984) model for the Taylor bubble velocity. This is also to meet an underlying assumption of the segment and average approach that each segment has to be statistically independent from each other. Care must be taken with regard to this estimator, since it is typically used to eliminate measurement noise. In this case, the void fraction measurement is itself a stochastic process, as highlighted by Markov-chain model. Thus, several frequencies present in the signal are most likely related to the physics of the flow itself rather than to the measurement noise. As we are typically interested in the main frequency component, i.e., the frequency band with higher power density, smoothing out the adjacent ripples can help to better define a single frequency peak on the PSD. This is typically associated with the main passing frequency of the Taylor bubbles. However, increasing the number of blocks beyond $N_b = 20$ tends to smooth out the main frequency peak as well. This is because the total time at each block is shorter and only the physics in this time scale is well captured by the PSD estimate.

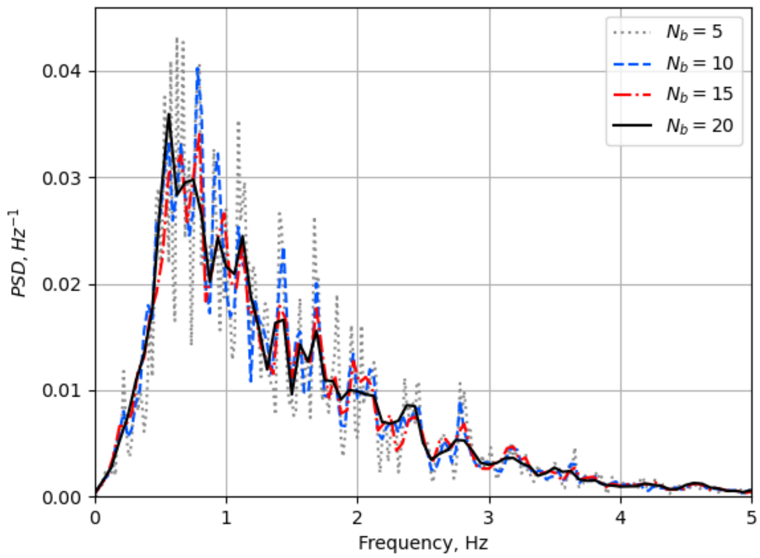

Figure 4.9 – Power spectral density of a single measurement point for different number N_b of blocks on the Welch's segment and average.

Figure 4.10 presents the PSD estimate for all the experimental points, estimated with $N_b = 20$. It can be noticed a very good agreement between the results from the original measurements and the Otsu threshold while the MC model presents a good agreement only for higher frequencies. This is expected from the inspection on the autocorrelation results. Shorter correlation lags τ on the autocorrelation are represented by higher frequencies on the PSD. Similarly, longer correlation lags are associated to lower frequencies on the PSD. These results also show that reducing the signal to a two-state representation does not causes a great loss on its spectral content. However, the first order MC model clearly does not capture the main peak, which typically represents the frequency of passage of the unit cell, f_U. The estimation of this parameter is discussed in detail in the following section. In other words, the first order MC model does not capture the fundamental component of periodic content of the signal. This effect is highlighted by the amplitude value of the coefficients of the Fourier series from the periodic representation of the slug flow given by Equation 1.6, as presented by Vieira *et al.* (2021) and reviewed in Section 1.1.3.

The Fourier series presents a discrete spectrum due to its periodic nature. The amplitude of the coefficients are normalised such that they can be compared to a PSD. The fundamental component of the periodic representation matches that of the PSD peak because this is set as the fundamental period of the Fourier series. Notice that the higher frequency content decays following a different amplitude decay when compared to the Markov Chain model and the experimental results, both with a significant reduction on the power density compared to the periodic case. This result suggests that the actual stochastic process representing the slug flow is somewhere between these two representations. Following the principle of a parsimonious and physically interpretable model, ideally the stochastic process representing the slug flow has to be as simple as possible. However, the first order MC model clearly fails to capture the long term behaviour indicating the need of increasing its order. In the next section the appropriate choice of the order of the MC model is investigated aiming at the simplest stochastic representation for the features of interest.

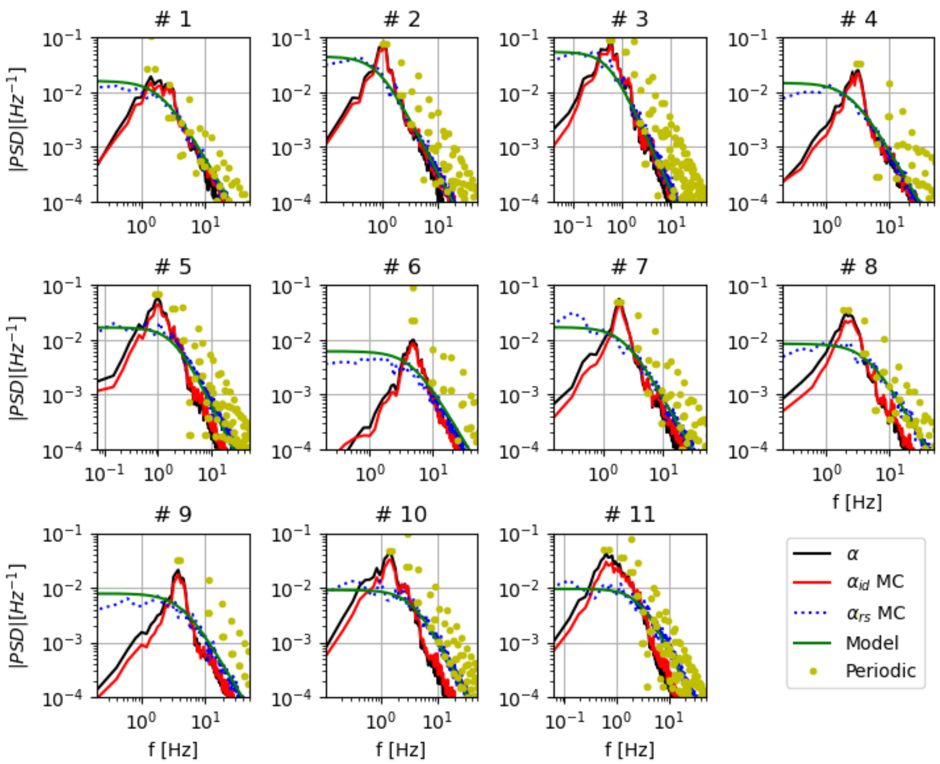

Figure 4.10 – Power spectral density from each original measurement point (black full line), time series from Otsu threshold (red full line), a first order MC sample (blue dotted line), the first order MC analytical model (green full line) and the periodic case (yellow dots).

4.2.3 Higher order Markov Chain model

In this section, the estimation of the higher order Markov chain model is investigated. The estimation of the order of the chain is discussed in terms of two classical information criteria, which are not conclusive. Subsequently, a criterion for the chain order estimation based on the zero-crossing of the autocorrelation function is proposed and it is shown to be consistent for all experimental points. Similar to the first order chain, the transition probabilities are also estimated using MLE approach.

The Akaike Information Criterion (AIC) (Akaike, 1974), originally proposed as a means of selecting competing models, can be used to determine the order m of the Markov Chain (Tong, 1975) that best suits the data by minimises the function (Rafteryt, 1985) $AIC(m) = -2L_L + 2m$, where $L_L = \sum_i n_{ti} \log t_i$ is the log-likelihood function of the transition probabilities and n_{ti} is the number of transitions occurring in a sequence and t_i is the corresponding transition probability. Similarly, the Bayesian Information Criterion (BIC) also establishes a metric for model selection (Schwarz, 1978) and has been proposed as a consistent estimator (Katz, 1981), unlike the AIC. The selected order m is such that it minimises (Rafteryt, 1985) $BIC(m) = 2L_L + m \log N_T$, where N_T is the sample size.

Figure 4.11 and 4.12 presents the AIC and BIC as a function of the Markov Chain order ranging from order $m = 1$ to $m = 20$, respectively. It can be notice the both AIC and BIC criteria fail to give a clear consistent minima for all of the experimental points, which indicates that both information criteria might not be suited for this particular problem.

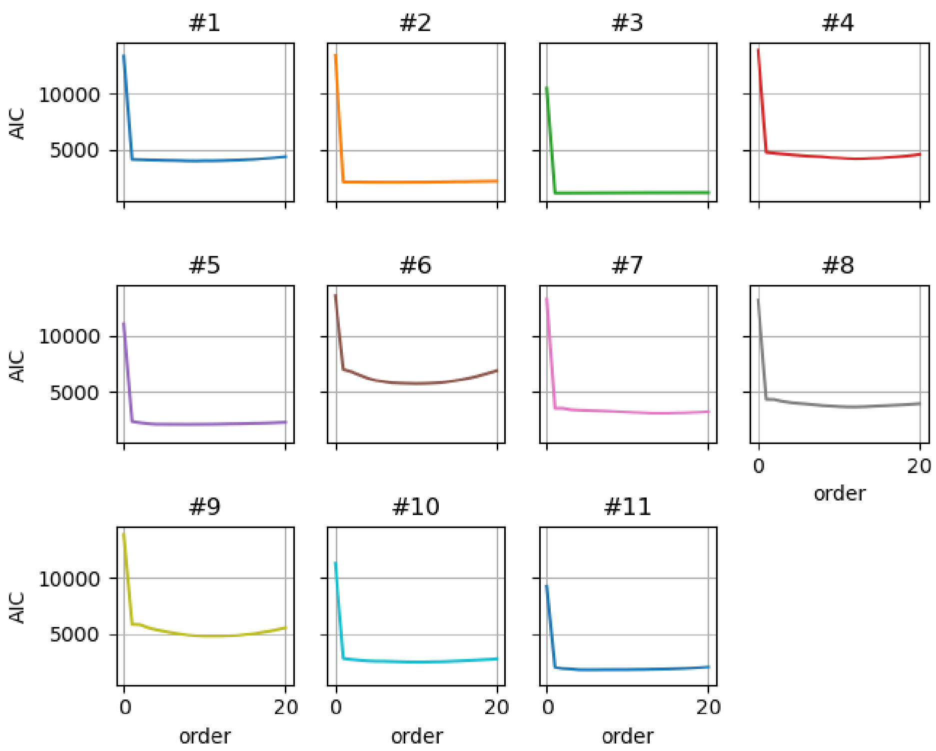

Figure 4.11 – Akaike information as function of the MC order for each experimental point.

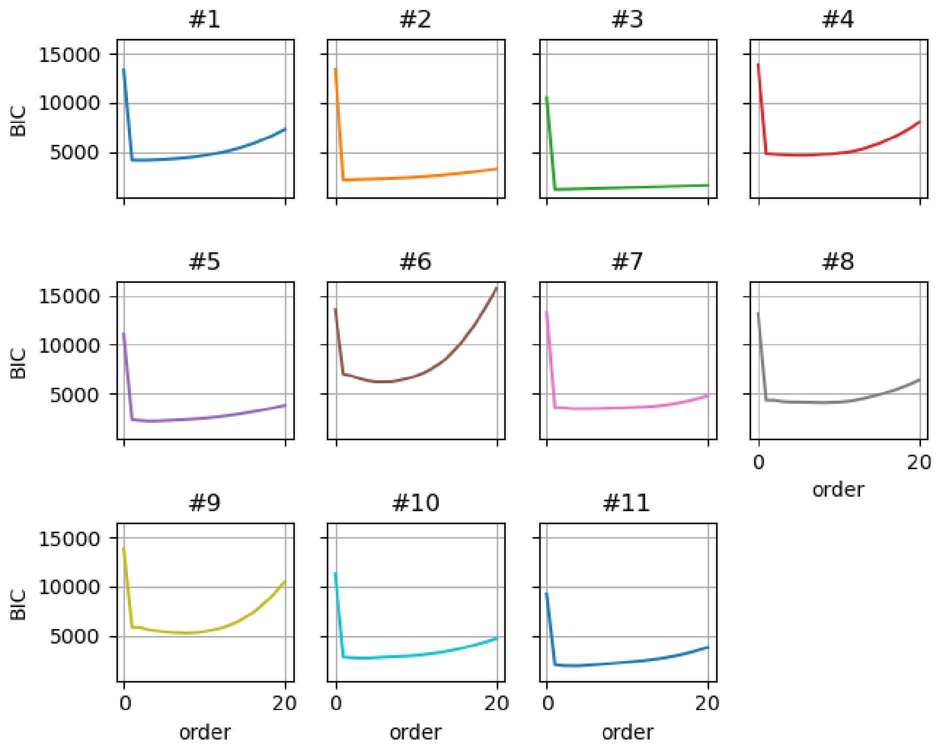

Figure 4.12 – Bayesian information as function of the MC order for each experimental point.

The main objective of order identification is to include the long term effects of the chain and, consequently, to represent the behaviour of the passage of the unit cell. From the previous section, it was discussed that this is closely related to the zero-crossing of the autocorrelation function shown in Figure 4.8. Consequently, it can be argued that the order of the Markov Chain must be such that it can capture the lags at the first autocorrelation zero-crossing. Following this rational, the order of the chain is chosen that it is twice the number of lags until the first zero-crossing, summarised in Table 4.4.

Table 4.4 – Estimated Markov chain order for every experimental point.

Experimental point	#1	#2	#3	#4	#5	#6	#7	#8	#9	#10	#11
Markov chain order	20	46	68	16	36	8	22	18	12	28	38

Figure 4.13 shows the autocorrelation function of the experimental and the one obtained from a random sample of higher order Markov Chain. Notice, that this order selection criterion provides an excellent approximation of the oscillations of the autocorrelation functions. In addition, Figure 4.14 presents the PSD estimate from each measured data and from a random sample of higher order Markov Chain. Clearly, both the main low frequency peak of each PSD and the high frequency are well represented. Further increasing the order of the the Markov would further improve the representation of the lower frequencies at the void fraction

measurements. However, following the principle of parsimonious and physically interpretable model selection, there is no evident gain in increasing the model complexity. Finally, Figure 4.15 presents, on the left, the time series for 3 seconds of the void fraction measurements and the corresponding time series from the Otsu thresholding and, on the right, the synthetically generated time series from the higher order Markov Chain model. It illustrates the suitability of the proposed order selection criterion.

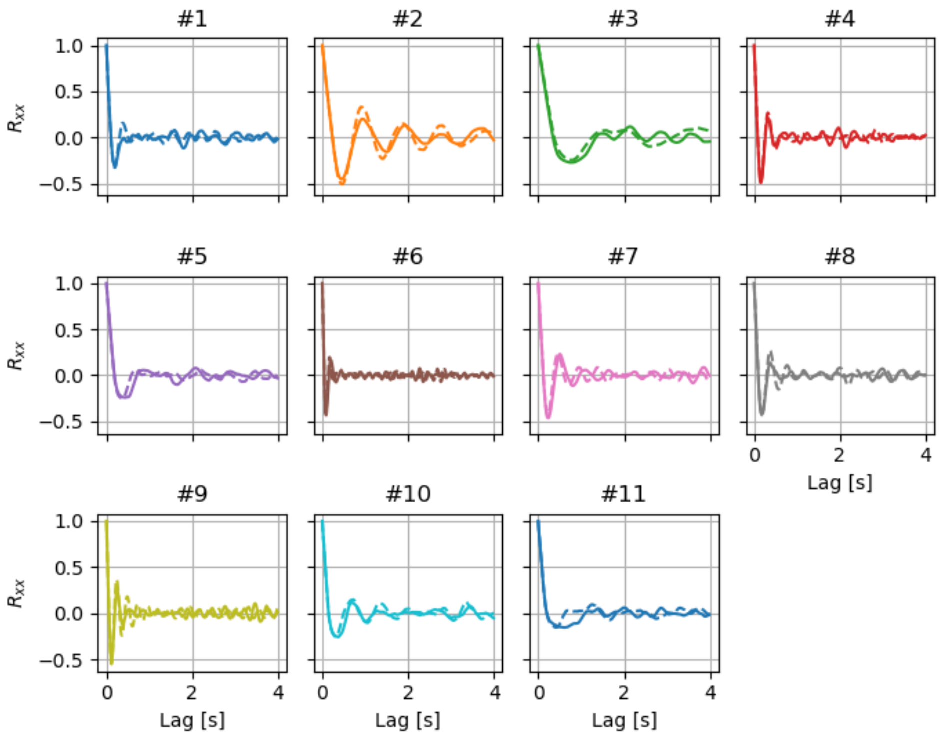

Figure 4.13 – Normalised autocorrelation from each original measurement point (full line) and higher order MC sample (dashed line).

In the following subsections, the characteristics and physical interpretation of the slug flow represented by the proposed two-state MC model is further investigated.

4.2.4 Model validation

In this section, slug flow features are calculated for validation and discussion of the proposed approach. The intermittent factor, β, and the unit cell frequency, f_u, are calculated from the two-state time series generated from the experimental measurements, classified by the Otsu's threshold, and from the higher order Markov chain random sample, generated from the corresponding estimated transition matrix. The transition between two consecutive states is used to calculate the time $t_{Xn=0}$ at $X_n = 0$, the liquid slug, and the time $t_{Xn=1}$ at state $X_n = 1$,

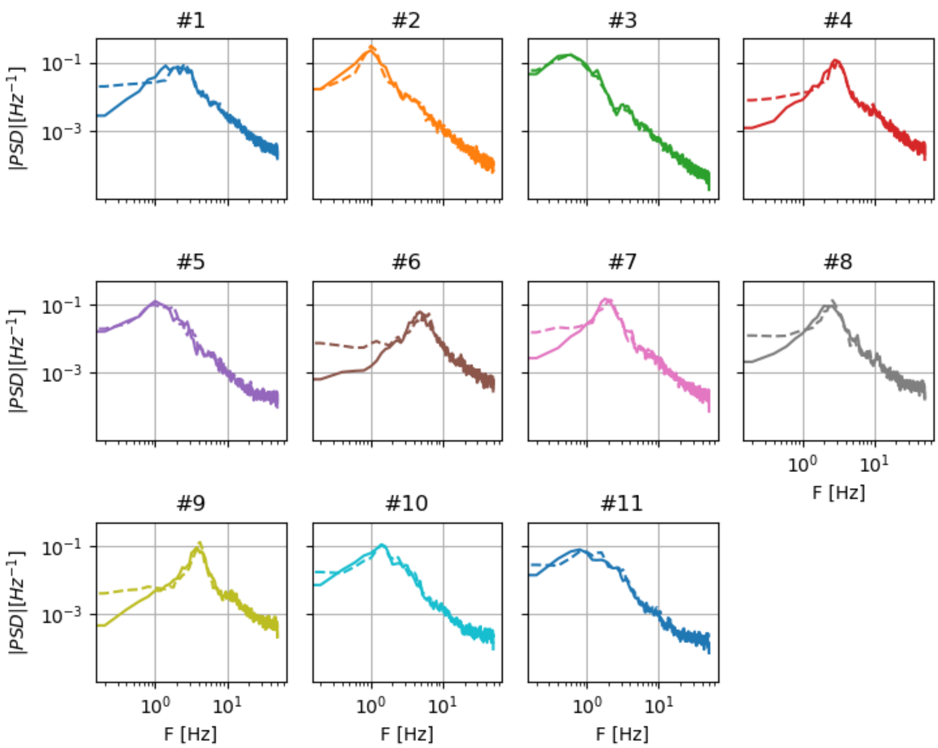

Figure 4.14 – Power spectral density from each original measurement point (full line) and from the higher order MC sample (dashed line).

the gas bubble. Assuming the the same velocity for the unit cell, the intermittent factor is then estimated by $\beta = t_{Xn=1}/(t_{Xn=0} + t_{Xn=1})$. In addition, the frequency of passage of the unit cell can be estimated by $f_u = 1/(t_{Xn=0} + t_{Xn=1})$. Note that this approach estimates both β and f_u for each unit cell, thus providing a probability distribution for both variables as a consequence of the stochastic assumption about the nature of the void fraction, α.

Figure 4.16 presents the histogram of the intermittent factor with 100 bins obtained from the measured time series and classified by the Otsu's threshold (Experimental - MC) and also from synthesised time series generated by a random sample of the Markov Chain (Sample - MC). Notice that for most experimental points, a good agreement between the estimates from experimental and model samples is found. This indicates the proposed two-state Markov chain model is representing well the statistics of the slug flow. The histogram of the experimental data can present a single dominant mode in the middle of the domain. In this cases, the mean values have a very good agreement. On the other hand, when the distribution presents some spikes of more than a single dominant mode outside the regions close to 0 and 1, the mean values present a greater divergence. But, in general, a very good representation is obtained for all cases.

Figure 4.17 presents the histogram of f_u with 100 bins obtained from the measured

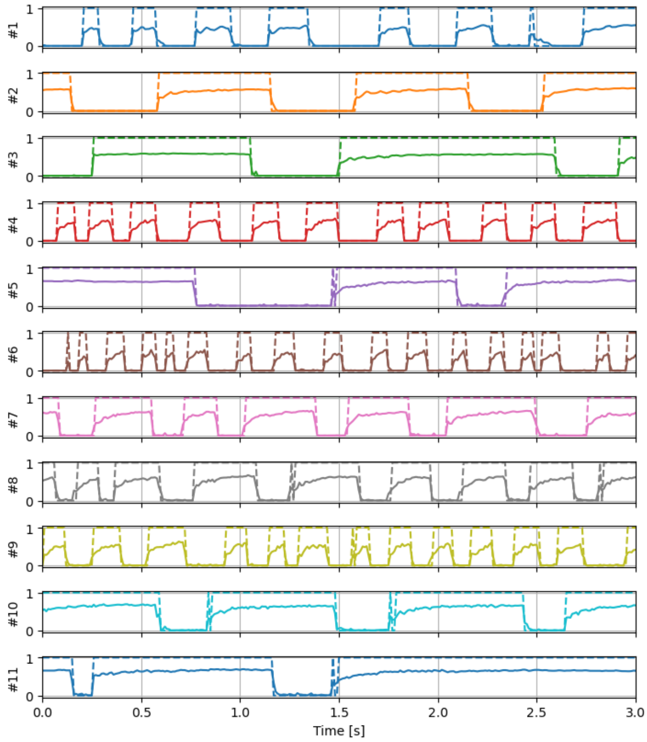

(a) Experimental (Full line) and Otsu's threshold generated time series (Dashed Line).

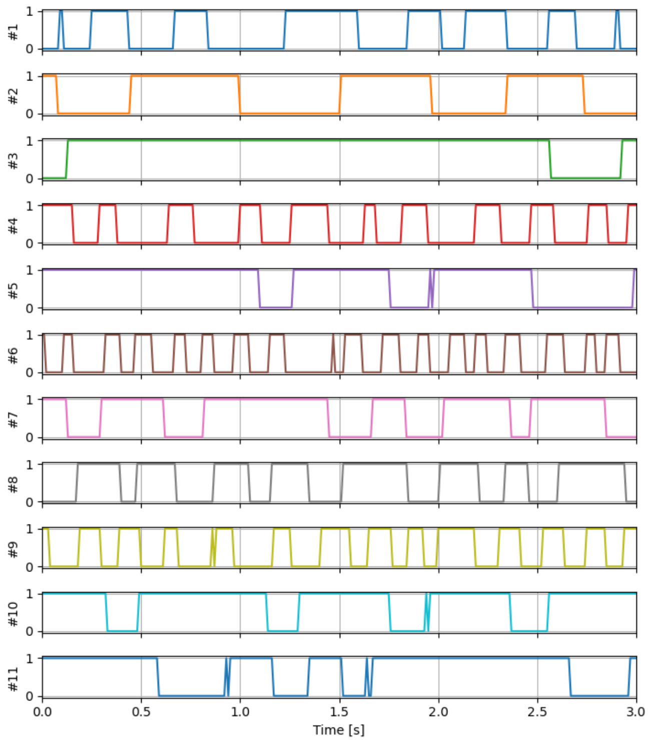

(b) Synthetic Generated time series.

Figure 4.15 – Void Fraction Time Series for each experimental point: (a) Experimental (Full line) and Otsu's threshold generated time series (Dashed Line); (b) Synthetically generated void fraction for each experimental point with higher order Markov Chain model.

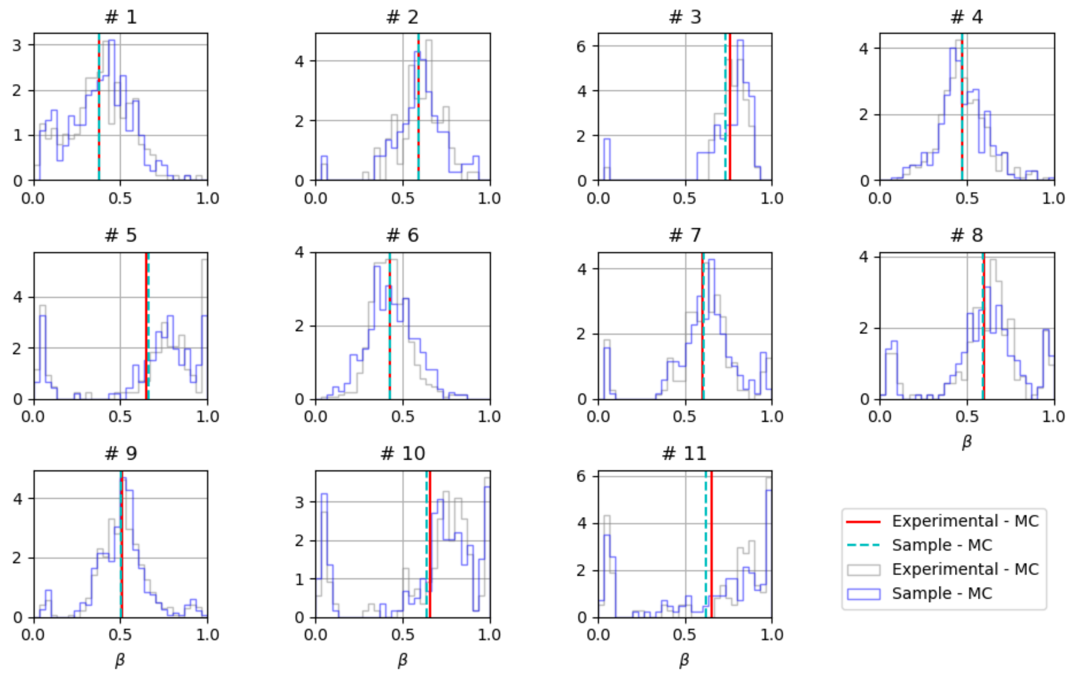

Figure 4.16 – Histogram of the intermittent factor from the experimental data (grey) and from the Markov Chain model (blue). Vertical lines show the mean value for the experimental data (red full vertical line, the Markov Chain model (cyan dashed vertical line) and the slug fraction (black dotted vertical line) based on the local mean of the Otsu threshold.

time series and classified by the Otsu's threshold (Experimental - MC) and also from synthesised time series generated by a random sample of the Markov Chain (Sample - MC). Similar to the previous case, the histograms in both cases present a very good agreement. The mean value for each case is also shown in the figure. In addition, the frequency of the peak value from the corresponding experimental PSDs, as shown in Figure 4.10 and 4.14, correspond to the dominant peak of histogram.

Some experimental points present histograms well distributed around a prominent peak, e.g. #1, #2, #3, #4 and #7, while others present a flatter distribution, such as #5, #6, #8, #9, #10 and #11. In addition, the f_u distribution is clearly not unimodal for all of the cases. The peak frequency value of the PSD typically matches the peak of the f_u distribution, i.e., the most frequent case, rather than the mean value, as given for both the experimental and sampled two-state time series.

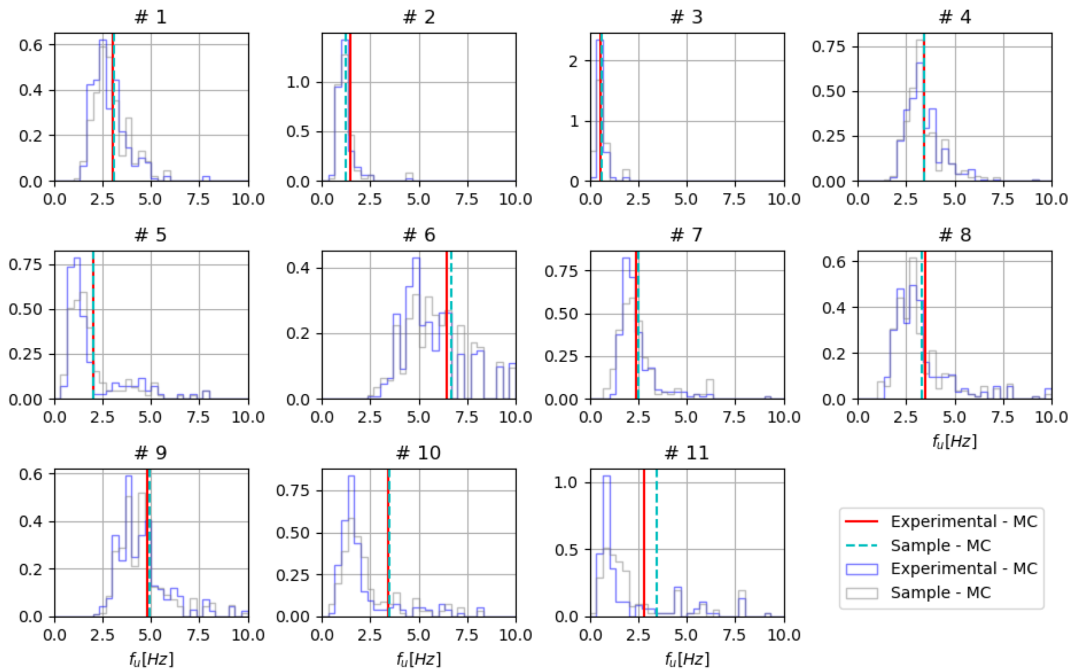

Figure 4.17 – Histogram of the unit cell frequency estimated from the experimental data (grey) em from the Markov Chain sample (blue). Vertical lines show the median value of the experimental data (red full vertical line), the Markov Chain sample (cyan dashed vertical line) and the maximum PSD value.

For comparison purposes, the f_u given by the PSD is compared with literature models proposed by Zabaras (2000) and by Vieira *et al.* (2020). In Figure 4.18 f_u is plotted against the Froude number of the slug Fr_{slug} as a function of the non-slip void fraction λ for different values of the Froude number of the mixture Fr_m. It can be seen that they are in good agreement showing the same trend. The latter model is applied assuming the development length $L/D = 60$, which is typically assumed for single-phase flow. It can be seen that the proposed approach performs well when compared to both models.

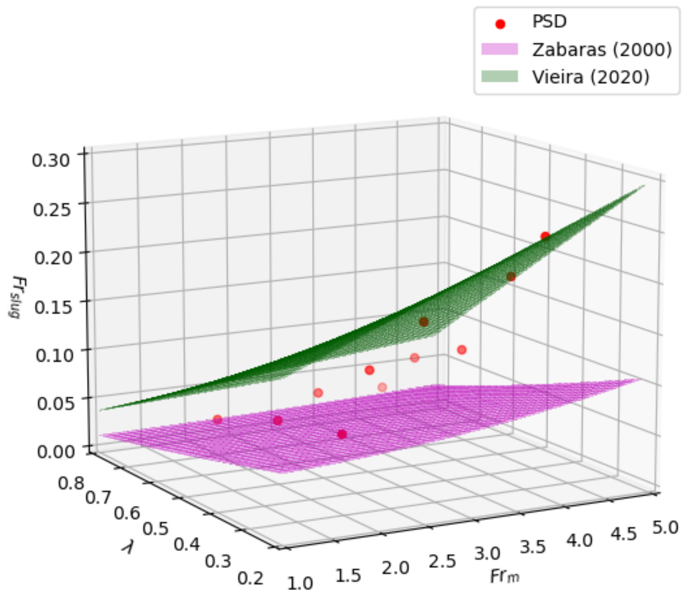

Figure 4.18 – Slug Froude number Fr_{slug} as function of the Mixture Froude number Fr_m and the non-slip void fracton λ. Estimation by the experimental data from the PSD peak (red circle). Also, Zabaras (Zabaras, 2000) (magenta lower surface) and Vieira et al. (Vieira *et al.*, 2020) (green upper surface).

4.3 Phase Space Reconstruction

In this section, the phase space reconstruction is investigated. The experimental void fraction time series were converted to the traveling wave reference frame as shown in Section 2.3 and the corresponding times series are presented in Figure 4.19. The Taylor bubble velocity adopted for the reference frame transformation was estimated based on the measured data using a frequency domain Generalised Cross-Correlation approach (GCC). The estimated velocities are summarized in Table 4.3, for all the points of the test matrix.

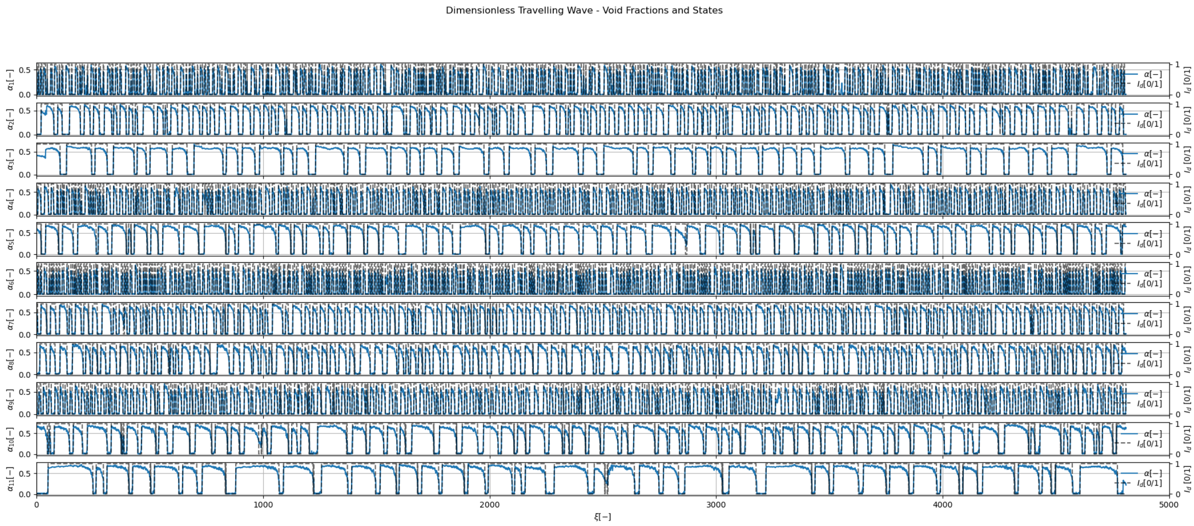

Figure 4.19 – Experimental void fraction (solid line) and states I_d (dashed line) time series on the traveling wave reference frame for all experimental points, from #1 (top) to #11 (bottom).

In order to estimate the phase space and its properties, the observed variable time delay embedding, i.e., the time delayed coordinate system, was estimated from a measured function of the dynamic system states. This process is based on Takens' theorem (Kantz; Schreiber, 2004; Strogatz; Dichter, 2016) which states that the observed variable time series stacked with delayed versions of itself reconstructs a phase space that is the result of a geometric transformation called diffeomorphism of the canonical phase space. The phase space topological properties are invariant to this transformation, therefore it is possible to estimate them from this transformed phase space. Takens' theorem states that any positive delay is sufficient to sustain such properties. Despite having practical implications in implementations, the minimum number of dimensions needed for this embedding is $2d + 1$ where d is the number of dimensions of the canonical phases space. Finally, it is important to highlight some aspects of the measured function of the observed variable. Although we have an estimate of one of the system states, the void fraction, this estimate is not accurate in the liquid piston due to the intrinsic features of the sensor (Dos Santos *et al.*, 2019). However this does not impact the reconstruction of the phase space as it is enough that the measured function for this region is smooth, which is the case.

In order to assemble a time series embedding, the methods of auto-correlation and mutual information were investigated (Kennel *et al.*, 1992; Kantz; Schreiber, 2004), as shown in Figure 4.20. The time delay is chosen such that the observations become statistically independent in a linear sense for auto-correlation and, in a non-linear and more general sense, for mutual information. However, the mutual information estimator did not prove to be suitable because it did not present a clear local minimum for most samples. Therefore, the zero-crossing of the auto-correlation was used as an estimate of the time delay.

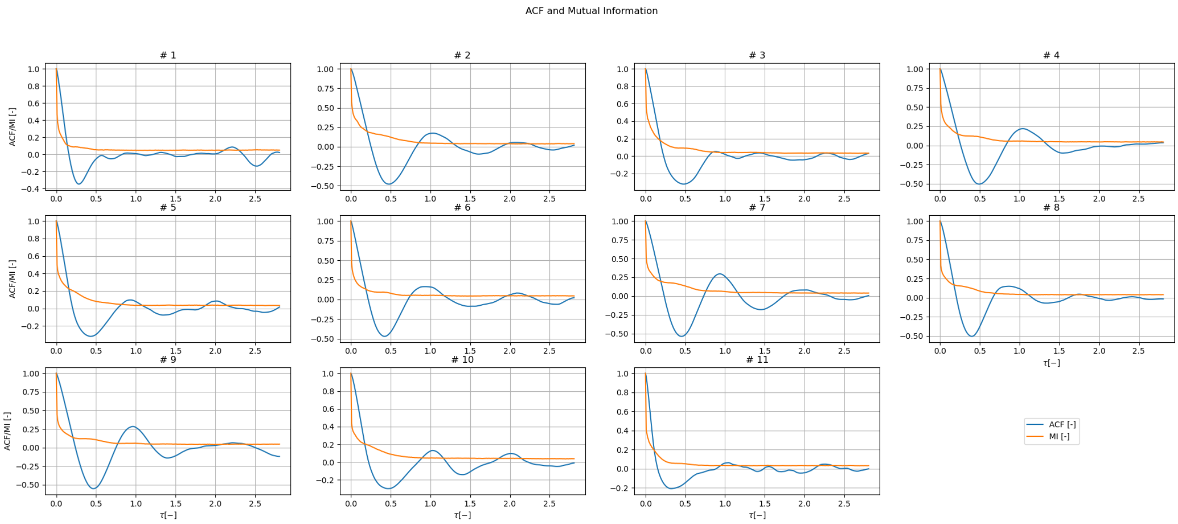

Figure 4.20 – Auto-correlation (blue) and mutual information (orange) of the experimental void fraction time series on the traveling wave reference frame normalized by the unit cell length L_u (unitary lag is the average period).

With the optimal time delays estimated, the false nearest neighbors method (Kennel *et al.*, 1992; Kantz; Schreiber, 2004) was used to estimate the appropriate time delay embedding dimension for describing the system dynamics. In this method, it is assumed that points that are neighbors in the canonical phase space will also be neighbors in diffeomorphic transformations of this space and also in low-dimensional projections of these spaces. However, low-dimensional projections can generate false neighbors, i.e., points that are neighbors in a lower order projection and are not in higher order one. Therefore, the adequate number of dimensions is such that it minimizes the false nearest neighbors fraction. Heuristically, this dimension is the one that leads to a fraction of false nearest between 0.1 and 0.2. It can be noticed from Figure 4.21 that this is around 7 dimensions. Consequently, according to Takens' Theorem, the slug flow pattern is a three-dimensional system. This estimated number of dimensions has great implications for the theoretical modeling because it shows that it is necessary to include the low magnitude effects of interfacial tensions.

A low three-dimensional projected view of the 7 dimensional embedding is shown in Figure 4.22. Bearing in mind that the void fraction time series resembles a pulse train oscillating between high and low void fraction values with a certain regularity, notice that when the three delayed versions of these time series are plotted with a delay such that it enforces statistical independence of these delayed observations, it is expected that the phase space resembles

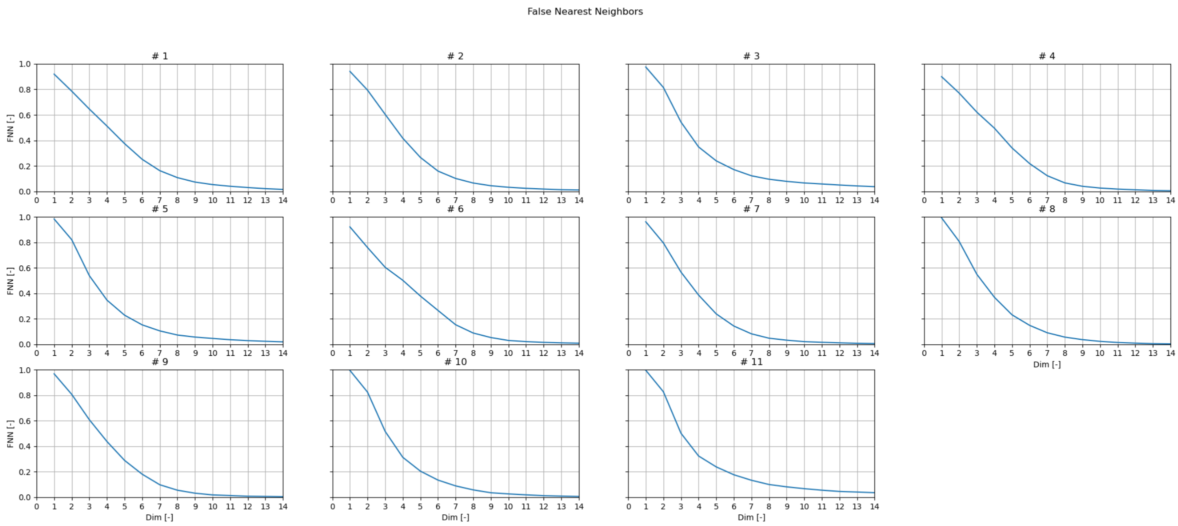

Figure 4.21 – Fraction of the false nearest neighbors as a function system dimension.

the edges and vertices of a hexahedron. Consequently, these vertices represent the combinations of high or low void fraction states of the delayed series. Also, the edges are the system trajectories connecting these possible states. The low dimensional projected view of the 7 dimensional embedding displays something very similar to this description. However, it fails to represent a visualization of the orbits centering around the equilibrium solutions, as expected from the modes of the probability density distributions of the void fraction time series, shown in Figure 4.6. This visualization and corresponding interpretation will be highlighted with the results from the next methods.

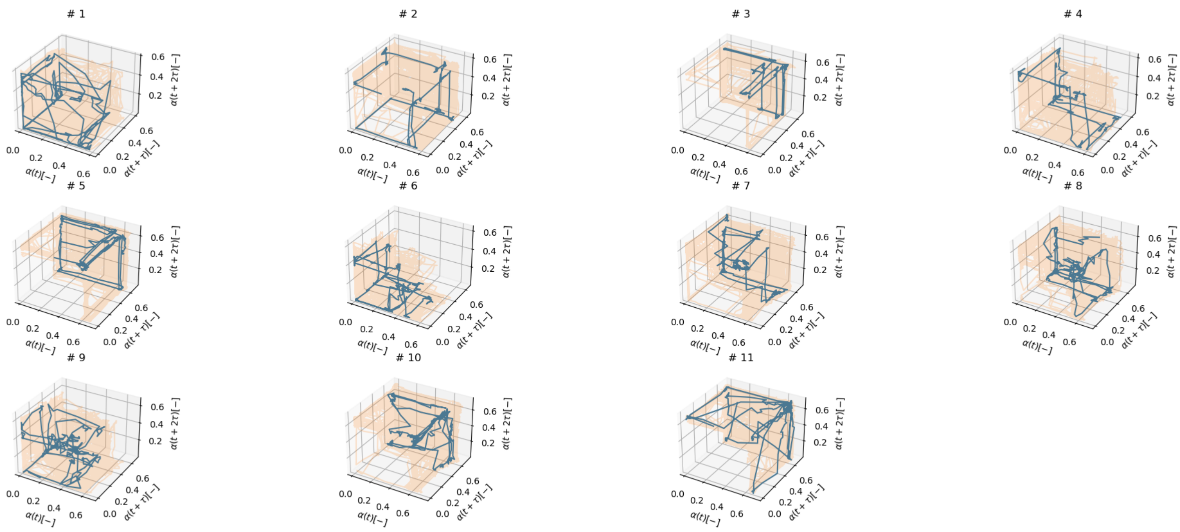

Figure 4.22 – First three delayed components of the experimental void fraction time series embedding for every experimental point of the test matrix using the delays of the autocorrelation zero crossing.

Given the estimated time series embedding, i.e., the time delayed coordinate system from Figure 4.22, the maximum averaged Lyapunov exponents are calculated (Rosenstein *et al.*, 1993; Kantz; Schreiber, 2004; Strogatz; Dichter, 2016) and presented in Figure 4.23 as a function of the normalized lag size in the travelling wave reference frame. In this method, pairs of neighboring points are sought in a neighborhood and the trajectories of these points are followed over time in the phase space by measuring the temporal evolution of theirs distance. In a stable or dissipative system, these distances tend to decrease over time, while in a chaotic system they tend to increase. The Lyapunov exponent measures the logarithmic evolution of these distances, being negative for a dissipative system or positive for a chaotic system. Numerically, the logarithmic distances for a series of pairs are estimated and an average is calculated. Hence, for a sequence of samples, the averaging operator is dominated by the highest exponent and subject to the sampling problems and biases typical of any averaging operator. All of the maximum averaged Lyapunov exponents shown in Figure 4.23 have a similar format and negative values, which does not indicate a chaotic response at first sight, showing oscillations with a regular periodicity before saturating, therefore, exhibiting dissipative behavior. This is caused by limitations on the method averaging process, worsened by the experimental signal noise and intermittent transient behavior. In the canonical state space, the distances might not grow everywhere or even decrease locally. As the estimated exponent is an average of these local rates, localized instabilities as the system singularities typically require a larger dataset in order to be properly estimated, because they are undersampled, as suggest by Kantz e Schreiber (2004). It can be noticed that the ripples are around the unitary normalized lag, i.e., they are of the same scale of the unit cell length L_u, thus can be associated with the periodicity of the interfacial waves in the Taylor bubble regions.

In order to build the canonical phase space, as one has a direct estimate of the system state, the experimental void fraction time series derivatives up to the third order were calculated using the Savitzky–Golay filter (Savitzky; Golay, 1964). It is a noise tolerant method commonly applied in experimental data. The void fraction derivatives time series consist of a succession of peaks trains due to the jumps at the mass shocks in the Taylor bubbles tails, as shown in Figures 4.24, 4.25 and 4.26.

The void fraction derivatives time series are then rearranged in its three-dimensional phase spaces and theirs corresponding fluxes, shown in Figures 4.27 and 4.28. Notice that the identification of the model as proposed in Chapter 2 at Eq. 2.196 is a function that maps both

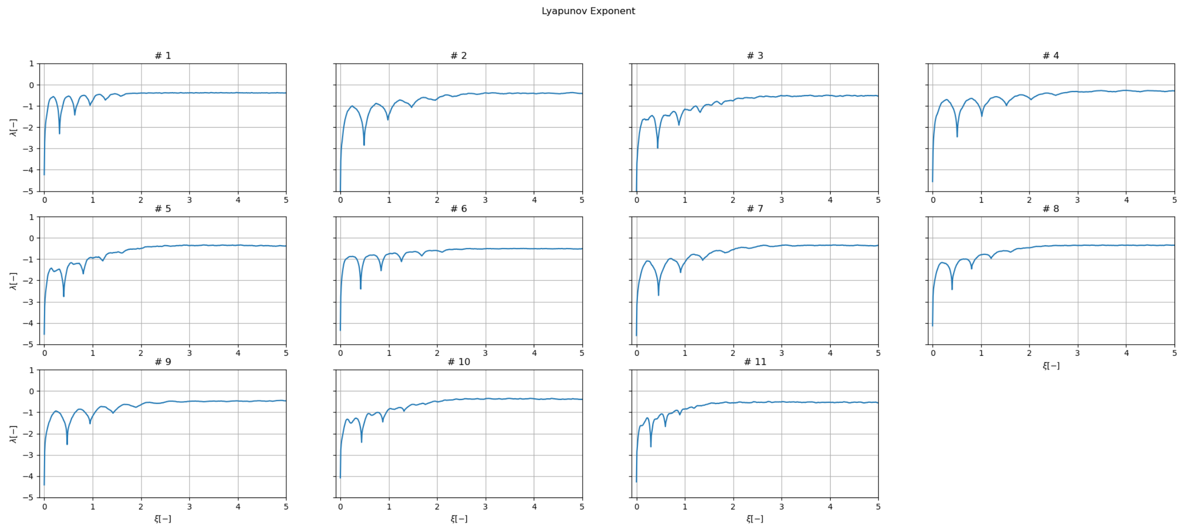

Figure 4.23 – Lyapunov exponents as a function of the lag size of the experimental void fraction time series embedding on the traveling wave reference frame normalized by the unit cell length L_u (unitary lag is the average period) for every experimental point of the test matrix.

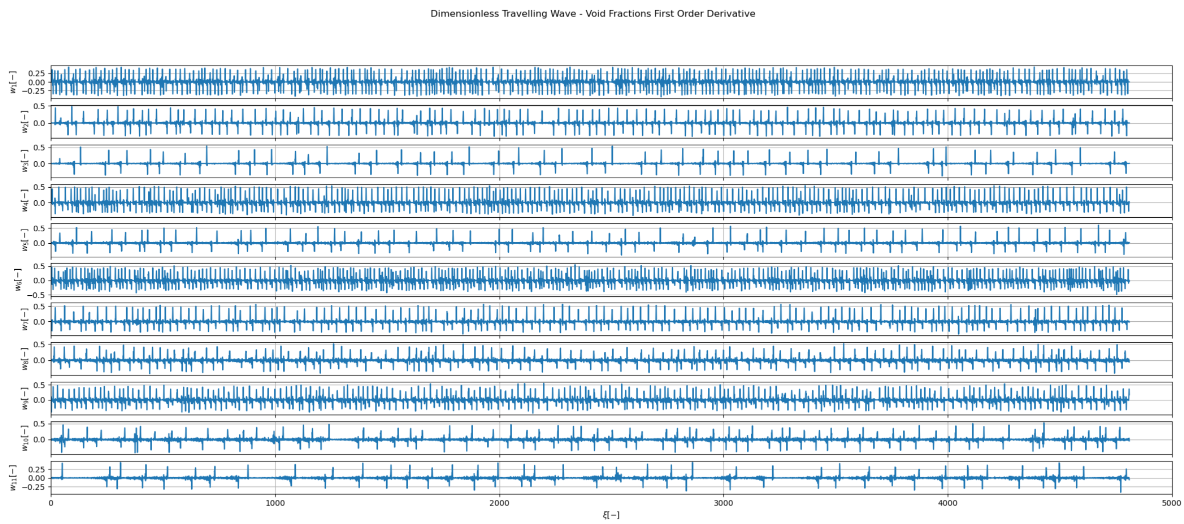

Figure 4.24 – First order experimental void fraction time series derivatives on the traveling wave reference frame.

displayed manifolds.

It can be noticed that all samples are geometrically similar. Thus, for simplicity, from now on, the focus will be on sample #7 which is the center of the test matrix, as it can be seen on the Figure 4.2. From Figure 4.29, the time series can be interpreted as a pulse train series due to the short-time and broadband energy surges present in the spectrogram and happening at a fundamental frequency rate, also highlighted at the PSD. The transitions between a high and a low void fraction can be clearly seen in the presented histogram. Another interesting aspect to be highlighted is that small amplitude waves can be observed on top of the pulses. These can

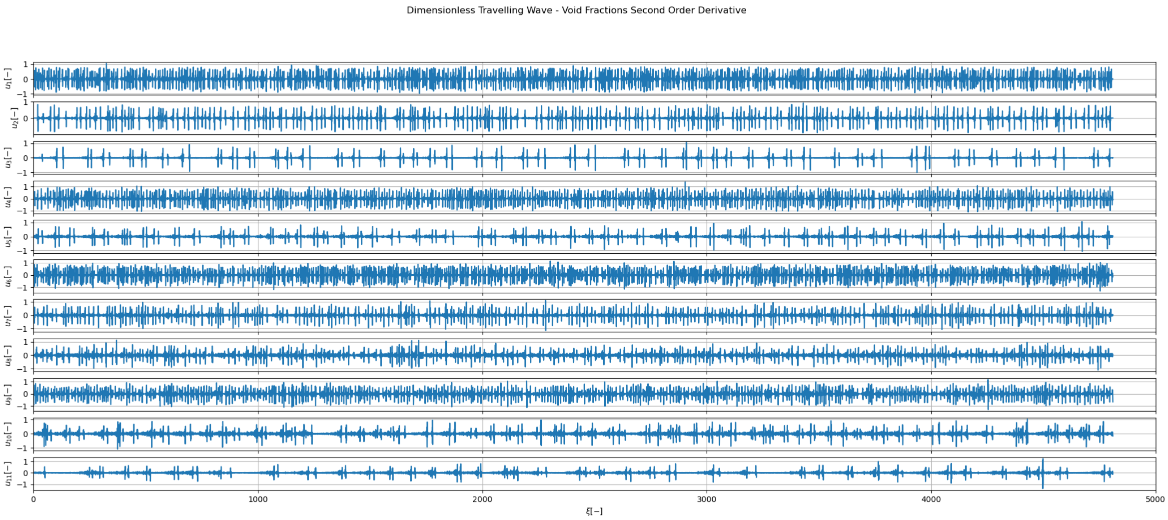

Figure 4.25 – Second order experimental void fraction time series derivatives on the traveling wave reference frame.

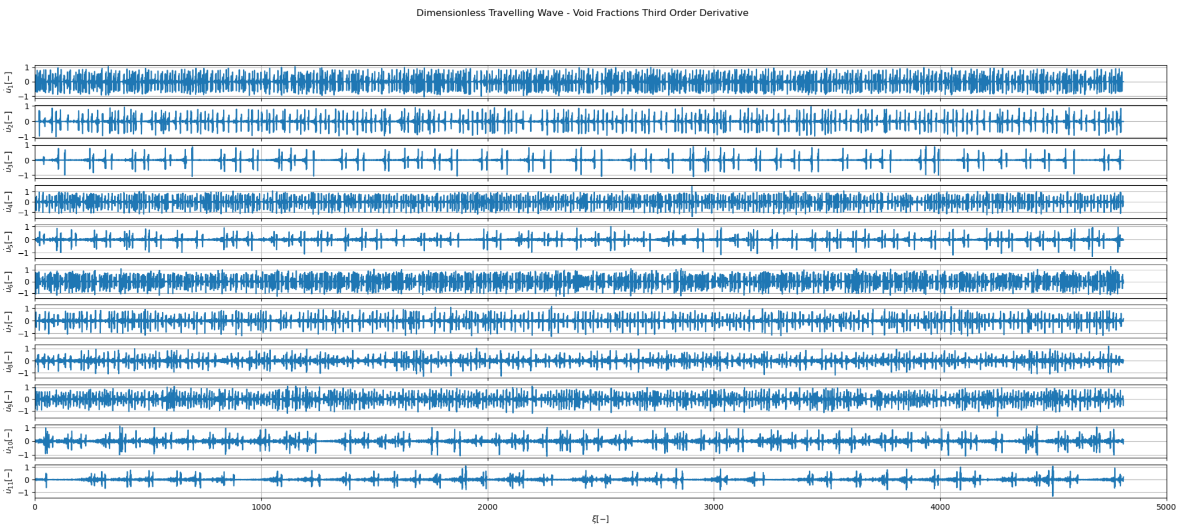

Figure 4.26 – Third order experimental void fraction time series derivatives on the traveling wave reference frame.

be associated with interfacial waves, already discussed with the maximum averaged Lyapunov exponents.

The experimental void fraction time series derivatives up to the second order were calculated using the Savitzky–Golay filter and then rearranged in its phase spaces as shown in Figures 4.30. It can be clearly observed that the system oscillates around two equilibrium solutions. One is in a high and the other is in a low void fraction divided into Taylor bubble and slug body regions. The presenting jumps are configured as transition surfaces that geometrically resemble wings in Figures 4.30. The interfacial waves are visible in the oscillations around the high void fraction solution that geometrically resembles a cyclone.

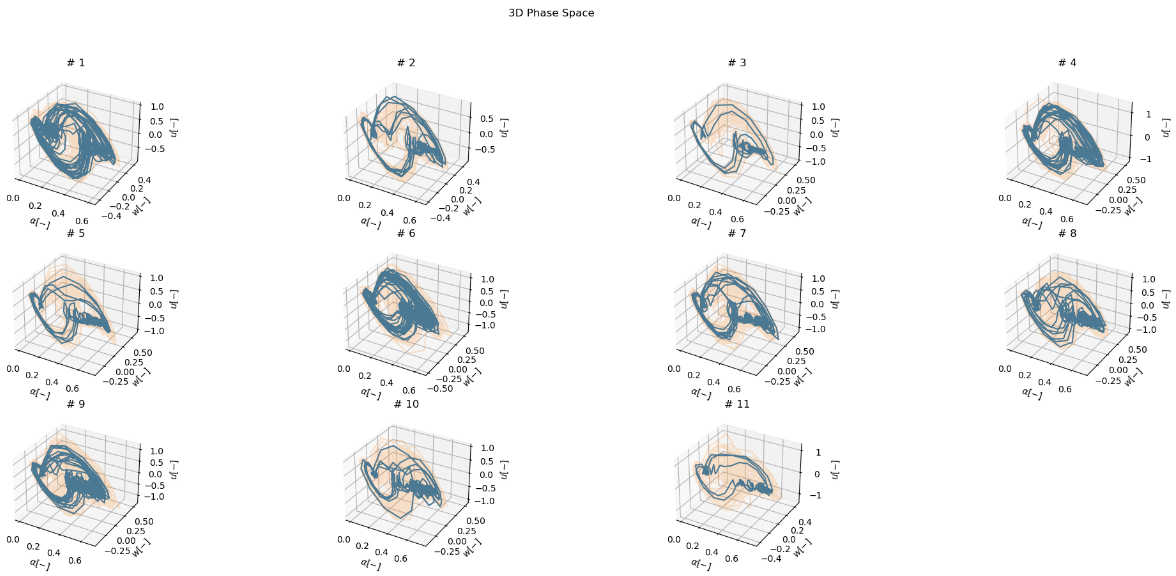

Figure 4.27 – Test matrix phase spaces.

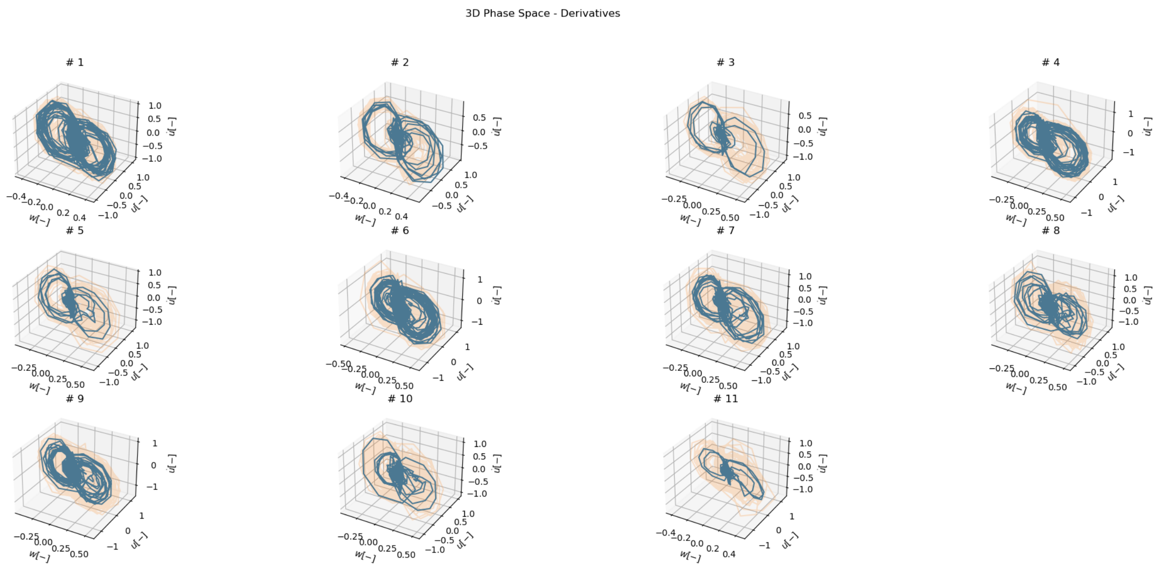

Figure 4.28 – Test matrix phase spaces fluxes.

Therefore, the center of each orbits, as shown in Figure 4.30, can be interpreted as the corresponding equilibrium void fractions solutions in the Taylor bubble and slug body regions α_F and α_S. Both points are, respectively, related to the modes of the probability density functions, presented in Figure 4.6. Additionally, it can be argued that the Otsu's method statistically estimates the vertical plane that optimally separate the center of the orbits that configures the modes of the probability density functions. From this interpretation, the two-state Markov chain stochastic process model, can additionally be interpreted as modelling the transition probabilities between the equilibrium void fractions solutions at the center of the orbits.

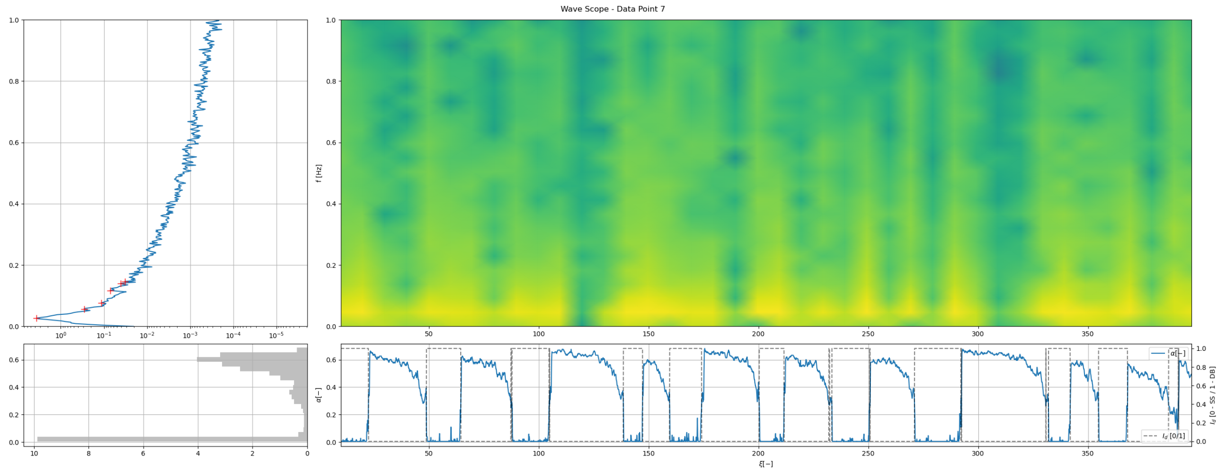

Figure 4.29 – Wave scope of sample 7: upper left - PSD, upper right - Spectrogram, lower left - Histogram, lower right - Void fraction time series.

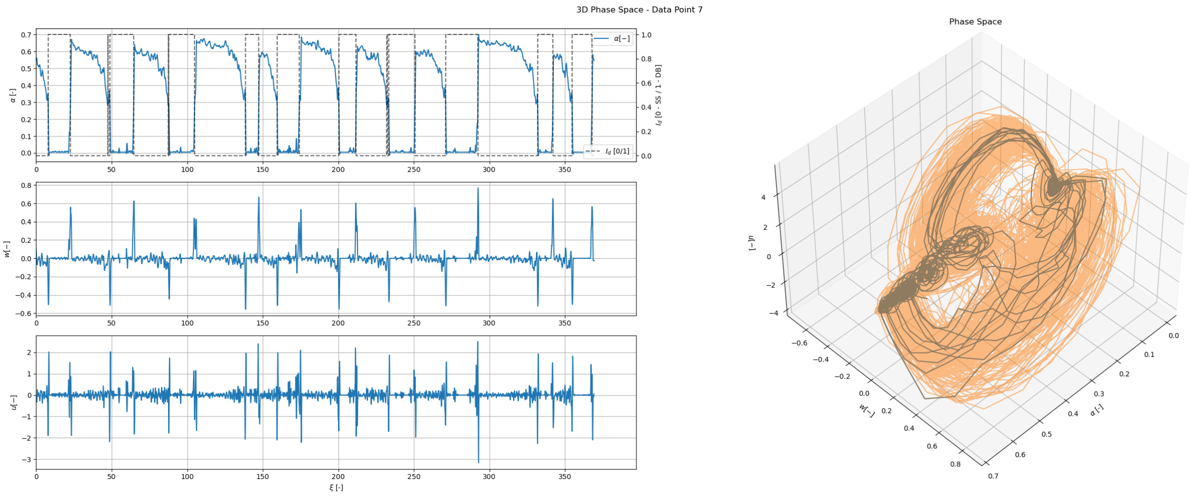

Figure 4.30 – Phase space of sample 7 and the corresponding time series.

The Poincare sections (Kantz; Schreiber, 2004; Strogatz; Dichter, 2016) of the estimated phase space are shown in Figure 4.31. The phase space in sectioned into the trivial planes $u = 0$, $w = 0$, $\alpha = 0.28$, given by the Otsu's classification treshold, and an arbitrary plane given by the 45º inclined plane intersecting both transition surfaces. The different colors indicate the direction in which the trajectory crosses these surfaces. The Poincaré sections show the structures of the oscillations due to the interfacial waves resembling geometrically a cyclone in the planes $u = 0$ and $w = 0$ at the high void fraction zone ($\alpha > 0.28$), where the cyclone radius indicates the amplitude of these waves, in addition to indicating that the transition surfaces have almost straight linear sections as can be seen in planes $u = 0$ and in the arbitrary plane. However, the most interesting result occurs in plane $\alpha = 0.28$, where the transition surfaces are sectioned at the Otsu threshold and the intersection points dispersion at the jumps is an indication of a chaotic behavior. This result contradicts the estimation obtained from the

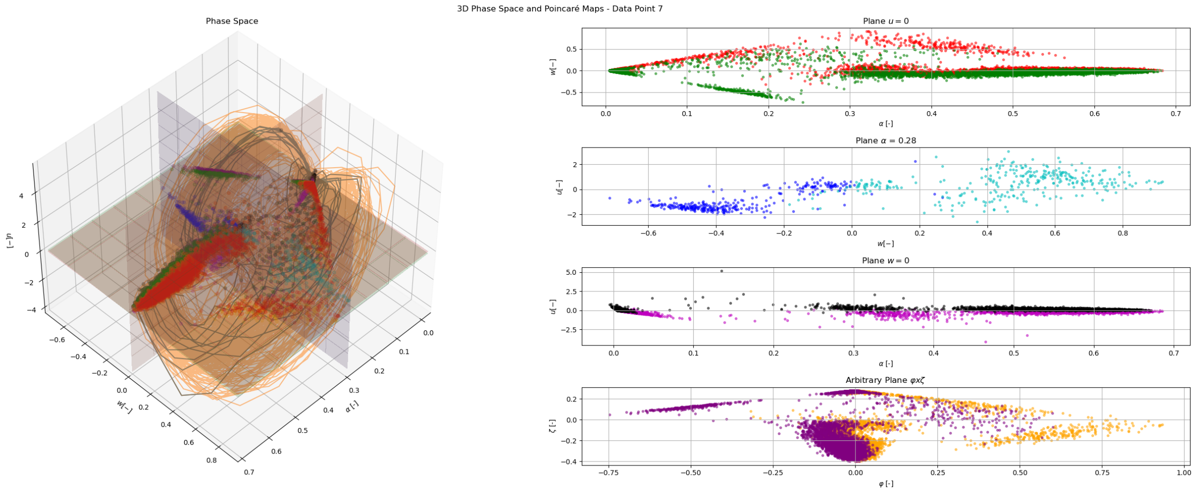

Figure 4.31 – Phase space and Poincare's sections of sample 7.

maximum averaged Lyapunov exponents, at first sight. However, they confirm the variability in the intermittency factors and unit cell frequency observed and modeled by the Markov chain that suggest a chaotic behavior. The full explanation for the discrepancy observed in the maximum averaged Lyapunov exponent estimation is still an open question, but it is mentioned in the literature that cases where the instability is very localized in the phase space, so that the chaos driven events are much less frequent (jumps that form the mass shocks), so the samples used in the averaging operator to estimate the maximum averaged Lyapunov exponent are dominated by the dissipative or non-chaotic part (interfacial waves inside the unit cell), biasing the result towards the more frequent dissipative solution, or a negative exponent (Rosenstein *et al.*, 1993; Kantz; Schreiber, 2004; Strogatz; Dichter, 2016).

4.4 Theoretical Model

In this section, the numerical results from the one and two-dimensional phase-space analytical models are presented and the results are interpreted in terms of the experimentally observed time series. For this analysis, the dimensionless numbers are estimated from the experimental data without turbulence effects, briefly presented and discussed in Section 4.1 and investigated in Section 4.3, summarized in Table 4.5.

Table 4.5 – Dimensionless Numbers

ρ	1.3×10^{-3}
ν	3.4
$\frac{1}{Re}$	8.7×10^{-3}
$\frac{1}{We}$	1.2×10^{-2}

It is possible to note on Table 4.5 that the laminar viscous terms are order $\mathcal{O}(-3)$, which is lower than the interfacial functions terms. So, an approximation that considers only the laminar viscous effects but disregards interfacial tensions or the turbulence phenomena would not make practical sense. However, the three-dimensional model considering the effects of surface tension only applies to the stratified pattern, which does not allow addressing the transition between the patterns observed in the unit cell. Therefore, the analysis displayed in this section will focus on the one-dimensional and two-dimensional phase-space models. For such analyses, the classical closure relationships in the literature discussed in Chapter 2 are adopted, summarized in Table 4.6

Table 4.6 – Closure relationships previously adopted

Variable	Description	Model
V_{TB}	Taylor bubble velocity	Bendiksen (1984)
α_S	Liquid slug void fraction	Gomez *et al.* (2000)
v_B	Liquid slug gas *in situ* velocity	Gomez *et al.* (2000)
f_2	Taylor bubble gas friction factor	Taitel e Dukler (1976)
f_1	Taylor bubble liquid friction factor	Taitel e Dukler (1976)
f_i	Taylor bubble interfacial friction factor	Taitel e Dukler (1976)
f_m	Liquid slug mixture friction factor	Bendlksen *et al.* (1991)
We_c	Bubble critical Weber number	Andreussi *et al.* (1999)
C_D	Bubble drag coefficient	Tomiyama *et al.* (1998)
$\hat{M}_2^D$	Bubble drag averaged momentum transfer	Ishii e Hibiki (2011)
C_V	Bubble added mass coefficient	Ishii e Hibiki (2011)
$\hat{M}_2^V$	Bubble added mass averaged momentum transfer	Ishii e Hibiki (2011)
C_C	Bubble collisions forces coefficient	Bertodano *et al.* (2016)

4.4.1 Experimental Data Overview

The objective of this section is to interpret the obtained raw experimental data using the developed model. A connection with the proposed two-state Markov chain model is discussed based on the transition boundary between the segregated and dispersed bubble flow patterns at the unit cell.

From Section 4.2, recall that the Otsu threshold is proposed for the states classification used in the Markov chain estimation. As discussed, it seeks to separate the unit cell regions by establishing a threshold over the jump section of the void fraction waveform profile. Figure 4.32 shows the given Otsu threshold for every experimental point of the test matrix, in addition to the classified Taylor bubble α_f and liquid slug α_S averaged void fractions. A clear separation between the two regions is observed, as expected. Moreover, the singularities from the one dimensional model at the dispersed bubble and stratified flow patterns, presented in Section 2.4.2, for each experimental point is shown. Remarkably, the statistically obtained threshold are very close to the singularities for every experimental point. This singularities promote the jumps in the dynamical system and are more deeply discussed in the following section.

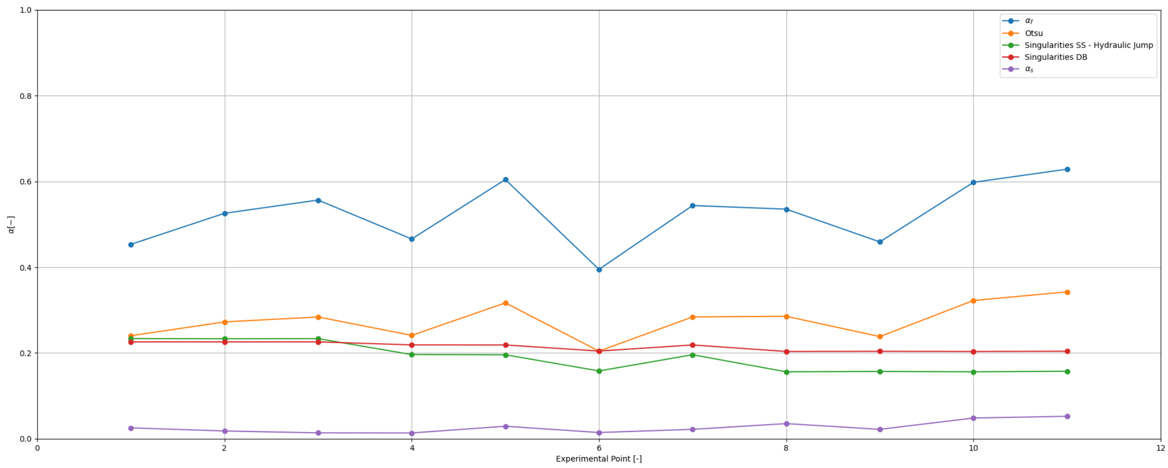

Figure 4.32 – Otsu classification threshold (orange), the Taylor bubble α_f (blue) and liquid slug α_S (purple) averaged void fractions and one dimensional model singularities at the dispersed bubble (red) and stratified (green) patterns for each experimental point.

For the sake of simplicity, the analysis is focused on the experimental point #7, a typical experimental point at the center of the test matrix, as it can be seen on Figure 4.2. In addition, a typical unit cell was selected from this specific experimental time series. The unit cell was select as being the one with the set of parameters closest to the median of the unit cell parameters estimated for all experimental data and represented in the histograms of the Markov chain, at Figures 4.16 and 4.17. It is presented in Figure 4.44 and further explored in the following section. Figure 4.33 presents the data points from the median unit cell series plotted on the flow pattern map, along with the constant mixture velocity flow curve, which defines the problem kinematics, as discussed in Section 2.3.1. Furthermore, the dynamical system fixed points are plotted along its singularities for each flow pattern. The fixed points delimit the extremes of the intervals for each region of the unit cell, as the trajectory of the dynamic system oscillates between them. The singularities points represent the jumps between flow patterns and are expected to be close to the Otsu threshold, as shown in Figure 4.32. Finally, the curve with the unity bublance, from Equation 3.33 at Section 3.2.3, is also presented, in this case calculated using the homogeneous model, which implies that the slip in the liquid piston was neglected.

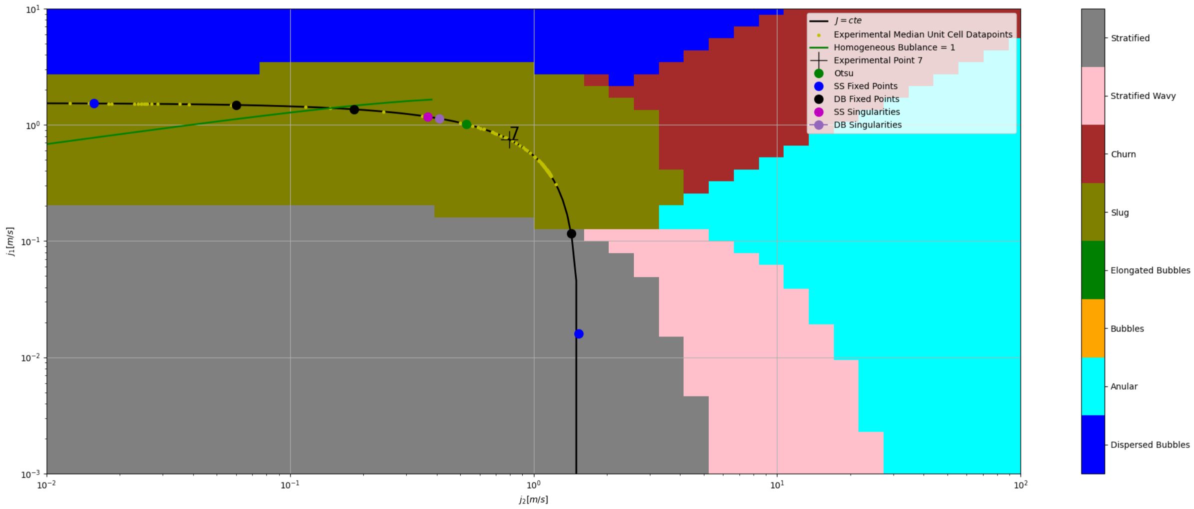

Figure 4.33 – The typical median unit cell data points plotted on the Barnea (1987) flow pattern map along with the constant mixture velocity line, homogeneous bublance classification threshold, fixed points and singularities of the one dimensional model.

It can be observed that all median unit cell samples lay on top of the constant mixture flow curve, as expected. The data samples are mainly at two well defined clusters, corresponding to the the high and low void fractions of the Taylor bubble and liquid piston regions. These clusters are well separated by the singularities, by the Otsu threshold and also by the point where the unity bublance curve crosses the constant mixture flow line. Of course, the transition that each of these points promotes occurs at different pairs of superficial velocities, as expected. However, the result given by the unitary bublance curve is important because it is a criterion that allows the classification of intermittent flow in dispersed (liquid piston) and separated (elongated bubble) regions even when the operational coordinates are all contained in the slug region of the Barnea (1987) flow pattern map, being, therefore, a transient classification criterion.

In order to briefly evaluate the developed model, while discussing the relevant physics for segregated and dispersed flow patterns and transition phenomena, the void fraction experimental time series are used to construct the model-based time series of some relevant flow parameters. First, some fundamental flow variables are investigated. Figure 4.34 presents the reconstructed time series obtained from the hydrodynamic model of the dimensionless liquid height $\tilde{h}$ from Equation 2.11 and the dimensionless curvature $\hat{\gamma}$ from Equation 2.22 and 2.152, in addition to the phase velocities series obtained through the constant mixture flow solution, from Equation 2.114 at Section 2.3.1, the pressure wave profile and the parietal shear stress τ_w, from the pressure coupling model at Section 2.3.3.

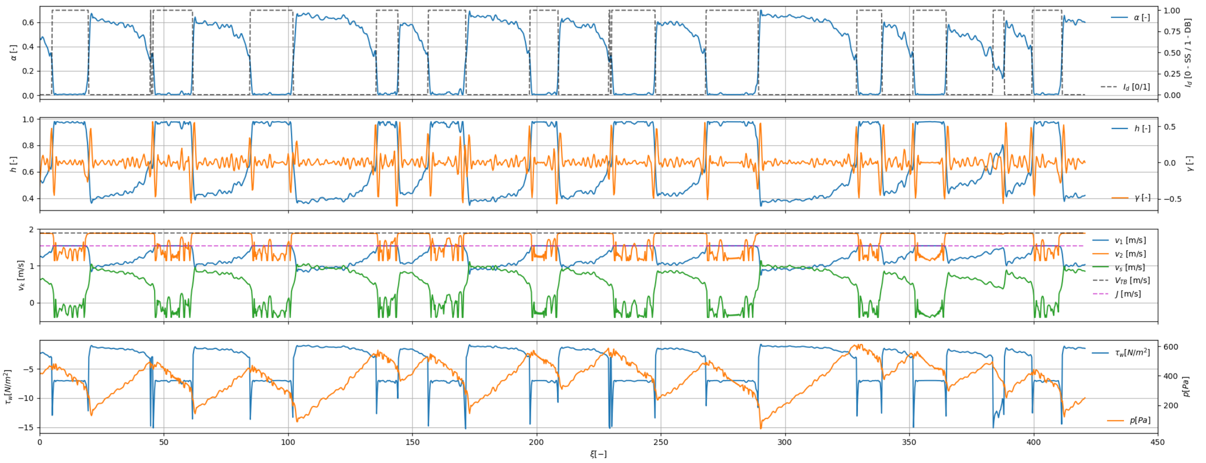

Figure 4.34 – The void fraction time series as function of ξ and the corresponding two-state classification (upper) from the experimental point #7. The reconstructed flow variables dimensionless liquid height h, dimensionless curvature $\hat{\gamma}$, constant mixture flow solution based phase velocities series and the parietal shear stresses τ_w along with the mixture pressure p.

The dimensionless curvature $\hat{\gamma}$ behavior on Figure 4.34 besides the transition thresholds is noteworthy, suggesting that it might be a good candidate for a unit cell classification feature. The gas velocity series converge asymptotically to the Taylor bubble velocity in the corresponding region, and the liquid velocity converges asymptotically to the mixture flow velocity in the liquid piston region, as expected. Finally, the parietal shear stress is much higher in the liquid piston region, as expected and the pressure wave profile series is in qualitative agreement with the literature (Dukler; Hubbard, 1975). It presents three distinct almost linear pressure derivative zones: the Taylor bubble, the liquid piston and a short mixture zone.

Figure 4.35 presents the reconstructed pressure wave profile and its components, discussed at section 2.3.3, p_{ca}, p_{ν}, p_{Δ}, p_f, i.e., the pressure oscillation components induced by the convective acceleration, viscous dissipation, pressures differences between phases and the body forces and shear stresses contributions, respectively. It can be noticed that the pressure wave profile is totally dominated by the components of convective acceleration and forces, gravity and parietal shear stress, as expected (Dukler; Hubbard, 1975).

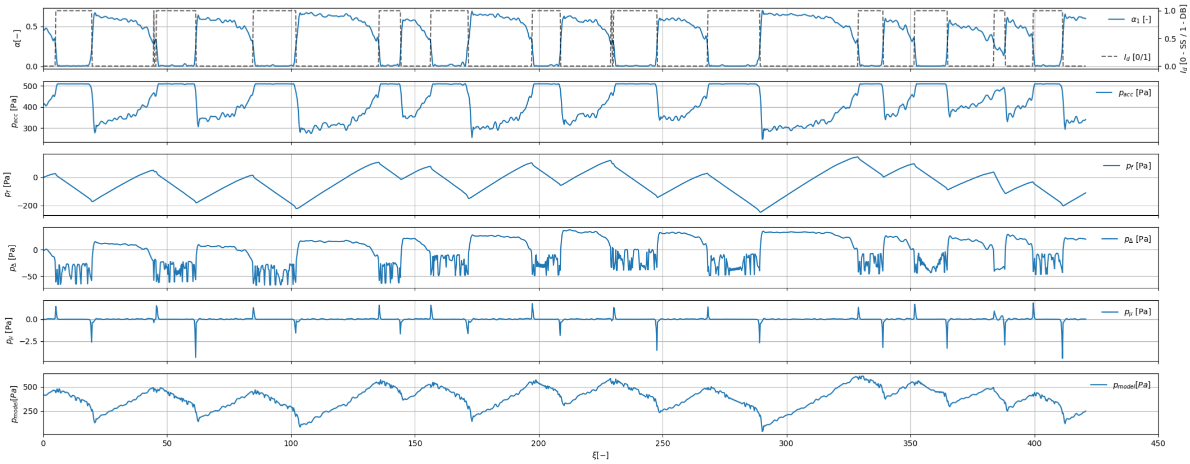

Figure 4.35 – The void fraction time series as function of ξ and the corresponding two-state classification (upper) from the experimental point #7. The reconstructed pressure wave profile (bottom - p_{model}) and its components (p_{ca}, p_{ν}, p_{Δ}, p_f, i.e., the pressure oscillation components induced by the convective acceleration, viscous dissipation, pressures differences between phases and the body forces and shear stresses contributions, respectively.).

Figure 4.36 presents the reconstructed stationary homogeneous component of the turbulent flow variables as discussed in Section 3.5. The equivalent averaged turbulent kinematic viscosity ν_k^T is calculated from Equation 3.125, using the stationary homogeneous component of the averaged turbulent kinetic energy $\bar{e}_k^{Re}$, which is estimated from the turbulent friction velocity, expressed in the Equation 3.129, a function depending on the parietal shear stress τ_w. The steady-state solution of the proposed one dimensional one equation turbulent model is also evaluated and compared with the friction velocity approach, as expressed by the Equation 3.134 at Section 3.5.1, which simplifies to

$$\bar{e}_k^{Re} = \left(-l_m \frac{\tau_w}{\rho_1} \frac{S}{A} J \right)^{\frac{2}{3}}. \tag{4.1}$$

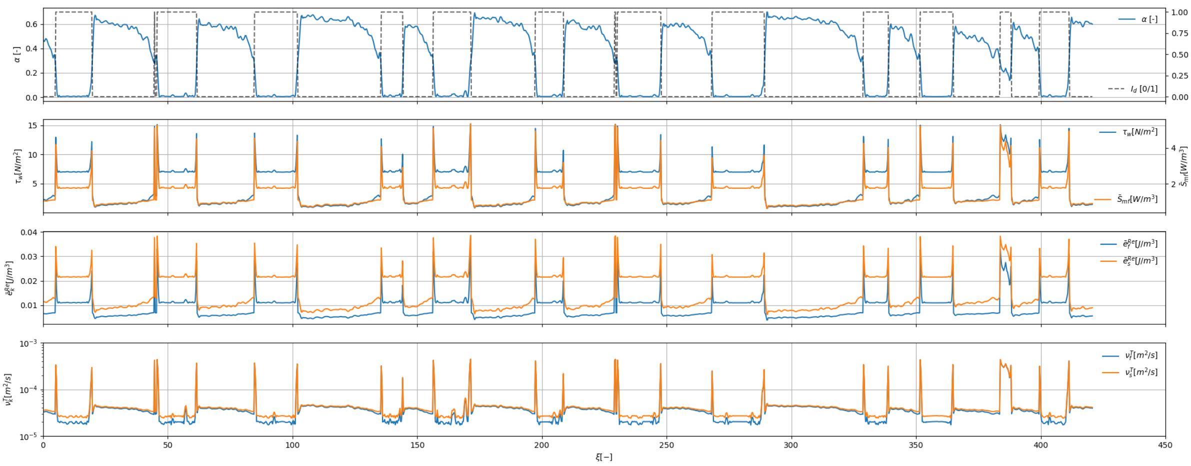

Figure 4.36 – Reconstructed stationary homogeneous turbulent flow variables from the experimental point 7, where α is the void fraction time series as function of ξ and the corresponding two-state classification (upper), τ_w is the parietal shear stress, $\bar{e}_k^{Re}$ is the homogeneous turbulent kinetic energy and ν_k^T is the averaged effective kinematic viscosity.

Higher equivalent kinematic viscosities are observed on Figure 4.36 for the proposed model steady state solution ν_s^T, which will be the preferred option from now on, as more dissipation is desired to stabilize the system near the jumps. Similar results were reported by Fullmer *et al.* (2011) regarding the stratified flow pattern, with equivalent kinematic viscosities between 1 m^2/s and 4×10^{-5} m^2/s at the Taylor bubble region, which indicates consistency of the adopted hypotheses in the model development. Peaks in equivalent kinematic viscosity are observed near the transitions, which indicates that they can be induced by the transition itself between the alternating unit cell flow patterns, where the causality should be investigated.

The equivalent kinematic viscosities components are shown in Figure 4.37, where ν_s^T, ν^{TW}, ν^{TI} and ν^{TB} are the averaged effective kinematic viscosities obtained from the proposed model steady state solution, the shear induced components due to the wall and interface shear stresses and the bubble-induced component, respectively, as indicated in Section 3.5. The aforementioned peaks observed in the equivalent kinematic viscosities are due to the bubble induced component at the transition from the stratified pattern to the dispersed bubble pattern. As stated by Vaidheeswaran *et al.* (2016), such viscosity peaks are important to stabilize the flow in the jump regions, which leaves us questioning if the transition to the dispersed bubbles flow pattern is the system stabilization mechanism, otherwise there would not be an abrupt increase in equivalent kinematic viscosity by an order of magnitude.

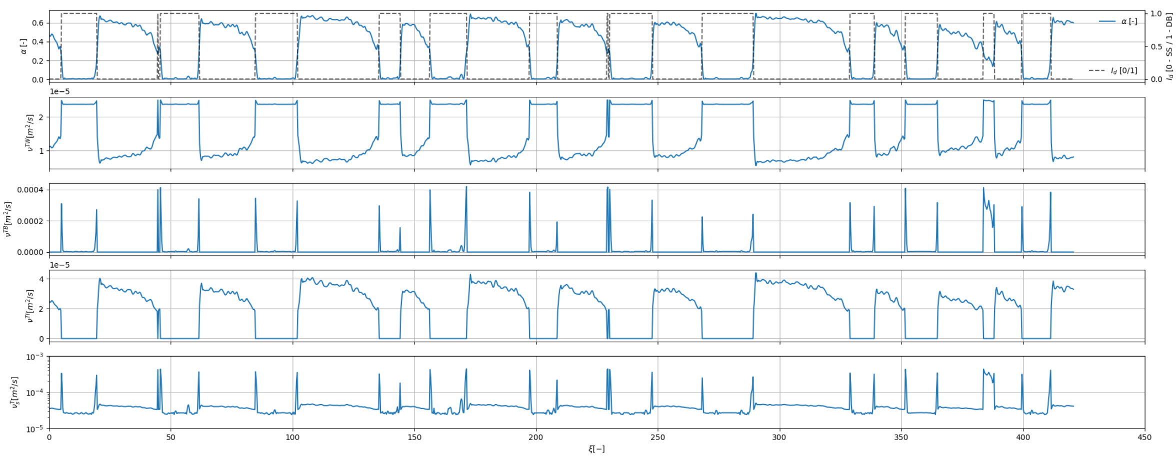

Figure 4.37 – Reconstructed stationary homogeneous turbulent equivalent kinematic viscosities from the experimental point #7, where α is the void fraction time series as function of ξ and the corresponding two-state classification (upper), ν_s^T, ν^{TW}, ν^{TI} and ν^{TB} are the averaged effective kinematic viscosities obtained from the proposed model steady state solution, the shear induced components due to the wall and interface shear stresses and the bubble-induced component, respectively.

The specific power source components of the proposed one dimensional one equation turbulent model are calculated and shown in Figure 4.38, as expressed by the Equation 3.134 at Section 3.5.1. As expected, it can be noticed that the specific power source is dominated by the parietal shear stress and convective acceleration components, $\bar{S}_{mf}$ and S_{mf}^{acc} respectively, while the viscosity dissipation and surface energy components are negligible, S_{mf}^{ν} and S_{mf}^{σ} respectively. Therefore, the simplifications made for the power based transition criterion evaluation are suitable, as peaks are observed in the specific power source next to the jumps, confirming the hypothesis that the transitions are close to its maximum.

The estimated bublance B is also shown, as defined in Equation 3.32 at Section 3.2.3. However, in this case, the complete model considering the phases slip velocities and the *in situ* void fraction is used rather than the homogeneous one, as shown in Figure 4.33. It is observed that the jumps in the bublance coincide with the jumps in the void fraction wave profile, which indicates that the unit bublance could be the threshold for classification between flows dominated by turbulence (DB) or coalescence (SS). Finally, the net specific power source derivative is compared with the bublance along the states estimated by the Otsu method in Figure 4.39.

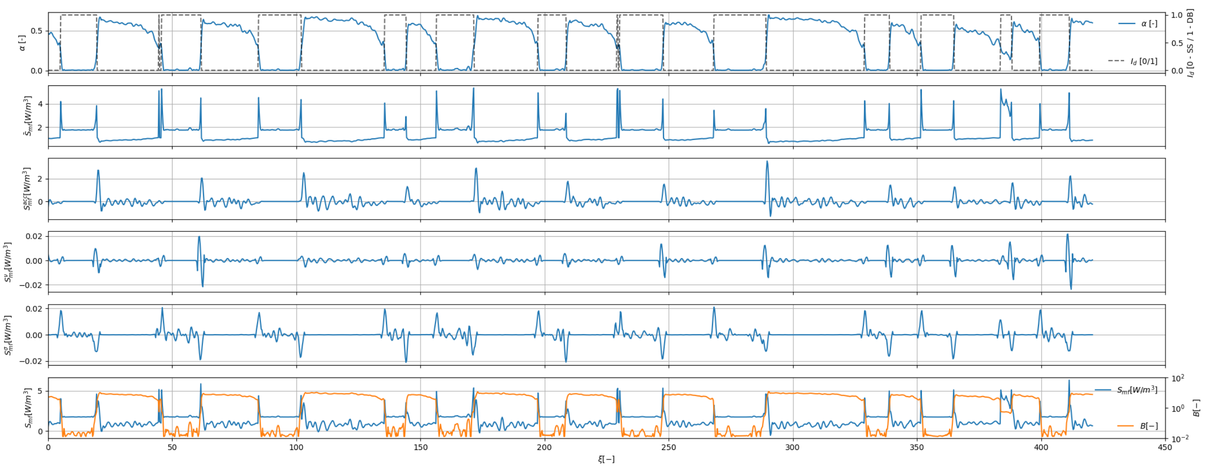

Figure 4.38 – Reconstructed specific power source components of the proposed one dimensional one equation turbulent model from the experimental point #7, where α is the void fraction time series as function of ξ and the corresponding two-state classification (upper), $\bar{S}_{mf}$, S^{acc}_{mf}, S^{ν}_{mf} and S^{σ}_{mf} are the specific power sources parietal shear stress, convective acceleration, viscosity dissipation and surface energy components, respectively. Finally, the net specific power source S_{mf} and bublance B (bottom).

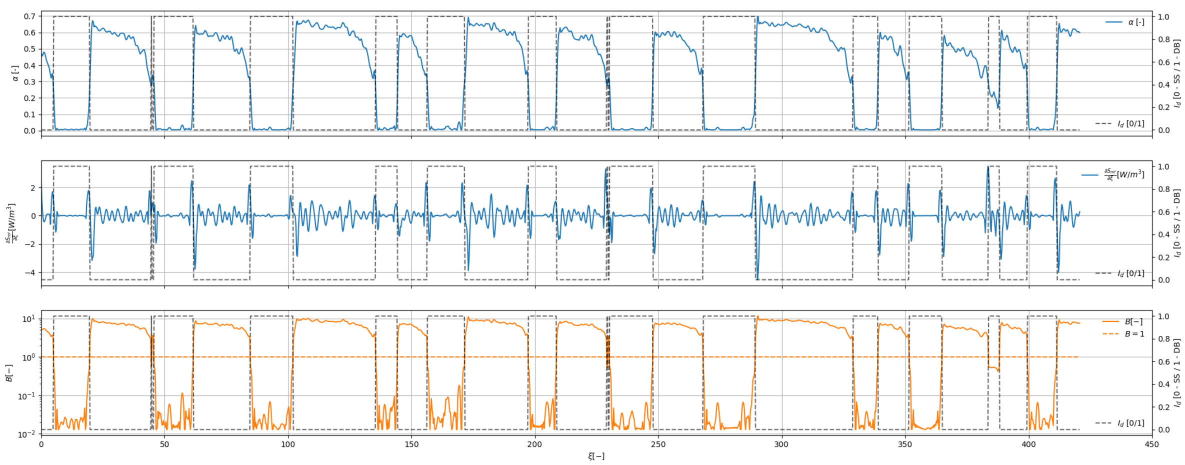

Figure 4.39 – Reconstructed transition criteria over flow variables from the experimental point #7. Void fraction and two-state classification (top), first derivative of the specific dissipated power (centre) and bublance (bottom).

In general, the transitions mapped by the Otsu threshold are very close to the unity bublance and the zero crossing in the specific power derivative. It should be noted that, as the void fraction signals that were used to reconstruct the time series are experimental and noisy, the derivatives of the series reconstructed from the model are also noisy, which makes the identification of the zero crossing less obvious, even with the adoption of noise-resistant derivation methods such as the Savitzky-Golay filter. These results show that the proposed transition criteria is suitable to represent the transition between the different regions of the unit cell and can be implemented as a switching criterion for the source terms of the two-fluid model.

It suggests that the bublance and the net specific power source are entangled concepts, as it can be seen adopting the one equation approach, expressed in the Equation 3.123, for the dissipated turbulent energy rate and substituting in the bublance concept, expressed in Equation 3.33. It leads to

$$B = \alpha\left(1-\alpha\right)\frac{\left(\rho_1-\rho_2\right)}{\rho_1}\frac{1}{C_D}We_c^{\frac{3}{5}}\left[g\cos\theta\left(\frac{\sigma_{21}}{\rho_1}\right)^{\frac{3}{5}}\frac{l_m^{\frac{2}{5}}}{e^{Re^{\frac{8}{5}}}}\right], \tag{4.2}$$

which means the bublance is actually a function of the averaged turbulent kinetic energy, whose source is the net specific power source. Consequently, from now on, only the bublance concept will be adopted for the transition modeling due to its causal relation with the net specific power source.

Therefore, the dynamically evaluated flow pattern, alternating from one flow pattern to another, as the unit cell model suggests, represented by the sigmoid function I_d over the unity bublance classification boundary is defined as

$$I_d = H\left(B-1\right), \tag{4.3}$$

where H is the Heaviside function.

As the bublance is directly affected by the parietal shear stresses, that vary according to the observed flow patterns, one must evaluate its sensitivity to the segregated and dispersed bubble flow patterns, where they present different magnitudes, as can be observed at Figure 4.34. Furthermore, Figure 4.40 displays the bublance estimated from the closure relationships for the segregated B_{SS} and dispersed B_{DB} flow patterns. It can be seen that the intersection between the bublance curves, the two-state classification series I_d and the unity bublance threshold occurs at different points depending on the flow pattern. This indicates the phenomenon of hysteresis, since the transition threshold depends on the direction of the transition between the patterns, which is explained by the different magnitudes of the parietal shear stresses experienced by the flow depending on the current pattern.

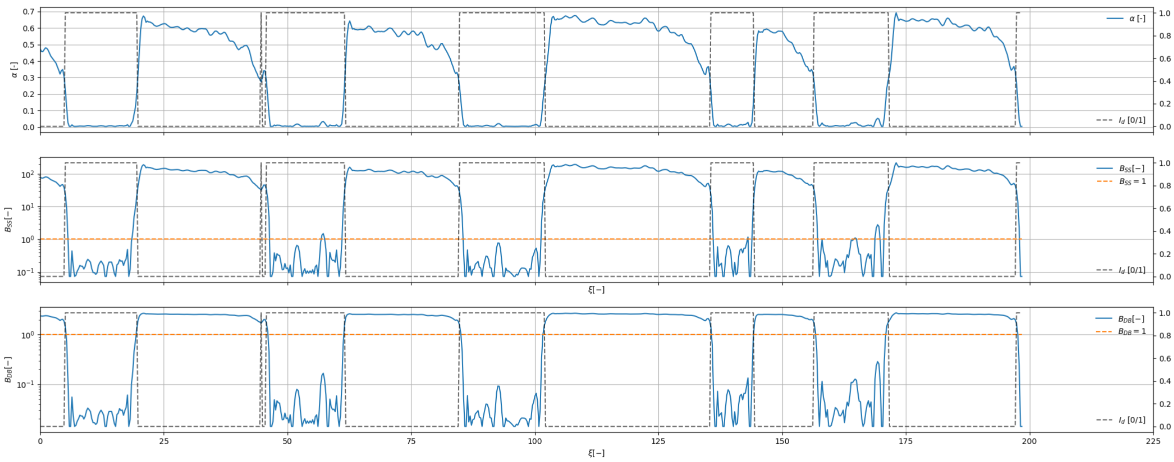

Figure 4.40 – Reconstructed transition criteria over flow variables from the experimental point #7. Void fraction (top), bublance on the stratified flow pattern B_{SS} (centre) and bublance on the dispersed bubbles flow pattern B_{DB} (bottom). All compared with the two-state classification series I_d and the unity bublance threshold.

Finally, it should be highlighted that all series of variables of interest presented in this section were reconstructed based on the experimental void fractions. They were obtained using the developed models. However, a similar approach can been done with numerically simulated data, indicating that the proposed model and corresponding numerical results can be used for the reconstruction of series of interest, such as the pressure series. The numerical integration of the models to obtain the waveform profile of the void fractions through the model is discussed in the next sections.

4.4.2 One-dimensional Model

The one-dimensional theoretical model on the phase space for the stratified and dispersed bubbles flow patterns, presented in Section 2.4.2, is investigated at the experimental condition #7 of the test matrix, as shown at Figure 4.2 and Table 4.1. Figures 4.41 and 4.42 present the numerical results of the kinematics, obtained from Equation 2.114 at Section 2.3.1, the force balance term F_{FB}, from Equation 2.161 whose roots are the dynamical system fixed points, the convective acceleration and pressure difference term $F_{CA-\Delta P}$, from Equations 2.160 and 2.162 whose roots are the dynamical system singularities and the one dimensional flows expressed at Equation 2.201.

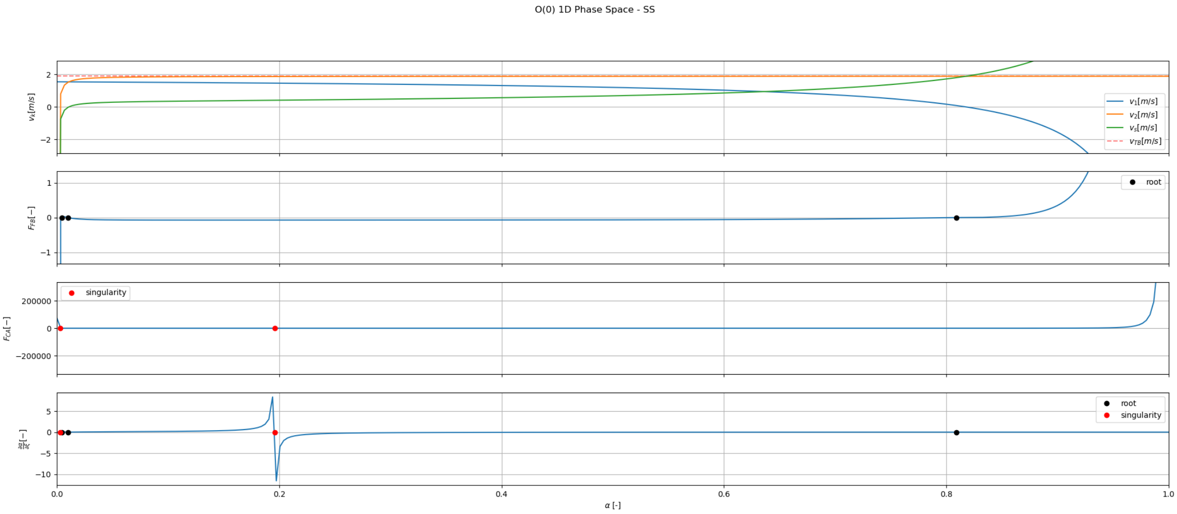

Figure 4.41 – One dimensional model for the stratified flow pattern: upper plot - kinematics, center plots - the force balance term F_{FB} and the convective acceleration and pressure difference term $F_{CA-\Delta P}$, lower plot - one dimensional flow.

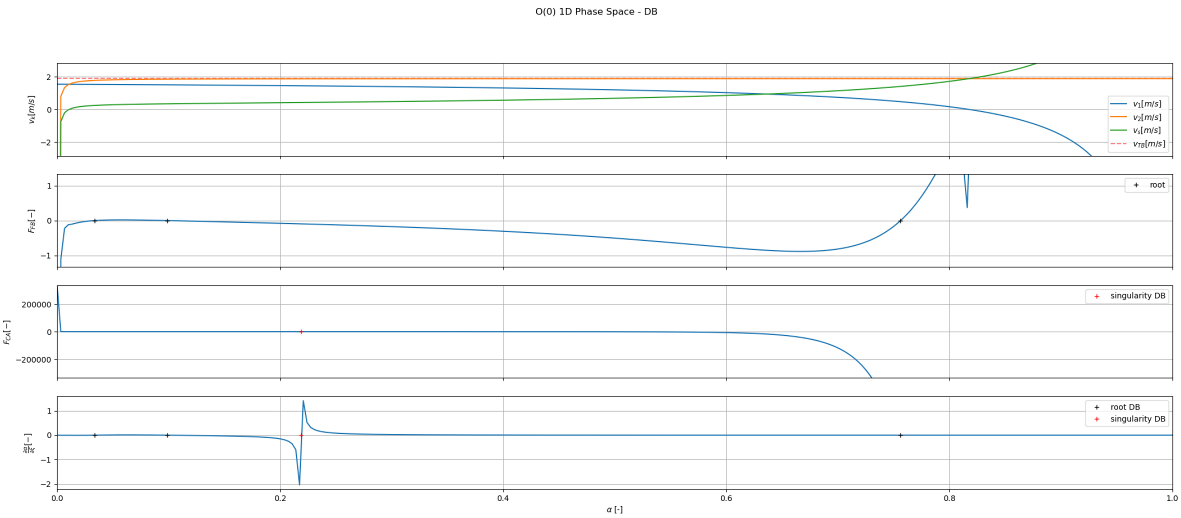

Figure 4.42 – One dimensional model for the dispersed bubble flow pattern: upper plot - kinematics, center plots - the force balance term F_{FB} and the convective acceleration and pressure difference term $F_{CA-\Delta P}$, lower plot - one dimensional flow.

The constant mixture flow solution allied with the traveling wave transformation, Equation 2.114 at Section 2.3.1, allows reconstructing the velocities series from the void fractions as shown at the upper plot in the Figures 4.41 and 4.42. It can be highlighted that the fixed points of the dispersed bubbles pattern shown on Figure 4.42 are far from the point where the slip velocity is zero, contradicting the widely used homogeneous model hypothesis for the bubbly liquid piston (Wallis, 1969; Shoham, 2006).

The one dimensional flow, as shown at the lower plots in the Figures 4.41 and 4.42, is the $\mathcal{O}(0)$ approximation of the system dynamics and has fixed points at both high and low void fractions, the force balance term F_{FB} roots from the Equation 2.161. Note that they correspond to the solutions between which the system oscillates in the higher dimensional models, as displayed in the Figure 4.33 at Section 4.4.1, but this oscillations cannot occur in an one dimensional model for topological reasons (Strogatz; Dichter, 2016). The most remarkable features are the singularities for the stratified and dispersed bubbles flow patterns, the convective acceleration and pressure difference term $F_{CA-\Delta P}$ roots from the Equations 2.160 and 2.162, both close to the Otsu's threshold, as displayed in the Figure 4.33 at Section 4.4.1. These singularities promote the jumps in the system dynamics switching between the stratified and dispersed bubbles flow patterns. Recall that this switch can be modelled as a stochastic process. The presence of these singularities is in line with the localized instabilities in the phase space reported in the literature that explain the bias of the Lyapunov exponent estimator, as discussed in Section 4.3. Such singularities can be associated with an empty space found in the phase space between the transition surfaces that repel any trajectory near them, as shown in Figure 4.30.

Both numerically obtained system responses from the one dimensional flows expressed by Equation 2.201 and shown at the lower plots in the Figures 4.41 and 4.42 are presented in Figure 4.43, where the stratified and dispersed bubbles flow patterns are subsequently combined around the singularity, in order to form the complete unit cell void fraction profile. The initial conditions are set at the higher fixed point vicinity for the stratified flow pattern response and lower fixed point vicinity for the dispersed bubble flow pattern response. The system response is integrated by the implicit multi-step variable-order BDF method implemented in the Scipy library (Virtanen *et al.*, 2020) because the problem is stiff experimenting different times scales due to the jumps at the mass shocks because of the hydraulic jump near the flow pattern transition.

Note that the slug unit void fraction wave profile solution plotted in Figure 4.43 represents an advance when compared to the Taitel e Barnea (1990) model. It manages to model more accurately the physics of the problem, including the region of the aerated piston in the dispersed bubble pattern, where the region with the highest void fraction at the piston can be observed. This region can be associated with the greater presence of bubbles in the recirculation mixing zone after the hydraulic jump.

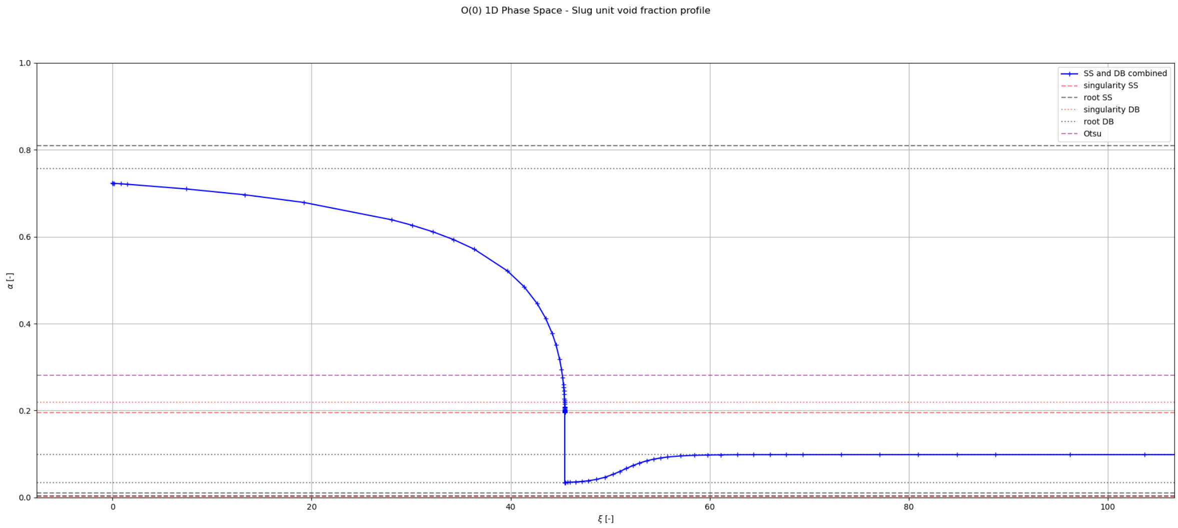

Figure 4.43 – Slug unit profile obtained by integrating the one dimensional model for the stratified and dispersed bubble flow patterns combined.

4.4.2.1 Taylor Bubble Experimental Profile

In this section, a typical unit cell was selected from the time series at the experimental condition #7 of the test matrix, as shown at Figure 4.2 and Table 4.1. The unit cell was select as being the one with the set of parameters closest to the median of the histograms successfully estimated and sampled by the Markov chain, as shown in Figures 4.16 and 4.17. This unit cell is presented in Figure 4.44 along with its first and second order derivatives, calculated using the Savitzky–Golay filter.

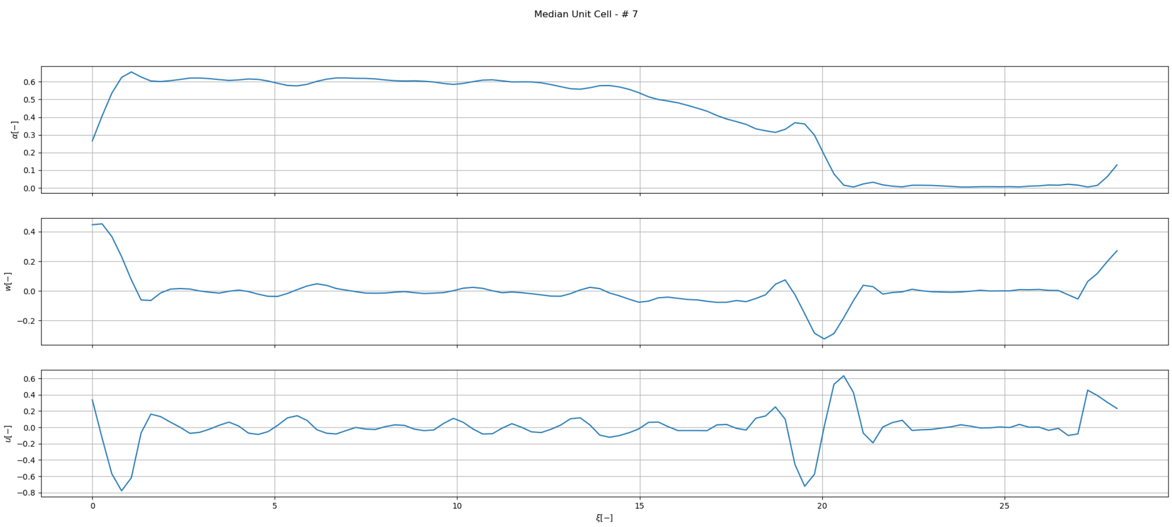

Figure 4.44 – Typical median unit cell at the experimental condition #7 of the test matrix void fraction wave profile (top), first (middle) and second (bottom) order derivatives.

Unfortunately, as stated earlier, there are greater uncertainties on the measurement in the liquid piston region. Thus, only information from the Taylor bubble region will be evaluated. Using the Taylor bubble velocity estimated by the GCC SCOT, as shown in Figure 4.5 and Table 4.3, all the closure relationships reviewed in Chapter 2 were tested and compared to the experimental data. It is important to highlight that hundreds of combinations of closure relationships are possible. The results for the more suitable closure models listed in Table 4.7 are presented in Figure 4.45 along with the experimental data.

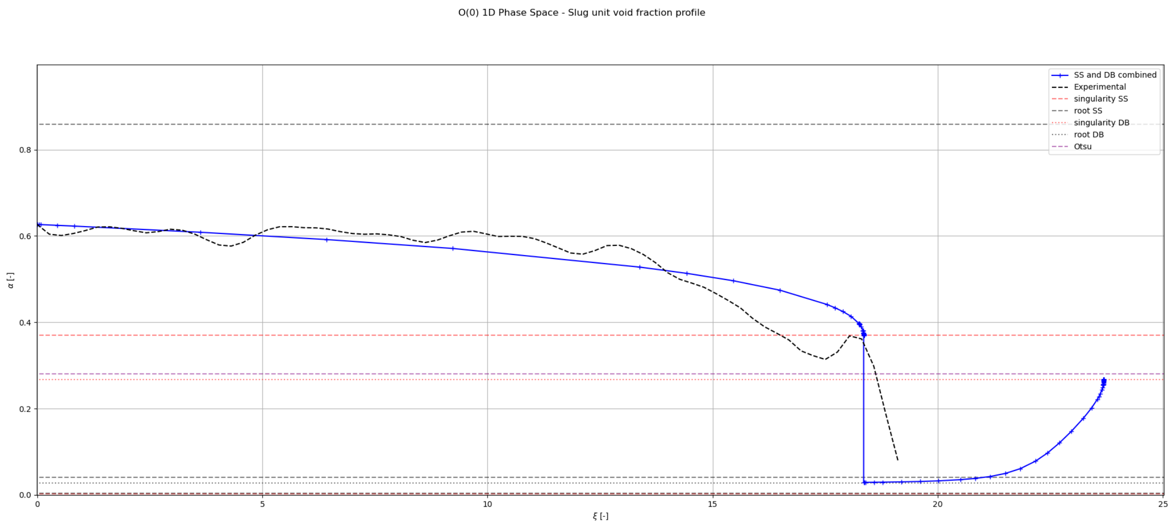

Figure 4.45 – Typical experimental slug unit cell void fraction wave profile along with the numerical result obtained with selected closure models listed in Table 4.7.

The best model for the liquid phase friction was the Nossen *et al.* (2000), as shown in Equations 2.31 to 2.34. This is an expected result because in addition to being the most modern closure model, it considers the effects of interface friction on liquid phase friction, that is, as the slip at the interface affects the velocity profile of the liquid phase. For interfacial friction, the Andreussi e Persen (1987), given by Equations 2.38 to 2.40, was the best. It was also expected because such a model considers the slip between phases and is based on the Kelvin-Helmholtz instability mechanisms. The best model for relative volumetric flow of the gas phase M_2 was the one by Barnea e Brauner (1985), expressed in Equation 2.123, to estimate the void fraction in the liquid piston together with the Gomez *et al.* (2000) Drift Flux model for the *in situ* velocity of the gas phase considering that the experimentally estimated Taylor bubble velocity was used. Another expected result, since this model is mechanistic and is based on the transition mechanisms of the dispersed bubble pattern. Additionally, from Figure 4.45, it can be seen that the void fraction wave profile at the Taylor bubble region is well represented and the numerical model captures the overall profile except by the short wavelength oscillations. It presents an apparently increasing wavelength, which can be associated with interfacial waves at the stratified region. Investigating this behaviour is outside the scope of this thesis.

Unfortunately, due to the high uncertainty of the measurement in the liquid piston region, a similar procedure cannot be done for the closure relationships of the dispersed bubble pattern because the measurements at low void fraction are not reliable (Dos Santos *et al.*, 2019). Therefore, the chosen closure models for the dispersed bubbles flow pattern are arbitrary, relying on the author qualitative perception of the void fraction wave profile at the liquid piston.

From now on, the following adjusted closure relationships are adopted, as shown in Table 4.7

Table 4.7 – Adjusted closure relationships

Variable	Description	Model
V_{TB}	Taylor bubble velocity	Experimental from Table 4.3
α_S	Liquid slug void fraction	Barnea e Brauner (1985)
v_B	Liquid slug gas *in situ* velocity	Gomez *et al.* (2000)
f_2	Taylor bubble gas friction factor	Taitel e Dukler (1976)
f_1	Taylor bubble liquid friction factor	Nossen *et al.* (2000)
f_i	Taylor bubble interfacial friction factor	Andreussi e Persen (1987)
f_m	Liquid slug mixture friction factor	Bendlksen *et al.* (1991)
We_c	Bubble critical Weber number	Calderbank (1958)
C_D	Bubble drag coefficient	Tomiyama *et al.* (1998)
$\hat{M}_2^D$	Bubble drag averaged momentum transfer	Ishii e Hibiki (2011)
C_V	Bubble added mass coefficient	Ishii e Hibiki (2011)
$\hat{M}_2^V$	Bubble added mass averaged momentum transfer	Ishii e Hibiki (2011)
C_C	Bubble collisions forces coefficient	Bertodano *et al.* (2016)

4.4.3 Two-dimensional Model

In this section, the numerical results for the two-dimensional model from the Section 2.4.3 on the phase space are presented, at the experimental condition #7 of the test matrix, as shown at Figure 4.2 and Table 4.1.

Considering that the slug initiation mechanism from the stratified equilibrium solution is the Kelvin Helmholtz instability, indicating an unstable fixed point at the segregated flow pattern, where perturbations are amplified until high amplitude nonlinear waves are obtained (Barnea, 1987; Barnea; Taitel, 1994; Shoham, 2006), one will first analyze the void fraction wave profile only in the stratified flow pattern looking for limit cycles solutions that are similar to the experimental data, which implies that there will be no transition to the dispersed bubble flow pattern, hence, the wave crest will not touch the pipe upper dorsal line.

Following the results from the previous section, the closure relationships chosen as the most suitable for the segregated pattern listed at Table 4.7 are adopted for the two-dimensional model, which was then integrated by the implicit multi-step variable-order BDF method for stiff problems only for the stratified pattern, thus, without the transition modeling, where the only remaining parameter is the equivalent kinematic viscosity that will be addressed by a sensitivity analysis. Figure 4.46 presents the obtained results, along with the two dimensional stratified flow model (light blue), its trajectory (magenta) with its fixed points and nullclines (dark blue) (Strogatz; Dichter, 2016).

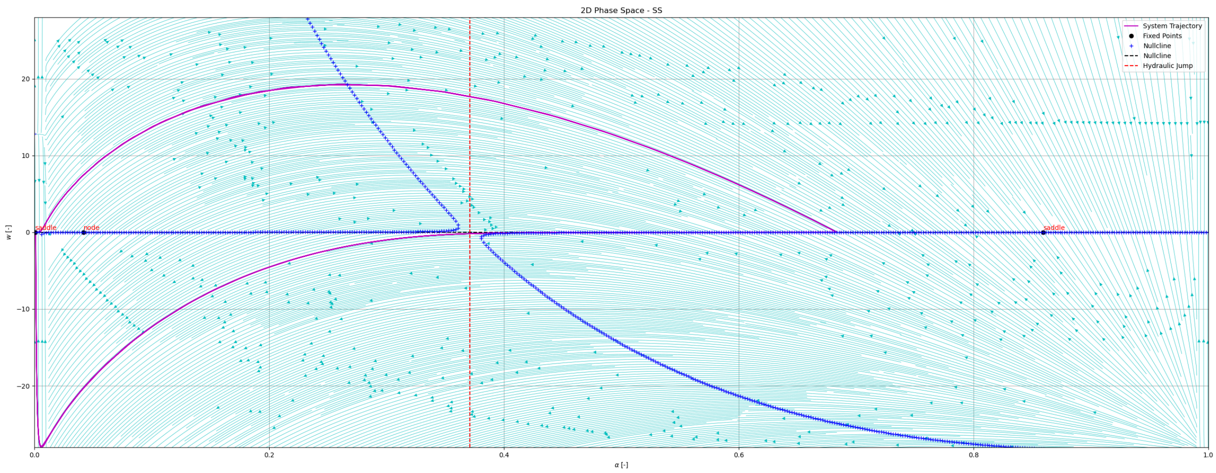

Figure 4.46 – Numerical result from the two dimensional model at the stratified flow pattern (magenta), its nullclines (dark blue), two dimensional flow (light blue) and the hydraulic jump (red dashed line).

It is possible to note that the nullclines are very similar to the one dimensional flow, as expected, since they are an $\mathcal{O}(0)$ approximation of the problem solution. However, for high values of w, the viscosity effects are apparent by changing the nullcline slope, which qualitatively impacts the void fraction amplitude at the jump on the mass shock near the hydraulic jump, with bigger and slower jumps as the averaged equivalent turbulent kinematic viscosity increases. The Taylor bubble void fraction wave profile is dominated by the system trajectory that is tangent to the nullcline. The higher and lower void fractions fixed points furthest from the one dimensional model singularity, i.e., the hydraulic jump, are saddle points, attracting trajectories vertically and expelling them horizontally. The periodic solution in this case is a limit cycle on the two dimensional phase space laying between those two saddle fixed points and around a unstable node fixed point with a unitary index, as the index theory suggests (Strogatz; Dichter, 2016). Considering that the limit cycle orbit is near the lower saddle point, returning to it periodically, this trajectory is a homoclinic orbit (Strogatz; Dichter, 2016). The numerical results are presented as a function of ξ in Figure 4.47 and compared with the experimental data from the median unit cell. It can be seen that it presents a very good agreement, specially at the first numerically integrated cycle. However, the steady state Taylor bubble length are longer than the observed experimentally, which means that further adjustments are needed.

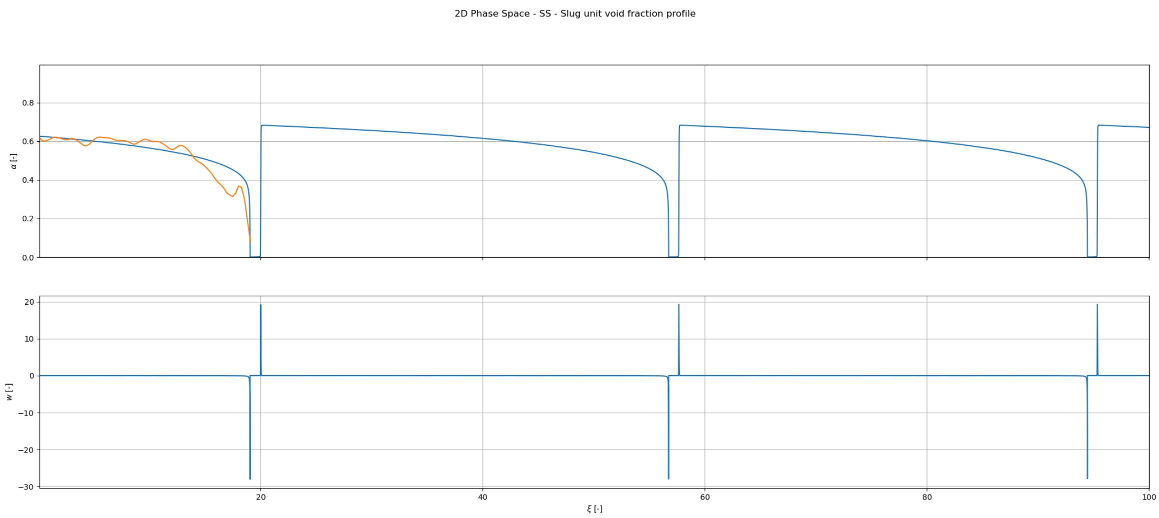

Figure 4.47 – Slug unit void fraction wave profile for the two dimensional model on the phase space.

It should be noted that the turbulent viscosity was assumed to be a constant and chosen from a sensitivity analysis to obtain such results, with equivalent kinematic viscosities greater than 20×10^{-5} m^2/s producing limit cycles, values at least 5 times bigger than the results reported by Fullmer *et al.* (2011) for nonlinear waves modelling on the stratified flow pattern at rectangular channels with higher viscosity operational fluids, which indicates that more dissipation is needed in order to have limit cycles and the estimation of the equivalent kinematic viscosities should be more precisely addressed. If the turbulent viscosity is too small, the system response explodes beyond its domain support $\alpha \in [0, 1]$ becoming unstable. This is a similar result as the one from Vaidheeswaran *et al.* (2016), which highlights the importance of turbulent viscosity for the stabilization of the system, especially close to shocks and discontinuities. Moreover, notice that as no transition is imposed, the entire series is in the stratified pattern. It can be seen that at the region where the liquid piston would be present, there is a very short region of low void fraction. This is most likely happening due to the fact that the transition and higher averaged equivalent turbulent kinematic viscosity are necessary to stabilize the system in this region, giving longer liquid pistons.

4.4.3.1 Bifurcation Diagrams

In this section, a bifurcation diagram of the two-dimensional stratified model from the Section 2.4.3 on the phase space is investigated, at the experimental condition #7 of the test matrix, as shown at Figure 4.2 and Table 4.1. The fixed points and their respective stabilities were calculated through the nonlinear system Jacobian eigenvalues considering the closure models highlighted on Table 4.7, the results are presented in Figure 4.48 as a function of the V_{TB} and M_2, the main nonlinear dynamical system parametric variables, alongside with the averaged equivalent turbulent kinematic viscosity considered here as a constant at 20×10^{-5} m^2/s, as discussed in the previous section. The Taylor bubble velocity V_{TB} values from the Bendiksen (1984) model and the experimentally characterized from the GCC SCOT estimate are also highlighted alongside with the relative gas volumetric flow M_2 from the Barnea e Brauner (1985) model.

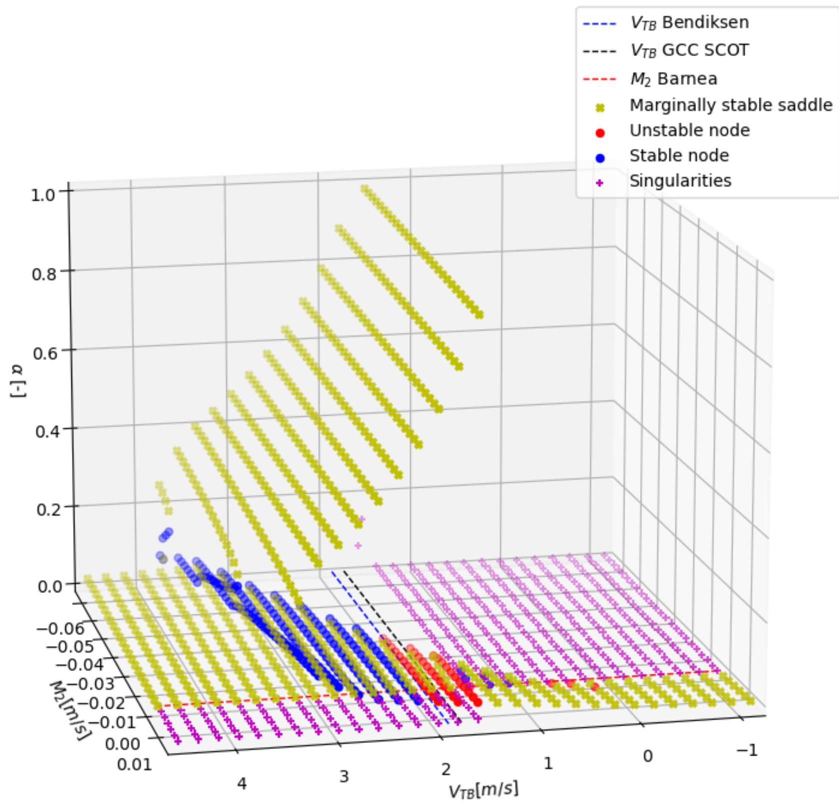

Figure 4.48 – Bifurcation diagram of the two-dimensional stratified model.

As the unit cell model suggests, the bifurcation diagram presented in Figure 4.48 shows a higher and lower void fractions unstable saddle fixed points surface branches (yellow squares), furthest from the one dimensional model singularity, i.e., the hydraulic jump $\alpha_{HJ} \approx$

0.2, whose values are relatively close to average void fractions of the Taylor bubbles α_F and liquid pistons α_S shown at Table 4.3. As the system oscillates almost periodically between these two higher and lower void fractions states as described and modelled by the Markov Chain, both were expected to be unstable, as it is shown in the bifurcation diagram, otherwise the system would eventually converge to one stable solution.

Additionally, it can be seen at the bifurcation diagram presented in Figure 4.48 that there is a branch of singularities (magenta crosses) at lower void fractions, where this branch collides with the lower void fractions unstable saddle branch (yellow squares). This is specially interesting because this collision occurs around a line of near zero relative gas volumetric flow M_2 having a unstable saddle fixed point only for negative values, which can be physically interpreted as the majority of the gas phase is displaced in the form of a Taylor bubble, its relative gas volumetric flow M_2 is near zero, however, this value must be negative, representing the bubbles swarm that detaches from the Taylor bubble at the mixing recirculating zone after the hydraulic jump, having, consequently, a negative relative gas volumetric flow M_2, which is consistent with the fact that the Barnea e Brauner (1985) model was chosen by the sensitivity analysis, because it gives the nearest zero negative relative gas volumetric flow M_2.

Moreover, it can be noticed at the bifurcation diagram presented in Figure 4.48 that there is a third branch of intermediary void fractions fixed points, which consists mostly of stable (blue dots) and unstable (red dots) nodes. As stated previously, this branch is mandatory and extremely important in order to have a closed orbit around it oscillating between the higher and lower branches, as stated by the Index Theory, a closed orbit is only possible if it involves fixed points whose combined indices are unitary in $\mathcal{R}^2$ (Strogatz; Dichter, 2016). As apparently such orbits do not involve the upper e lower fixed points branches, it only involves the nodes fixed points of this third branch, which, in order to have unit indices, it needs to be nodes, centers or spirals, that is the case. For higher values of Taylor bubble velocities V_{TB}, this branch of stable nodes fixed points (blue dots) eventually collides with the higher branch of unstable saddle fixed points (yellow squares), producing a saddle-node bifurcation, being the first region on the nonlinear dynamical system parametric variables space as a candidate for a closed orbit around this bifurcation (Strogatz; Dichter, 2016; Giddings, 2017; Giddings; Billingham, 2019; Needham; Merkin, 1984; Needham *et al.*, 2008). For lower values of V_{TB}, this third branch undergoes a series of interesting transformations that are going to be detailed at the zoomed bifurcation diagrams presented in Figures 4.49 and 4.50, however the most important fact here is that there is a lower Taylor bubble velocity V_{TB} limit at the bifurcation diagram presented in Figure 4.48, where there are not any higher nor lower void fractions unstable saddle fixed points anymore (yellow squares), with the appearance of a branch of singularities (magenta crosses) at lower void fractions. Therefore, the aforementioned saddle-node bifurcation, near zero negative relative gas volumetric flow M_2 line and this lower Taylor bubble velocity V_{TB} limit is going to be the references adopted in the following zoomed bifurcation diagrams, in order to detail the interesting transformations observed at the third branch of intermediary void fractions nodes fixed points, bearing in mind that the highlighted reference values of the Taylor bubble velocity V_{TB} and the relative gas volumetric flow M_2 obtained from the chosen closure models from the Table 4.7 are surrounded by these boundaries.

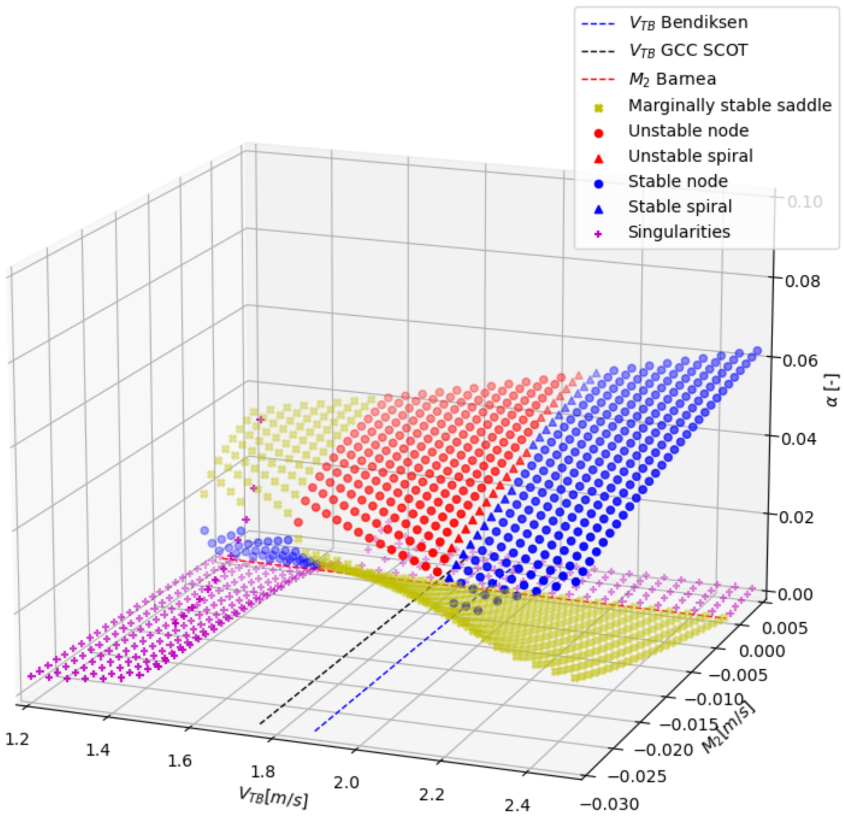

Figure 4.49 – Bifurcation diagram of the two-dimensional stratified model. Detailed view.

It can be seen at the third branch of intermediary void fractions fixed points from the zoomed bifurcation diagram presented in Figures 4.49 and 4.50, that it transitions from stable nodes (blue dots) to stable spirals (blue triangles), and, subsequently, turns into unstable spirals (red triangles) and then unstable nodes (red dots) as the Taylor bubble velocity V_{TB} decreases, thus, there is a line between stables and unstable spirals, i.e., between the blue and red triangles, with pure imaginary eigenvalues, hence, passing through a Hopf bifurcation, being the second region on the nonlinear dynamical system parametric variables space as a candidate for a closed orbit around this bifurcation (Strogatz; Dichter, 2016; Giddings, 2017; Giddings; Billingham, 2019; Needham; Merkin, 1984; Needham *et al.*, 2008). As V_{TB} decreases even more, there is another saddle-node bifurcation with the collision of these unstable nodes (red dots) with the unstable saddle fixed points (yellow squares), similarly, the same occurs when the relative gas volumetric flow M_2 decreases, configuring another saddle-node bifurcation, colliding with the lower void fraction saddle nodes branch (yellow squares), being the third and fourth regions on the nonlinear dynamical system parametric variables space as a candidate for a closed orbit around these bifurcations (Strogatz; Dichter, 2016; Giddings, 2017; Giddings; Billingham, 2019; Needham; Merkin, 1984; Needham *et al.*, 2008). It has to be pointed out that the highlighted reference values of the Taylor bubble velocity V_{TB} and the relative gas volumetric flow M_2 obtained from the chosen closure models from the Table 4.7 are surrounded by these boundaries, again. Therefore, these boundaries delimit the nonlinear dynamical system parametric variables space where the parameter of closed orbit configuring a periodic solution can be.

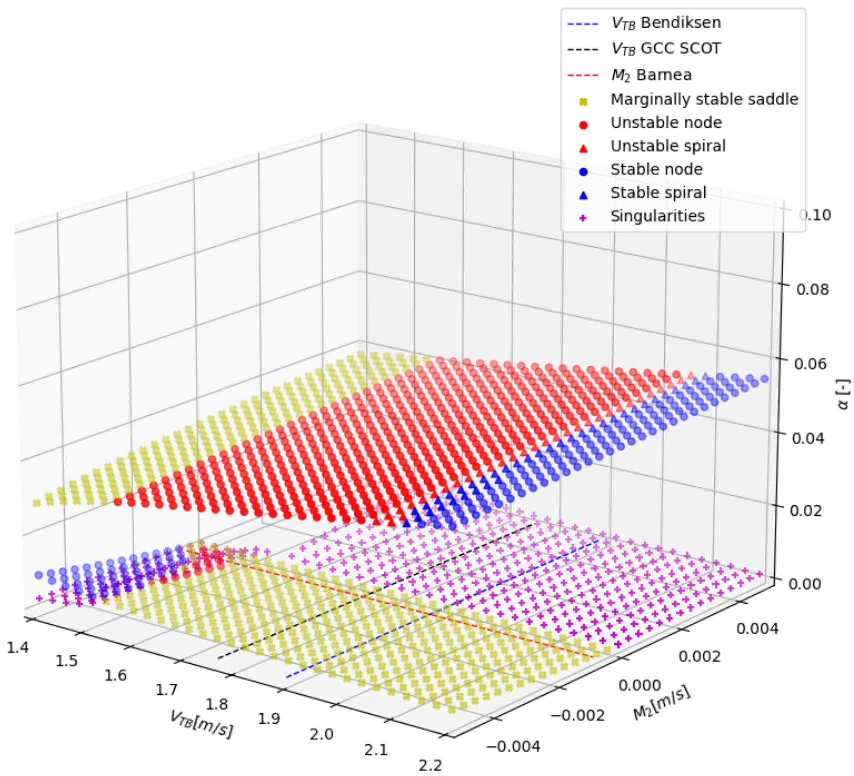

Figure 4.50 – Bifurcation diagram of the two-dimensional stratified model. Second detailed view.

Mathematically, the bifurcations indicate regions in the the nonlinear dynamical system parametric variables space where there are eigenvalues with a zero component. It indicates that the nonlinear dynamical system response can be linearly represented by a lower dimensional reduced-order manifold in the vicinity of this region, exactly the case of a closed orbit that can be represented by a parametric lower order one dimensional curve (Strogatz; Dichter, 2016) in the two dimensional phase space.

A closer inspection at Figure 4.46, with the numerical results of the two dimensional phase space for the stratified pattern, reveals that there is a section of the phase space whose flow is practically vertically attracting the solutions towards the lower void fraction saddle fixed point, like a bottleneck. From this point, the system trajectory rises vertically, meeting the vicinity of the lower void fraction saddle fixed point, which then expels the trajectory horizontally. Thus, the system trajectory meets a stable manifold, in this case a homoclinic orbit as previously discussed, therefore, being a homoclinic bifurcation, when the stable lower order manifold around the intermediary third branch unstable node from the Hopf bifurcation meets the saddle node, a global bifurcation case (Strogatz; Dichter, 2016; Giddings, 2017; Giddings; Billingham, 2019; Needham; Merkin, 1984; Needham *et al.*, 2008).

4.4.3.2 Two Dimensional Model with Transition Criteria

In this section, the numerical results for the two-dimensional model from the Section 2.4.3 on the phase space are presented for the segregated and dispersed bubbles flow patterns, at the experimental condition #7 of the test matrix, as shown at Figure 4.2 and Table 4.1. The closure relationships previously chosen as the most suitable and listed at Table 4.7 are adopted for the two-dimensional model, which was then integrated by the implicit multi-step variable-order BDF method for stiff problems, however, the transition modeling and the equivalent kinematic viscosity are now considered as discussed in Section 4.4.1. Figure 4.51 presents the obtained results, along with the two dimensional flow model with the transition modeling and the equivalent kinematic viscosity (light blue), its integrated trajectory (magenta) with its fixed points and nullclines (dark blue) (Strogatz; Dichter, 2016). The transition mechanisms considers the hysteresis as discussed in Section 4.4.1, whose unity bublance thresholds are represented in Figure 4.51 for the SS-DB transition (orange dashed vertical line) and the DB-SS transition (green dashed vertical line), thus, the model switches between both flow patterns successfully.

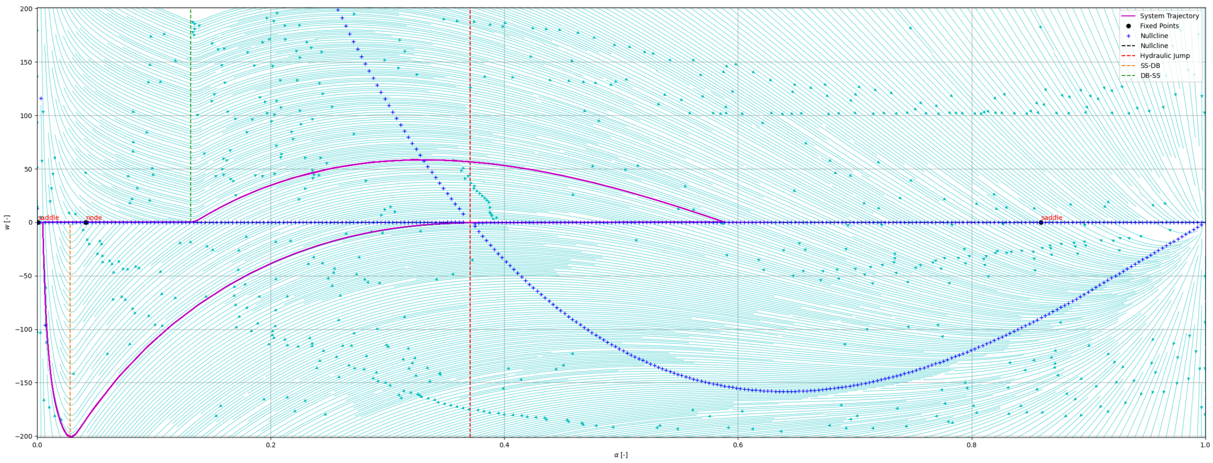

Figure 4.51 – Numerical results from the two dimensional model with the transition modeling and the equivalent kinematic viscosity (magenta), its nullclines (dark blue), two dimensional flow (light blue), hydraulic jump (red dashed line), SS-DB transition (orange dashed vertical line) and the DB-SS transition (green dashed vertical line).

The numerical results are presented as a function of ξ in Figure 4.52 and compared with the experimental data from the median unit cell. It can be seen that they are in very good agreement, specially at the first numerically integrated cycle. However, the steady state Taylor bubble length is now shorter than the observed experimentally, which means that further adjustments in the closure relations and parameters are needed.

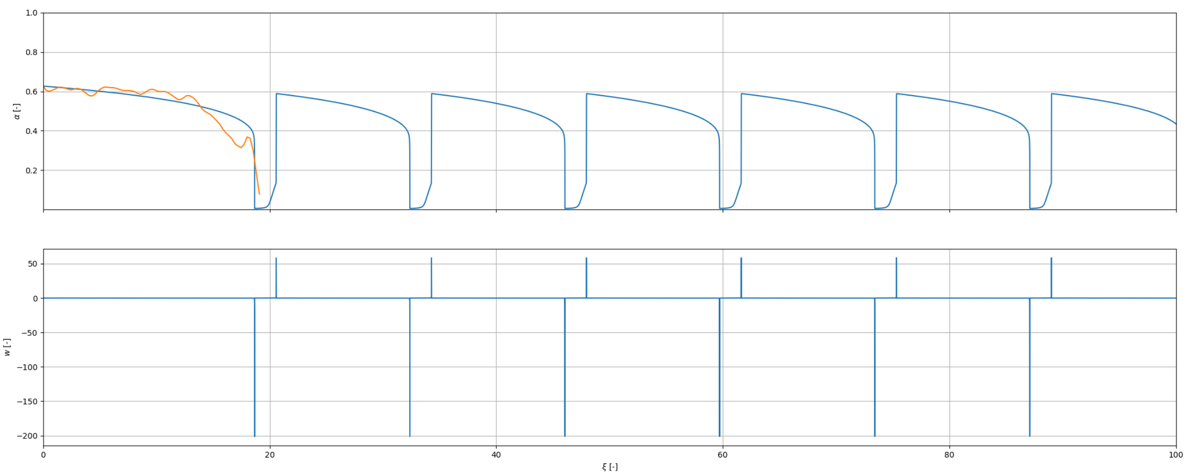

Figure 4.52 – Slug unit void fraction wave profile for the two dimensional model on the phase space.

It can be observed that, in addition to the results for the stratified flow pattern expressed in the Figure 4.46, the transition results represented at Figure 4.52 shows a non flat void fraction wave profile at the liquid piston, resembling the mixing zone. However, the liquid slug length is small when compared with the experimental data, which indicates that further adjustments in the closure relations and parameters are needed alongside with more dissipation, what can be achieved solving completely the averaged turbulent energy equation, instead of using only its steady state solution, as it was done here.

4.5 Concluding remarks

In this chapter, the available experimental data is analyzed and compared with the model, where all relevant parameters of the unit cell are identified, converting it to the traveling wave coordinate system, through a correlation-based estimation approach of the Taylor bubble velocity from two double wire measurement station, directly applied to the data with no need of pre-processing and analytical expressions are available for the error estimate.

The system chaos was quantified and the phase space was reconstructed from the experimental data where the minimum number of dimensions for the deterministic dynamics of the slug flow was estimated as three, which has a physical interpretation, that the variability of the unit cell parameters derive from a three-dimensional chaotic dynamics and that such dimensionality is only achieved with the inclusion of the terms of the interfacial tensions.

A two-state Markov chain model was proposed and validated for modelling the transition times between states. The system states were estimated from the experimental data by a simple data-driven non-parametric automatic approach. The Markov chain was related to the reconstructed phase space as a model for the transition probabilities between the equilibrium void fractions solutions at the center of the orbits separated by the transition surfaces.

The description of the transition between the two flow patterns in the slug is addressed, where a physically and data-driven based transition model is proposed, based on the concept of bublance and the corresponding energy conversion processes in the region of the mixing length after the hydraulic jump. The numerical results from the one and two-dimensional phase-space analytical models are presented and the results are interpreted in terms of the experimental time series. Model-based time series of some relevant flow parameters are obtained and then used to discuss the relevant physics for segregated and dispersed flow patterns and transition phenomena. It is shown that the proposed transition threshold depends on the direction of the transition between the patterns, thus indicating the phenomenon of hysteresis.

Based on the one-dimensional model, slug unit void fraction wave profile solution is obtained representing an advance when compared to the currently available model. However, the oscillation of the void fraction is only possible for the two-dimensional system, due to the topology of the dynamical system. Thus, a periodic solution is obtained and the importance of the turbulent viscosity for the stabilization of the system is highlighted.

A bifurcation diagram of the two-dimensional stratified model is also investigated. It is constructed with the fixed points and their corresponding stability and it highlights the main features of the dynamical system and the necessary conditions for the void fraction profile and oscillation. Subsequently, the two-dimensional model is integrated using the proposed transition criteria. The obtained results follows very closely a typical unit cell and and it shown that this strategy is very promising for further numerical schemes.

5 CONCLUSIONS

In this thesis, a two-fold modelling approach was proposed for the slug flow in horizontal pipes with the overall aim of investigating the void fraction wave profile and its statistical properties. The proposed approach was towards a parsimonious model that captures the essential physical mechanisms and explains the unit cell formation, its evolution dynamics and the intermittent state transitioning between segregated and dispersed flow patterns, compared to available experimental data.

First, a rigorous and parsimonious deterministic two-fluid model for the stratified and dispersed flow patterns was proposed. Additionally, a simple but physically insightful stochastic model was proposed for the random transition between the dispersed and segregated patterns at the slug flow in horizontal pipes. A physically based transition model is proposed, based on energy conversion processes in the region of the mixing length after the hydraulic jump. Then, the physical connections between the two models, with seemingly unrelated assumptions, were explored at the light of the transition criteria and of the system's chaotic dynamics.

In the deterministic approach, the two-fluid model is developed for the stratified and dispersed patterns, including all the identified relevant physical mechanisms for the unit cell formation, growth and propagation, leading to a well-posed and bounded model. This is the first work considering all the mechanisms adopted for the flow patterns of interest at circular cross section pipelines and with such rigour. A parsimonious model was proposed adopting suitable assumption, which allowed a significant simplification through the constant flow solution and the travelling wave transformation, with no loss of generality. The assumptions are:

- low Mach numbers; and
- approximately constant Taylor bubble propagation velocity V_{TB}.

The former, follows from the incompressibility due to low phases velocities when compared to sound velocities. The latter is supported by a vast literature and experimental observations. These assumptions allows converting a non-linear system of PDE's into ODE's by condensing the analysis of the system dynamics in a phase space for the void fraction series, i.e., a simpler model. Thus, this allows to investigate the system dynamics in order to understand the slug flow pattern influencing parameters and the transitions between the separate and dispersed alternating flow patterns. Moreover, a bottom-up approach is proposed, based on the orders of magnitude of each model term. The models were sequentially developed describing the dynamical system flow in phase space for both patterns in one, two and three dimensions.

The statistical properties of the two-phase flow were also investigated. A two-state Markov chain model was proposed to represent the stochastic dynamics of developed slug flow in horizontal pipes aiming at a simple but intuitive description of the phenomenon. As suggested by the unit cell model, it is shown that the void fraction time series data are naturally separated into two groups, one with higher void fractions and another with the lower ones, separated according to a given threshold. For the flow conditions used in this paper, the void fraction presented marginal PDF with multimodal features, thus no obvious split in two groups. Thus, the Otsu method is proposed as an unsupervised and non-parametric approach for finding this threshold based on the experimental time series. Increasing the order of the model significantly improves the accuracy of the results and a criteria based on first zero-crossing of the autocorrelation is proposed for parsimonious and representative model.

The PSD estimation process from the time series data was also discussed using the Welch's segment and average approach. The suitable choice of the averaging parameters was discussed in terms of the physical interpretation of the void fraction series.

The experimental void fraction time series were converted to the traveling wave reference frame and the phase space reconstruction using the experimental data is discussed. A interpretation of the estimated dynamical system is proposed in terms of equilibrium void fractions at both segregated pattern and dispersed bubble pattern, and in terms of the jumps between these two points.

The transition domain bounds were discussed, allowing to have an estimate of the region where the transition occurs and its parameters. Subsequently, the existence and stability of the dispersed bubble flow pattern were evaluated, giving the first proposed transition criterion based on the bublance concept. Afterwards, the energy conversion mechanisms were mapped and discussed, giving the second proposed transition criterion based on the maximum dissipated mean flow energy. The proposed transition criteria are discussed together with a data-driven identified one in order to craft a two-state Markov Chain model in order to model the stochastic nature of the uni cell. Furthermore, a discussion on the estimation of the turbulent equivalent kinematic viscosity was presented.

Finally, the numerical results from the one and two-dimensional phase-space analytical models are presented and the results are interpreted in terms of the experimental time series. Model-based time series of some relevant flow parameters are obtained and then used to discuss the relevant physics for segregated and dispersed flow patterns and transition phenomena. It is shown that the proposed transition threshold depends on the direction of the transition between the patterns, thus indicating the phenomenon of hysteresis. A bifurcation diagram of the two-dimensional stratified model is also investigated. It is constructed with the fixed points and their corresponding stability and it highlights the main features of the dynamical system. Subsequently, the two-dimensional model is integrated using the proposed transition criteria. The obtained results follows very closely a typical unit cell and and it shown that this strategy is very promising for further numerical schemes.

5.1 Summary of the main findings

- The void fraction time series was processed estimating its probability density functions through kernel methods, where the modes were interpreted as the equilibrium void fractions solutions in the Taylor bubble and slug body regions α_F and α_S.
- It is shown that a generalized correlation-based approach is suitable for estimating the void fraction wave phase velocity V_{TB}. With this approach, no pre-processing in the data is required and analytical expressions for error estimates are readily available.
- It is shown that the proposed two-state Markov chain model can adequately model the probability of transition times between the two flow patterns in the slow flow. It is shown that the proposed first order Markov Chain model can successfully describe the shorter time scales of the void fraction time series. Increasing the order of the model significantly improves the accuracy of the results and a criteria based on first zero-crossing of the autocorrelation is proposed for parsimonious and representative model. It is shown that this two-state representation is a reduced order representation that is suitable to describe second-order statistics of the two-phase flow.
- The proposed stochastic model leads to the representation of the intermittency factor and unit cell frequency as random variables, with given probability distribution. It is shown that the peak frequency value of the void fraction PSD typically matches the most prominent peak of the probability distribution, i.e., its most frequent case, rather than its mean

value. It is also shown that the distribution of the frequency of passage of the unit cell is clearly not unimodal for some experimental points. It is further shown that the proposed Markov Chain model can provide a good estimate of some slug flow features, such as the intermittency factor and the unit cell frequency.

- It is shown that the several frequency peaks typically present in the estimated PSD can be closely related to the stochastic nature of the void fraction dynamics rather than measurement noise. In addition, a correlation-based time delay estimation is proposed for the estimation of the velocity of the Taylor bubble.
- The system chaos was quantified and the phase space was reconstructed from the experimental data where the minimum number of dimensions for the deterministic dynamics of the slug flow was estimated as three, which has a physical interpretation, that the variability of the unit cell parameters derive from a three-dimensional chaotic dynamics and that such dimensionality is only achieved with the inclusion of the terms of the interfacial tensions.
- Based on the reconstructed phase space of the dynamical system, estimated from the experimental data, it is shown that the systems orbits around high and low void fraction values, corresponds to the equilibrium void fraction solutions in the Taylor bubble and slug body regions. The transition between these regions is governed by the chaotic dynamics, which is directly related to the random transition times, modelled by the Markov chain model.
- From the analytical model, it is shown that the fixed points delimit the extremes of the intervals for each region of the unit cell, as the trajectory of the dynamic system oscillates between them. The singularities points represent the jumps between flow patterns and are expected to be close to the Otsu threshold.
- The description of the function I_d is addressed where a physically and data-driven based transition model is presented, based on energy conversion processes in the region of the mixing length after the hydraulic jump.
- It is shown that the steady-state transition criterion cannot be used to assess the transient transition between the patterns.

5.2 Suggestions for further work

Based on the discussions and findings of this thesis, the following recommendations are proposed for further work:

- to consider a variable averaged kinematic equivalent viscosity in the model instead of a constant one;
- to consider a variable bubble diameter in the model instead of a constant one;
- to solve entirely the average turbulent kinetic energy equation alongside the momentum equations;
- to include additional closure relations in the investigation of the system dynamics;
- to design an experiment that allows to measure the bubble diameter distributions and the average turbulent kinetic energy in the liquid piston at the mixing length, in order to investigate experimentally the dissipation mechanisms in relation to bubble formation;
- to design an experiment that allows to measure the pressure wave signature, synchronized with void fraction measurements, in order to investigate experimentally the coupling between the pressure and void fraction wave profiles;
- investigate the generalization of the two-state Markov chain directly from the model rather than the experimental data.

BIBLIOGRAPHY

Akaike, H. A new look at the statistical model identification. **IEEE Transactions on Automatic Control**, v. 19, p. 716–723, 1974.

Ali, N.; Viggiano, B.; Tutkun, M.; Cal, R. B. Cluster-based reduced-order descriptions of two phase flows. **Chemical Engineering Science**, v. 222, 8 2020.

Andersson, R.; Andersson, B. On the breakup of fluid particles in turbulent flows. **AIChE Journal**, v. 52, n. 6, p. 2020–2030, 2006.

Andreussi, P.; Paglianti, A.; Silva, F. S. Dispersed bubble flow in horizontal pipes. **Chemical Engineering Science**, v. 54, n. 8, p. 1101–1107, 1999.

Andreussi, P.; Persen, L. Stratified gas-liquid flow in downwardly inclined pipes. **International journal of multiphase flow**, v. 13, n. 4, p. 565–575, 1987.

Andritsos, N.; Hanratty, T. Influence of interfacial waves in stratified gas-liquid flows. **AIChE journal**, v. 33, n. 3, p. 444–454, 1987.

Barnea, D. A unified model for predicting flow-pattern transitions for the whole range of pipe inclinations. **International journal of multiphase flow**, v. 13, n. 1, p. 1–12, 1987.

Barnea, D.; Brauner, N. Holdup of the liquid slug in two phase intermittent flow. **International Journal of Multiphase Flow**, v. 11, n. 1, p. 43–49, 1985.

Barnea, D.; Shoham, O.; Taitel, Y. Flow pattern transition for vertical downward two phase flow. **Chemical Engineering Science**, v. 37, n. 5, p. 741–744, 1982.

Barnea, D.; Taitel, Y. A model for slug length distribution in gas-liquid slug flow. **International Journal of Multiphase Flow**, v. 19, n. 5, p. 829–838, 1993.

Barnea, D.; Taitel, Y. Interfacial and structural stability of separated flow. **International Journal of Multiphase Flow**, v. 20, p. 387–414, 1994.

Bendiksen, K. H. An experimental investigation of the motion of long bubbles in inclined tubes. **International Journal of Multiphase Flow**, v. 10, n. 4, p. 467–483, 1984.

Bendlksen, K. H.; Malnes, D.; Moe, R.; Nuland, S. The dynamic two-fluid model olga: Theory and application. **SPE production engineering**, v. 6, n. 02, p. 171–180, 1991.

Bergles, A. E.; Collier, J.; Delhaye, J. M.; Hewitt, G.; Mayinger, F. **Two-phase flow and heat transfer in the power and process industries**. [S.l.]: Hemisphere New York, 1981.

Bertodano, M.; Fullmer, W.; Clausse, A.; Ransom, V. **Two-Fluid Model Stability, Simulation and Chaos**. Springer International Publishing, 2016. ISBN 9783319449685.

De Bertodano, M. L.; Lahey Jr, R.; Jones, O. Phase distribution in bubbly two-phase flow in vertical ducts. **International Journal of Multiphase Flow**, v. 20, n. 5, p. 805–818, 1994.

Bertodano, M. L. de; Fullmer, W. D.; Clausse, A. One-dimensional two-fluid model for wavy flow beyond the kelvin-helmholtz instability: Limit cycles and chaos. **Nuclear Engineering and Design**, v. 310, p. 656–663, 2016.

Bertodano, M. Lopez-de; Fullmer, W.; Vaidheeswaran, A. One-dimensional two-equation two-fluid model stability. **Multiphase Science and Technology**, v. 25, n. 2-4, 2013.

Bertodano, M. Lopez de; Lahey Jr, R.; Jones, O. Development of ak-ε model for bubbly two-phase flow. 1994.

Billingsley, P. **Statistical inference for Markov processes**. [S.l.]: University of Chicago Press, 1961. v. 2.

Bonizzi, M. **Transient one-dimensional modelling of multiphase slug flows**. Tese (Doutorado) — Imperial College London, 2003. Imperial College London (University of London). Disponível em: <https://spiral.imperial.ac.uk/bitstream/10044/1/8746/1/Marco_Bonizzi-2003-PhD-Thesis.pdf>.

Bonizzi, M.; Andreussi, P.; Banerjee, S. Flow regime independent, high resolution multi-field modelling of near-horizontal gas–liquid flows in pipelines. **International Journal of Multiphase Flow**, v. 35, n. 1, p. 34–46, 2009.

Bonizzi, M.; Issa, R. A model for simulating gas bubble entrainment in two-phase horizontal slug flow. **International journal of multiphase flow**, v. 29, n. 11, p. 1685–1717, 2003.

Brennen, C. **Fundamentals of Multiphase Flow**. Cambridge University Press, 2005. ISBN 9781107717671.

Brown, M.; Dellar, P. **Gas entrainment at a propagating slug front**. [S.l.], 2007.

Calderbank, P. Physical Rate Processes in Industrial Fermentation. Part I:The Interfacial Area in Gas–Liquid Contacting with MechanicalAgitation. **Trans. Inst. Chem.**, v. 36, p. 443–463, 1958.

Carneiro, J. N. E. **Simulação Numérica de Escoamentos Bifásicos no Regime de Golfadas em Tubulações Horizontais e Levemente Inclinadas**. Tese (Doutorado) — PUC-Rio, 2006.

Chanson, H. **Air bubble entrainment in free-surface turbulent shear flows**. [S.l.]: Elsevier, 1996.

Clift, R.; Grace, J.; Weber, M. **Bubbles, Drops, and Particles**. Dover Publications, 2005. (Dover Civil and Mechanical Engineering Series). ISBN 9780486445809.

Dos Santos, E. N.; Wrasse, A. D. N.; Vendruscolo, T. P.; Reginaldo, N. S.; Torelli, G.; Alves, R. F.; Naidek, B. P.; Morales, R. E.; Da Silva, M. J. Sensing Platform for Two-Phase Flow Studies. **IEEE Access**, v. 7, p. 5374–5382, 2019.

Dressler, R. F. Mathematical solution of the problem of roll-waves in inclined open channels. **Communications on Pure and Applied Mathematics**, v. 2, n. 2-3, p. 149–194, 1949.

Drew, D.; Passman, S. **Theory of Multicomponent Fluids**. Springer, 2014. ISBN 9781468492262.

Dukler, A. E.; Hubbard, M. G. A model for gas-liquid slug flow in horizontal and near horizontal tubes. **Industrial & Engineering Chemistry Fundamentals**, v. 14, n. 4, p. 337–347, 1975.

Fabre, J.; Liné, A. Modeling of two-phase slug flow. **Annual review of fluid mechanics**, v. 24, n. 1, p. 21–46, 1992.

Fabre, J.; Line, A. S.; Peresson, L. Two-fluid/two-flow-pattern model for transient gas-liquid flow in pipes. n. July, 1989.

Fagundes Netto, J.; Fabre, J.; Peresson, L. Shape of long bubbles in horizontal slug flow. **International Journal of Multiphase Flow**, v. 25, n. 6, p. 1129–1160, 1999.

Fullmer, W.; Bertodano, M. Lopez de; Ransom, V. *et al.* The kelvin-helmholtz instability: comparisons of one-and two-dimensional simulations. In: **14th International Topical Meeting on Nuclear Reactor Thermal Hydraulics (NURETH-14)**. [S.l.: s.n.], 2011.

Gao, Y.; Brennan, M. J.; Joseph, P. F. A comparison of time delay estimators for the detection of leak noise signals in plastic water distribution pipes. **Journal of Sound and Vibration**, v. 292, n. 3-5, p. 552–570, may 2006.

Géron, A. **Hands-On Machine Learning with Scikit-Learn and TensorFlow: Concepts, Tools, and Techniques to Build Intelligent Systems**. O'Reilly Media, 2017. ISBN 9781491962244.

Giddings, J. A. **One dimensional models for slugging in channel flow**. 2017. Disponível em: <http://eprints.nottingham.ac.uk/38801/>.

Giddings, J. A.; Billingham, J. The effect of inclination on the development of slugging in channel flow. **IMA Journal of Applied Mathematics**, v. 84, n. 2, p. 366–384, 2019.

Gomez, L. E.; Shoham, O.; Schmidt, Z.; Chokshi, R. N.; Northug, T. Unified mechanistic model for steady-state two-phase flow: Horizontal to vertical upward flow. **SPE Journal**, v. 5, n. 3, p. 339–350, sep 2000.

Hassab, J. C.; Boucher, R. E. Optimum Estimation of Time Delay by a Generalized Correlator. **IEEE Transactions on Acoustics, Speech, and Signal Processing**, v. 27, n. 4, p. 373–380, 1979.

Hinze, J. O. Fundamentals of the hydrodynamic mechanism of splitting in dispersion processes. **AIChE Journal**, v. 1, n. 3, p. 289–295, 1955.

Hoque, A.; Aoki, S.-I. A quantitative analysis of energy dissipation among three typical air entrainment phenomena. **Environmental Fluid Mechanics**, v. 5, n. 4, p. 325–340, 2005.

Ishii, M.; Hibiki, T. **Thermo-fluid dynamics of two-phase flow**. [S.l.]: Springer Science & Business Media, 2011.

Issa, R.; Kempf, M. Simulation of slug flow in horizontal and nearly horizontal pipes with the two-fluid model. **International Journal of Multiphase Flow**, v. 29, n. 1, p. 69–95, 2003.

Kantz, H.; Schreiber, T. **Nonlinear time series analysis**. [S.l.]: Cambridge university press, 2004. v. 7.

Kataoka, I.; Serizawa, A. Basic equations of turbulence in gas-liquid two-phase flow. **International Journal of Multiphase Flow**, v. 15, n. 5, p. 843–855, 1989.

Katz, R. W. On some criteria for estimating the order of a markov chain. **Technometrics**, v. 23, p. 243, 8 1981.

Kennel, M. B.; Brown, R.; Abarbanel, H. D. Determining embedding dimension for phase-space reconstruction using a geometrical construction. **Physical review A**, v. 45, n. 6, p. 3403, 1992.

Kolmogorov, A. On the disintegration of drops in a turbulent flow. In: **Dokl. Akad. Nauk SSSR**. [S.l.: s.n.], 1949. v. 66, p. 30.

Lance, M.; Bataille, J. Turbulence in the liquid phase of a uniform bubbly air-water flow. **Journal of fluid mechanics**, v. 222, p. 95–118, 1991.

Launder, B. E.; Spalding, D. B. The numerical computation of turbulent flows. In: **Numerical prediction of flow, heat transfer, turbulence and combustion**. [S.l.]: Elsevier, 1973. p. 96–116.

LeVeque, R. **Numerical Methods for Conservation Laws**. Birkhäuser Basel, 2013. (Lectures in mathematics ETH Zürich). ISBN 9783034851169.

Liu, D.; Yu, J. Otsu method and k-means. In: **2009 Ninth International Conference on Hybrid Intelligent Systems**. [S.l.: s.n.], 2009. v. 1, p. 344–349.

Mahvash, A.; Ross, A. Two-phase flow pattern identification using continuous hidden markov model. **International Journal of Multiphase Flow**, v. 34, p. 303–311, 3 2008.

Malnes, D. **Slug flow in vertical, horizontal and inclined pipes**. 1982.

Mazzitelli, I.; Lohse, D. Evolution of energy in flow driven by rising bubbles. **Physical Review E**, v. 79, n. 6, 2009.

Morel, C. **Mathematical Modeling of Disperse Two-Phase Flows**. Springer International Publishing, 2015. (Fluid Mechanics and Its Applications). ISBN 9783319201030.

Munkejord, S. T. **Analysis of the two-fluid model and the drift-flux model for numerical calculation of two-phase flow**. 2006.

Needham, D.; Billingham, J.; Schulkes, R.; King, A. The development of slugging in two-layer hydraulic flows. **IMA journal of applied mathematics**, v. 73, n. 1, p. 274–322, 2008.

Needham, D. J.; Merkin, J. H. On roll waves down an open inclined channel. **Proceedings of the Royal Society of London. A. Mathematical and Physical Sciences**, v. 394, n. 1807, p. 259–278, 1984.

Nguyen, T. P. K. **Analyse mathématique et simulation numérique des modèles d'écoulements bouillants pour la thermohydraulique des centrales nucléaires**. Tese (Doutorado) — Université Paris-Saclay, 2016. Thèse de doctorat dirigée par Chalons, Christophe et Ndjinga, Michaël Mathématiques appliquées Université Paris-Saclay (ComUE) 2016. Disponível em: <http://www.theses.fr/2016SACLV007/document>.

Norris, J. R. **Markov Chains**. Cambridge University Press, 1997. ISBN 9780521481816.

Nossen, J.; Shea, R. H.; Rasmussen, J. New developments in flow modelling and field data verification. In: **2nd North American conference on multiphase technology, BHR Group conference series**. [S.l.: s.n.], 2000.

Nydal, O.; Andreussi, P. Gas entrainment in a long liquid slug advancing in a near horizontal pipe. **International Journal of Multiphase Flow**, v. 17, n. 2, p. 179–189, 1991.

Otsu, N. A threshold selection method from gray-level histograms. **IEEE transactions on systems, man, and cybernetics**, v. 9, n. 1, p. 62–66, 1979.

Ouyang, L.-B.; Aziz, K. Development of new wall friction factor and interfacial friction factor correlations for gas-liquid stratified flow in wells and pipelines. In: OnePetro. **SPE Western Regional Meeting**. [S.l.], 1996.

Panton, R. L. **Incompressible flow**. [S.l.]: John Wiley & Sons, 2013. 912 p. ISBN 9781118013434.

Park, J.-W.; Drew, D.; Lahey, Jr, R. The analysis of void wave propagation in adiabatic monodispersed bubbly two-phase flows using an ensemble-averaged two-fluid model. **International Journal of Multiphase Flow**, v. 24, n. 7, p. 1205–1244, 1999.

Pope, S.; Eccles, P.; Pope, S.; Press, C. U. **Turbulent Flows**. Cambridge University Press, 2000. ISBN 9780521598866.

Rafteryt, A. E. A model for high-order markov chains. **Journal of the Royal Statistical Society. Series B (Methodological). J. R. Statist. Soc. B**, v. 47, p. 528–539, 1985.

Robinson, M.; Fowler, A. C.; Alexander, A.; O'Brien, S. B. Waves in guinness. **Physics of Fluids**, v. 20, n. 6, p. 067101, 2008.

Rodrigues, R. L.; Cozin, C.; Naidek, B. P.; Marcelino Neto, M. A.; da Silva, M. J.; Morales, R. E. Statistical features of the flow evolution in horizontal liquid-gas slug flow. **Experimental Thermal and Fluid Science**, v. 119, p. 110203, 2020.

Rosa, E.; Mazza, R.; Morales, R.; Rodrigues, H.; Cozin, C. Analysis of slug tracking model for gas–liquid flows in a pipe. **Journal of the Brazilian Society of Mechanical Sciences and Engineering**, v. 37, n. 6, p. 1665–1686, 2015.

Rosenstein, M. T.; Collins, J. J.; De Luca, C. J. A practical method for calculating largest lyapunov exponents from small data sets. **Physica D: Nonlinear Phenomena**, v. 65, n. 1-2, p. 117–134, 1993.

Di Salvo, F. R. **Mechanistic Models to Simulate Slug Flow in Horizontal and Vertical Pipes**. Tese (Doutorado) — Imperial College London, 2014.

Sarica, C.; Zhang, H.-Q.; Wilkens, R. J. Sensitivity of slug flow mechanistic models on slug length. **Journal of energy resources technology**, v. 133, n. 4, 2011.

Sato, Y.; Sekoguchi, K. Liquid velocity distribution in two-phase bubble flow. **International Journal of Multiphase Flow**, v. 2, n. 1, p. 79–95, 1975.

Savitzky, A.; Golay, M. J. E. Smoothing and differentiation of data by simplified least squares procedures. **Analytical Chemistry**, v. 36, n. 8, p. 1627–1639, 1964.

Schlichting, H.; Gersten, K. Boundary layer theory (chapter 21). **Springer**, v. 8, p. 523, 1979.

Schwarz, G. "estimating the dimension of a model.". **The Annals of Statistics**, v. 6, p. 461 – 464, 1978.

Shin, K.; Hammond, J. **Fundamentals of signal processing for sound and vibration engineers**. [S.l.]: John Wiley & Sons, 2008. 403 p. ISBN 978-0470511886.

Shippen, M.; Bailey, W. J. Steady-state multiphase flow past, present, and future, with a perspective on flow assurance. **Energy & Fuels**, v. 26, n. 7, p. 4145–4157, 2012.

Shoham, O. **Mechanistic Modeling of Gas-liquid Two-phase Flow in Pipes**. Society of Petroleum Engineers, 2006. ISBN 9781555631079.

Soedarmo, A. A.; Rodrigues, H. T.; Pereyra, E.; Sarica, C. A new objective and distribution-based method to characterize pseudo-slug flow from wire-mesh-sensors (wms) data. **Experimental Thermal and Fluid Science**, v. 109, p. 109855, 2019.

Soize, C. **Uncertainty Quantification - An Accelerated Course with Advanced Applications in Computational Engineering**. 1st. ed. [S.l.]: Elsevier, 2017. (Interdisciplinary Applied Mathematics). ISBN 978-3-319-54339-0.

Soto-Cortes, G.; Pereyra, E.; Sarica, C.; Torres, C.; Soedarmo, A. Signal processing for slug flow analysis via a voltage or instantaneous liquid holdup time-series. **Flow Measurement and Instrumentation**, v. 79, p. 101968, 2021.

Spedding, P.; Hand, N. Prediction in stratified gas-liquid co-current flow in horizontal pipelines. **International journal of heat and mass transfer**, v. 40, n. 8, p. 1923–1935, 1997.

Strogatz, S.; Dichter, M. **Nonlinear Dynamics and Chaos, 2nd ed. SET with Student Solutions Manual**. Avalon Publishing, 2016. (Studies in Nonlinearity). ISBN 9780813350844.

Stuhmiller, J. The influence of interfacial pressure forces on the character of two-phase flow model equations. **International Journal of Multiphase Flow**, v. 3, n. 6, p. 551–560, 1977.

Taitel, Y.; Barnea, D. Two-phase slug flow. **Advances in Heat Transferl**, v. 20, p. 83–132, 1990.

Taitel, Y.; Dukler, A. E. A model for predicting flow regime transitions in horizontal and near horizontal gas-liquid flow. **AIChE Journal**, v. 22, n. 1, p. 47–55, 1976.

Teodorescu, I. Maximum Likelihood Estimation for Markov Chains. may 2009.

Tomiyama, A.; Kataoka, I.; Zun, I.; Sakaguchi, T. Drag coefficients of single bubbles under normal and micro gravity conditions. **JSME International Journal Series B Fluids and Thermal Engineering**, v. 41, n. 2, p. 472–479, 1998.

Tong, H. Determination of the order of a markov chain by akaike's information criterion. **Journal of Applied Probability**, v. 12, p. 488–497, 1975.

Vaidheeswaran, A.; Fullmer, W. D.; Chetty, K.; Marino, R. G.; Bertodano, M. Lopez de. Stability analysis of chaotic wavy stratified fluid-fluid flow with the 1d fixed-flux two-fluid model. In: American Society of Mechanical Engineers. **Fluids Engineering Division Summer Meeting**. [S.l.], 2016. v. 50299, p. V01BT33A013.

Vela-Martín, A.; Avila, M. Deformation of drops by outer eddies in turbulence. **Journal of Fluid Mechanics**, v. 929, 2021.

Vieira, S. C.; Geest, C. van der; Fabro, A. T.; Castro, M. S. de; Bannwart, A. C. Experimental study and modelling of developing intermittent slug flow in inclined annular pipelines. **Journal of Petroleum Science and Engineering**, p. 107204, mar 2020.

Vieira, S. C.; van der Geest, C.; Fabro, A. T.; Castro, M. S. de; Bannwart, A. C. Intermittent slug flow identification and characterization from pressure signature. **Mechanical Systems and Signal Processing**, v. 148, p. 107148, 2021.

Virtanen, P.; Gommers, R.; Oliphant, T. E.; Haberland, M.; Reddy, T.; Cournapeau, D.; Burovski, E.; Peterson, P.; Weckesser, W.; Bright, J.; van der Walt, S. J.; Brett, M.; Wilson, J.; Millman, K. J.; Mayorov, N.; Nelson, A. R. J.; Jones, E.; Kern, R.; Larson, E.; Carey, C. J.; Polat, İ.; Feng, Y.; Moore, E. W.; VanderPlas, J.; Laxalde, D.; Perktold, J.; Cimrman, R.; Henriksen, I.; Quintero, E. A.; Harris, C. R.; Archibald, A. M.; Ribeiro, A. H.; Pedregosa, F.; van Mulbregt, P.; SciPy 1.0 Contributors. SciPy 1.0: Fundamental Algorithms for Scientific Computing in Python. **Nature Methods**, v. 17, p. 261–272, 2020.

Wallis, G. **One-dimensional two-phase flow**. [S.l.]: McGraw-Hill, 1969.

Whitham, G. **Linear and Nonlinear Waves**. Wiley, 2011. (Pure and Applied Mathematics: A Wiley Series of Texts, Monographs and Tracts). ISBN 9781118031209.

Zabaras, G. Prediction of slug frequency for gas/liquid flows. **SPE Journal**, v. 5, n. 03, p. 252–258, 2000.

Zhang, D.; Deen, N.; Kuipers, J. Numerical simulation of the dynamic flow behavior in a bubble column: a study of closures for turbulence and interface forces. **Chemical Engineering Science**, v. 61, n. 23, p. 7593–7608, 2006.

Zhang, H.-Q.; Wang, Q.; Sarica, C.; Brill, J. P. A unified mechanistic model for slug liquid holdup and transition between slug and dispersed bubble flows. **International journal of multiphase flow**, v. 29, n. 1, p. 97–107, 2003.

Zhong-Ke, G.; Li-Dan, H.; Ning-De, J. Markov transition probability-based network from time series for characterizing experimental two-phase flow. **Chinese Physics B**, v. 22, 5 2013.

Annex

ANNEX A – KINEMATIC OR CONTINUITY WAVE

The purpose of this Section is to relate the Taylor bubble velocity V_{TB} to the kinematic wave velocity V_w, showing that they are equivalent in the context of this thesis. In addition, the Taylor bubble velocity V_{TB} is related with the discontinuity propagation speed that configure the mass shocks at the hydraulic jump in the mixing region after the Taylor bubble tail.

The propagation speed of the kinematic or continuity wave can be obtained from the averaged mass conservation law for incompressible fluids (Ishii; Hibiki, 2011)

$$\frac{\partial \alpha_k}{\partial t} + \frac{\partial}{\partial z}\left(\alpha_k v_k\right) = 0. \tag{A.1}$$

Considering the volumetric flux $j_k = \alpha_k v_k$ and substituting

$$\frac{\partial \alpha_k}{\partial t} + \frac{\partial j_k}{\partial z} = 0. \tag{A.2}$$

Applying the chain rule and standardizing for the gas phase, we have the kinematic wave equation for the void fraction α

$$\frac{\partial \alpha}{\partial t} + \frac{\partial j_2}{\partial \alpha}\frac{\partial \alpha}{\partial z} = 0, \tag{A.3}$$

$$\frac{\partial \alpha_k}{\partial t} + V_w \frac{\partial \alpha_k}{\partial z} = 0, \tag{A.4}$$

where $V_w = \partial j_2 / \partial \alpha$ is the kinematic or continuity wave velocity (Wallis, 1969). Considering the velocity field obtained through the constant mixture flow solution, from Equation 2.114 at Section 2.3.1

$$V_w = \frac{\partial j_2}{\partial \alpha} = \frac{\partial}{\partial \alpha}\left(\alpha v_2\right) = \frac{\partial}{\partial \alpha}\left[\alpha\left(V_{TB} + \frac{M_2}{\alpha}\right)\right] = V_{TB}. \tag{A.5}$$

Therefore, the Taylor bubble velocity V_{TB} and the kinematic wave velocity V_w are equivalent.

The slug flow pattern presents a quasi-periodic succession of coexisting alternating patterns (stratified and dispersed bubbles in the horizontal case) called the unit cell model and a discontinuity in these transitions that need to be addressed (Shoham, 2006). These discontinuities can be interpreted as shock waves that are formed when two or more characteristic parametric curves meet along the z domain. As each characteristic transports a certain constant value of the void fraction α, when they meet, it would be as if at the meeting point the field had all the values carried simultaneously, thus configuring a jump or a discontinuity. Since the derivatives are not defined in the moving discontinuity at $z_s(t)$, the problem must be addressed in its weak conservative form. It will be treated as a Cauchy initial value problem but with a jump from constant levels over a moving domain interval $\Omega_s(t) = [z_L(t), z_R(t)]$ that contains the discontinuity at $z_s(t)$, which is commonly called the Riemann problem (LeVeque, 2013; Whitham, 2011)

$$\int_{\Omega_s(t)} \left[\frac{\partial \alpha}{\partial t} + \frac{\partial}{\partial z} \left(\alpha v_2 \right) \right] dz = 0, \tag{A.6}$$

$$\int_{\Omega_s(t)} \frac{\partial \alpha}{\partial t} dz = - \left[\left(\alpha_R v_2^R \right) - \left(\alpha_L v_2^L \right) \right]. \tag{A.7}$$

Applying the Leibniz rule on the LHS

$$\frac{d}{dt} \int_{z_L(t)}^{z_R(t)} \alpha dz + \alpha_L \frac{d}{dt} \left[z_L(t) \right] - \alpha_R \frac{d}{dt} \left[z_R(t) \right] = - \left(\alpha_R v_2^R - \alpha_L v_2^L \right). \tag{A.8}$$

Let's assume the moving domain interval $\Omega_s(t)$ has the arbitrary length ζ around $z_s(t)$

$$\Omega_s(t) = [z_L(t), z_R(t)] = [z_s(t) - \zeta, z_s(t) + \zeta]. \tag{A.9}$$

Substituting the moving domain interval and considering a constant arbitrary length ζ and that the void fraction profile α does not change over the moving discontinuity reassembling a Heaviside distribution

$$\frac{d}{dt} \int_{z_s(t)-\zeta}^{z_s(t)+\zeta} \alpha dz + \alpha_L \frac{d}{dt} \left[z_s(t) - \zeta \right] - \alpha_R \frac{d}{dt} \left[z_s(t) + \zeta \right] = - \left(\alpha_R v_2^R - \alpha_L v_2^L \right), \tag{A.10}$$

$$\frac{d}{dt} \left[z_s(t) \right] = \frac{\left(\alpha_R v_2^R - \alpha_L v_2^L \right)}{\left(\alpha_R - \alpha_L \right)} = V_{TB}, \tag{A.11}$$

where V_{TB} is the unit cell or the discontinuity translation velocity describing the Rankine-Hugoniot jump condition for the kinematic void fraction wave equation (LeVeque, 2013; Whitham, 2011) .